

Alma Mater Studiorum – Università di Bologna

DOTTORATO DI RICERCA IN
Scienze della Terra, della Vita e dell' Ambiente

Ciclo XXXIV

Settore Concorsuale: 04/A3

Settore Scientifico Disciplinare: GEO/04

Landslide activity in contrasting land-cover settings constrained by
multi-temporal inventorying

Presentata da: Sharon Pittau

Coordinatore Dottorato

Prof.ssa Maria Giovanna Belcastro

Supervisore

Prof. Francesco Brardinoni

Esame finale anno 2022

Contents

ABSTRACT	1
CHAPTER 1: Introduction	3
1.1 Evaluating landslide activity and sediment transfer through multi-temporal inventorying.....	3
1.2 Landsliding and land-cover history.....	4
1.3 Aims and Structure.....	8
References	8
CHAPTER 2: A multi-temporal mapping approach for improving the temporal and spatial characterization of landslide activity in clay-rich terrain.....	17
Abstract	18
1. Introduction	19
2. Study area	21
3. Data Collection and Methods	23
4. Results.....	26
5. Discussion	33
6. Conclusions	35
Acknowledgements.....	36
References	36
CHAPTER 3: Historical (1954-2018), basin-wide earthflow activity, agricultural land abandonment and the role of badlands in a changing climate	40
Abstract	41
1. Introduction	42
2. Study area	43
3. Methods.....	46
4. Historical background	51
4.1 Hydro-meteorological forcing (1950-2018).....	51
4.2 Historical land-cover changes (1853-2018).....	53
5. Results.....	57

5.1 Landslide activity across lithologies.....	58
5.2 Landslide geometry across lithologies and land cover types.....	60
5.3 Temporal variability.....	63
6. Discussion and conclusions.....	69
Acknowledgements.....	73
References.....	73
Supplementary materials.....	77

CHAPTER 4: Glaciated landscape structure, cutblock location, and the response of shallow rapid failures to forest clearing in coastal British Columbia 80

Abstract.....	81
1. Introduction.....	82
2. Study area.....	84
3. Methods.....	87
3.1 Landslide inventories.....	87
3.2 Landslide magnitude-frequency analysis.....	91
4. Results.....	92
4.1 Integrating field-based and API-derived landslide data.....	92
4.2 Time scales of disturbance and recovery.....	97
4.3 Effects on landslide geometry, magnitude and frequency.....	100
5. Discussion.....	105
5.1 Effects of landslide geometry and sediment transfer.....	105
5.2 Landscape structure, cutblock positioning and the size-frequency relation of shallow rapid failures.....	107
6. Conclusions.....	113
Acknowledgements.....	114
References.....	114
Tables.....	124
Supplementary material.....	128

CHAPTER 5: Concluding Remarks and Summary131

ABSTRACT

This doctoral thesis focuses on the study of historical shallow landslide activity over time in response to anthropogenic forcing on land use, through the compilation of multi-temporal landslide inventories. The study areas, located in contrasting settings and characterized by different history of land-cover changes, include the Sillaro River basin (Italy) and the Tsitika and Eve River basins (coastal British Columbia). The Sillaro River basin belongs to clay-dominated settings of the Northern Apennines, characterized by unglaciated terrain with extensive badland development, and dominated by earth slides and earthflows. Here, forest removal began in the Roman period and has been followed by agricultural land abandonment and natural revegetation in recent time. By contrast, the formerly glaciated Tsitika-Eve River basins sit in the temperate rainforest of the Pacific Northwest, characterized by granitic and basaltic lithologies, and dominated by debris slides, debris flows and debris avalanches. In this setting, anthropogenic impacts started in 1960's and have involved logging operation for industrial forest management.

In Emilia-Romagna (E-R), where the Sillaro River basin is located, the regional Geological Survey has compiled and has been managing a region-wide landslide inventory, whose historical (i.e., post-1954) degree of completeness is presently unknown. To address this gap, the existing E-R inventory is integrated and compared with a multi-temporal landslide mapping approach, which includes visual interpretation of thirteen sequential aerial photo sets in the 1954-2020 period and confirmatory fieldwork, applied to four landslide sites of the Sillaro River basin. Specific objectives include evaluating the advantages of higher resolution mapping for characterizing (i) landslide extent, geometry and activity through time; and (ii) landslide interaction with the drainage network. Results display that the proposed multi-temporal mapping approach allows to record occurrences and recurrences and to reduce mapping uncertainty on existing landslide polygons, but mostly provides insights on process understanding. Therefore, an added value of this mapping approach lies in its ability to detect different styles of landsliding and define most likely scenarios of evolution at the site-scale, through detection of (i) source-to-sink pathways, (ii) revegetation patterns, (iii) headscarp migration, (iv) changes at landslide terminus and/or induced changes in the geometry of the channel bed.

This multi-temporal approach is then applied at the Sillaro River basin-scale (1954-2018) and used to investigate landslide activity in relation to lithologies (i.e., claystones of the Ligurian, Epiligurian and Padano-Adriatic Units, as well as sandstones & marls of the terrigenous Flysch Complex), historical land-cover changes (i.e., land abandonment followed by natural vegetation regrowth) and precipitation. Results show that landslides occur mainly in badlands and transitional shrubs of claystones and are strongly controlled by lithology. In the time window considered, recurring landslides are dominant and at a site can recur up to 9 times. With respect to landslide geometry, lengths and areas are chiefly conditioned by terrain morphometry and lithology, whereas land cover appears to play a secondary role, except on a limited cluster of occurrences in arable crops and meadows, which resulted distinctively shorter and smaller. Analyses on landslide temporal variability suggest complex interactions between landsliding and land cover types, modulated by slope gradient

and lithology. Overall, landslide activity is highest during a period of land-cover stability (i.e., between 1997 and 2018), where a decrease in total precipitation and increase of extreme events is recorded. Accordingly, high correlation values between landslide activity and specific precipitation indices were found. In particular, badlands turned out being the most sensitive sites to changes in precipitation, with highest landslide density between 1997 and 2018 in all but the Padano-Adriatic claystones. In these latter, landslide densities in badlands are highest between 1955 and 1976, when agricultural pressure peaked, interpreted as consequence of the temporary expansion of cropland onto unstable badlands terrain.

Finally, the effects of forest harvesting in the Tsitika and Eve basins on landslide activity are evaluated by integrating field- and remotely-derived landslide inventories with historical information on logging. In particular, the work examines the geometry of debris slides and long runout failures (i.e., debris flows and avalanches) in cut and uncut terrain, and evaluates the effects of forest harvesting on landslide frequency and size. Results display no significant dependency of landslide depth with length, width and therefore area, regardless of land use and movement type. Post-logging landslide occurrences are highest after 7-9 years and recover to undisturbed rates after 16-19 years since timber harvesting has ceased. Due to the low elevation of cutblock development, logging generates landslides at low elevations and low slopes, where they would not normally occur. This topographic position has no effect on the size-frequency relation of debris slides, but limits the size of logging-related long runout failures. In pristine forest, analyses suggest that glaciated landscape structure exerts primary control on the elevation and slope gradient of landslide initiation, imposing constraints on local relief (available energy), slope length, and therefore maximum landslide length. When morphologic position at initiation is considered, constraints on landslide size and consequently on the size-frequency relation become apparent. Accordingly, the rollover occurs at transition among different morphologic position at initiation, controlled by first-order valley wall geometry for primary movements (i.e., gully headwall and open slope) and by the geometry of second-order features, such as incisions on the hillslopes (i.e., gully depth) and valley floors (i.e., escarpment depth), for secondary movements (i.e., gully sidewall and escarpment).

CHAPTER 1

Introduction

1.1 Evaluating landslide activity and sediment transfer through multi-temporal inventoring

Landslides are dominant geomorphic processes of sediment production in mountain environments. They modulate sediment and carbon fluxes from hillslopes and steep, high-order streams, down to lowland, fluvial systems (Gomi et al., 2002). Owing to the variety of physiographic settings on which a combination of tectonic, climatic and anthropogenic forcing interact at different characteristic time scales, understanding landslide activity and landslide sediment dynamics remain complex topics of investigation. In this context, improved knowledge is critical for addressing basic scientific issues, like sediment delivery to streams (Dadson et al., 2004; Imaizumi & Sidle, 2007; Brardinoni et al., 2009) and landscape evolution (Hovius et al., 1998; Korup et al., 2010), as well for solving practical problems, including sediment management and the prevention of landslide-induced disasters (Fan et al., 2019).

Depending on the study objectives and the landslide types involved (Cruden & Varnes, 1996; Hungr et al., 2014), landslide dynamics may be addressed at a variety of spatial and temporal scales, by means of different techniques. For example, at the site scale, in single instrumented landslides, real-time hydraulic, geophysical, and geodetic monitoring has yielded valuable insights into the physical behavior of earthflow surges (Bertello et al., 2018; Squarzoni et al., 2020). Similarly, in instrumented reaches, monitoring of the flow and the channel bed conditions have been critical for characterizing the mechanics of debris-flow events (McArdell et al., 2007; McCoy et al., 2010) and validate prior mechanical formulations (Iverson, 1997, 2005). More recently, the combination of both classical and novel techniques, including geodetic surveys, radar interferometry (InSAR) and UAV-based photogrammetry, have allowed documenting the response of single (and a few) deep-seated, gravitational deformations to meteorological forcing at seasonal, annual, and decadal resolution (Corsini et al., 2009; Bayer et al., 2017; Confuorto et al., 2017; Guerriero et al., 2017). In the past decade, LiDAR- and Structure-from-Motion technology have proved extremely useful - through the differencing of sequential, high-resolution DEMs - for mapping topographic change and quantifying volumetric rates of erosion and deposition along steep headwater systems, over scales of 5-10 km² (e.g., Theule et al., 2012; Cavalli et al., 2017; Barnard et al., 2020).

When wishing to pursue a rapid evaluation of landslide activity and sediment transfer at basin, regional and even orogen scales across effective time scales of environmental change (i.e., decades), despite recent dramatic technological advances in remote sensing, an increasing degree of spatial and temporal resolution is inevitably

lost, and higher levels of uncertainty are involved. At such spatial and temporal scales, investigation typically relies on multi-temporal landslide inventories, compiled through visual interpretation of historical sets of optical imagery (Guzzetti et al., 2012). Quantification of landslide sediment transfer via landslide inventorying is particularly well suited for rapid slope failures (Cruden & Varnes, 1996), including avalanches, flows and slides characterized by high mobility (e.g., Brardinoni et al., 2013), which deliver discrete sediment pulses from initiation sites down to well-defined deposition zones, or directly into the channel network (Reid & Dunne, 1996). Indeed, inventories of high mobility, rapid slope failures are critical tools for evaluating sediment transfer in response to individual storms (Rickenmann & Koschni, 2010; Mondini et al., 2011) and earthquakes (Keefer, 2000; Parker et al., 2011) over their characteristic spatial scales of disturbance (Nakamura et al., 2000). Similar inventories are also instrumental for assessing lithological (Guzzetti et al., 1996; Brardinoni et al., 2012) and land-use effects (Jacob, 2000; Sidle & Ochiai, 2006) on decadal landslide sediment transfer, and allow disentangle local variability (e.g., monitored at instrumented sites) from representative regional patterns.

For predictive purpose, the compilation of inventories forms an indispensable preliminary step for the statistical characterization of landslide size-frequency relations (e.g., Brardinoni & Church, 2004; Malamud et al., 2004). These, in turn, provide empirical reference for hazard assessment (Hung et al., 1999; Guzzetti et al., 2002), as well as for modelling slope stability (e.g., Montgomery & Dietrich, 1994; Wu & Sidle, 1995; Cislighi et al., 2017) and landslide sediment transfer across landscape components (Benda & Dunne, 1997; Benda et al., 1998; Bennett et al., 2014). When integrated with field measurements, inventory-based estimates of volumes mobilized by rapid slope failures, aid identification of interactions between landslide and fluvial sediment yield (Dadson et al., 2004; Brardinoni et al., 2009), and may help detect transient responses to climatic (Meyer et al., 1992) and anthropogenic (Imaizumi et al., 2008) disturbance.

1.2 Landsliding and land-cover history

Since the development of agricultural communities in Europe and Asia in the mid-Holocene, humans have substantially altered the landscape through land cover changes. The most striking of these anthropogenic changes is undoubtedly forest removal for agriculture and grazing, and as a source of fuel and construction material (Kaplan et al., 2009). In an epoch of global change, where humans have become dominant agents of geomorphic disturbance (Tarolli et al., 2019), addressing the effects of land cover changes on landslide activity gains importance beyond the local scale, considering the spatial variability in: (i) land cover history; and (ii) sociopolitical priorities that drive land cover change today (Mensing et al., 2018). On one hand, mountain forests are undergoing increasing anthropogenic pressure (e.g., Forbes & Broadhead, 2013; Zeng et al., 2018), for example across the tropics. On the other hand, agricultural land abandonment across large parts of Europe has led to progressive expansion of transitional brushland and woodland.

Expansion of forest cover in a given basin implies an increase in rainfall interception (Gallart et al., 1997; Llorens et al., 1997) and a consequent reduction of direct runoff. This leads to more buffered hydrological

responses, accompanied by significant decrease in surficial erosion and sediment redistribution (e.g., García-Ruiz & Lana-Renault, 2011). The effects of land cover changes are particularly relevant for shallow rapid failures, where trees ensure increased slope stability through root cohesion and additional water interception capacity, thus reducing soil water content (e.g., Asdak et al., 1998; Bischetti et al., 2009; Reid & Lewis, 2009; Winkler et al., 2010). Consequently, land cover changes can modify landslide typology and behaviour, their frequency and spatial distribution (see Sidle & Ochiai, 2006 for a comprehensive review).

This doctoral thesis examines basin-wide landslide activity over decadal time scales in contrasting physiographic settings characterized by different history of land cover change. Specifically, we look at the Northern Apennines (Italy) in unglaciated, claystone-dominated terrain, where significant forest removal began since the Roman Period and was followed by widespread agricultural land abandonment after WW2. This setting is contrasted with the heavily glaciated Vancouver Island (coastal British Columbia, Canada), where forest practices began in 1960's. We assess landslide activity through the compilation of multi-temporal landslide inventories.

In many European countries, the onset of significant and systematic forest removal dates back to the Roman Period, with forests in many countries being substantially cleared before the Industrial Revolution (ca. 1790-1900) (Kaplan et al., 2009; Mensing et al., 2018). Across the Mediterranean, population started to grow steadily from the end of the 15th century, reaching a peak in the middle of the 19th century. Population growth pushed forest conversion to cultivated land and pasture (García-Ruiz & Lana-Renault, 2011), possibly inducing widespread badlands formation (or expansion) in clay-dominated settings. In this context, sociopolitical changes associated with post-WW2 recovery and modern industrial development, led to widespread people displacement from rural areas to cities and thus to agricultural land abandonment, with consequent recolonization by transitional shrubs and natural forests (Keestra et al., 2009; Preciso et al., 2012; Pavanelli et al., 2019). While lowland Mediterranean fluvial systems have responded to these land cover changes with peculiar channel adjustments (e.g., Scorpio & Piégay, 2021), research efforts on landslide response are mainly concerned with susceptibility assessment (Table 1). As a result, a quantitative evaluation of landslide activity and relevant sediment transfer is missing.

With reference to clay-dominated Mediterranean terrain, where badlands are common, existing work is mainly focused on soil erosion and badland evolution (Gallart et al., 2013; Martínez-Murillo & Nadal-Romero, 2018; Nadal-Romero et al., 2021). Erosion rates on badlands are typically analysed by dynamic or volumetric methods (De Ploey & Gabriels, 1980; Sirvent et al., 1997; Nadal-Romero & García-Ruiz, 2018). Dynamic methods typically measure water and sediment fluxes over plots (e.g., Regüés et al., 1995) and micro-catchments (e.g., Mathys et al., 2003). Volumetric methods aim to measure erosion rates through the analysis of topographic changes. Historically, volumetric methods have relied on sparse observations across relatively small areas, based on erosion pins (e.g., Benito et al., 1992; Barnes et al., 2016) or microprofile metrics (e.g., Sirvent et al., 1997; Descroix & Olivry, 2002). Small-scale measurements, although crucial, are associated

with a number of limitations, especially when wishing to extrapolate findings at the watershed scale for basic and applied purposes (Sidle et al., 2017). In this context, there is a need to address issues of spatial scaling.

In the past decade, advances in high-resolution topographic surveying (e.g., Tarolli, 2014; Passalacqua et al., 2015) have offered the opportunity to examine topographic changes in a more spatially distributed fashion. Nonetheless, most of the recent quantitative work on badlands is conducted over small study areas (e.g., Lucia et al., 2011; Vericat et al., 2014; Smith & Vericat, 2015; Stöcker et al., 2015; Llana et al., 2020), with only few examples addressing the topic at the basin scale (e.g., Descroix & Olivry, 2002; Aucelli et al., 2016, Bosino et al., 2019). Indeed, there is a general lack of quantitative knowledge on landslide activity in badland-dominated settings, and on how land cover changes may affect landslide occurrence across catchments.

Table 1. Basin-wide studies on landslide activity in relation to land cover changes in the Mediterranean.

Location	Study area (km²)	Number of landslides	Methodology	Time interval	Reference
Ijuez River basin, Spain	55	288	API (3 sets)	1957-2002	Begueria, 2006
Ormazal River basin, Spain	25	307	API	2006	García-Ruiz et al., 2017
Frate Creek basin, Italy	2	245	API	2009*	Persichillo et al., 2017
Versa River basin, Italy	38	196 193	SAPI	2009* 2013*	Persichillo et al., 2017
Upper Tidone R. basin, Italy	94	90	SAPI and field surveys	2014*	Persichillo et al., 2017
Rivo River basin, Italy	82	1202	API (3 sets)	1954-2007	Pisano et al., 2017
Zezeze River basin, Portugal	5064	259	SAPI	2005	Meneses et al., 2019
Vernazza R. basin, Italy	6	364	API and field surveys	2011*	Pepe et al., 2019
Val d'Aran Region, Spain	336	393	API	2013*	Shu et al., 2019

API = Aerial photo interpretation; SAPI = Satellite imagery and aerial photo interpretation; * Rainstorm.

In the temperate rainforest of the Pacific Rim, shallow rapid failures are the main geomorphic players of sediment transfer (Dietrich & Dunne, 1978; Sidle et al., 1985, Benda & Dunne, 1997), and control the geometry, the morphology, and bed texture of headwater streams (Grant & Swanson, 1995; Brummer & Montgomery, 2003; Brardinoni & Hassan, 2007). Here, forest practices and logging road construction represent the major sources of slope instability and hydro-geomorphic disturbance (see Sidle & Ochiai, 2006

for a comprehensive review). Timber harvesting (i.e., clearcutting and subsequent regeneration of secondary forest cover) history is well documented, and the impact on slope instability has been quantitatively investigated starting from 1970's. These studies have shown that timber harvesting can increase landslide sediment flux (e.g., O'Loughlin, 1972; Swanston & Swanson, 1976) and sediment delivery to streams (e.g., Reid & Dunne, 1984; Guthrie, 2002; Jordan et al., 2010) by orders of magnitude.

Table 2. Natural and logging related landslide sediment yield in basins of coastal British Columbia (modified from Hassan et al., 2005).

Location	Area (km ²)	Percent logged	Sediment delivery to	Yield (m ³ /km ² /yr)		
				Natural	Logged	Acceleration
Chapman Creek, Coast Mountains	56.0	36.3	Permanent streams	15.9	153.9	10x
			Gullies	1.9	150.5	79x
			Unchannelled slopes	1.9	66.9	35x
Centre Creek, Cascade Mountains	38.0	28.2	Permanent streams	18.5	451.6	24x
			Gullies	53.6	293.9	5x
			Unchannelled slopes	3.9	151.6	39x
Nesakwatch Creek, Cascade Mountains	48.0	10.1	Permanent streams	3.6	496.3	138x
			Gullies	32.5	1096.5	34x
			Unchannelled slopes	7.4	454.1	61x
Howe Sound, Coast Mountains	26.8	25.0	Permanent streams	65.6	920.6	14x
			Gullies	5.3	254.6	48x
			Unchannelled slopes	7	327.3	47x
San Juan River ¹ , Insular Ranges	517.0	25.0	Permanent streams	20.8	247.2	12x
			Gullies	3.6	61.6	17x
			Unchannelled slopes	1.3	74	47x
Capilano River ² , Coast Mountains	12.9	27.9	Permanent streams	175.8	102	0.6x
			Gullies	22.9	59.3	3x
			Unchannelled slopes	3.7	133.7	36x
Queen Charlotte Islands ³ , Insular Ranges	350.0	13.4	Permanent streams	60	2760	46x
			Gullies	21	370	18x
			Unchannelled slopes	79	2690	34x

¹Northwest Hydraulic Consultants (1997, unpublished report).

²Modified from Brardinoni et al., 2003b.

³Modified from Rood (1984).

With reference to the formerly glaciated landscape of coastal British Columbia, quantitative investigations on post-logging sediment transfer, associated with both timber harvesting and road construction, have reported accelerations of sediment production on the slopes comprise between 34 and 61 times, and sediment delivery to streams increased by a factor of 0.6 to 138 (Table 2). In particular, previous work on shallow landslides yielded ambiguous results on the effects that logging operations may have on the size of shallow landslides (e.g., Schwab, 1983; Jakob, 2000; Brardinoni et al., 2003a). This ambiguity may be related to different movement types and to the peculiar positions in which cutblocks are developed within the glaciated landscape

of coastal British Columbia. Indeed, a systematic statistical evaluation of the effects of forest harvesting on the magnitude and frequency of shallow landslides in relation to glaciated landscape structure, is still missing.

1.3 Aims and Structure

This PhD thesis focuses on the study of historical shallow landslide activity over time in response to anthropogenic forcing on land cover. Through the compilation of multi-temporal landslide inventories, we investigate two areas located in contrasting physiographic settings that have experienced different history of land-cover change. Study areas include the Sillaro River basin (Northern Apennines), and the Tsitika and Eve River basins (Vancouver Island, coastal British Columbia). The former belongs to the Mediterranean bio-geoclimatic zone, underlain by clayey lithology with extensive badland development, and the unglaciated terrain is dominated by earth slides and earthflows. The latter sits in the mountain temperate rainforest of the formerly glaciated Pacific Northwest, is underlain by granitic and basaltic lithologies blanketed by thick glacial and glaciofluvial deposits, and is dominated by debris slides, debris flows and debris avalanches. In the Northern Apennines, forest removal began in the Roman Period and has been followed in recent times by agricultural land abandonment and natural revegetation. By contrast, anthropogenic impacts in coastal British Columbia started at the beginning of the 20th century (i.e., in 1960's in the study basins) and have involved logging operation for industrial forest management. The general objective of this work is to evaluate and contrast the influence of different land-cover histories on settings dominated by different landslide types.

Following this introductory chapter, the thesis begins with a methodological section (Chapter 2), where a multi-temporal mapping approach is proposed and tested at four landslide sites of the Sillaro River basin. Results, in terms of inventory completeness in time and space, are compared against the existing region-wide Emilia-Romagna inventory. This approach is then applied at the Sillaro River basin scale, where the multi-temporal inventory obtained is used to investigate the landslide activity in relation to historical land cover changes (i.e., abandonment of cropland and meadows, and contingent natural forest regrowth) across geologic domains and in relation to hydro-meteorological forcing (Chapter 3). Chapter 4 is concerned with the impact of timber harvesting and road construction on landslide activity and sediment transfer in the Tsitika and Eve River basins, with a focus on the controls that interactions between landscape morphometry and cutblock location may have on landslide size-frequency relations. The thesis ends with a summary of the main findings and briefly discusses advantages and limitations associated with the compilation of multi-temporal inventories in the two physiographic settings during different periods of human-driven, land-cover dynamics (Chapter 5).

References

- Asdak, C., Jarvis, P. G., van Gardingen, P., & Fraser, A. (1998). Rainfall interception loss in unlogged and logged forest areas of Central Kalimantan, Indonesia. *Journal of Hydrology*, 206 (3-4), 237-244.
- Aucelli P.P.C., Conforti M., Della Seta M., Del Monte M., D'uva L., Roskopf C.M., & Vergari F. (2016). Multi-temporal digital photogrammetric analysis for quantitative assessment of soil erosion rates in

- the Landola catchment of the Upper Orcia Valley (Tuscany, Italy). *Land Degradation and Development*, 27, 1075–1092.
- Barnes N., Luffman I., & Nandi A. (2016). Gully erosion and freeze–thaw processes in clay-rich soils, northeast Tennessee, USA. *GeoResJ* 9–12, 67–76.
- Bayer B., Simoni A., Schmidt D., & Bertello L. (2017). Using advanced InSAR techniques to monitor landslide deformations induced by tunneling in the Northern Apennines, Italy. *Engineering Geology*, 226, 20–32.
- Beguiría S. (2006). Changes in land cover and shallow landslide activity: a case study in the Spanish Pyrenees. *Geomorphology*, 74, 196–206.
- Benda L., & Dunne T. (1997). Stochastic forcing of sediment supply to the channel network from landsliding and debris flow. *Water Resources Research*, 33(12), 2849–2863.
- Benda L., Miller D., Dunne T., Agee J., & Reeves G., (1998). Dynamic landscape systems. In: Naiman R., Bilby R. (Eds.), *River Ecology and Management: Lessons from the Pacific Coastal Ecoregion*. Springer, New York, 261–288.
- Benito G., Gutiérrez M., & Sancho C. (1992). Erosion rates in badland areas of the Central Ebro Basin (NE-Spain). *Catena* 19, 269–286.
- Bennett G. L, Molnar P., McArdeell B.W., & Burlando P. (2014). A probabilistic sediment cascade model of sediment transfer in the Illgraben. *Water Resources Research*, 50(2), 1225–1244.
- Bernard M., Steer P., Gallagher K., & Lundbek Egholm D. (2020). Modelling the effects of ice transport and sediment sources on the form of detrital thermochronological age probability distributions from glacial settings. *Earth Surface Dynamics*, 8, 931–953,
- Bertello L., Berti M., Castellaro S., & Squarzone G. (2018). Dynamics of an active earthflow inferred from surface wave monitoring. *Journal of Geophysical Research: Earth Surface*, 123 (8), 1811–1834.
- Bischetti G.B., Chiaradia E. A., Epis T., & Morlotti E. (2009). Root cohesion of forest species in the Italian Alps. *Plant Soil*, 324, 71–89.
- Bosino A., Omran A., & Maerker M. (2019). Identification, characterisation and analysis of the Oltrepo Pavese calanchi in the Northern Apennines (Italy). *Geomorphology*, 340, 53–66.
- Brardinoni F., & Church M. (2004). Representing the landslide magnitude–frequency relation: Capilano River basin, British Columbia. *Earth Surface Processes and Landforms*, 29, 115–124.
- Brardinoni F., Church M., Simoni A., & Macconi P. (2012). Lithologic and glacially conditioned controls on regional debris-flow sediment dynamics. *Geology*, 40 (5), 455–458.
- Brardinoni F., Crosta G.B., Cucchiario S., Valbuzzi E., Frattini P. (2013). Landslide Mobility and Landslide Sediment Transfer in Val di Sole, Eastern Central Alps. In: Margottini C., Canuti P, Sassa K. (Eds.), *Landslide Science and Practice*, 315–320. Springer Berlin Heidelberg: Berlin, Heidelberg.
- Brardinoni F., & Hassan M.A. (2007). Glacially-induced organization of channel-reach morphology in mountain streams. *Journal of Geophysical Research*, 112, F03013.

- Brardinoni F., Hassan M.A., Rollerson T., & Maynard D. (2009). Colluvial sediment dynamics in mountain drainage basins. *Earth and Planetary Science Letters*, 284: 310-319.
- Brardinoni, F., Hassan, M. A., & Slaymaker, H. O. (2003a). Complex mass wasting response of drainage basins to forest management in coastal British Columbia. *Geomorphology*, 49(1-2), 109-124.
- Brardinoni, F., Slaymaker, O., & Hassan, A. M. (2003b). Landslide inventory in a rugged forested watershed: a comparison between air-photo and field survey data. *Geomorphology*, 54(3-4), 179-196.
- Brummer C.J., & Montgomery D.R. (2003). Downstream coarsening in headwater channels. *Water Resources Research*, 39 (10), 1294.
- Cavalli M., Goldin B., Comiti F., Brardinoni F., & Marchi L. (2017). Assessment of erosion and deposition in steep mountain basins by differencing sequential digital terrain models. *Geomorphology*, 291, 4-16.
- Cislaghi A., Chiaradia E.A., & Bischetti G.B. (2017). Including root reinforcement variability in a probabilistic 3D stability model. *Earth Surface Processes and Landforms*, 42(12), 1789-1806.
- Confuorto P., Di Martire D., Centolanza G., Iglesias R., Mallorqui J.J., Novellino A., Plank S., Ramondini M., Thuro K., & Calcaterra D. (2017). Post-failure evolution analysis of a rainfall-triggered landslide by multi-temporal interferometry SAR approaches integrated with geotechnical analysis. *Remote Sensing of Environment*, 88, 51-72.
- Corsini A., Borgatti L., Cervi F., Dahne A., Ronchetti F., & Sterzai P. (2009). Estimating mass-wasting processes in active earth slides – earth flows with time-series of High-Resolution DEMs from photogrammetry and airborne LiDAR. *Natural Hazards and Earth System Sciences*, 9 (2), 433–439.
- Cruden D.M., & Varnes D.J. (1996). Landslide types and processes. In: Turner A.K. & Schuster R.L. (Eds.), *Landslides, Investigation and Mitigation*. Transportation Research Board, Special Report 247. National Academy Press, 36-75.
- Dadson S.J., Hovius N., Chen H., Dade W.B., Lin J.C., Hsu M.L., Lin C.W., Horng M.J., Chen T.C., Milliman J., & Stark C.P. (2004). Earthquake-triggered increase in sediment delivery from an active mountain belt. *Geology*, 32 (8), 733–736.
- De Ploey J., & Gabriels D. (1980). Measuring soil loss and experimental studies. In: Kirkby MJ, Morgan RPC (Eds.), *Soil Erosion*, 63–108. Wiley, New York.
- Descroix L., & Olivry J.C. (2002). Spatial and temporal factors of erosion by water of black marls in the badlands of the French southern Alps. *Hydrological Sciences Journal*, 47, (2), 227–242.
- Dietrich W. E., & Dunne T. (1978). Sediment budget for a small catchment in mountainous terrain. 1170 *Zeitschrift für Geomorphologie, Supplement*, 29, 191-206.
- Fan X., Scaringi G., Korup O., West A.J., van Westen C.J., Tanyas H., Hovius N., Hales T.C., Jibson R.W., Allstadt K.E., Zhang L., Evans S.G., Xu C., Li G., Pei X., Xu Q., & Huang R. (2019). Earthquake-induced chains of geologic hazards: Patterns, mechanisms, and impacts. *Reviews of Geophysics*, 57, 421– 503.

- Forbes K., & Broadhead J. (2013). Forests and landslides: The role of trees and forests in the prevention of landslides and rehabilitation of landslide-affected areas in Asia (RAP Publication No. 2013/02). Bangkok, Thailand: Food and Agriculture Organization of the United Nations, Regional Office for Asia and the Pacific.
- Gallart F., Llorens P., Latron J., Rabadà D. (1997). Hydrological functioning of Mediterranean mountain basins in Vallcebre, Catalonia: Some challenges for hydrological modelling. *Hydrological Processes*, 11, 1263–1272.
- Gallart F., Marignani M., Pérez-Gallego N., Santi E., & Maccherini S. (2013). Thirty years of studies on badlands, from physical to vegetational approaches. A succinct review. *Catena* 106, 4–11.
- García-Ruiz J.M., & Lana-Renault N. (2011). Hydrological and erosive consequences of farmland abandonment in Europe, with special reference to the Mediterranean region - a review. *Agriculture, Ecosystems & Environment*, 140 (3-4), 317–338.
- García-Ruiz J.M., Beguería S., Arnáez J., Sanjuán Y., Lana-Renault N., Gómez-Villar A., Álvarez-Martínez J., & Coba-Pérez P. (2017). Deforestation induces shallow landsliding in the montane and subalpine belts of the Urbión Mountains, Iberian Range, Northern Spain. *Geomorphology*, 296, 31–44.
- Gomi T., Sidle R.C., & Richardson J.S. (2002). Understanding Processes and Downstream Linkages of Headwater Systems: Headwaters differ from downstream reaches by their close coupling to hillslope processes, more temporal and spatial variation, and their need for different means of protection from land use. *BioScience*, 52 (10), 905–916.
- Grant G.E., & Swanson F.J. (1995). Morphology and Processes of Valley Floors in Mountain Streams, Western Cascades, Oregon. In: Costa J.E., Miller A.J., Potter K.W., & Wilcock P.R. (Eds.), *Natural 1189 and Anthropogenic Influences in Fluvial Geomorphology*, Geophysical Monograph Series (Vol. 89, 1190 pp. 83-101). Washington, DC: American Geophysical Union.
- Guerriero L., Bertello L., Cardozo N., Berti M., Grelle G., & Revellino P. (2017). Unsteady sediment discharge in earth flows: A case study from the Mount Pizzuto earth flow, southern Italy. *Geomorphology*, 295, 260-284.
- Guthrie R.H. (2002). The effects of logging on frequency and distribution of landslides in three watersheds 1195 on Vancouver Island, British Columbia. *Geomorphology*, 43(3-4), 273–292.
- Guthrie R.H., & Evans S.G. (2004). Analysis of landslide frequencies and characteristics in a natural system, coastal British Columbia. *Earth Surface Processes and Landforms*, 29(11), 1321-1339.
- Guzzetti F., Cardinali M., & Reichenbach P. (1996). The influence of structural setting and lithology on landslide type and pattern. *Environmental and Engineering Geosciences*, 2-4, 531-555.
- Guzzetti F., Malamud B.D., Turcotte D.L., & Reichenbach P. (2002). Power-law correlations of landslide areas in Central Italy. *Earth and Planetary Science Letters*, 195 (3-4), 169-183.
- Guzzetti F., Mondini A.C., Cardinali M., Fiorucci F., Santangelo M., & Chang K. (2012). Landslide inventory maps: New tools for an old problem. *Earth-Science Reviews*, 112 (1–2), 42-66.

- Hassan M.A., Church M., Lisle T.E., Brardinoni F., Benda L., & Grant G.E. (2005). Sediment transport and channel morphology of small, forested streams. *Journal of the American Water Resources Association*, 41, 835-851.
- Hovius N., Stark C.P., Tutton M.A., & Abbott L.D. (1998). Landslide-driven drainage network evolution in a pre-steady-state mountain belt: Finisterre Mountains, Papua New Guinea. *Geology*, 26 (12), 1071–1074.
- Hungr O., Evans S.G., & Hazzard J. (1999). Magnitude and frequency of rock falls and rock slides along the main transportation corridors of south-western British Columbia. *Canadian Geotechnical Journal*, 36, 224-268.
- Hungr O., Leroueil S., & Picarelli, L. (2014). The Varnes classification of landslide types, an update. *Landslides* 11, 167–194.
- Imaizumi F., & Sidle R. C. (2007). Linkage of sediment supply and transport processes in Miyagawa Dam catchment, Japan, *Journal of Geophysical Research*, 112, F03012.
- Imaizumi F., Sidle R.C., & Kamei R. (2008). Effects of forest harvesting on the occurrence of landslides and debris flows in steep terrain of central Japan. *Earth Surface Processes and Landforms*, 33 (6), 827-840.
- Iverson R.M. (1997). The physics of debris flows. *Reviews of Geophysics*, 35 (3), 245– 296.
- Iverson R.M. (2005). Regulation of landslide motion by dilatancy and pore pressure feedback. *Journal of Geophysical Research*, 110, F02015.
- Jakob M. (2000). The impacts of logging on landslide activity at Clayoquot Sound, British Columbia. *Catena*, 38 (4), 279-300.
- Jordan P., Millard T.H., Campbell D., Schwab J.W., Wilford D.J., Nicol D., & Collins D. (2010). Forest Management Effects on Hillslope Processes. In: Pike R. G., Redding T. E., Moore R. D., Winke R. D., & Bladon K.D. (Eds.), *Compendium of forest hydrology and geomorphology in British Columbia, Land Management Handbook (Vol. 66, 275-329)*. British Columbia Ministry of Forests and Range, Forest Science Program, Victoria, B.C. and FORREX Forum for Research and Extension in Natural Resources, Kamloops, BC.
- Kaplan J.O., Krumhardt K.M., & Zimmermann N. 2009. The prehistoric and preindustrial deforestation of Europe. *Quaternary Science Reviews*, 28, 3016-3034.
- Keefer D.K. (2000). Statistical analysis of an earthquake-induced landslide distribution — the 1989 Loma Prieta, California event. *Engineering Geology*, 58 (3–4), 231-249.
- Keesstra S.D., van Dam O., Verstraeten G., & van Huissteden J. (2009). Changing sediment dynamics due to natural reforestation in the Dragonja catchment, SW Slovenia. *Catena* 78, 60–71.
- Korup O., Densmore A.L., & Schlunegger F. (2010). The role of landslides in mountain range evolution. *Geomorphology*, 120 (1–2), 77-90.
- Llena M., Smith M.W., Wheaton J.M., & Vericat D. (2020). Geomorphic process signatures reshaping sub-humid Mediterranean Badlands: 2. Application to 5-year dataset. *Earth Surface Processes and Landform*, 45, 1292–1310

- Llorens P., Poch R.M., Latron J., Gallart F. (1997). Rainfall interception by a *Pinus sylvestris* forest patch overgrown in a Mediterranean mountainous abandoned area. Monitoring design and results down to the event scale. *Journal of Hydrology*, 199, 331–345.
- Lucía A., Martín-Duque J.F., Laronne J.B., & Sanz-Santos M.A. (2011). Geomorphic dynamics of gullies developed in sandy slopes of Central Spain. *Landform Analysis*, 17, 91–97.
- Malamud B. D., Turcotte D. L., Guzzetti F., & Reichenbach P. (2004). Landslide inventories and their statistical properties. *Earth Surface Processes and Landforms*, 29 (6), 687-711.
- Martínez-Murillo J.F., & Nadal-Romero E. (2018). Chapter 1 - Perspectives on Badland Studies in the Context of Global Change. In: Nadal-Romero E., Martínez-Murillo J.F., & Kuhn N.J. (Eds.), *Badlands Dynamics in a Context of Global Change*, 1-25. Elsevier.
- Mathys N., Brochot S., Meunier M., & Richard D. (2003). Erosion quantification in the small marly experimental catchments of Draix (Alpes de Haute Provence, France). Calibration of the ETC rainfall–runoff– erosion model. *Catena* 50, 527–548.
- McArdell B.W., Bartelt P., & Kowalski J. (2007). Field observations of basal forces and fluid pore pressure in a debris flow. *Geophysical Research Letters*, 34, L07406
- McCoy S.W., Kean J.W., Coe J.A., Staley D.M., Wasklewicz T.A., & Tucker G.E. (2010). Evolution of a natural debris flow: In situ measurements of flow dynamics, video imagery, and terrestrial laser scanning. *Geology*, 38 (8), 735–738.
- Meneses B.M., Pereira S., & Reis E. (2019). Effects of different land use and land cover data on the landslide susceptibility zonation of road networks. *Natural Hazards and Earth System Sciences*, 19, 471–487.
- Mensing S.A., Schoolman E.M., Tunno I., Noble P.J, Sagnotti L., Florindo F., & Piovesan G. (2018). Historical ecology reveals landscape transformation coincident with cultural development in central Italy since the Roman Period. *Scientific Reports*, 8 (1), 2138.
- Meyer G.A., Wells S.G., Balling R.C., & Jull A.J.T. (1992). Response of alluvial systems to fire and climate change in Yellowstone National Park. *Nature*, 357, 147–150.
- Mondini A.C., Guzzetti F., Reichenbach P., Rossi M., Cardinali M., & Ardizzone F. (2011). Semi-automatic recognition and mapping of rainfall induced shallow landslides using optical satellite images. *Remote Sensing of Environment*, 115 (7), 1743-1757.
- Montgomery D. R., & Dietrich W. E. (1994). A physically based model for the topographic control on shallow landsliding. *Water Resources Research*, 30 (4), 1153– 1171.
- Montgomery D.R., Schmidt K.M., Greenberg H.M., & Dietrich W.E. (2000). Forest clearing and regional landsliding. *Geology*, 28 (4), 311-314.
- Nadal-Romero E., & García-Ruiz J.M. (2018). Rethinking spatial and temporal variability of erosion in badlands. In: Nadal-Romero E., Martínez-Murillo J.F., & Kuhn N.J. (Eds.), *Badland Dynamics in the Context of Global Change*. Elsevier, Amsterdam.

- Nadal-Romero E., Rodríguez-Caballero E., Chamizo S., Juez C., Cantón Y., García-Ruíz J.M. (2021). Mediterranean badlands: Their driving processes and climate change futures. *Earth Surface Processes and Landforms*, 1-15.
- Nakamura F., Swanson F.J., & Wondzell S.M. (2000). Disturbance regimes of stream and riparian systems — a disturbance-cascade perspective. *Hydrological Processes*, 14 (16-17), 2849-2860.
- O'Loughlin C. L. (1972). An investigation of the slope stability of the steepland forest soils in the coast mountains, southwest British Columbia (Doctoral dissertation). Retrieved from UBC Library. Vancouver, British Columbia: Department of Forestry, University of British Columbia.
- Passalacqua P., Belmont P., Staley D.M., Simley J.D., Arrowsmith J.R., Bode C.A., Crosby C., DeLong S.B., Glenn N.F., Kelly S.A., Lague D., Sangireddy H., Schaffrath K., Tarboton D.G., Wasklewicz T., & Wheaton J.M. (2015). Analyzing high resolution topography for advancing the understanding of mass and energy transfer through landscapes: a review. *Earth- Science Reviews* 148, 174–193.
- Parker R., Densmore A., Rosser N., de Michele M., Li Y., Huang R., Whadcoat S., & Pettley D. (2011). Mass wasting triggered by the 2008 Wenchuan earthquake is greater than orogenic growth. *Nature Geoscience* 4, 449–452.
- Pavanelli D., Cavazza C., Lavmic S., & Toscano A. (2019). The Long-Term Effects of Land Use and Climate Changes on the Hydro-Morphology of the Reno River Catchment (Northern Italy). *Water*, 11, 1831.
- Pepe G., Mandarino A., Raso E., Scarpellini P., Brandolini P., & Cevasco A. (2019). Investigation on Farmland Abandonment of Terraced Slopes Using Multitemporal Data Sources Comparison and Its Implication on Hydro-Geomorphological Processes. *Water* 11, 1552.
- Persichillo M.G., Bordoni M., & Meisina C. (2017). The role of land use changes in the distribution of shallow landslides. *Science of the Total Environment*, 574, 924–937.
- Pisano L., Zumpano V., Malek Ž., Roszkopf C.M., & Parise M. (2017). Variations in the susceptibility to landslides, as a consequence of land cover changes: A look to the past, and another towards the future. *Science of The Total Environment*, 601-602, 1147-1159.
- Preciso E., Salemi E., & Billi P. (2012). Land use changes, torrent control works and sediment mining: effects on channel morphology and sediment flux, case study of the Reno River (Northern Italy). *Hydrological Processes*, 26 (8), 1134-1148.
- Regüés D., Pardini G., & Gallart F. (1995). Regolith behavior and physical weathering of clayey mudrock as dependent on seasonal weather conditions in a badland area at Vallcebre, Eastern Pyrenees. *Catena* 25, 199–212.
- Reid L.M., & Dunne T. (1984). Sediment production from forest road surfaces. *Water Resources Research*, 20(11), 1753-1761.
- Reid L.M., & Dunne T. (1996). *Rapid Evaluation of Sediment Budgets*. Reiskirchen, Germany: Catena Verlag.
- Reid L.M., & Lewis J. (2009). Rates, timing, and mechanisms of rainfall interception loss in a coastal redwood forest. *Journal of Hydrology*, 375 (3-4), 459-470.

- Rickenmann D., & Koschni, A. (2010). Sediment loads due to fluvial transport and debris flows during the 2005 flood events in Switzerland. *Hydrological Processes*, 24 (8), 993-1007
- Rood K. M. (1984). An Aerial Photograph Inventory of the Frequency and Yield of Mass wasting on the Queen Charlotte Islands, British Columbia. Land Management Report No.34, British Columbia Ministry of Forests, Victoria, British Columbia, 55 pp.
- Scorpio V., & Piégay H. (2021). Is afforestation a driver of change in Italian rivers within the Anthropocene era? *Catena*, 198, 105031.
- Schwab J.W. (1983). Mass wasting: October-November 1978 storm, Rennell Sound, Queen Charlotte Islands, British Columbia. Research Note. (Vol. 91). Victoria, Canada: BC Ministry of Forests.
- Shu H., Hürlimann M., Molowny-Horas R., González M., Pinyol J., Abancó C., & Ma J. (2019). Relation between land cover and landslide susceptibility in Val d'Aran, Pyrenees (Spain): Historical aspects, present situation and forward prediction. *Science of the Total Environment*, 693, 133557.
- Sidle R.C., Gomi T., Loaiza Usuga C., & Jarihani B. (2017). Hydrogeomorphic processes and scaling issues in the continuum from soil pedons to catchments. *Earth-Science Reviews*, 175, 75-96.
- Sidle R.C., & Ochiai H. (2006). Landslides Processes, Prediction, and Land Use. Water Resources Monograph Series, 18. Washington DC, USA: American Geophysical Union.
- Sidle R.C., Pearce A.J., & O'Loughlin C.L. (1985). Hillslope stability and land use. Water Resources Monograph Series. (Vol. 11). Washington DC, USA: American Geophysical Union.
- Sirvent J., Desir G., Gutierrez M., Sancho C., & Benito G. (1997). Erosion rates in badland areas recorded by collectors, erosion pins and profilometer techniques (Ebro Basin, NE-Spain). *Geomorphology* 18, 61–75.
- Smith M.W., & Vericat D. (2015). From experimental plots to experimental landscapes: topography, erosion and deposition in sub-humid Badlands from structure-from-motion photogrammetry. *Earth Surface Processes and Landforms*, 40, 1656–1671.
- Squarzoni G., Bayer B., Franceschini S., & Simoni A. (2020). Pre- and post-failure dynamics of landslides in the Northern Apennines revealed by space-borne synthetic aperture radar interferometry (InSAR). *Geomorphology*, 369, 107353.
- Stöcker C., Eltner A., & Karrasch P. (2015). Measuring gullies by synergetic application of UAV and close range photogrammetry – a case study from Andalusia, Spain. *Catena*, 13, 1–11.
- Swanston D.N., & Marion D.A. (1991). Landslide response to timber harvest in southeast Alaska. *Proceedings of the Fifth Federal Interagency Sedimentation Conference*, 2, 10.49-10.56.
- Swanston D.N., & Swanson F.J. (1976). Timber harvesting, mass erosion, and steep-land forest geomorphology in the Pacific Northwest. In: Coates D.R. (Eds.), *Geomorphology and Engineering*, 1392, 199-221. Stroudsburg, Pennsylvania: Dowden, Hutchinson & Ross, Inc.
- Tarolli P. (2014). High-resolution topography for understanding earth surface processes: opportunities and challenges. *Geomorphology* 216, 295–312.

- Tarolli P., Cao W., Sofia G., Evans D., & Ellis E.C (2019). From features to fingerprints: A general diagnostic framework for anthropogenic geomorphology. *Progress in Physical Geography: Earth and Environment*, 43, 95–128.
- Theule J. I., Liébault F., Loye A., Laigle D., & Jaboyedoff M. (2012). Sediment budget monitoring of debris-flow and bedload transport in the Manival Torrent, SE France. *Natural Hazard Earth Sciences*, 12, 731–749.
- Vericat D., Smith M.W., & Brasington J. (2014). Patterns of topographic change in sub-humid badlands determined by high resolution multi-temporal topographic surveys. *Catena*, 120, 164–176.
- Winkler R.D., Moore R.D., Redding T.E., Spittlehouse D.L., Smerdon B.D., & Carlyle-Moses D.E. (2010). The Effects of Forest Disturbance on Hydrologic Processes and Watershed Response. In: Pike R.G., Redding T. E., Moore R. D., Winker R.D., & Bladon K.D. (Eds.), *Compendium of forest hydrology and geomorphology in British Columbia, Land Management Handbook* (Vol. 66, 179-212). British Columbia Ministry of Forests and Range, Forest Science Program, Victoria, B.C. and FORREX Forum for Research and Extension in Natural Resources, Kamloops, B.C.
- Wolter A., Ward B., & Millard T. (2010). Instability in eight sub-basins of the Chilliwack River Valley, British Columbia, Canada: A comparison of natural and logging-related landslides. *Geomorphology*, 120 (3-4), 123-132.
- Wu W., & Sidle R.C. (1995), A Distributed Slope Stability Model for Steep Forested Basins. *Water Resources Research*, 31 (8), 2097– 2110.
- Zeng Z., Estes L., Ziegler A. D., Chen A., Searchinger T., Hua F., Guan K., Jintrawet A., & Wood E.F. (2018). Highland cropland expansion and forest loss in Southeast Asia in the twenty-first century. *Nature Geoscience*, 11, 556–562.

CHAPTER 2

A multi-temporal mapping approach for improving the temporal and spatial characterization of landslide activity in clay-rich terrain

Sharon Pittau *¹, Marco Pizziolo², Mauro Rossi³, Francesco Brardinoni¹

1. Department of Biological, Geological and Environmental Sciences, University of Bologna, Bologna, Italy
2. Servizio Geologico Sismico e dei Suoli, Regione Emilia-Romagna, Bologna, Italy
3. CNR-IRPI, Perugia, Italy

* Corresponding author: sharon.pittau2@unibo.it

Modified from the final version published in:

Rendiconti Online della Società Geologica Italiana

July 2021

<https://doi.org/10.3301/ROL.2021.06>

Abstract

In mountain, clay-rich physiographic settings of the Northern Apennines, earth slides and earthflows are dominant processes of hillslope sediment transfer, which cause hazard and pose risk to lives and man-made structures. In Emilia-Romagna (E-R), information drawn from a region-wide inventory is customarily used for assessing landslide hazard potential and partly guides decision making on land management and urban planning. However, the inventory's historical (i.e., post-1954) degree of completeness is presently unknown. To address this gap, we integrate and compare the existing E-R inventory with a multi-temporal landslide mapping approach at four selected study sites of the Sillaro River basin, where we perform visual interpretation of thirteen sequential aerial photo sets in the 1954-2020 period and conduct confirmatory fieldwork. Specific objectives include evaluating the advantages of higher resolution mapping for characterizing (i) landslide extent, geometry and activity through time; and (ii) landslide interaction with the drainage network. With reference to the E-R inventory, multi-temporal mapping allowed identifying additional first occurrences and recurrences (up to a 5-fold increase), additional mapped landslide area (up to a 12-fold increase), and combined footprint area (up to a 9-fold increase). Our findings indicated that the proposed approach does not always result in mapping larger (or smaller) landslide polygons, or previously undetected landslides, but provides insights on process understanding. Therefore, an added value of this mapping approach lies in its ability to detect different styles of landsliding and define most likely scenarios of evolution at the site scale. Insights were drawn through detection of: (i) headscarp upslope migration (or revegetation); (ii) newly formed gully channels and/or revegetation on landslide depositional features; and (iii) changes at landslide terminus, which allowed identifying new sediment pulses, exact delivery targets (e.g., fan, valley floor, and stream channel), as well as induced changes in channel bed texture and geometry.

Keywords:

Landslides; landslide inventory, temporal resolution, recurring activity, sediment delivery to streams

1. Introduction

Multi-temporal landslide inventories are efficient tools for the rapid evaluation of geomorphic change and landslide-driven sediment flux over large areas (Reid & Dunne, 1996; Brardinoni et al., 2012), as well as for assessing sediment supply to stream channels (Schuerch et al., 2006; Finnegan et al., 2019), relevant disturbance regimes (Nakamura et al., 2000), effects on channel-reach morphology and geometry (Brummer & Montgomery, 2003; Green et al., 2013; Hassan et al., 2019) and hazard potential (Guzzetti et al., 2005). Their basin-to-regional approach complements site-specific monitoring efforts on single landslides (e.g., Baum & Reid, 1995; Corsini et al., 2009; Berti & Simoni, 2010; Nereson & Finnegan, 2018), and radar interferometry investigations on slow-moving bodies (e.g., Colesanti & Wasowski, 2006; Roering et al., 2009; Bayer et al., 2018; Bekaert et al., 2020).

Multi-temporal landslide inventories may be compiled through integration of aerial photo and/or satellite imagery interpretation, field surveys, and historical documentation. Methods adopted in the compilation -- which depend on the study objectives, available resources, spatial and temporal resolution needed, and the spatial extent to be investigated (Guzzetti et al., 2000) -- will affect the quality and the completeness of the inventory maps, hence the reliability of the derived (basic or applied) products.

In Emilia-Romagna (E-R), the regional Geological Survey has compiled and has been managing a region-wide multi-temporal landslide inventory (Regione Emilia-Romagna, 2021), which is intended as a complementary tool to guide land planning. The bulk of the inventory, including the attribution of the activity status, was built between the mid 1980's and late 1990's, through stereoscopic inspection of historical aerial photo sets (i.e., 1954, 1969, 1976 and 1996) and complementary field visits. The inventory was digitized in 2005 and since then has undergone annual updating via manual delineation of landslide polygons on post-1996 aerial orthophoto sets and Google Earth imagery, as well as directly, drawing information from field surveys, local newspapers, historical archives, and technical reports associated with slope stability monitoring programs (Piacentini et al., 2018).

In the inventory, each landslide is mapped as a polygon feature, where the polygon outline comprises the total (i.e., initiation, transport and deposition zones) landslide area. Each polygon is characterized by categorical and geometric attributes, such as movement type (e.g., fall, flow, slide, complex), state of activity (i.e., active or dormant), scar area, and scar length (Table 1). Attribution of activity should be regarded as indicative, except otherwise documented by direct historical information. Specifically, classification of landslide features in active or dormant is mostly based on their morphologic expression as interpreted on aerial photos.

Table 1. Landslide attributes of the Emilia-Romagna inventory.

Attribute	Category
Landslide type	Rock fall
	Slide
	Earth flow
	Debris flow
	Deep-seated gravitational slope deformation (DGSD)
	Complex
	Indefinite
State of activity	Active
	Dormant
Geometry	Area
	Length

To date, the inventory comprises 80,985 landslides, including respectively 44,377 active and 36,608 dormant failures (Figure 1). Collectively, landslides occupy an area of about 2,600 km², out of the 10,500 km² hilly and mountain terrain of Emilia-Romagna. Prevalent movement types are earth slides and earth flows that typically recur on pre-existing scars (Bertolini & Pizziolo, 2008) and mainly involve clay-dominated Ligurian Units (Berti et al., 2012; Simoni et al., 2013; Pizziolo et al., 2015).

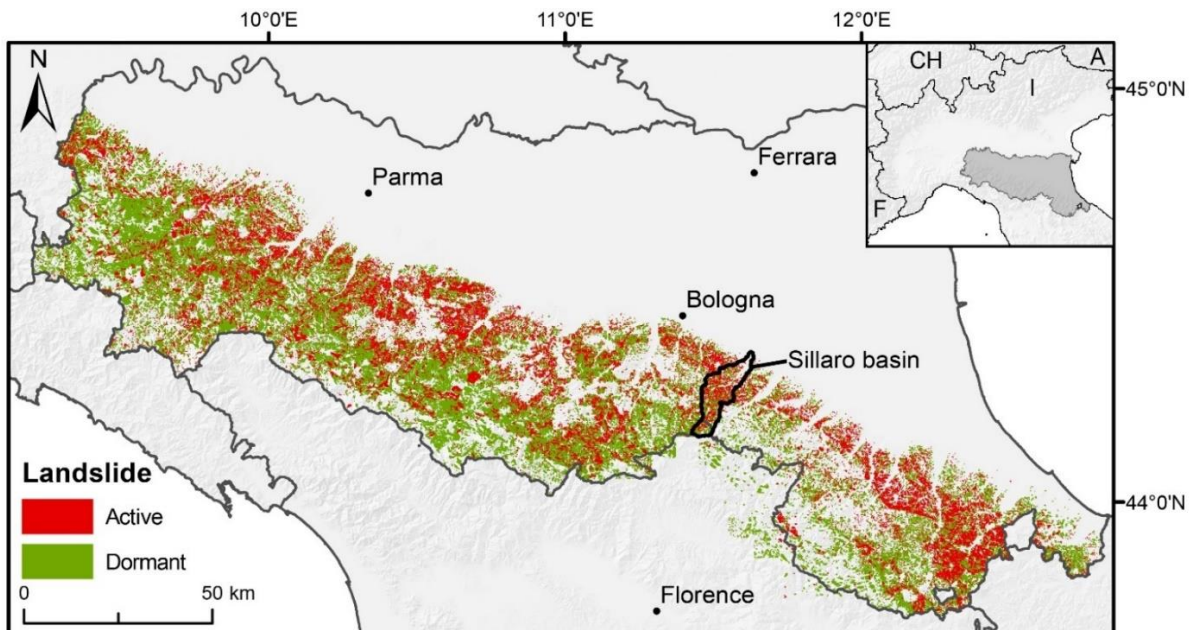


Figure 1. Emilia-Romagna landslide inventory map (version updated on January 1st 2021). Solid grey linework indicates coastlines and regional administrative boundaries, black open polygon delimits the Sillaro River basin. The inset shows the location of the Emilia-Romagna within Italy.

Considering the inventory’s main purpose, its regional extent and available resources, the updating process is conducted each year in different areas, mainly where landslides have caused damage and/or pose immediate risk to structures and infrastructure, or where ad hoc contingent land planning is needed. Therefore,

information such as date of first recorded occurrence, subsequent recurrences and possible cause of activation is limited to a subset ($n = 2,558$) of so-called “historical” landslide polygons. When the size of a historical activation is too small to be drawn on a 1:5000 map, or the exact location (or geometry) is uncertain, the landslide is treated as a point feature in the database (Piacentini et al., 2018).

With reference to post-1954 landslide activity, the degree of E-R inventory completeness, is presently unknown. This is a critical shortcoming, both for addressing basic scientific questions on landscape evolution (e.g., Finnegan et al., 2019) and for tackling more applied issues, such as landslide hazard assessment (e.g., Wieczorek, 1984) or watershed sediment management. In this paper, we aim to explore the advantages of adopting a higher temporal resolution mapping for (i) documenting landslide extent and activity through time; and (ii) landslide interaction with the drainage network. To this purpose, we integrate and compare the existing Emilia-Romagna inventory with systematic visual inspection of all available historical aerial photo sets and confirmatory fieldwork. In particular, we focus on four landslide sites within the Sillaro River, a mountain basin representative of the physiographic, clay-dominated context of the Northern Apennines. The four study sites were selected so to encompass a range of characteristics including system size and complexity, landslide type, landslide lateral confinement, and sediment delivery to the drainage network (Figure 2). Accordingly, they include simple, unconfined earth flow (site A) and earth slide (site B) that interact directly with the Sillaro River, a channelized earth flow that interferes with a road (site C), and three earth flows that converge towards an old landslide deposit and interact with the secondary ephemeral drainage network (site D) (Figure 3).

2. Study area

The mountain portion of the Sillaro River basin (139 km^2), Northern Apennines, originates at the orogen divide in Mt. La Fine (993 m a.s.l.), and develops northeast down to the town of Castel San Pietro Terme (56 m a.s.l.) in Emilia-Romagna, within the Bologna Metropolitan Area (Figure 2). The channel main stem displays a complex planform structure, characterized by a large northward bend in its middle portion. The area has a Mediterranean climate with distinct cold and dry seasons, and mean annual rainfall of 824 mm (1990-2020) at San Clemente (166 m a.s.l.) meteorological station (ARPAE, 2021).

According to the Emilia-Romagna inventory, the basin hosts 1,981 landslides (1,247 active and 734 dormant), for a combined area of 34 km^2 (Figure 2a). Among these, 13 hold historical records of occurrence, including study site C.

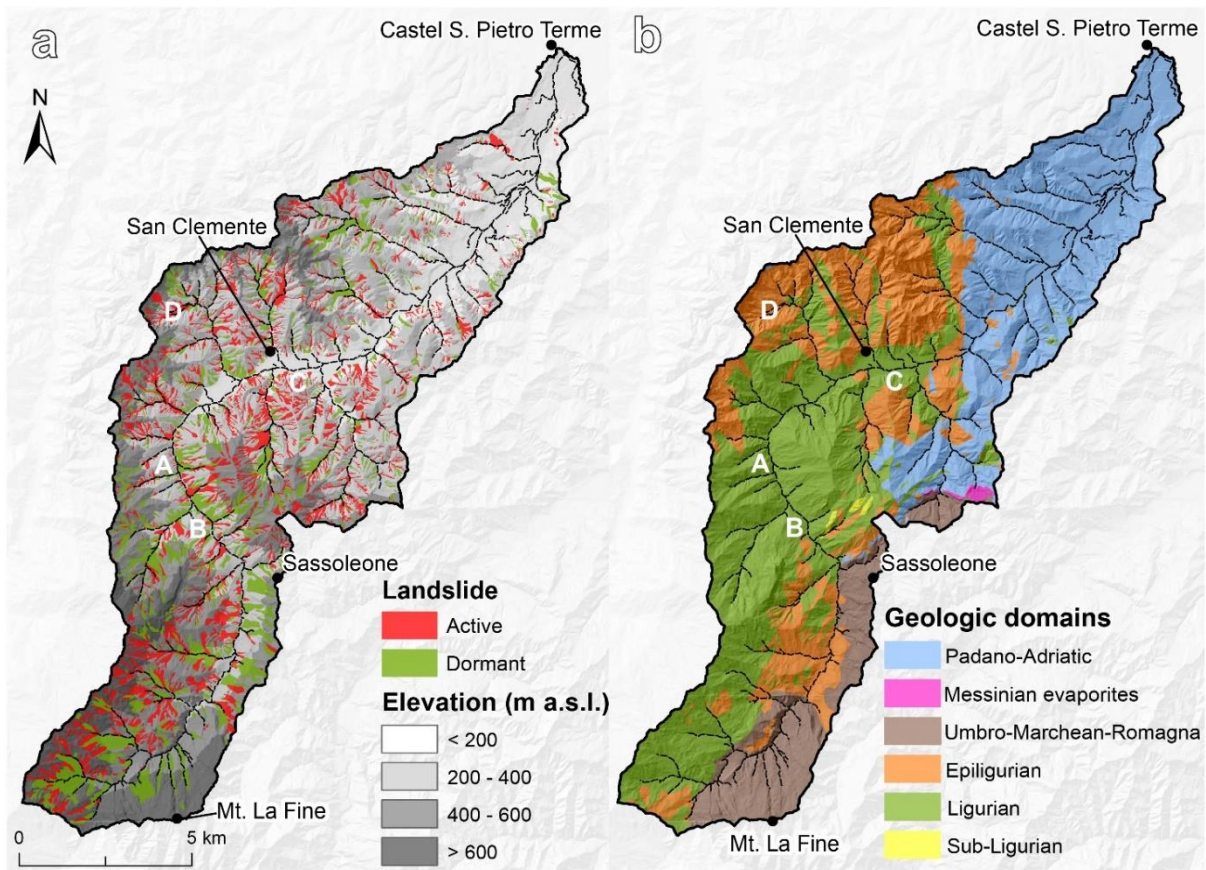


Figure 2. Maps of the Sillaro River basin showing: (a) active (red polygons) and dormant (green polygons) landslides of the Emilia-Romagna inventory, as well as elevation bands shown with different grey tones; and (b) geological domains. Capital letters indicate the four sites of interest.

The study basin is located at a key regional geologic transition, where the Ligurian Unit (Cretaceous-Eocene) and the Umbro-Marchean-Romagna succession (Miocene-Pleistocene) come into contact in proximity of its south-eastern side (Zattin et al., 2002; Benini et al., 2009; Bettelli et al., 2012) (Figure 2b). Bedrock geology consists primarily of alternations of marls and clays of the Ligurian (Cretaceous-Eocene), Sub-Ligurian (Eocene-Oligocene) and Epiligurian (Eocene-Miocene) domains in the upper-to-mid portions of the basin, and of clays and sands of the Padano-Adriatic (Upper Messinian-Pleistocene) domain in the remainder lower part (Figure 2b). In particular, tectonized clays of the Ligurian Unit, which underlain most part of the study landscape, incorporate large limestone blocks and exhibit chaotic texture. Foredeep turbidities of the Umbro-Marchean-Romagna succession (Mamoso-Arenacea Formation, Serravallian-Tortonian), consisting of sandstone-pelite alternations, outcrop on the south-eastern part (Figure 2b). Of the four study sites, A, B and C are underlain by Ligurian lithologies, whereas D is characterized by Epiligurian substrates (Figure 2b).

Most of the basin likely underwent forest clearing in unknown historical times, with forest cover reaching a minimum immediately after Second World War. Since then, societal changes, including the abandonment of the countryside, have induced a substantial increase in forest cover (Preciso et al., 2012; Pavanelli et al., 2019). Today, land cover consists primarily of arable crops and meadows, which occupy about one third of the basin, mainly in its mid-to-lower portions. Bushes and managed forest together cover about half of the basin, mainly at higher elevations, in the mid-to-upper portions of the basin, including terrain of the Mamoso-Arenacea

Formation. Badlands, which accounts for over 12% in area, are clustered in the central part of the basin, in correspondence of Ligurian and Epiligurian lithologies. Urban areas are restricted along the distalmost parts of the Sillaro main valley floor, around Castel San Pietro Terme, which is the only town in the basin (Figure 2).

3. Data Collection and Methods

Landslide identification and delineation at the four study sites was performed through visual inspection of ten sequential aerial photosets (i.e., stereoscopic photographs and/or digital ortho-imagery taken in 1954, 1969, 1976, 1985-88, 1996, 2000, 2006, 2008, 2011, and 2014), and Google Earth imagery (i.e., 2016, 2018 and 2020) (Table 2). We mapped the areal extent of each mass movement observed on optical imagery, setting a minimum level of landslide width detection of 4 meters. Below this threshold, it was not possible to consistently delineate the landslide perimeter, especially on the 1954 photos, due to coarse resolution and poor contrast. Our inventory targets landslides associated with a clear transfer of material from an initiation zone, through a transport zone and down to a deposition zone. Therefore, it does not include incremental seasonal movements, which may be detected through direct monitoring, InSAR, and/or feature tracking. Landslide tracks were digitized in GIS environment on the sequential orthophoto mosaics. We first delineated polygons of total disturbed landslide area, which includes initiation, transport and deposition zones; then, when possible, we subdivided total disturbed area into initiation-transport and deposition polygons.

Table 2. Stereoscopic photographs and digital ortho-imagery used for multi-temporal landslide identification and mapping.

Year	Nominal scale	Pixel size (m)	Imagery type	Source
1954	1:55,000	1	Black and white	Istituto Geografico Militare
1969	1:15,000	0.7	Black and white	Regione Emilia-Romagna
1976	1:13,000	0.9	Color	Regione Emilia-Romagna
1985-88	1:25,000	1	Black and white	Regione Emilia-Romagna
1996		1	Black and white	Regione Emilia-Romagna
2000		1	Color	WMS GN*
2006		0.5	Color	WMS GN*
2008		0.5	Color	WMS E-R**
2011		0.5	Color	WMS E-R**
2014		0.5	Color	Regione Emilia-Romagna
2016		0.3	Color	Google Earth
2018		0.3	Color	Google Earth
2020		0.3	Color	Google Earth

* Geoportale Nazionale: <http://www.pcn.minambiente.it/mattm/servizio-wms/>

** Geoportale Regione Emilia-Romagna: <https://geoportale.regione.emilia-romagna.it/servizi/servizi-ogc/elenco-capabilities-dei-servizi-wms>

Recorded landslide attributes for each landslide polygon include: photo year of occurrence, landslide type, morphologic position at initiation (source), lateral confinement, and sediment delivery target at landslide terminus (sink) (Table 3). Photo year represents the minimum landslide age, where temporal constraint is given by the date of the preceding aerial photo set. Consequently, year of occurrence for landslides first identified in 1954 is unknown. Classification of landslide type follows the scheme proposed by Cruden and Varnes (1996). In the Sillaro River basin, mapped types include earth slides, earth flows and complex ones. We use the term terminus (as opposed to toe) to indicate the downslope end of visible landslide disturbance, since several cases did not exhibit a well-defined toe (e.g., Brardinoni et al., 2009).

Table 3. Landslide attributes of the multi-temporal inventory (this study).

Attribute	Category or Units
Landslide size	Total disturbed area (m ²)
Landslide type	Earth flow Earth slide Complex
Photo year of activity	From 1954 to 2020 (cf. Table 2)
Morphologic position at initiation (Initiation zone)	Gully headwall Open slope
Lateral confinement (Transport zone)	Confined Channelized Unconfined
Sediment delivery target (Deposition zone)	Hillslope Gully channel Permanent tributary Main channel Anthropogenic structure
Headscarp activity	Upslope migration Revegetation
Deposition lobe activity	Gully incision Revegetation
Stream channel changes	Occlusion Avulsion Bed coarsening

Definition of morphologic position at initiation and sediment delivery target are important to identify sites of sediment production and delivery, and consequently the sediment transfer pathways (hereafter termed source-to-sink pathways) that dominate on the hillslopes and along the steep ephemeral drainage network. Initiation

positions include gully headwall and open slope sites. Following previous classification schemes (Maynard, 1991; Brardinoni et al., 2015), sediment delivery targets encompass four “natural” categories, listed in order of increasing sediment delivery potential (or deliverability), and an additional one associated to anthropogenic structures. Categories include: (i) hillslopes (unchannelled topography); (ii) gully channels (v-notched, first and second order streams flowing on bedrock or on colluvial deposits) (Figures 3c and 3d); (iii) permanent tributaries (higher order streams with an alluvial channel bed that drain secondary valleys); (iv) main channels (i.e., the Sillaro River main stem) (Figures 3a and 3b); and (v) roads, or other anthropogenic structures that may concentrate drainage water, trap sediment and deflect landslides, sometimes preventing them from reaching the drainage network. An example of a source-to-sink pathway affected by man-made structures is provided in Figure 3c. Here a channelized earth flow originates at a gully headwall, flows along a steep, confined gully channel and stops by a road, which was deflected downslope. Degree of lateral confinement was defined with reference to the transport zone, where we distinguished between confined (mostly channelized) tracks and landslides that move down an unconfined hillside.

Each mapped landslide was provided with a unique identifier. Recurring initiations, typically associated with channelized earth flows, were also mapped and recorded. In these instances, a secondary identifier (i.e., equal for all landslides that originate from the same initiation site) was also added to each recurring landslide. Information about landslide recurrence is useful to evaluate landslide hazard (e.g., Crovelli, 2000; Guzzetti et al., 2006), sediment transfer through time (e.g., Hovius et al., 1997; Brardinoni et al., 2009), as well as potential rates of sediment recharge across the gully channel network (Bovis & Jakob, 1999; May & Gresswell, 2003). For recurring landslides, we noted whether the movement involved: (i) the entire track of an antecedent slope failure or only part of it; (ii) headscarp retreat; (iii) advance of an existing landslide terminus; and (iv) downslope stream channel changes. Within landslide deposition zones, we recorded the temporal pattern of revegetation and/or the development of gully channel incision. The former indicates the degree of site stability across photo years, the latter indicates the degree of ongoing fluvial reworking.

In the results, we will compare at each site our multi-temporal mapping with that of the E-R inventory, where morphological scar changes (e.g., headscarp retreat, terminus advance or erosion, and downslope secondary activation) within a given landslide system are progressively incorporated in the pre-existing “old” polygon (i.e., change of polygon outline) as the inventory gets updated. We start from simple landslide systems and continue with increasingly larger and more composite configurations.

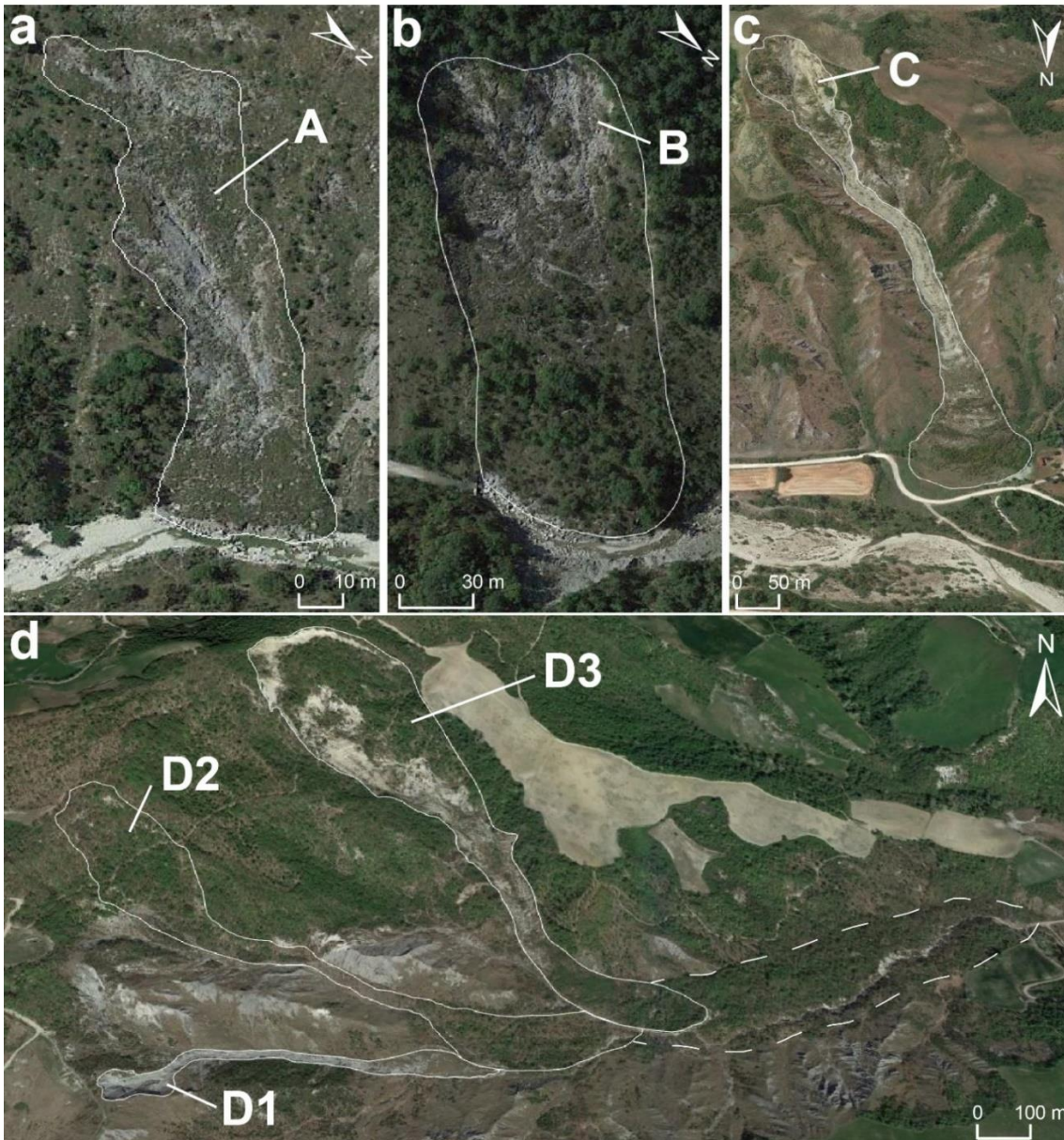


Figure 3. (a) Site A: unconfined, earth flow delivers sediment from an open-slope position within badlands morphology to the Sillaro River channel (source: Google Earth, 2014); (b) Site B: unconfined, rotational earth slide delivers sediment from an open-slope position in managed forest to the Sillaro River channel (source: Google Earth, 2018); (c) Site C: channelized earth flow developed within a ravine in badlands delivers sediment from a gully headwall, flows along a second-order gully channel, and stops by a road, behind older landslide deposits (source: Google Earth, 2017); (d) Site D: three earth flows (D1, D2, and D3), within a third-order tributary basin, which interfere with each other and deliver sediment to a gully channel that cuts through an older landslide deposit (dashed outline) (source: Google Earth, 2020).

4. Results

At site A, detailed multi-temporal mapping allowed: (i) integrating the three (active) landslide scars included in the E-R inventory (Figure 4a) with additional ones, and (ii) showing that landslides are recurrent in nature. On 1954 photos, we could distinguish six landslide scars, whose year of last mobilization is uncertain. In this study, existing (active) polygon outlines were also enlarged (cf. Figure 4a and 4b). Overall, landslide area in 1954 adds up to 48,700 m², as opposed to 5,700 m² in the existing inventory. In subsequent photo years (i.e., 1969, 1988, 2011, 2014 and 2016), we mapped a total of six recurring landslides (Figure 4b).

One earth flow, which records two post-1954 recurrences, illustrates a dynamic style of landslide-fluvial interaction. The earth flow front (thickness = 4 m) entered the Sillaro River in 2011, almost occluding the stream channel (Figure 4d). By 2014, we observe that fluvial reworking had obliterated in-channel landslide deposits, leaving behind large blocks (b-axis up to 2 m) of the Argille a Palombini Formation, which likely have prevented further fluvial undercutting, and locally have generated boulder-cascade channel morphology. The diamicton fabric of the Argille a Palombini, characterized by a pelitic matrix bearing limestone blocks (the so-called palombini), is possibly responsible for the observed fluvial response to sudden landslide sediment supply. Following this logic, we expect that most of the fine matrix was typically flushed downstream as suspended load.

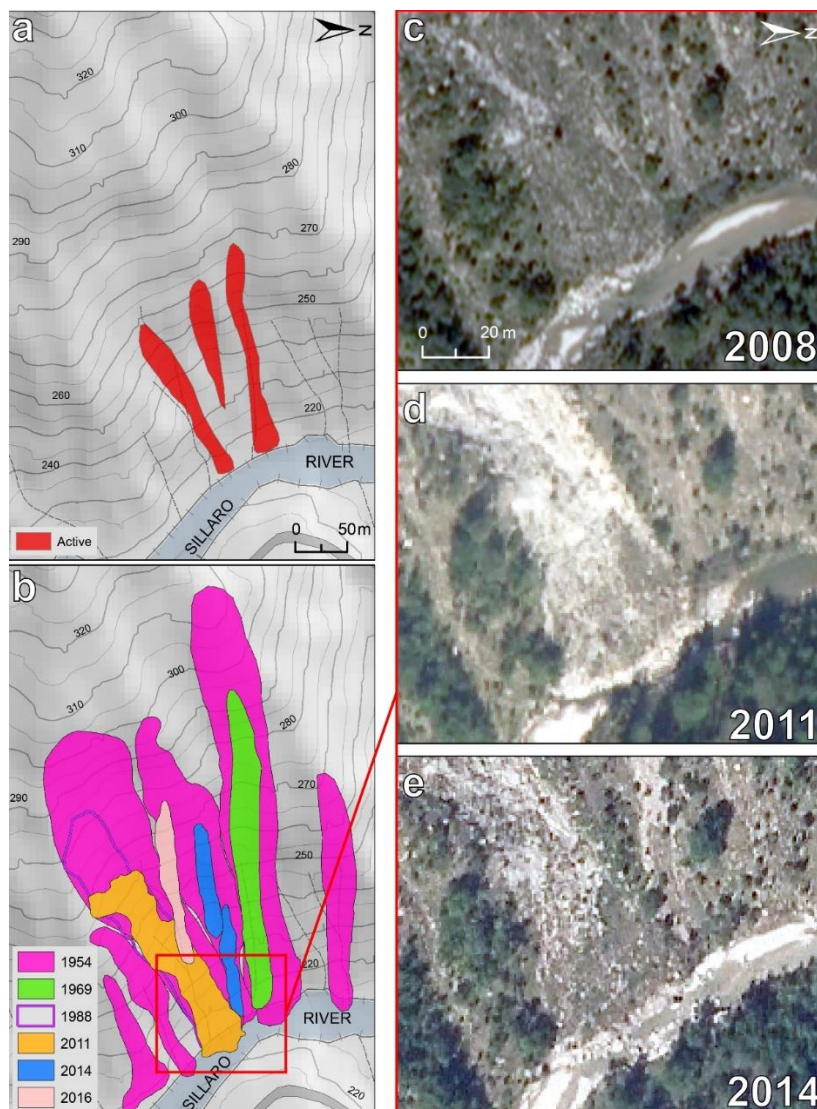


Figure 4. Site A: (a) landslide polygons of the Emilia-Romagna inventory; (b) corresponding multi-temporal landslide polygons mapped in this study; and close-up views of the landslide terminus (c) before (2008), (d) during (2011), and (e) after (2014) its advance in the Sillaro River channel. Note white limestone blocks of the Argille a Palombini Formation (Ligurian Domain) on the landslide surface and then forming lag deposits in the Sillaro River channel. In panel b, different colors indicate different photo years of landslide occurrence. Thick grey linework indicates roads. North arrow and scale in panel a apply also to panel b; north arrow and scale in panel c apply also to panels d and e.

At site B, multi-temporal mapping proved being critical for: (i) constraining landslide first appearance in photo year 1969 (Figure 5a); (ii) elucidating landslide movement style and its interaction with the Sillaro River channel across decades; and (iii) identifying a small, previously undetected earth slide (Figure 5f). In terms of size, landslide area increases from 7,800 m² in the E-R inventory (Figure 5e), to 12,900 m², as mapped in photo year 2020 (Figure 5f). Through the years, we note headward migration of the main headscarp and a progressive downslope movement of the main landslide body (thickness = 4 m), with concurrent revegetation at the toe (e.g., Figures 5b through 5d). Differently from site A, in this case we observe that the earth slide protrudes slowly into the Sillaro River channel and opposes resistance to fluvial undercutting. Accordingly, from 1996 (cf. Figures 5a and 5b) we start observing significant river deflection to northeast -- hence instability on the opposite valley side -- and an increase in river planform sinuosity. To date, these dynamics continue altering the local morphology of the Sillaro River channel (e.g., Figures 5c and 5d). As noted at site A, we also observe limestone blocks in the main channel bed, freshly supplied in proximity of the landslide front.

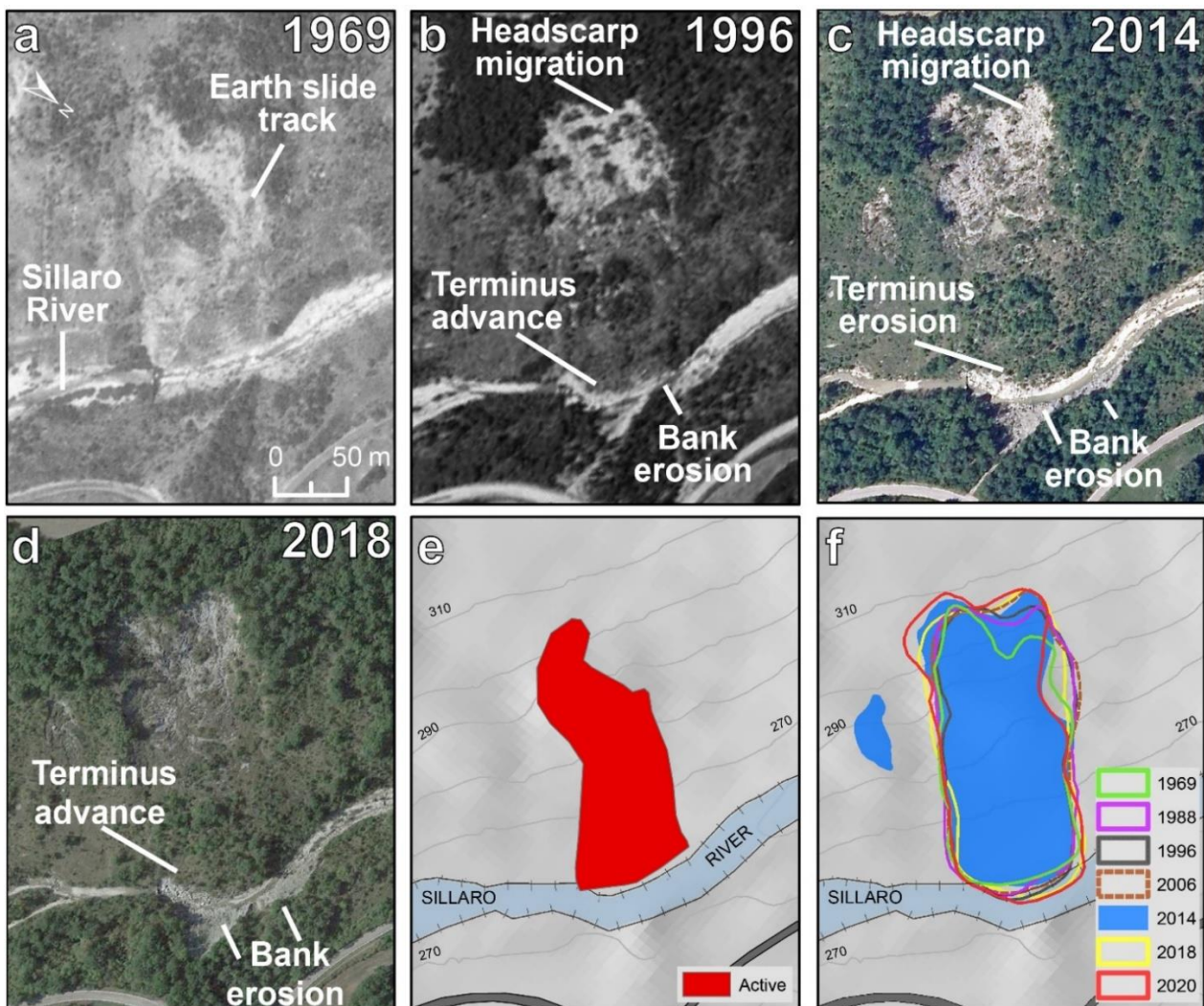


Figure 5. Site B: historical plan-view in photo year: (a) 1969; (b) 1996; (c) 2014; and (d) 2018. (e) Landslide polygon of the Emilia-Romagna inventory; and (f) corresponding multi-temporal landslide polygons mapped in this study. In panel f, different colors indicate different photo years of landslide extent. Note that initiation-transport and deposition zones are clearly visible and how landslide downslope movement induces river deflection to northeast, instability on the opposite valley side, and an increase of river planform sinuosity. Thick grey linework indicates roads. North arrow and scale in panel a apply to all panels.

At site C, multi-temporal mapping allowed elucidating the highly dynamic nature of this larger and more complex earth-flow system. At this site, the E-R inventory reports two historical earth-flow pulses -- one in late 2001, and one on May 5th, 2019 (Figure 6h) -- as opposed to the eight activations documented between 1988 and 2020 (Figure 6i). Overall, E-R mapping approach does a good job at delineating the total disturbed area, in that the existing combined polygon outline (Figure 6h) is very similar to that we would get by merging all multi-temporal polygons together (Figure 6i). However, the sum of the eight mapped polygons makes up an area of 113,700 m², compared to the 42,400 m² of the E-R inventory, implying a much larger sediment flux over the study period than previously expected.

In photo year 1976, along this steep tributary valley we observe old, partly vegetated landslide deposits that extend down to its mouth. We also observe that these deposits, emplaced at least before 1954, are incised by a gully channel draining north, then westward. This period of relative stability is followed by at least eight distinct channelized earth-flow pulses that have recurred between photo year 1988 and 2020 (Figure 6). In some instances, earth flows travel down to the valley mouth, where they have damaged and altered the road course (photo years 1988, 2000, 2016, 2018 and 2020 in Figure 6i), in others they have involved only the upper part of the gully system (e.g., 2006 and 2014) or a secondary drainage branch (2011). Largest occurrences, like those visible in 2000 and 2018, have produced significant headward migration of the gully network, causing loss of agricultural land. In no instance, recurring earth flows have reached the Sillaro River channel.

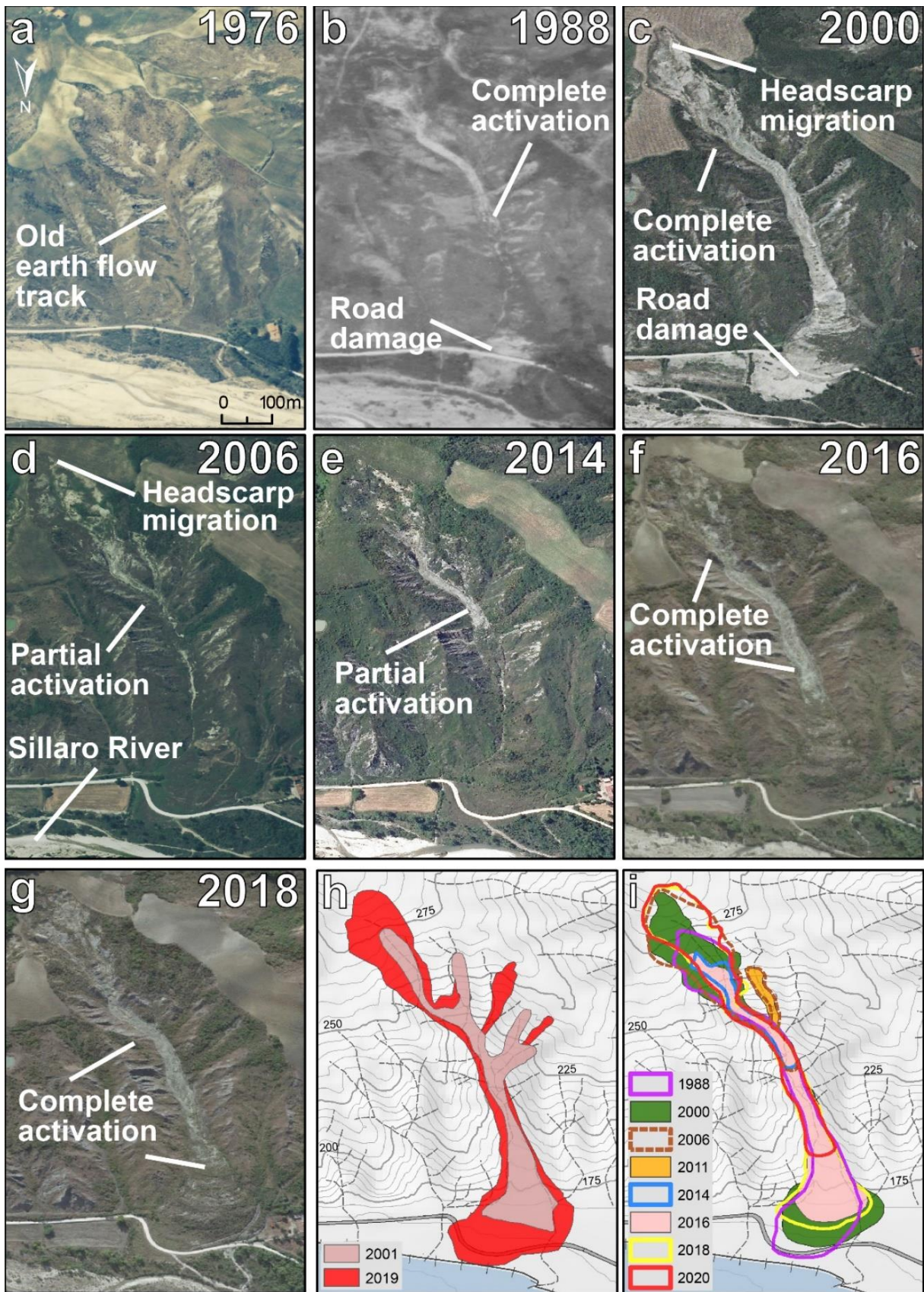


Figure 6. Site C: historical plan-view in photo year: (a) 1976; (b) 1988; (c) 2000; (d) 2006; (e) 2014; (f) 2016; and (g) 2018. (h) Landslide polygons of the Emilia-Romagna inventory; and (i) corresponding multi-temporal landslide polygons mapped in this study. Dashed black linework indicates drainage network. Thick grey linework indicates roads. In panel i, different colors indicate different photo years of landslide extent. Note road disturbance from photo year 1988 onward. North arrow and scale in panel a apply to all panels.

Site D is an earth flow-dominated tributary basin (1.2 km²), where the main valley floor stands out for being entirely occupied by a densely vegetated landslide deposit (Figure 3d). In this context, multi-temporal mapping helped to elucidate that the nine coalescent “active” polygons (Figure 7a): (i) are indeed the result of several landslides originating at multiple initiation sites between photo year 1954 and 2020 (Figure 7b); and (ii) the distal portion of the valley trunk may be considered as an older depositional landslide feature. The latter interpretation is supported by the stability of the gully channel that has been cutting through it (Figures 8b and 8e), the lack of dislocation signs, and increasingly denser and undisturbed forest cover since photo year 1954 (Figure 8). Some discrepancies between the regional and the site-specific multi-temporal mapping are also obvious along small lateral tributaries. For example, on the northern valley side we could not confirm landslide activity in any of the three distalmost lateral tributaries previously mapped as active sites (Figure 7).

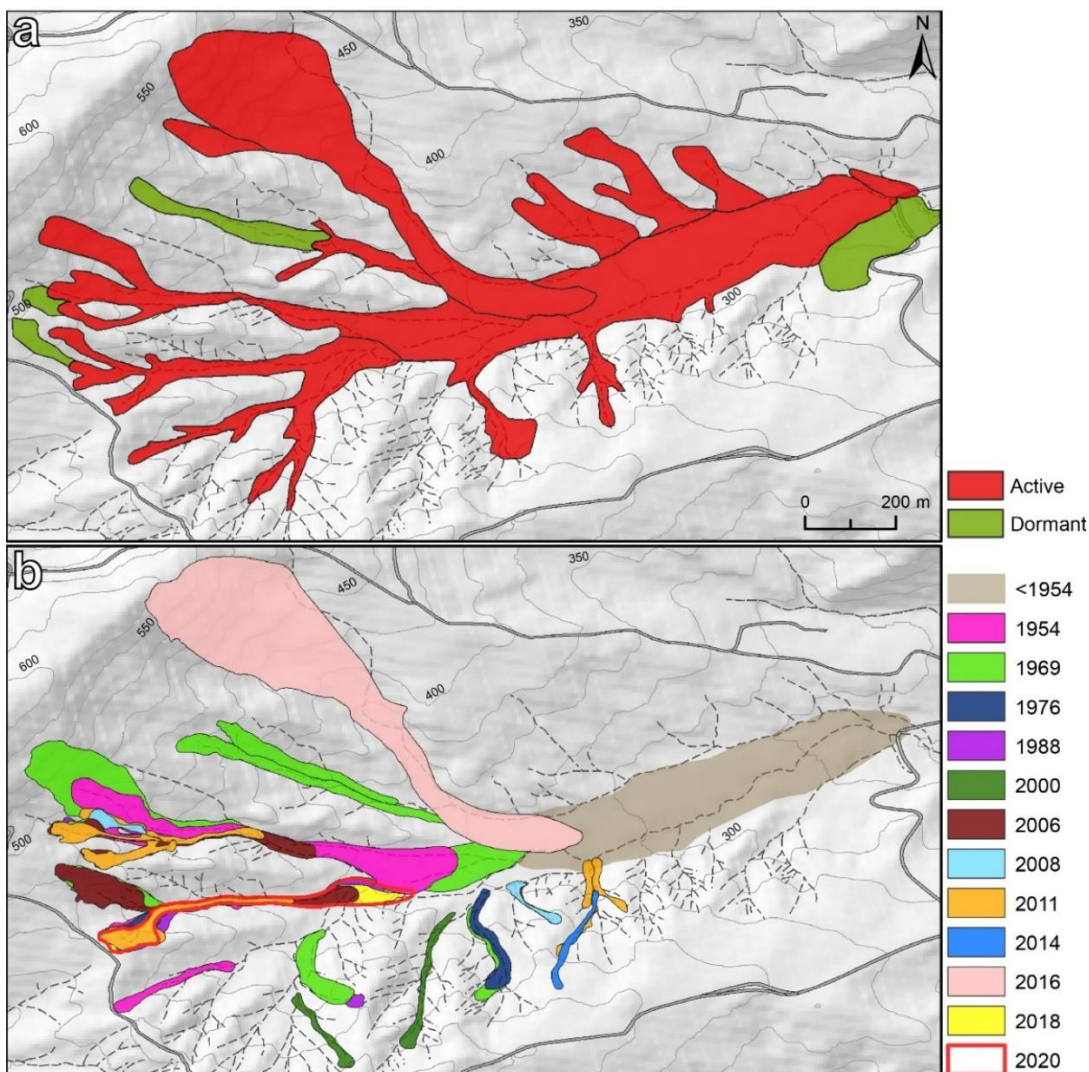


Figure 7. Site D: (a) landslide polygons of the Emilia-Romagna inventory; and (b) corresponding multi-temporal landslide polygons mapped in this study. In panel b, different colors indicate different photo years of landslide extent. Dashed black linework indicates drainage network. Thick grey linework indicates roads. North arrow and scale in panel a apply to all panels.

Interestingly, the sub-basin hosts a high diversity of landslide styles, including both recurring (sites D1 and D2) and episodic (site D3) movements. All three landslide initiation sites deliver material to the ephemeral gully network. D1 is a very narrow channel that experiences earth-flow activity in virtually all photo years, as

testified by newly developed deposition lobes, lateral levees (Figure 8c) and scarp headward migration (Figures 7a and 8b). At D2, we observe recurring spoon-shaped landslide initiations developing into narrowly channelized earth flows (i.e., 1954, 1969, 2006, 2008, and 2011), the largest of which (52,600 m²) occurred in 1969. These sediment slugs sometimes stop along the gully channel (2006 and 2011), sometimes reach the main valley floor, at the confluence with D1. Substantial vegetation regrowth at both the initiation and the deposition zones is evident over time (cf. dashed yellow outline in Figures 8a and 8b). D3 is the largest landslide (97,600 m²) occurred between 1954 and 2020 at any of the four sites here examined. It was first observed in photo year 2016, initiated as a 25 m-thick rotational slide (Figure 8d), which transformed into an earth flow forcing the existing gully channel southward (Figure 8b).

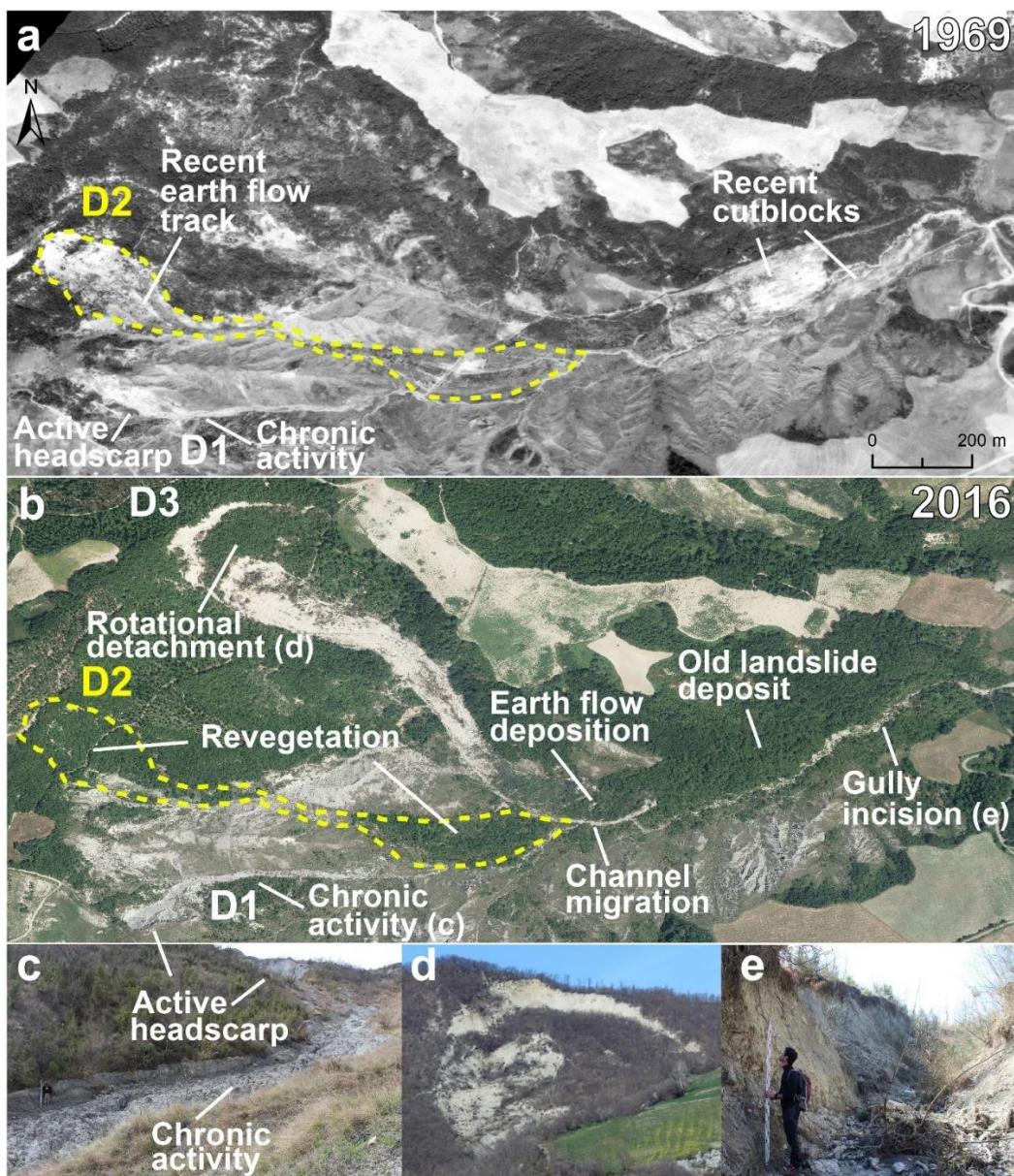


Figure 8. Vertical view of sub-basin D in photo year (a) 1969; and (b) 2016. Dashed yellow outline indicates the perimeter of an earth-flow track at site D2, occurred after photo year 1954 and before 1969, which appears completely revegetated in photo year 2016. Field, oblique views of: (c) active headscarp and earth-flow channel at site D1 (height of lateral levee = 1.5 m); (d) rotational slide developing into an earth flow at site D3; and (e) gully channel cutting through old landslide deposit (thickness: 4 to 6 meters).

5. Discussion

When considering a mapped landslide polygon of a multi-temporal inventory, critical information of interest to an end user, either for basic or applied purposes, include landslide size (e.g., area), how frequently landslide activity has occurred at that same location in a given time period and how landslide geometry developed in time. Indeed, landslide size, geometry and frequency modulate downslope/stream sediment flux and geomorphic disturbance, hence determine landslide hazard and risk to lives and man-made structures.

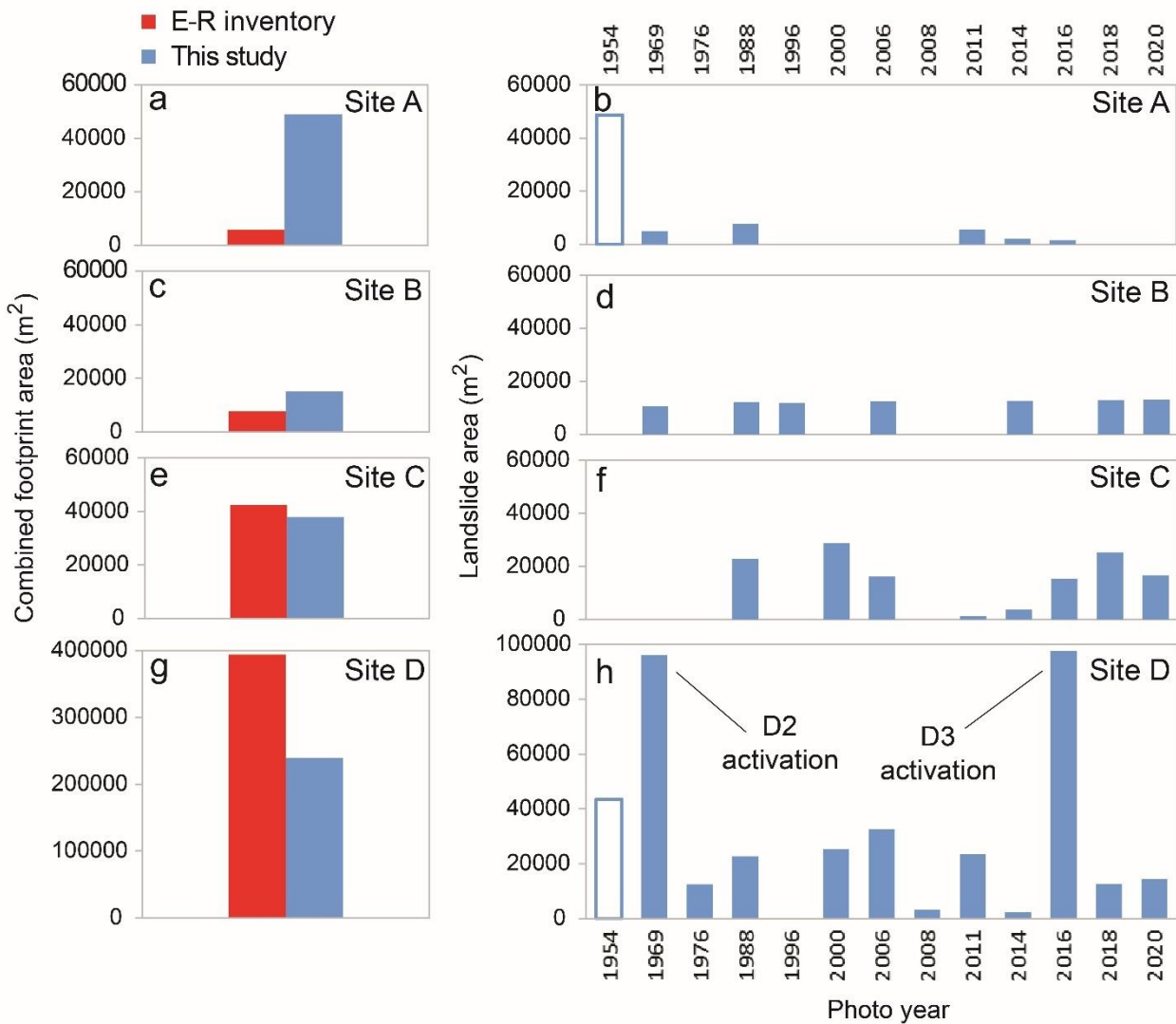


Figure 9. Comparison of landslide combined footprint area between the E-R inventory and this study (left hand-side panels). Landslide area across photo years obtained through the multi-temporal mapping approach (right hand-side panels). Empty bars indicate landslide areas of landslides visible on 1954 aerial photos, whose time of last activation is unknown.

Comparative analysis between multi-temporal and E-R landslide mapping shows diverse outcomes across the four study sites. Inter-site variability, observed in terms of combined footprint area -- defined as the area of the polygon outline that results from merging all historically mapped landslides appeared between photo years 1954 and 2020 at a given site -- in part reflects landslide type and the number of recurrences mapped in the study period (Figure 9). Combined footprint area is respectively 9 (site A) and 2 (site B) times larger than

previously mapped in the E-R inventory (Table 4 and Figures 9a and 9c). In the former, most of this difference is due to six landslide polygons mapped in photo year 1954; in the latter, this is related to progressive headscarp upslope migration, otherwise previously undetected. Combined footprint area is about the same at earth-flow site C (Table 4 and Figure 9e), where the spatial extent of the two historically documented earth flows (Figure 6h) substantially match that resulting from the eight multi-temporal activations (Figure 6i). At site D, combined footprint area in the E-R inventory is about 1.7 times larger than the corresponding multi-temporal case (Table 4 and Figure 9g). In this context, the E-R inventory was critical for identifying the primary depositional feature on the sub-basin valley floor, whereas the multi-temporal approach allowed deciphering which portion of this deposit was indeed associated with post-1954 landslide activity (Figures 7 and 8).

Table 4. Landslide combined footprint area of the two inventories and landslide area across photo years obtained through the multi-temporal mapping approach (this study). At site B, landslide area across photo years refers to a single landslide feature evolving in time.

	Inventory	Photo year	Site A	Site B	Site C	Site D	
Combined footprint area (m ²)	E-R		5,700	7,800	42,400	399,300	
	This study		48,800	15,200	37,900	239,300	
Landslide area (m ²)	This study	1954	48,700			43,400	
		1969	4,900	10,500		96,200	
		1976				12,400	
		1988	7,700	12,200	22,900	22,700	
		1996			11,900		
		2000				28,900	25,400
		2006			12,400	16,200	32,700
		2008					3,200
		2011	5,600			1,300	23,500
		2014	2,000	12,600	3,700	2,300	
		2016	1,600		15,300	97,600	
2018		12,800	25,300	12,600			
2020		12,900	16,700	14,300			

Our findings indicated that the multi-temporal approach does not always result in mapping larger (or smaller) landslide polygons, or previously undetected landslides, but provides insights on process understanding. Consequently, an added value of this mapping approach lies in its ability to detect different styles of landsliding and improve the degree of inventory completeness in post-1954 time (Figure 9). For example, we could disentangle the origin of a combined footprint area in the E-R inventory: either as the result of multiple recurring landslides at site A (Figure 9b), site C (Figure 9f), and D (Figure 9h), or as the progressive evolution of a single landslide scar at site B (Figure 9d). In this context, the case of site D is instructive (Figures 7, 8 and 9h). Within this sub-basin, we could show that: (i) sites D1 and D2 have been continuously active since 1954; and (ii) site D3 is the result of a new earth flow, presently at the early stage of evolution. From an applied perspective, enhanced process-based understanding of landslide activity at the study sites provides critical insights on possible future scenarios of evolution, lending fundamental support for landslide hazard and risk

assessment, as shown by previous geomorphological approaches (e.g., Cardinali et al., 2002; Van Westen et al., 2006; Wieczorek, 1984).

Information and inferences on process-response dynamics were drawn: (i) at landslide initiation sites, through observation of headscarp headward migration (as opposed to stability or vegetation regrowth), which implies downslope sediment supply; (ii) at landslide transport and deposition zones, the spatial pattern of revegetation through time, in conjunction with the development of gully channels, allowed inferring periods of stability; and (iii) changes at landslide terminus, allowed identifying new sediment pulses, exact sediment targets (e.g., fan, valley floor, and stream channel), as well as induced changes in channel morphology and geometry.

Combining similar process-based information at initiation, transport and deposition zones allows making inferences on landslide mobility and downslope/downstream effects. For example, we found that landslides that initiate at gully headwalls (e.g., sites C, D1 and D2), move along confined gully channels and tend to stop before reaching a permanent stream channel. In particular, deliverability appears to be conditioned by previous landslides that have travelled along the same path and have formed depositional plugs, which now constitute a barrier to further landslide runout.

Although beyond the scope of this paper, the four study sites within the Sillaro River basin display a high temporal variability in landslide activity (cf. panels b, d, f and h in Figure 9), suggesting complex responses to hydro-meteorological forcing in relation to the history of each site, in terms of previous landslide activity, as well as natural and anthropogenic land cover dynamics.

6. Conclusions

With reference to the existing regional landslide inventory, we show that the multi-temporal approach proposed in this study can enhance relevant degree of completeness, through identification of previously undetected landslides, and reduce mapping uncertainties on existing polygons. In particular, by providing a dynamic view of landslide activity through time, the multi-temporal approach proved useful for gaining: (i) better time constraint to first time landslide occurrences and subsequent recurrences; (ii) improved estimation of landslide area, in relation to the episodic or recurring nature of activation(s); and (iii) insights on a surprisingly wide range of hillslope-channel interactions that control the pace of landscape change.

Major improvements, in terms of landslide detection and quantification of the relevant areas, relate to gully systems and secondary tributary basins that experience recurring channelized earth-flows. In this context, our observations suggest that ephemeral gully systems may play a key role in the sediment budget of these clay-rich mountain settings. Specifically, we show that gullies can convey frequent earth-flow sediment slugs from headwall positions down to gully confluences (i.e., up to at least eight pulses in 30 years), where depositional lobes may pile up through time and choke the gully system, limiting the run out of subsequent earth-flow activations. During extended periods of stability, these sediment stores have shown to undergo partial reworking, through development and headward migration of newly-formed gully channels, which therefore

promote sediment transfer downstream. To corroborate our preliminary interpretations and elucidate further these dynamics of gully recharge and evacuation, we believe ad hoc monitoring efforts are needed.

To constrain landslide-derived sediment fluxes over more representative spatial scales, future work in the Sillaro River will aim at extending the present multi-temporal mapping experiment at the basin scale, while complementing it with an assessment of landslide thickness, hence volumes of mobilized debris.

Acknowledgements

This work was partly funded by Fondazione Cassa di Risparmio in Bologna through 2018/0348 BEDFLOW and 2019/0228 BEDFLOW PLUS projects. SP was funded through a PhD scholarship of the Italian Ministry of University (cycle XXXIV). We thank Giovanna Daniele, Giulio Ercolessi, and the Archivio Cartografico della Regione Emilia-Romagna for providing information on historical aerial imagery and the Emilia-Romagna landslide inventory.

References

- ARPAE (Agenzia prevenzione ambiente energia Emilia-Romagna) (2021). *Annali idrologici*. (Last accessed: 25th March 2021).
- Baum R.L., & Reid M.E. (1995). Geology, hydrology and mechanics of a slow-moving, clay-rich landslide, Honolulu, Hawaii. In: Haneberg W.C., & Anderson S.A. (eds.), *Clay and Shale Slope Instability*. Geological Society of America, *Reviews in Engineering Geology*, 10, 79-105.
- Bayer B., Simoni A., Mulas M., Corsini A., & Schmidt D. (2018). Deformation responses of slow moving landslides to seasonal rainfall in the Northern Apennines, measured by InSAR. *Geomorphology*, 308, 293-306.
- Bekaert D.P.S., Handwerger A.L., Agram P., & Kirschbaum D.B. (2020). InSAR-based detection method for mapping and monitoring slow-moving landslides in remote regions with steep and mountainous terrain: An application to Nepal. *Remote Sensing of Environment*, 249, 111983.
- Benini A., De Nardo M.T., Severi P., Borsetti A.M., Negri A., & Vaianni S.C. (2009). *Note Illustrative della Carta Geologica d'Italia alla scala 1:50.000, F. 238 Castel San Pietro Terme*. 124 pp., S.EL.CA. Firenze.
- Berti M., Martina M.L.V., Franceschini S., Pignone S., Simoni A., & Pizziolo M. (2012). Probabilistic rainfall thresholds for landslide occurrence using a Bayesian approach. *Journal of Geophysical Research*, 117 (F4), F04006.
- Berti M., & Simoni A. (2010). Field evidence of pore pressure diffusion in clayey soils prone to landsliding. *Journal of Geophysical Research*, 115 (F3), F03001.
- Bertolini G., & Pizziolo M. (2008). Risk assessment strategies for the reactivation of earth flows in the Northern Apennines (Italy). *Engineering Geology*, 102 (3-4), 178-192.

- Bettelli G., Panini F., Fioroni C., Nirta G., Remitti F., Vannucchi P., & Carlini M. (2012). Revisiting the Geology of the “Sillaro Line”, Northern Apennines, Italy. *Rendiconti Online della Società Geologica Italiana*, 22, 14-17.
- Bovis M.J., & Jakob M. (1999). The role of debris supply conditions in predicting debris flow activity. *Earth Surface Processes and Landforms*, 24 (11), 1039– 1054.
- Brardinoni F., Cavalli M., Heckmann T., Liebault F., & Rimbock A. (2015). Guidelines for assessing sediment dynamics in alpine basins and channel reaches. *SedAlp WP4 Final Report*, Alpine Space, 71 pp.
- Brardinoni F., Church M., Simoni A., & Macconi P. (2012). Lithologic and glacially-conditioned controls on debris-flow sediment dynamics. *Geology*, 40, 455-458.
- Brardinoni F., Hassan M.A., Rollerson T., & Maynard D. (2009). Colluvial sediment dynamics in mountain drainage basins. *Earth and Planetary Science Letters*, 284, (3-4), 310-319.
- Brummer C.J., & Montgomery D.R. (2003). Downstream coarsening in headwater channels. *Water Resources Research*, 39 (10), 1294.
- Cardinali M., Reichenbach P., Guzzetti F., Ardizzone F., Antonini G., Galli M., Cacciano M., Castellani M., & Salvati P. (2002). A geomorphological approach to the estimation of landslide hazards and risks in Umbria, Central Italy. *Natural Hazards and Earth System Sciences*, 2 (1/2), 57-72.
- Colesanti C., & Wasowski J. (2006). Investigating landslides with space-borne Synthetic Aperture Radar (SAR) interferometry. *Engineering Geology*, 88 (3–4), 173-199.
- Corsini A., Borgatti L., Cervi F., Dahne A., Ronchetti F., & Sterzai P. (2009). Estimating mass-wasting processes in active earth slides – earth flows with time-series of High-Resolution DEMs from photogrammetry and airborne LiDAR. *Natural Hazards Earth System Sciences*, 9 (2), 433-439.
- Crovelli R.A. (2000). Probability models for estimation of number and costs of landslides. U.S. Geological Survey Open File Report 00-249, 24 pp.
- Cruden D.M., & Varnes D.J. (1996). Landslide types and processes. In: Turner A.K. & Schuster R.L. (eds.), *Landslides, Investigation and Mitigation*. Transportation Research Board, Special Report 247. National Academy Press, 36–75.
- Finnegan N.J., Broudy K.N., Nereson A.L., Roering J.J., Handwerker A.L., & Bennett G. (2019). River channel width controls blocking by slow-moving landslides in California’s Franciscan mélangé. *Earth Surface Dynamics*, 7 (3), 879-894.
- Green K.G., Brardinoni F., & Alila Y. (2013). Channel morphology and bed-load yield in fluvial, formerly-glaciated headwater streams of the Columbia Mountains, Canada. *Geomorphology*, 188, 96-109.
- Guzzetti F., Cardinali M., Reichenbach P., & Carrara A. (2000). Comparing Landslide Maps: A Case Study in the Upper Tiber River Basin, Central Italy. *Environmental Management*, 25 (3), 247–263.
- Guzzetti F., Galli M., Reichenbach P., Ardizzone F., & Cardinali M. (2006). Landslide hazard assessment in the Collazzone area, Umbria, Central Italy. *Natural Hazards Earth System Sciences*, 6 (1), 115-131.
- Guzzetti F., Reichenbach P., Cardinali M., Galli M., & Ardizzone F. (2005). Probabilistic landslide hazard assessment at the basin scale. *Geomorphology*, 72, 272–299.

- Hassan M.A., Bird S., Reid D., Ferrer-Boix C., Hogan D., Brardinoni F., & Chartrand S. (2019). Variable hillslope-channel coupling and channel characteristics in forested mountain streams of glaciated landscapes. *Earth Surface Processes and Landforms*, 44 (3), 736-751.
- Hovius N., Stark C.P., & Allen P.A. (1997). Sediment flux from a mountain belt derived by landslide mapping. *Geology*, 25 (3), 231-234.
- May C.L., & Gresswell R.E. (2003). Processes and rates of sediment and wood accumulation in headwater streams of the Oregon Coast Range, USA. *Earth Surface Processes and Landforms*, 28 (4), 409-424.
- Maynard D. (1991). Tsitika River Watershed Sediment Source Inventory. Unpublished internal report. Vancouver Region, British Columbia Ministry of Forests.
- Nakamura F., Swanson F.J., & Wondzell S.M. (2000). Disturbance regimes and riparian systems – a disturbance-cascade perspective. *Hydrological Processes*, 14 (16-17), 2849-2860.
- Nereson A.L., & Finnegan N.J. (2018). Drivers of earthflow motion revealed by an 80 yr record of displacement from Oak Ridge earthflow, Diablo Range, California, USA. *Geological Society of America Bulletin*, 131 (3-4), 389-402.
- Pavanelli D., Cavazza C., Lavmic S., & Toscano A. (2019). The Long-Term Effects of Land Use and Climate Changes on the Hydro-Morphology of the Reno River Catchment (Northern Italy). *Water*, 11, 1831.
- Piacentini D., Troiani F., Daniele G., & Pizziolo M. (2018). Historical geospatial database for landslide analysis: the Catalogue of Landslide OCcurrences in the Emilia-Romagna Region (CLOCKER). *Landslides*, 15 (4), 811–822.
- Pizziolo M., Bernardi M., Daniele G., Generali M., & Piacentini D. (2015). Landslide occurrences during the high-intensity rainfall event of March–April 2013 in the Emilia-Romagna region (North Apennines, Italy). In: Lollino G., Manconi A., Guzzetti F., Culshaw M., Bobrowsky P., & Luino F. (eds), *Engineering Geology for Society and Territory - Volume 5*. Springer, 777-780.
- Preciso E., Salemi E., & Billi P. (2012). Land use changes, torrent control works and sediment mining: effects on channel morphology and sediment flux, case study of the Reno River (Northern Italy). *Hydrological Processes*, 26 (8), 1134-1148.
- Regione Emilia-Romagna (2021). Cartografia del dissesto della Regione Emilia-Romagna. https://geo.regione.emilia-romagna.it/cartografia_sgss/user/viewer.jsp?service=dissesto (Last accessed: 8th April 2021).
- Reid L.M., & Dunne T. (1996). *Rapid Evaluation of Sediment Budgets*. Catena Verlag, Reiskirchen, 164 pp.
- Roering J.J., Stimely L.L., Mackey B.H., & Schmidt D.A. (2009). Using DInSAR, airborne lidar, and archival air photos to quantify landsliding and sediment transport. *Geophysical Research Letters*, 36 (19), L19402.
- Schuerch P., Densmore A.L., McArdell B.W., & Molnar P. (2006). The influence of landsliding on sediment supply and channel change in a steep mountain catchment. *Geomorphology* 78 (3-4), 222–235.
- Simoni A., Ponza A., Picotti V., Berti M., & Dinelli E. (2013). Earthflow sediment production and Holocene sediment record in a large Apennine catchment. *Geomorphology*, 188, 42-53.

- Van Westen C.J., van Asch T.W., & Soeters R. (2006). Landslide hazard and risk zonation—why is it still so difficult?. *Bulletin of Engineering geology and the Environment*, 65(2), 167-184.
- Wieczorek G.F. (1984). Preparing a detailed landslide-inventory map for hazard evaluation and reduction. *Bulletin of the Association of Engineering Geologists*, 21(3), 337-342.
- Zattin M., Picotti V., & Zuffa G.G. (2002). Fission-track reconstruction of the front of the Northern Apennine thrust wedge and overlying Ligurian Unit. *American Journal of Science*, 302 (4), 346-379.

CHAPTER 3

Historical (1954-2018), basin-wide earthflow activity, agricultural land abandonment and the role of badlands in a changing climate

Sharon Pittau¹, Mauro Rossi² and Francesco Brardinoni¹

1. Department of Biological, Geological and Environmental Sciences, University of Bologna, Bologna, Italy
2. CNR-IRPI, Perugia, Italy

Manuscript in preparation for submission to *Catena/Geomorphology*

Abstract

Drainage basins of the Northern Apennines, and in particular those developed on the Allochthonous Ligurian Complex, are dominated by intense landslide activity operated by earth slides and flows, and by widespread badland erosion. Today, a long history of deforestation and land cover changes has generated a landscape with sparse, coppice managed, forest cover. In these settings, quantitative knowledge on landslide occurrence in relation to inherited and ongoing land cover changes is limited, hence preventing suitable strategies of land management. To address this gap, we conduct a multi-temporal inventory in clay-dominated terrain of the Sillaro River basin (139 km²) across four lithologies: claystones of the Ligurian (L claystones), Epiligurian (E claystones), and Padano-Adriatic (P-A claystones) Units, as well as sandstones & marls of the terrigenous Flysch Complex. Historical landslide activity, investigated by visual inspection of 12 sequential aerial photo sets between 1954 and 2018, is quantified in terms of landslide density. Landslides are classified according to movement type (earth slide, flow and complex) and temporal nature (episodic and recurring). Land use change is evaluated across four periods: pre 1954, 1955-1976, 1977-1996, and 1997-2018. To account for the historical variability of meteorological forcing, we examine three precipitation indices: (i) the annual total precipitation (PRCPTOT); (ii) the annual maximum daily precipitation (RX1day); and (iii) the precipitation fraction (R99pTOT) due to extremely wet days.

Results show that recurring landslides prevail over episodic counterparts, and that recurrence at a site can reach a maximum of 9 times across the 12 photo years examined. Landslide activity is highest in claystones and landsliding appears strongly controlled by lithology. Terrain morphometry and lithology affect landslide geometry (lengths and areas), whereas land cover appears to play a secondary role, except in arable crops and meadows where landslides are distinctively shorter and smaller. Exploring landslide temporal variability in relation to land-cover changes across geologic domains, our findings suggest complex interactions between landsliding and land cover types, modulated by slope gradient and lithology. We find that in claystone-dominated terrain, landslides density is highest in badlands across all four time periods examined, followed by transitional shrublands, managed forest, and arable crops. Conversely, in sandstones & marls landslide density is highest in managed forest, followed by shrubland and arable crops. When land use effects are assessed as a function of slope gradient, different behaviours are observed in the four geologic domains. Overall, landslide activity is highest in the last twenty years, during a period of land-cover stability, where a decrease in total precipitation and increase of extreme events is recorded. In this context, we find high correlation between landslide activity and specific precipitation indices. In particular, badlands result being the most sensitive sites to changes in precipitation, with the highest landslide densities between 1997 and 2018 in all lithologies, with the only exception of the Padano-Adriatic claystones. These stand out for their highest density scores between 1955 and 1976, a pattern that we explain with the agricultural encroachment of unstable badlands terrain.

1. Introduction

During the last few decades, there has been a growing interest on assessing the relative contribution of climate change and land cover changes on the vulnerability of water resources and the impacts on sediment transfer in Mediterranean areas (e.g., García-Ruiz et al., 1996; Piccarreta et al., 2006; Buendia et al., 2015). These studies have highlighted a decrease in runoff and sediment yield during the second half of the 20th century, mainly due to forest cover development following rural abandonment, and to a transition to drier climatic conditions. Forest development implies an increase in rainfall interception (e.g., Gallart et al., 1997; Llorens et al., 1997) and a reduction in runoff generation. These conditions, combined with the decrease of precipitation and the transition from arable crops to dense shrubland on steep slopes, have led to buffered hydrological responses, and consequently, to a decrease in sediment fluxes. Following this logic, in Mediterranean settings, similar land cover changes may increase slope stability due to positive effects on hillslope hydrology and root reinforcement (Sidle & Ochiai, 2006). Vice versa, areas with little or no forest cover, such as badlands, could display high landslide activity.

Badlands are bare, highly dissected areas developed on impermeable, unconsolidated sediment and/or highly erodible lithologies, typically characterized by high clay content (Yair et al., 1980; Howard, 1994; Gallart et al., 2002). Dominant geomorphic processes shaping badland morphologies include surface flow-based mechanisms of diffused (i.e., rain splash and sheet washing) or concentrated (i.e., rilling and gullying) erosion, subsurface erosion (i.e., piping or tunnelling), and landsliding (i.e., earth slides and earthflows) (Yair et al., 1980; Bryan & Yair, 1982; Clotet-Perarnau et al., 1988; Kusanin-Grubin, 2013; Moreno-de las Heras & Gallart, 2018; Llena et al., 2020).

The Mediterranean basin is a region of high badland density (Torri et al., 2018; Nadal-Romero et al., 2021) due to abundant clayey geology and to climatic seasonal contrasts. In these settings, typically characterised by easily accessible, gentle slopes, forest clearing began in the Roman Period and continued through the 20th century, likely promoting widespread erosion and badland development. In this context, traditional field-based monitoring using sediment traps and turbidimeters are common means for investigating erosion processes and quantifying erosion rates (e.g., Mathys et al., 2003; Nadal-Romero et al., 2012). Usually, badlands monitoring has been performed at gully (e.g., Torri et al., 2013; Vericat et al., 2014) or plot scales (e.g., Benito et al., 1992; Regüés et al., 1995), at high temporal resolution over seasons, years, or decades. More recently, the development of novel technologies of topographic acquisition, such as Terrestrial Laser Scanning (TLS) and Structure from Motion (SfM) photogrammetry has allowed monitoring volumetric topographic changes (i.e., degradation and aggradation) at high spatial resolution (Ballesteros-Cánovas et al., 2015; Nadal-Romero et al., 2015; Llena et al., 2020; 2021). However, while surficial erosion has been the object of intense investigation, the role of landsliding has been virtually neglected. Indeed, there is a lack of knowledge on the quantification of basin-wide landslide activity in relation to badlands evolution, and on how land cover changes may affect landslide occurrence within and around badlands in relation to ongoing climatic changes.

To address this gap, we selected a clay-dominated basin in the Northern Apennines, where badlands are common, and earth slides and earthflows are the dominant types of mass movement. In this setting, socio-political changes associated with post-WW2 recovery and modern industrial development, led to widespread people displacement from rural areas to cities and thus to agricultural land abandonment, with consequent recolonization by transitional shrubs and natural forests in drainage basins of the Northern Apennines (Preciso et al., 2012; Pavanelli et al., 2019).

This work aims to evaluate basin-wide, historical trends of landslide occurrence and recurrence in relation to ongoing land cover and climatic changes. To this end, we have compiled a multi-temporal landslide inventory (1954-2018) across 12 sequential sets of optical imagery (Table 1). This ensures higher temporal resolution, hence higher inventory completeness, compared to existing land-cover related landslide susceptibility efforts, which typically rely on two to four photosets over similar historical time windows. We start with the examination of the landslide spatial distribution, investigating correlations with lithology. We continue with the evaluation of lithological and land cover effects on landslide geometry, and conclude with the analysis of the landslide temporal distribution in relation to historic precipitation indices and land cover changes across different lithologies.

2. Study area

Study area is the mountain portion of the Sillaro River basin (139 km²) located in the Bologna Metropolitan Area, Italy (Figure 1a). Elevations range from 56 m a.s.l. in Castel San Pietro Terme, at the basin outlet, to 993 m, at Mt. La Fine, on the main divide of the Northern Apennines.

The Sillaro River basin encompasses four main geologic domains, in which clayey lithologies are prevalent. Specifically, claystones and lesser sandy, poorly cemented arenites of the Padano-Adriatic domain (Upper Messinian-Pleistocene; hereafter termed Padano-Adriatic claystones) make up 22% of the area in the lower portion of the basin (Figures 1b and 2b). Alternations of claystones and lesser marls, and poorly cemented arenites of the Epiligurian domain (Eocene-Miocene; hereafter termed Epiligurian claystones), mainly outcrop in the central part of the basin (24% of basin area). Alternations of claystones and lesser marls of the Ligurian domain (Cretaceous-Eocene; hereafter termed Ligurian claystones), outcrop chiefly in the middle and upper part of the basin (36% of basin area; Figures 1b and 2b). Ligurian claystones incorporate highly tectonized limestone blocks and exhibit chaotic texture. Finally, sandstones and marls of the Umbro-Marchean flysch complex (Serravallian-Tortonian; hereafter termed Sandstones & Marls) cover the remainder 10% of the area, in the upper south-eastern portion of the basin (Figures 1b and 2b).

The hillslopes and the ephemeral gully network carved on clay-bearing lithologies host widespread badland systems (i.e., the so-called *calanchi* in Italian). Dominant landslide types are earth slides and earthflows (Pittau et al., 2021). These geomorphic processes produce and deliver sediment to major alluvial fans at tributary confluences and to the main Sillaro River floodplain, which collectively occupy 8% of the basin area. The Sillaro River has a complex channel pattern. It starts as a single-thread, semi-confined channel, characterized

by riffle-pool and plane-bed morphology, nested in a plateau-like upper valley segment. In proximity of Sassoleone (Figure 1a), the channel becomes substantially steeper and flows along tightly confined and strongly coupled reaches, fed by lateral earth slides and earthflows. Upstream of San Clemente (Figure 1a), the river degrades to multi-thread unconfined and semi-confined channel reaches, along the main alluvial floodplain.

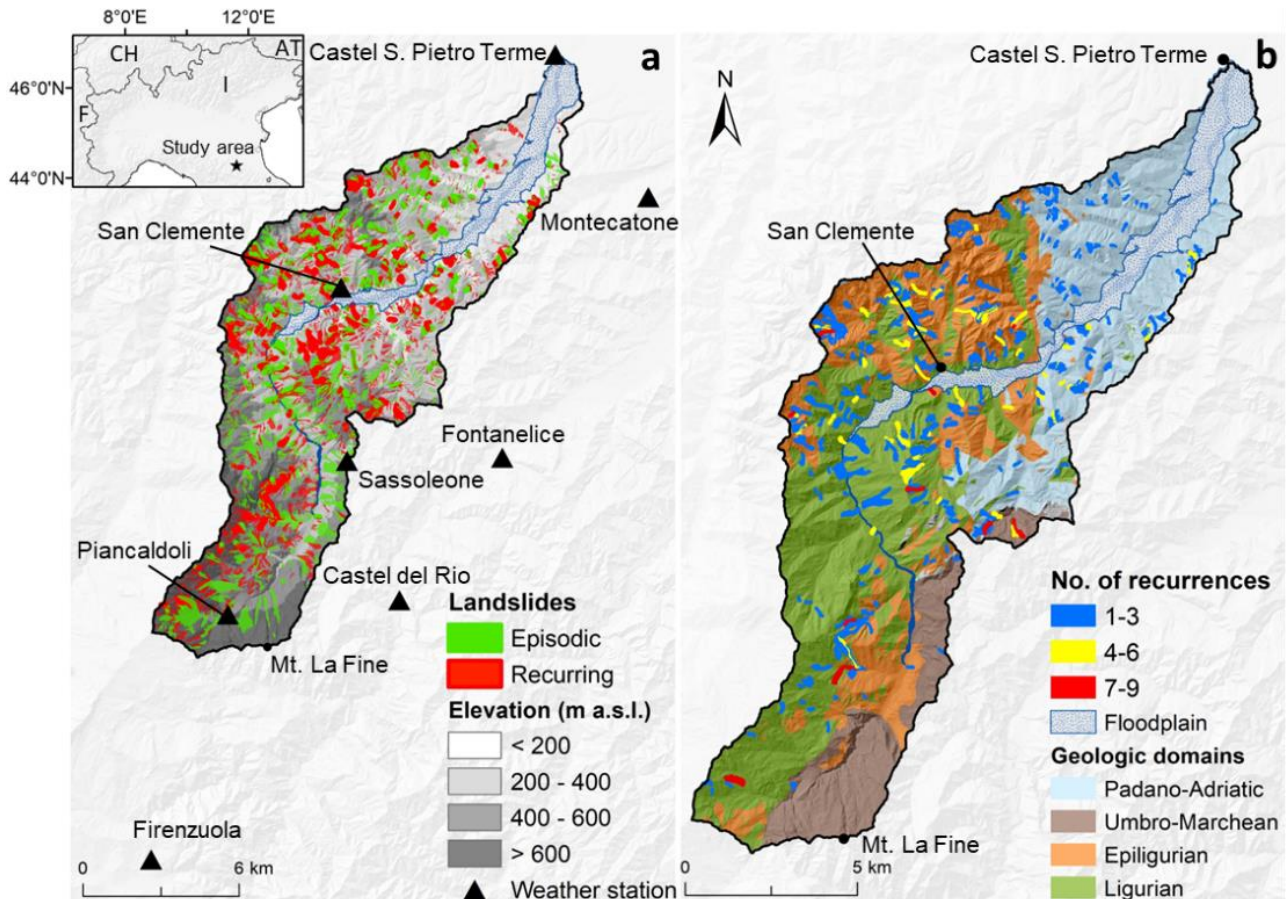


Figure 1. Multi-temporal inventory maps (1954-2018) of the Sillaro River basin showing: (a) landslide polygons classified into episodic and recurring types on elevation bands (grey shades); and (b) landslide polygons classified by number of recorded recurrences in the context of the main geologic domains. In panel a, triangles indicate weather stations. Floodplain in the legend of panel b indicates terrain occupied by the Sillaro River floodplain and the main alluvial fans. The inset map shows the location of the Sillaro River basin (black star).

The variation of slope gradient as a function of elevation (Figure 2a), as well as the frequency distributions of elevation (Figure 2b) and slope gradient (Figure 2c) across geologic domains reflect the foregoing basin configuration. Accordingly, median slope increases directly with elevation across the area occupied by the main alluvial floodplain and the alluvial fans at major tributary confluences (i.e., < 200 m a.s.l., Figure 2a). At higher elevation, slope gradient ranges between 25 and 30%, displaying a subtle inflection between 600 and 800 m a.s.l., in correspondence of the aforementioned plateau, before reaching the main summits at the orogen divide (Figure 2a). In line with the spatial distribution of the main geologic domains (Figure 1b), the Padano-Adriatic (P-A) claystones plot at lowest elevations (i.e., peak at about 200 m a.s.l. in Figure 2b). Epiligurian (E) claystones sit at intermediate elevations (i.e., peak at about 350 m a.s.l.), whereas Ligurian (L) claystones,

and even more so, sandstones & marls of the Umbro-Marchean domain, prevail above 500 m a.s.l. (Figure 2b). Slope frequency distributions across lithologies are similar, and display peaks comprised between 22% and 28%. Interestingly, Ligurian and Epiligurian lithologies tend to occupy respectively the lowest and highest proportion of steep terrain (i.e., > 50%) (Figure 2c).

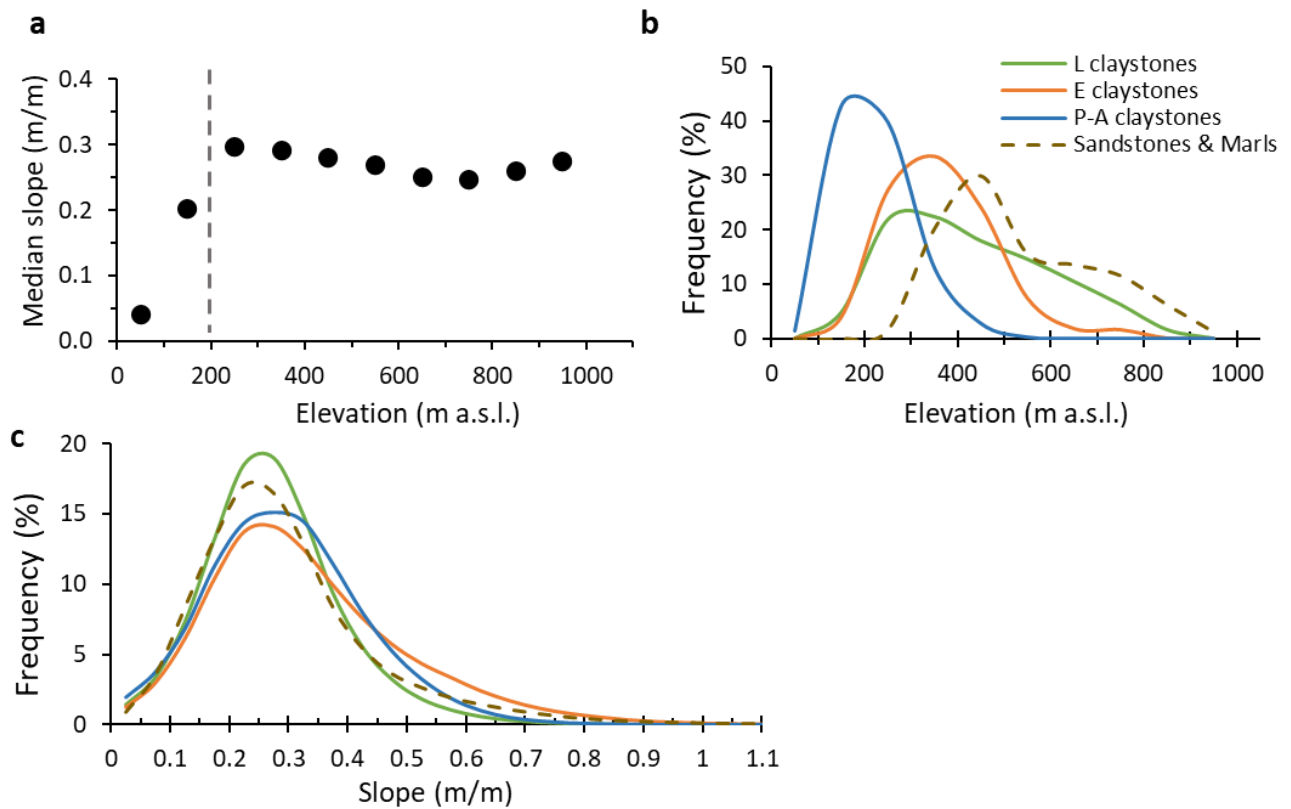


Figure 2. (a) Median slope as a function of elevation of the Sillaro River basin; (b) elevation frequency distribution of geologic domains; (c) slope frequency distribution of geologic domains. Dashed line in panel a marks the approximate altitudinal limit of terrain occupied by the Sillaro River floodplain and the main alluvial fans.

According to the Köppen-Geiger climate classification, the study area belongs to the Mediterranean climatic zone, characterized by four seasons including hot, dry summers, cool, moderately dry winters and wetter springs and falls. Mean annual precipitation (1991-2019) increases with elevation, from 770 mm at Castel San Pietro Terme (59 m a.s.l.) to 1230 mm at Firenzuola (476 m a.s.l.), and is chiefly concentrated in the fall and in springtime. Mean monthly precipitation ranges from 35 mm in July to 188 mm in November (Figure 3a) at Firenzuola, and between 40 mm in July and 92 mm in November (Figure 3b) at Castel San Pietro Terme. Mean monthly temperature is highest between July and August and lowest in winter, from December to February i.e., averages below 0°C in Firenzuola (Figure 3a).

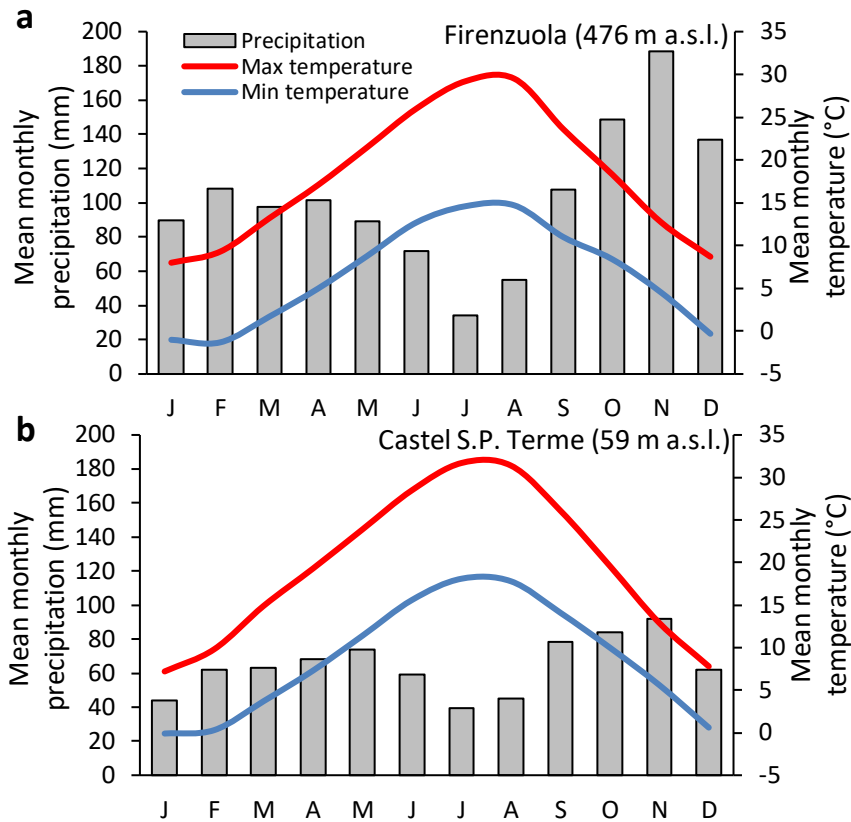


Figure 3. Climographs (1991-2019) at weather stations in: (a) Firenzuola; and (b) Castel San Pietro Terme (cf. Figure 1a for locations). Data source: ARPAE, 2021b.

Today, land cover on the slopes includes arable crops and meadows (33%), transitional shrubs (25%) dominated by rush broom (*Spartium junceum*), juniper (*Juniperus communis*), and dog rose (*Rosa canina*), and coppice-managed forest (22%), where downy oak (*Quercus pubescens*) and manna ash (*Fraxinus Ornus*) prevail. Badlands occupy about the 12% of the hillslopes and subordinately by urban areas (5%), orchards (1%), and water bodies (2%) (Figure 8d).

3. Methods

The multi-temporal landslide inventory was compiled in GIS environment. First, we identified and mapped landslide tracks through visual inspection of ten sequential aerial photosets (i.e., stereoscopic photographs and/or digital ortho-imagery taken in 1954, 1969, 1976, 1985-88, 1996, 2000, 2006, 2008, 2011, and 2014) and two more recent sets of Google Earth imagery (i.e., 2016 and 2018) (Table 1). Following the morphologic classification scheme detailed in chapter 2 (Pittau et al., 2021), for each landslide we recorded movement type, morphologic position at initiation point, lateral confinement, and sediment delivery target (Table 2). During aerial photo interpretation (API) we have identified three main types of landslides: rotational earth slides (slumps), earthflows and complex earth movements. Morphologic position at initiation includes gully headwalls, gully sidewalls, and open slopes (Table 2), with gully-related slope failures generally occurring within badlands systems.

For each landslide polygon, we extracted a series of additional attributes, including length, area, photo year of first identification, temporal nature of occurrence, geological domain, and land use at initiation (Table 2). Each landslide polygon encloses the perimeter of the total disturbed area, composed by an initiation and transportation zone - down to the point where scouring could be identified - and by a deposition zone, where bulging was apparent. For consistency with the companion inventory compiled in coastal British Columbia (see chapter 4), the characterization of landslide geometry presented in this paper follows the specifics adopted by Brardinoni et al. (2009). As such, landslide length and area refer to the initiation and transportation zones only. Although in this thesis we do not pursue landslide volume estimation (see Chapter 5 for further discussion), in perspective, this geometric approach avoids doubling volumetric estimations of mobilized debris. Due to the coarser quality and resolution of aerial photos acquired before 1976, we set a minimum width of about 4 meters, beyond which we found it was not possible to delineate consistently the landslide polygon outline through time. Landslides below this threshold width were not mapped in any of the photo sets considered. Our inventory targets landslides associated with a clear transfer of material from an initiation zone, through a transport zone and down to a deposition zone. Therefore, it does not include incremental seasonal movements, which may be detected through direct monitoring, InSAR, and/or feature tracking.

In the inventory, the photo year represents the minimum age for each landslide, the upper temporal boundary being constrained by the date of the antecedent aerial photo set. Following this logic, landslides mapped on 1954 photos lack of a definite temporal constraint. Finally, temporal classification of landslides (i.e., episodic and recurring) and number of recurrences at any given recurring site were also recorded (see methods in Chapter 2 for more details).

Table 1. Stereoscopic photographs and digital ortho-imagery used for multi-temporal landslide identification and mapping (modified from Pittau et al., 2021).

Photo Year	Photo month	Nominal scale	Flying height (m a.s.l.)	Focal length (mm)	Pixel size (m)	Bands	Source
1954	Jul	1:55,000	3048	153.89	1	B&W	IGM
1969	Jun-Sept	1:15,000	1400	151.79	0.7	B&W	E-R Region
1976	Apr-Jul	1:13,000	1091	153.15	0.9	RGB	E-R Region
1985-88	Apr-Jul	1:25,000	1358	153.26	1	B&W	E-R Region
1996	Sept				1	B&W	E-R Region
2000	Jun-Jul				1	RGB	WMS GN*
2006	Apr-Jul				0.5	RGB	WMS GN*
2008	Jun-Aug		6000		0.5	RGB	WMS E-R**
2011	May-Jun		3368	100.50	0.5	RGB	WMS E-R**
2014	May-Sept				0.5	RGB	E-R Region
2016	Sept				0.3	RGB	Google Earth
2018	Sept				0.3	RGB	Google Earth

Table 2. Landslide attributes included in this inventory (modified from Pittau et al., 2021).

Attribute	Category or Units
Landslide size	Total disturbed area (m ²)
Landslide type	Earthflow Earth slide Complex
Photo year of activity	From 1954 to 2018 (cf. Table 1)
Temporal nature	Episodic Recurring
Morphologic position at initiation (Initiation zone)	Gully headwall Gully sidewall Open slope
Lateral confinement (Transport zone)	Confined Channelized Unconfined
Sediment delivery target (Deposition zone)	Hillslope Gully channel Permanent tributary Main channel Anthropogenic structure
Geologic Domain (dominant lithologies)	Ligurian (L claystones) Epiligurian (E claystones) Padano-Adriatic (P-A claystones) Umbro Marchean (Sandstones & marls)
Land cover at initiation	Arable crops (and meadows) Transitional shrubland Managed forest Badlands

To better constrain the time window associated with the detection of landslides in photo year 1954, we run a landslide visibility test in the post-2000 period, when sequential photosets are 2 to 3 years apart from each other. In particular, we selected 53 landslides that first appeared (and/or last recurred) in photo years 2006 and 2008, and evaluated through time our ability to identify and map: (i) the entire landslide polygon outline (i.e., initiation and transport zones); (ii) a portion of it; or (iii) none of it, due to vegetation regrowth, surficial erosion, and/or fluvial reworking (Figure 4). Landslides considered range in size between 580 m² to 35,700 m². Of these, 3 initiate in cultivated fields, 24 in shrublands, 9 in managed forests, and 17 in badland terrain.

We found that after 2 years, 64% of the landslides were still entirely visible, and that an additional 13% became partly visible (Figure 4a). Complete visibility drops to 42% after 5 years and to 19% after 8 years. After 10 years, complete visibility - hence our ability to delineate the polygon outline - becomes rare (9%), with an

additional 7% of landslides that are still partly visible (Figure 4a). Considering the 5-year uncertainty around photo year 2006 (i.e., antecedent photo year is 2000) and applying a conservative approach, complete visibility becomes rare after 15 years. Landslide persistence on sequential aerial photos did not increase directly with landslide size, since landslide scars completely visible after 15 years ranged between 2,100 m² and 27,000 m².

When classifying landslides by land cover conditions at initiation (i.e., shrubs, managed forest, and badlands) we observe some differences in the time windows associated with complete visibility. In particular, complete visibility may be achieved in roughly 1 out of 10 cases after: (i) 8 years, in terrain covered by shrubs (12%); (ii) 10 years, in badlands (12%); and (iii) 12 years, in forested terrain (11%) (Figure 4b). As noted above, in view of the temporal uncertainty around photo year 2006, we consider that complete visibility becomes rare (hence mapping unreliable) respectively after 13 years in landslide occurred in shrublands, 15 years in badlands, and 17 years in managed forests. These visibility time windows are applied to landslides identified and mapped in photo year 1954.

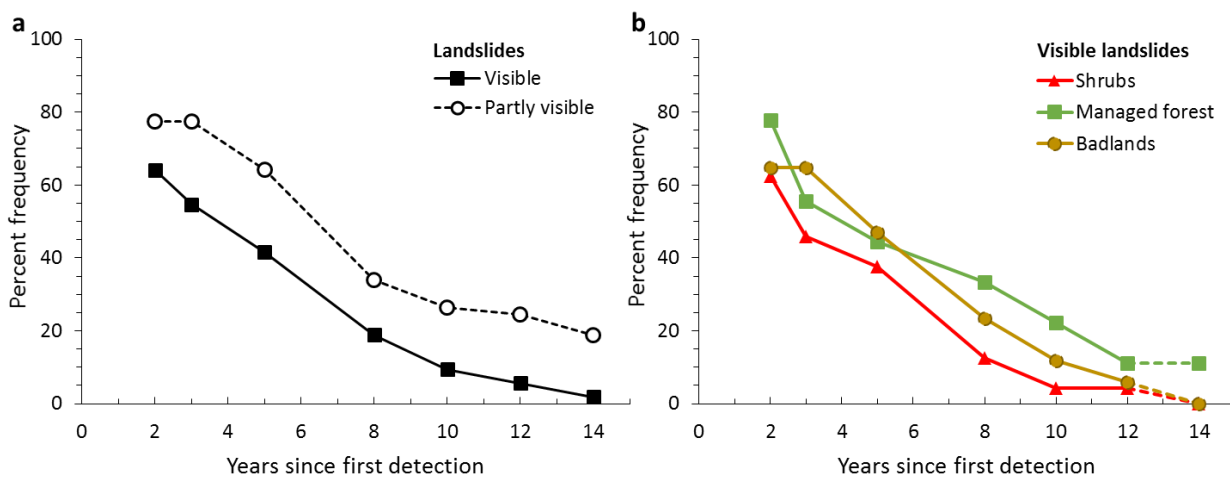


Figure 4. Landslides (expressed as percent frequency) as a function of time since first detection in aerial photo that: (a) remain entirely and partly visible; and (b) remain entirely visible across different land cover conditions at initiation. Dashed lines in panel b indicate uncertain trends, due to the limited number of landslides that have remained completely visible after 12 years.

To assess land cover effects on landslide activity through time, we have drawn historical data in vector format from regional webgis data repositories (<https://geoportale.regione.emilia-romagna.it/catalogo/dati-cartografici> and <https://dati.toscana.it/dataset/ucs>). These digital cartographic data, which cover years 1853, 1954, 1976, 1994, 2003, 2008, 2011, 2014, and 2017, were checked through visual inspection of the relevant orthophoto mosaics, and mapping discrepancies identified were manually corrected. Starting from Corine-based classification scheme (<https://land.copernicus.eu/pan-european/corine-land-cover>), we have subdivided land cover into four main categories, including: (i) arable crops and meadows (for brevity termed *arable crops*), (ii) transitional shrubland (for brevity termed *transitional*), (iii) managed forest, and (iv) badlands. Conceptually, based on highest root cohesion and water interception, we expect that landslide activity will be lowest in managed forest (most stable terrain), and that will increase progressively in transitional shrubland, arable crops,

and badlands (least stable terrain). However, considering that the spatial distribution of land cover within a watershed depends tightly on logistical access (e.g., arable crops may occupy gentler terrain compared to managed forest), we will examine land cover effects on landslide activity through time, also in relation to slope gradient (Section 5.3).

To evaluate possible causal linkages between landslide activity and hydro-meteorological forcing during the study period (1954-2018), we have looked at historical records of daily and annual precipitation (Figure 5). At the annual scale, first we have considered the temporal variability of annual precipitation and relevant anomaly. Due to incomplete historical records (Figure 5), the entire annual series was reconstructed by combining data from Piancaldoli (500 m a.s.l.) and San Clemente (166 m a.s.l.) weather stations.

Owing to largely incomplete historical records at any of the weather stations within the Sillaro River basin (cf., Figure 5) and wishing to explore additional precipitation metrics against which evaluate landslide activity across sequential photo sets (Table 1), we decided to use E-OBS meteorological data analogues, available on the Climate Data Store website (CDS, 2021). E-OBS is a high-resolution daily gridded (0.25 degrees) land-only observational dataset over Europe formed through the interpolation of data collected from meteorological stations. The terrain of the Sillaro River basin falls within three of such grid cells (Supplementary Figure 1). In this work, we have used data from the cell that occupies the central part of the basin, where the majority of the landslide clusters and where the San Clemente station is located (Supplementary Figure 1). Starting from gridded daily rainfall data, we derived the (i) PRCPTOT, (ii) Rx1day and (iii) R99pTOT climate change indices, corresponding respectively to: (i) the annual total precipitation (mm), (ii) the annual maximum daily precipitation (mm), and (iii) the precipitation fraction (%) due to extremely wet days (i.e., when daily precipitation amount exceeds the 99th percentile in the 1950-2020 period). These indices are typically used in climatology to explore historical precipitation trends across different datasets worldwide. More recently, they have been considered as possible proxies for evaluating hydro-meteorological correlations with the occurrence of natural hazards including floods, flash floods and mass movements (e.g., Ávila et al., 2016; Mysiak et al., 2018; Coscarelli et al., 2021).

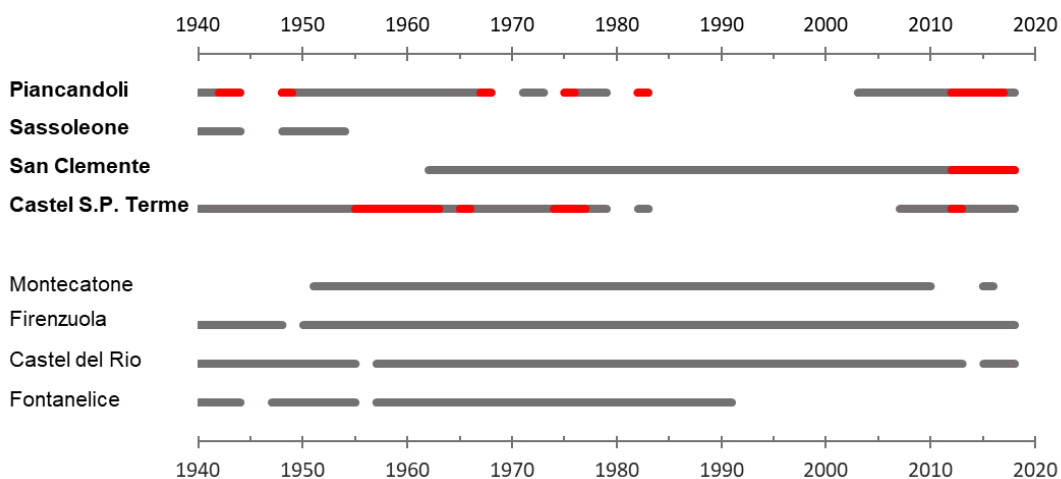


Figure 5. Historical precipitation data at local weather stations between 1940 and 2018. Grey lines indicate complete annual and daily records. Red lines indicate complete annual records but incomplete daily ones.

4. Historical background

4.1 Hydro-meteorological forcing (1950-2018)

The combined time series of annual precipitation anomaly at Piancaldoli (500 m a.s.l.; from 1950 to 1964) and San Clemente (166 m a.s.l.; from 1965 to 2018) stations (Figure 6a) starts with a high positive value in 1951. Subsequently, the 3- and 5-yr moving averages describe a negative trend in 1953-57, which is followed by a positive one until 1984 (with some isolated exceptions), in agreement with climate deterioration and concurrent glacier advance recorded in the Alps (Patzelt, 1985; Hoelzle et al., 2003; Scotti et al., 2014). Moving averages describe a 10-yr negative cycle, until 1995, which is then followed by a series of alternating weak positive and stronger negative, 3-to-5 yr cycles. E-OBS-based precipitation anomalies (Figure 6b) display a very similar time series, the only exception being the 1953-1965 period, where a more pronounced positive trend is observed (i.e., highest anomalies in 1959 and 1960).

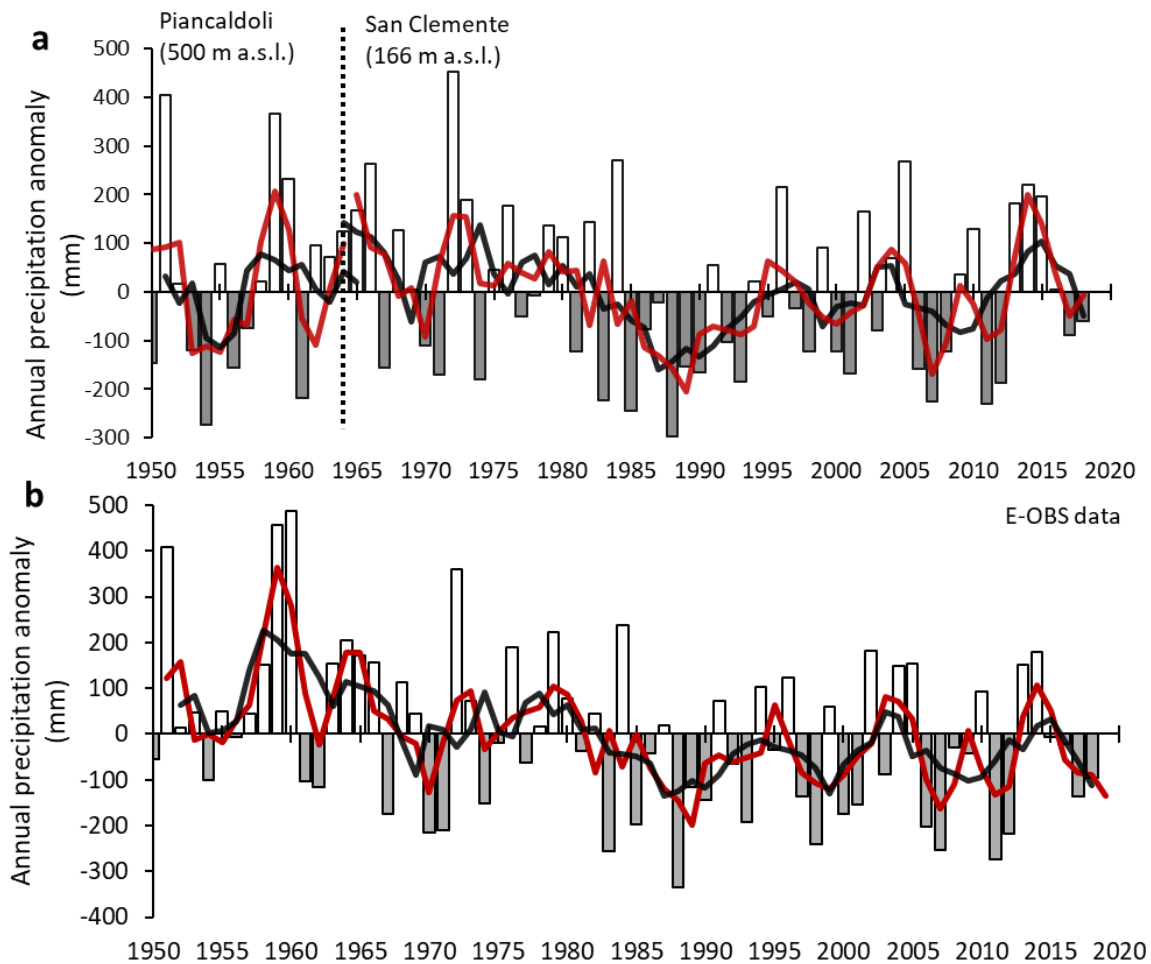


Figure 6. Historical annual precipitation anomaly (bars) and relevant 3-year (in red) and 5-year (in black) moving average drawn from: (a) Piancaldoli (1950-1964) and San Clemente (1965-2018) weather stations (cf., Figure 1a); and (b) E-OBS gridded data. Mean annual precipitation at Piancaldoli (1949-1968) and San Clemente (1962-2020) is respectively 1117 mm and 842 mm (ARPAE, 2021a; ISPRA, 2021). Mean annual precipitation (1950- 2018) of E-OBS gridded data is 807 mm (CDS, 2021).

Gridded data of PRCPTOT from 1950 to 2018, display decrease of annual precipitation over time (Figure 7a). The highest value is recorded in 1960 (1295 mm), while the lowest (471 mm) occurs in 1988. Annual maximum daily precipitation (RX1day) ranges from 23 mm in 1985 to 79 mm in 2005, with a mean of 44 mm (Figure 7b). Mean of annual extreme events (R99pTOT) is of 16%, with a peak of 34% in 1973 (Figure 7c). In 1955, 1970, 1974, 1985, 1988, and 1998 no extreme event is recorded.

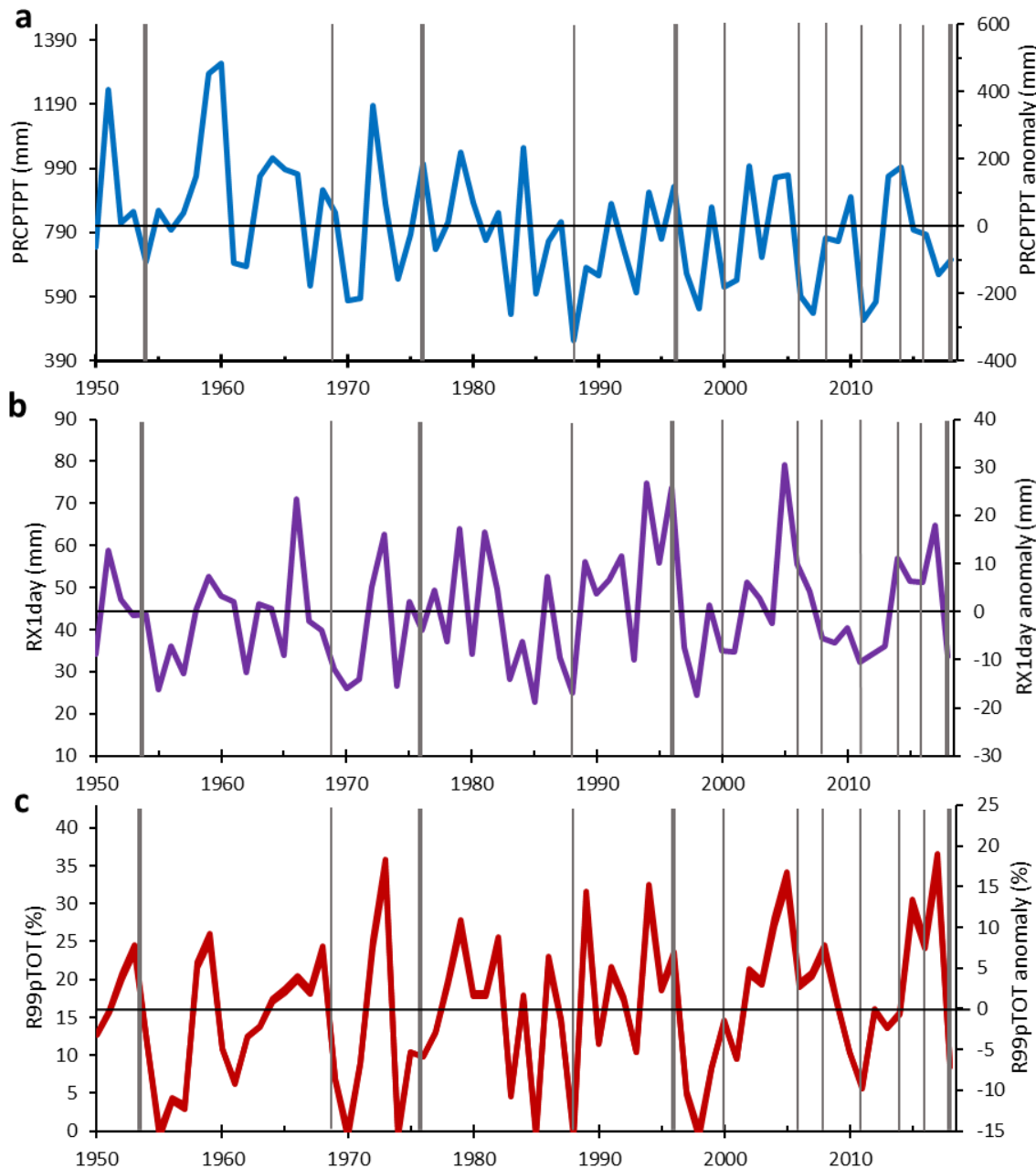


Figure 7. Historical time series (1950-2018) of climatic index values and respective anomalies calculated from E-OBS gridded data at San Clemente station: (a) total annual precipitation, (b) RX1day, and (c) R99pTOT. Vertical lines indicate the historical photo years used in the inventory. Thick vertical lines bound the time period used for assessing historical land cover effects.

4.2 Historical land-cover changes (1853-2018)

Basin-wide, historical land cover mapping (Figure 8 and Supplementary Figure 2) is instructive. In 1853, the basin is mainly covered by transitional shrubs, and subordinately by managed forest and orchards, with limited arable crops and no indication of badland patches (Figure 9 and Supplementary Figure 2). Between 1853 and 1954, we observe a sharp increase in arable crops (and pasture), and to a lesser extent of managed forest, at the expense of transitional shrubland (Figure 9). Interestingly, during this period badlands extent exhibits a significant increase, suggesting that land conversion to cropland and pasture favoured widespread surficial erosion and slope instability (Figure 9). Subsequently, between 1954 and 1976 cropland continues to grow (even though at a much slower rate) with a symmetrical decrease of transitional shrubs, whereas forests and badlands remain substantially stable (Figure 8). The latter extent continues to be stable until today. The 1976-1994 period displays dynamics of agricultural land abandonment. Accordingly, arable crops for the first time start shrinking and transitional shrubs continue to do so, this time compensated by a revived increase in coppice-managed forest (Figure 9). From 1994, changes across categories are minimal and the land cover spatial configuration remains about stable.

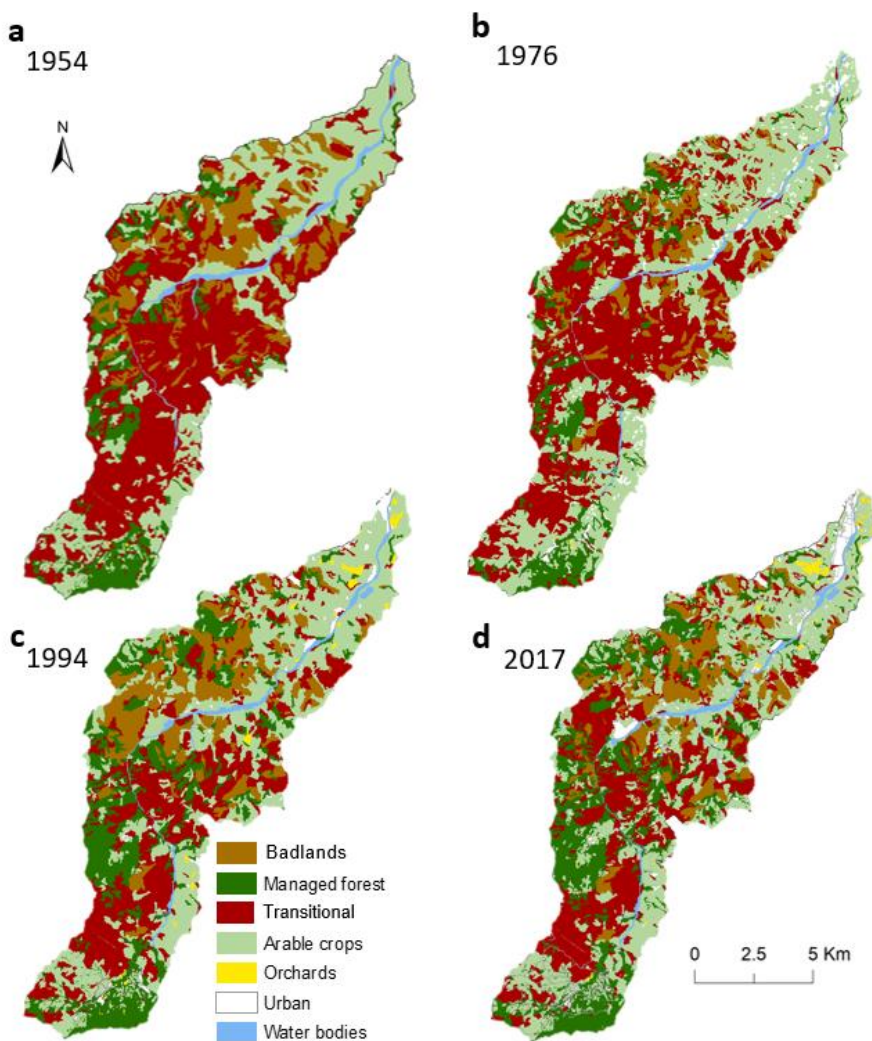


Figure 8. Land cover maps of the Sillaro River basin in: (a) 1954; (b) 1976; (c) 1994; and (d) 2017.

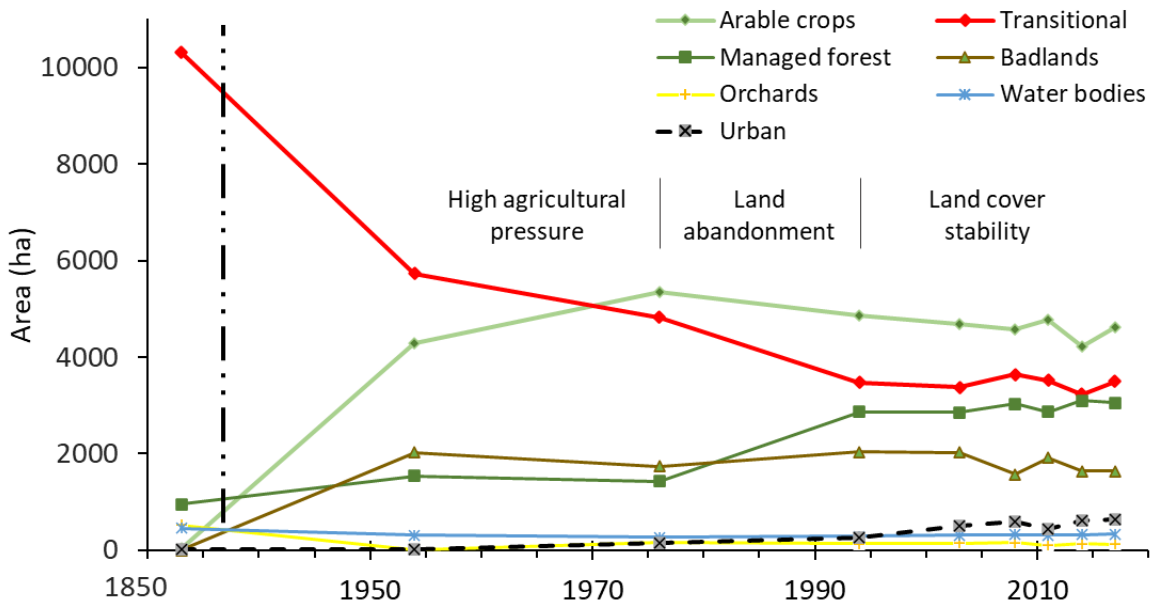


Figure 9. Historical land-cover changes of the Sillaro River basin. Values of 1853 are related to the 88% of the basin area. Vertical dashed line marks temporal truncation applied between 1850 and 1950.

Land cover spatial distribution over time varies across lithologies (Figure 10) and therefore some differences may be observed in comparison with basin-wide trends illustrated in Figure 9. For example, between 1954 and 1976, major changes involved an increase in arable crops in all lithologies, evidence of increasing agricultural pressure, and decrease of transitional shrubs, except in L claystones, where they continue to expand at the expense of managed forest (Figure 10a). The 1976-1994 period shows common land abandonment dynamics, with decrease of shrubs and arable crops paralleled by an increase of managed forest and badlands (i.e., except in sandstones & marls, which bear no significant badland terrain), regardless of lithology. Interestingly, we do not observe a consistent decline of cropland area in L claystones, where this land cover class stays about the same from 1976 onward.

In view of the foregoing historical changes at the basin scale and across geologic domains, we will examine landslide activity as a function of land cover across four main periods (see section 5.3). Before 1954, where temporal information on landslide occurrence is associated with highest uncertainty, between 1954 and 1976, where cropland development (hence agricultural pressure) peaks, between 1976 and 1994, a period characterized by dynamics of land abandonment, and after 1994, a phase of general land cover stability.

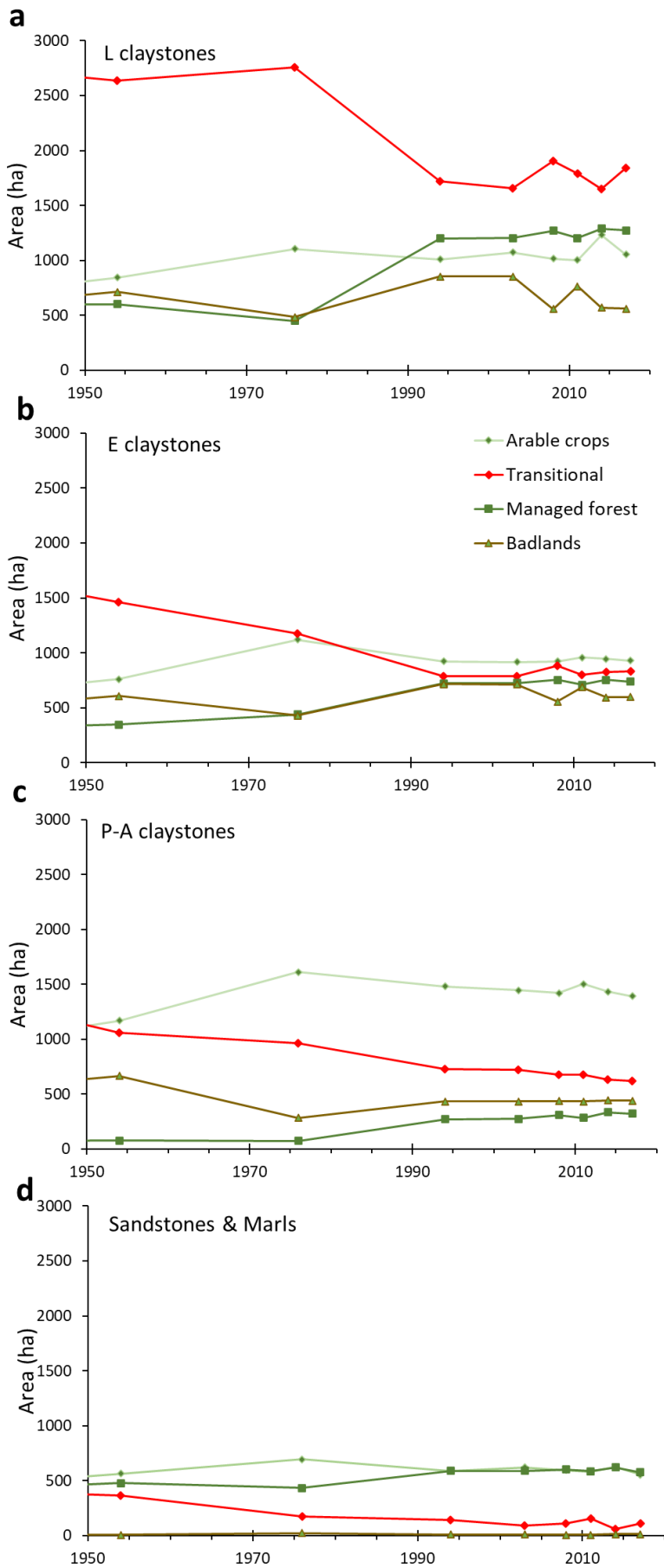


Figure 10. Historical land-cover changes across geologic domains, including: (a) Ligurian claystones; (b) Epiligurian claystones; (c) Padano-Adriatic claystones; and (d) Sandstones & marls.

In altitudinal terms, these historical land cover changes show that the post-1976 increase in managed forest occurs at elevations distributed below 600 m (Figure 11a), at the expense of transitional shrubland, which in the same period displays a symmetrical decrease (Figure 11c). Concurrently, after 1976, the decrease in arable crops is focused on elevations comprised between 300 m and 750 m (Figure 11e). The altitudinal distribution of badlands does not show any significant change through time and peaks consistently between 200 m and 400 m (Figure 11g).

The spatial distribution of land cover types does vary as a function of slope gradient (i.e., modal values and skewness towards high slopes). Accordingly, arable crops exhibit lowest modal slope (0.22 m/m) and a tail that extends up to about 0.70 m/m (Figure 11f). These two statistics increase progressively across transitional shrubland (mode equals 0.25 m/m and tail reaches 0.85 m/m; Figure 11d), and managed forest (mode equals 0.27 m/m and tail reaches 0.95 m/m; Figure 11b). By contrast, the slope distribution in badlands is about symmetrical and exhibits highest modal value (about 0.37 m/m) and a positive tail that touches 0.90 m/m (Figure 11h).

The shape of the slope distribution within each land cover category does not change significantly over time, the only exception being arable crops, where the secondary peak observed at about 0.38 m/m disappears after 1954 (Figure 11f). With reference to landslide susceptibility, we note that, part of the post-1976 forest expansion observed at the expense of shrubland area, involves steep terrain i.e., up to roughly 0.9 m/m (cf., Figures 11b and 11d). In principle, this historical shift suggests that after 1976 a portion of relatively steep terrain within the basin could be considered less prone to landsliding due to increased root reinforcement and water interception. To test this hypothesis and look for possible slope-land cover interactions, we will examine landslide activity in relation to both variables.

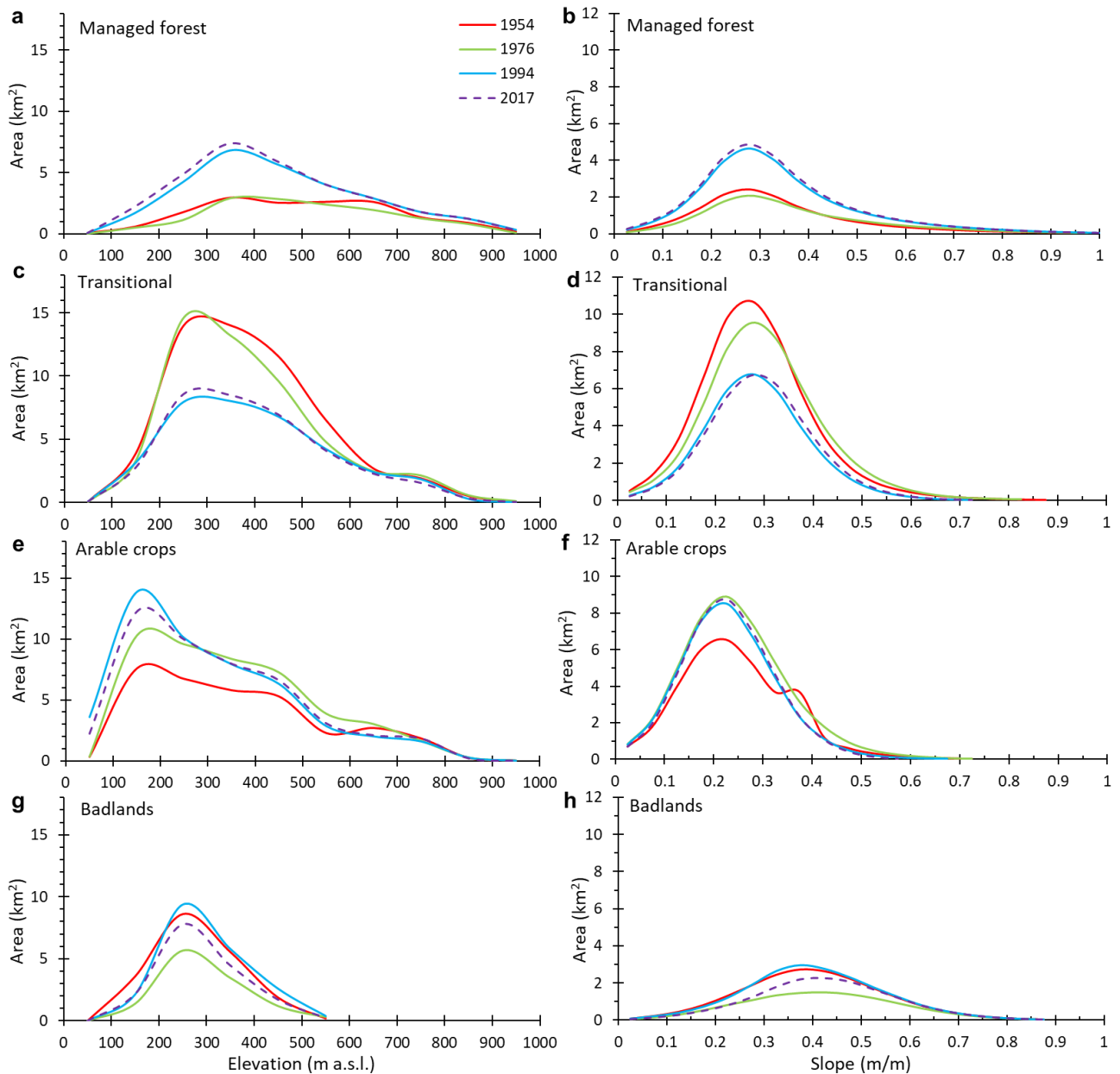


Figure 11. Historical land-cover distribution across terrain elevation in: (a) managed forest; (c) transitional shrubs; (e) arable crops; and (g) badlands. Historical land-cover distribution across slope gradient in terrain covered by: (b) managed forest; (d) transitional shrubs; (f) arable crops; and (h) badlands.

5. Results

We mapped 1164 landslides – 345 episodic and 819 recurring – to which collectively is associated an area of about 4.4 km² (Figure 1a). The number of recurrences at single landslide sites ranges from 1 to 9 (Figure 1b). Landslides are dominantly of the earthflow type ($n = 1022$), followed by earth slides ($n = 129$) and complex ones ($n = 13$). Their morphologic position at initiation (source) includes gully headwalls ($n = 952$), open slopes ($n = 147$), and gully sidewalls ($n = 65$). Sediment delivery targets include mainly gully channels ($n = 1008$), followed by unchannelled topography (hillslopes) ($n = 90$), main channels (i.e., the Sillaro River) ($n = 30$), anthropogenic structures ($n = 22$), and permanent tributaries ($n = 14$). Most of the movements (96%) occur in clay-dominated lithologies (i.e., 35% in L claystones, 35% in E claystones, and 26% in P-A claystones),

whereas 4% only are observed in sandstones & marls. Landslides preferentially occur on badlands (43%) and transitional shrubland (36%), and to a lesser extent in managed forest (14%) and arable crops (7%) (Table 3).

Table 3. Number of landslides and corresponding total landslide areas mapped across land-cover types.

	Total	Badlands	Managed forest	Transitional	Arable crops
Number of landslides	1164	499 (43%)	168 (14%)	420 (36%)	77 (7%)
Area (km ²)	4.4	1.7 (38%)	0.6 (14%)	1.8 (41%)	0.3 (7%)

5.1 Landslide activity across lithologies

In all lithologies, recurring movements overcome recurring counterparts. This dominance is particularly evident in sandstones & marls, where episodic landslides represent the 14% only, and tends to weaken in L and E claystones (26%), and in P-A claystones (40%) (Figure 12 and Table 4). Landslide count standardised by the relevant terrain extent (i.e., landslide density) provides a more reliable view of possible lithologic effects on landslide activity (Figure 12). Clay-dominated lithologies record highest landslide densities, with E claystones that display a maximum high of 12.3 landslides per km², followed by L (7.9 #/km²) and P-A (7.7 #/km²) claystones, and lastly by sandstones & marls (2.9 #/km²) (Table 4).

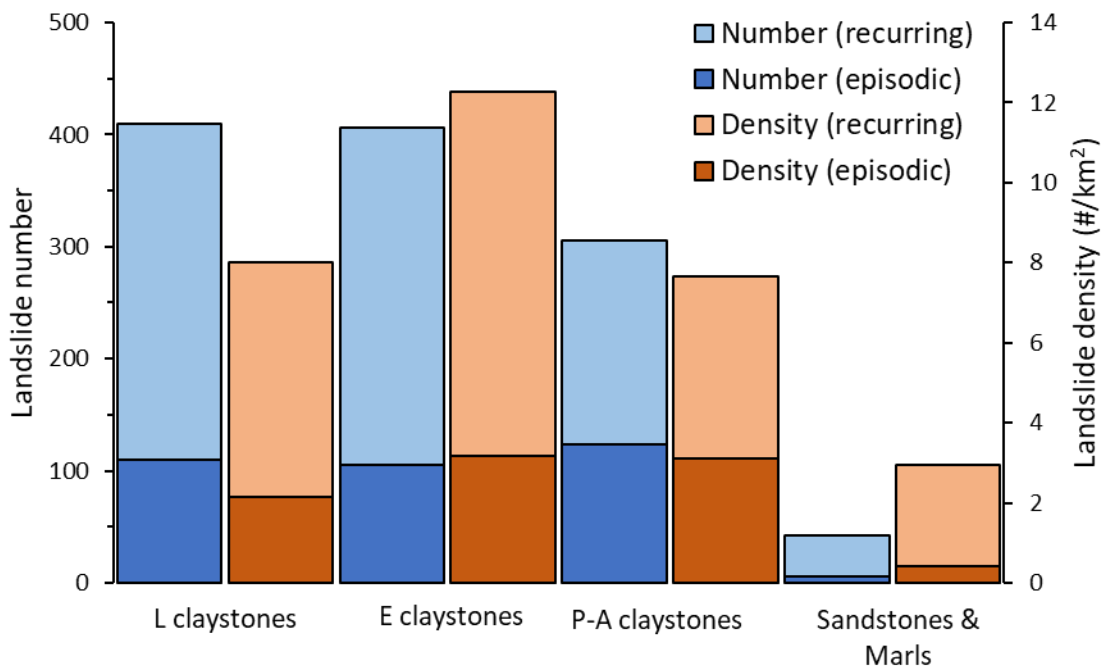


Figure 12. Number of landslides (blue bars) and landslide density (brown bars) across geologic domains. Dark tones indicate episodic landslides; lighter tones indicate recurring landslides.

Table 4. Landslide count, area, and density stratified by temporal nature and dominant lithology of occurrence.

	Temporal nature	L claystones	E claystones	P-A claystones	Sandstones & marls
Number of landslides	Episodic	110	105	124	6
	Recurring	300	301	182	36
	Total	410	406	306	42
Area (ha)	Episodic	59	36	17	2
	Recurring	168	116	30	11
	Total	220	152	47	13
Landslide density (#/km ²)	Episodic	2.1	3.2	3.1	0.4
	Recurring	5.8	9.1	4.6	2.5
	Total	7.9	12.3	7.7	2.9

The number of recurrences at a site in the study period records a maximum of 9 in L claystones, 8 in E claystones, 7 in sandstones & marls, and 6 in P-A claystones (Figure 13). Cumulative frequency distributions show striking overlap among claystones, which follow a non-linear increase, with more than 160 landslides (between 80% and 90% depending on claystone type) that have recurred less than 4 times (Figures 13a and 13c). By contrast, in sandstones & marls, whose cumulative frequency increases linearly, this figure drops by an order of magnitude, to about 10 landslides (< 65%) in agreement with prior results shown in Figure 12. When considering cumulative landslide areas across numbers of recurrences, the different absolute contribution of each claystone type becomes apparent, and the overlap previously observed in landslide count, disappears (Figure 13b). In relative terms, more than 80% of landslide area in P-A claystones is contributed by sites where landslide activity has recurred less than 5 times. This figure decreases to about 65% for E and L claystones, and to 40% for sandstones & marls (Figure 13d).

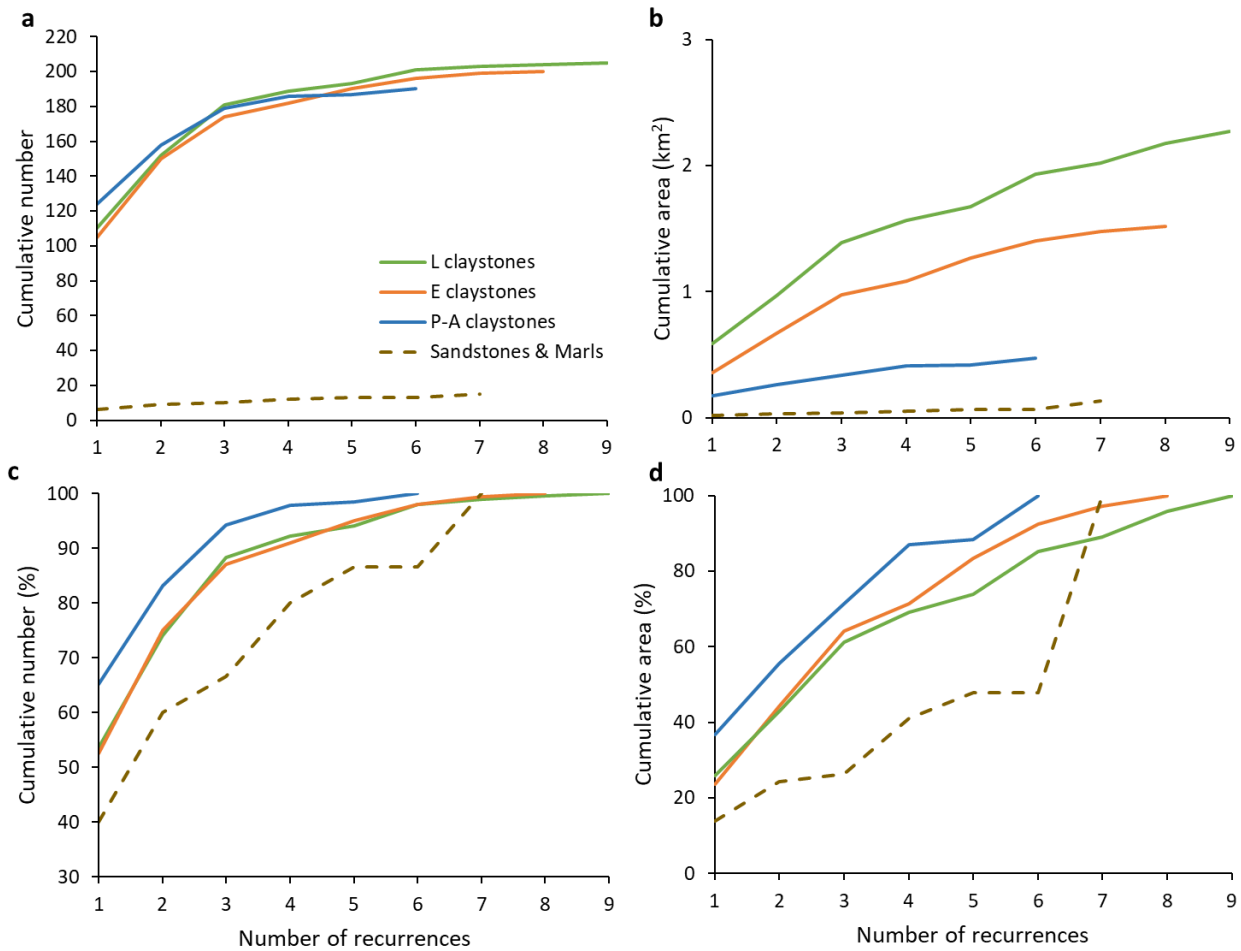


Figure 13. Cumulative frequency distributions as a function of landslide recurrences at initiation sites across geologic domains, represented by: (a) number of observations; (b) landslide area; (c) percent number of observations; and (d) percent landslide area.

5.2 Landslide geometry across lithologies and land cover types

Mapped landslide lengths range from a minimum of 12 m to a maximum of 830 m, and correspond to areas comprised between 112 m² and 75,570 m². Landslide lengths are highest in L and E claystones (i.e., median values >100 m), and display identical distributions (cf., green and yellow box-whiskers in Figure 14a). Landslides in sandstones & marls and in P-A claystones are comparatively shorter, with the latter showing the lowest median value (about 80 m; Figure 14a). A similar size ranking across lithologies is observed with regard to the distributions of landslide areas. In this respect, however, we note a distinct progressive decline in median values and interquartile ranges (i.e., the boxes) across claystones i.e., from L- through E- and down to P-A domains (i.e., median values decline from 2,500 m² down to about 1,000 m²; Figure 14b), in agreement with the ranking in cumulative area distribution (Figure 13b). In terms of land cover, the only apparent effect relates to landslides occurring in arable crops (and pastures), whose medians and interquartile ranges are distinctively lower, both in terms of length (i.e., median = 70 m; Figure 14c) and area (i.e., median = 1,200 m²; Figure 14d).

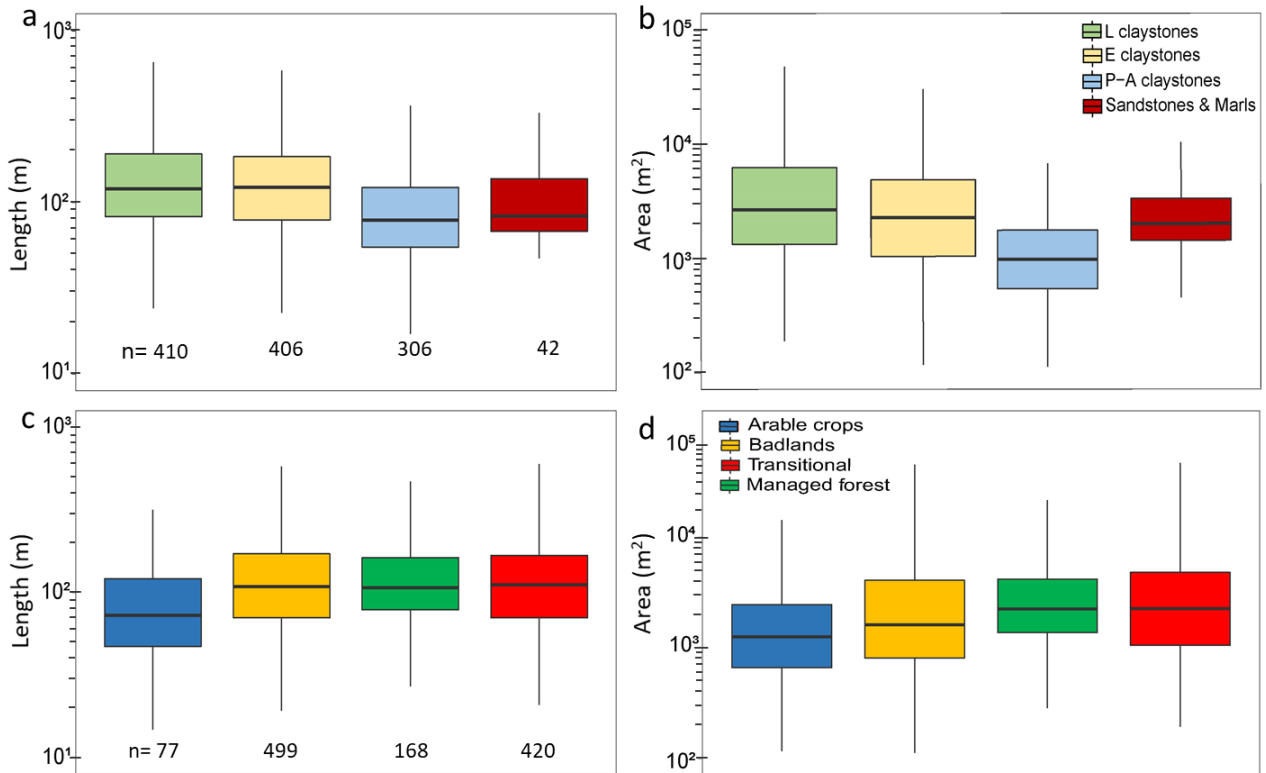


Figure 14. Boxplots showing the size distributions of landslide: (a) lengths; and (b) areas, stratified by geologic domain. Relevant landslide: (c) lengths; and (d) areas, stratified by land cover. Boxes enclose interquartile ranges and whiskers span from 5% to 95%.

Landslide geometry is elongated, with area-length ratio ranging from about 8:1 to over 100:1 (Figure 15a). Overall, landslide length grows as a 0.53 power function of area (see relation of the “combined” data set in Table 5). Lithologic-driven departure from this scaling exponent is observed in sandstones & marls (i.e., note the 0.82 exponent in Table 5 and graphically in Figure 15a), which therefore tend to approach isometric increase (i.e., a scaling exponent equal to 1 means that length and area grow at the same rate). In relation to land cover, we note higher than usual scaling exponents on arable crops underlain by L claystones (0.80) and P-A claystones (0.69). These exponents, however, derive from very limited numbers of observations (Table 5), and should be considered with care.

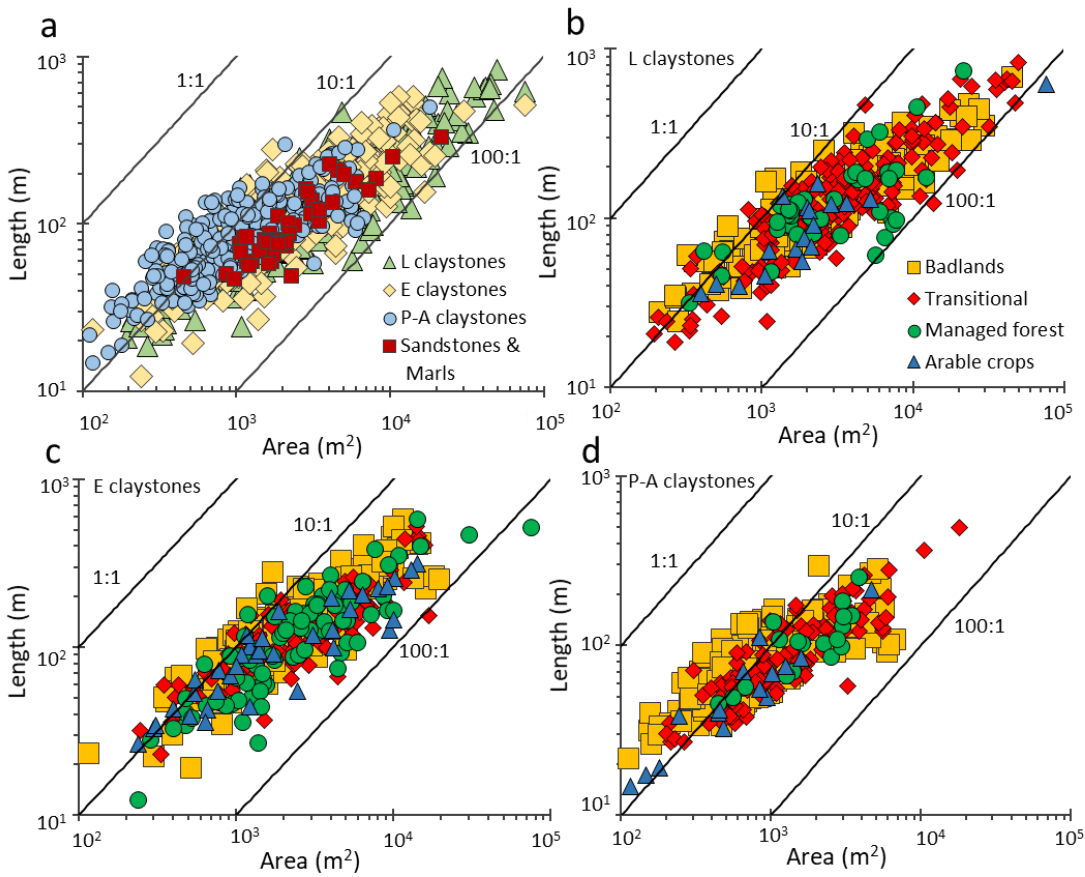


Figure 15. Landslide length as function of landslide area, classified by (a) geologic domains; and across land cover types within terrain of the: (b) L claystones, (c) E claystones and (d) P-A claystones. Due to the limited number of observations, landslides occurring in sandstones & marls were excluded from the analysis.

Table 5. Power-law fitting of landslide area-length relations stratified by dominant lithology and land-cover types. Due to the limited number of observations, landslides occurring in sandstones & marls were excluded from the analysis. A indicates landslide area. L indicates landslide length.

		n	Power-law fitting	R ²
Combined		1164	$L=1.89A^{0.53}$	0.74
Lithology	L claystones	410	$L=1.45A^{0.57}$	0.78
	E claystones	406	$L=1.46A^{0.57}$	0.67
	P-A claystones	306	$L=2.49A^{0.50}$	0.63
	Sandstones & marls	42	$L=0.94A^{0.82}$	0.82
L claystones	Arable crops	18	$L=1.33A^{0.80}$	0.96
	Badlands	163	$L=2.03A^{0.52}$	0.82
	Transitional	188	$L=0.99A^{0.60}$	0.80
	Managed forest	41	$L=3.31A^{0.45}$	0.50
E claystones	Arable crops	37	$L=1.81A^{0.53}$	0.81
	Badlands	180	$L=1.45A^{0.58}$	0.72
	Transitional	101	$L=1.95A^{0.52}$	0.69
	Managed forest	88	$L=0.87A^{0.62}$	0.65
P-A claystones	Arable crops	15	$L=0.59A^{0.69}$	0.85
	Badlands	156	$L=4.21A^{0.43}$	0.45
	Transitional	117	$L=1.50A^{0.57}$	0.77
	Managed forest	18	$L=1.64A^{0.55}$	0.56

5.3 Temporal variability

In all photo years, the number and area of recurring landslides are consistently higher than episodic counterparts (Figure 16), except for photo year 2016, which however covers a period of 2 years only (Table 2). Starting with photo year 1954, for which we have constrained a visibility time window of 15 years (Figure 4a), we detected a total of 88 landslides (Supplementary Table 1). This figure nearly doubles ($n = 148$) in photo year 1969 (Figure 16a), during a period of high agricultural pressure that witnessed highest historical cropland extent (Figure 9). From 1970 through 1996, in a period characterized by land abandonment, with highest recorded expansion of forest cover and concurrent shrubland decrease (Figure 9), we observe a steady decline in landslide occurrences. Subsequently, between 1997 and 2018, in a period of generalized land cover stability, we observe a high variability in landslide activity, with an historical high of 203 landslides in the 2008-2011 period.

The temporal variability of total landslide area shows obvious similarities with the variation of landslide count, but at the same time differs in many respects (Figure 16b). First, highest total area is recorded in 1969 (82 ha), as opposed to 2011 for landslide count (Supplementary Table 1). Second, the continuous decline in landslide count previously observed between 1969 and 1996, is now interrupted in photo year 1988, mostly due to a relative collapse in landslide areas recorded in photo year 1976. Third, the 1997-2018 period is still characterized by ample temporal variability, but the relative weight of these photo years in the overall historical (1954-2018) area budget is far less important than how observed in terms of landslide count, suggesting that landslides are comparably smaller. For example, landslide area in 2011 equals to 35 ha, compared to the historical high recorded in 1969.

To gain additional insights on possible environmental controls, we further examine historical landslide activity in conjunction with land-cover changes and across geologic domains (Figure 17). Considering the land cover dynamics detailed in section 4 (i.e., Figures 9 and 10), landslide activity though time was represented across four time periods, each covering about two decades: before 1954, 1955-1976, 1977-1996, and 1997-2018. In each study period, landslide density is standardized by the areal extent of each land cover category and by the relevant number of years.

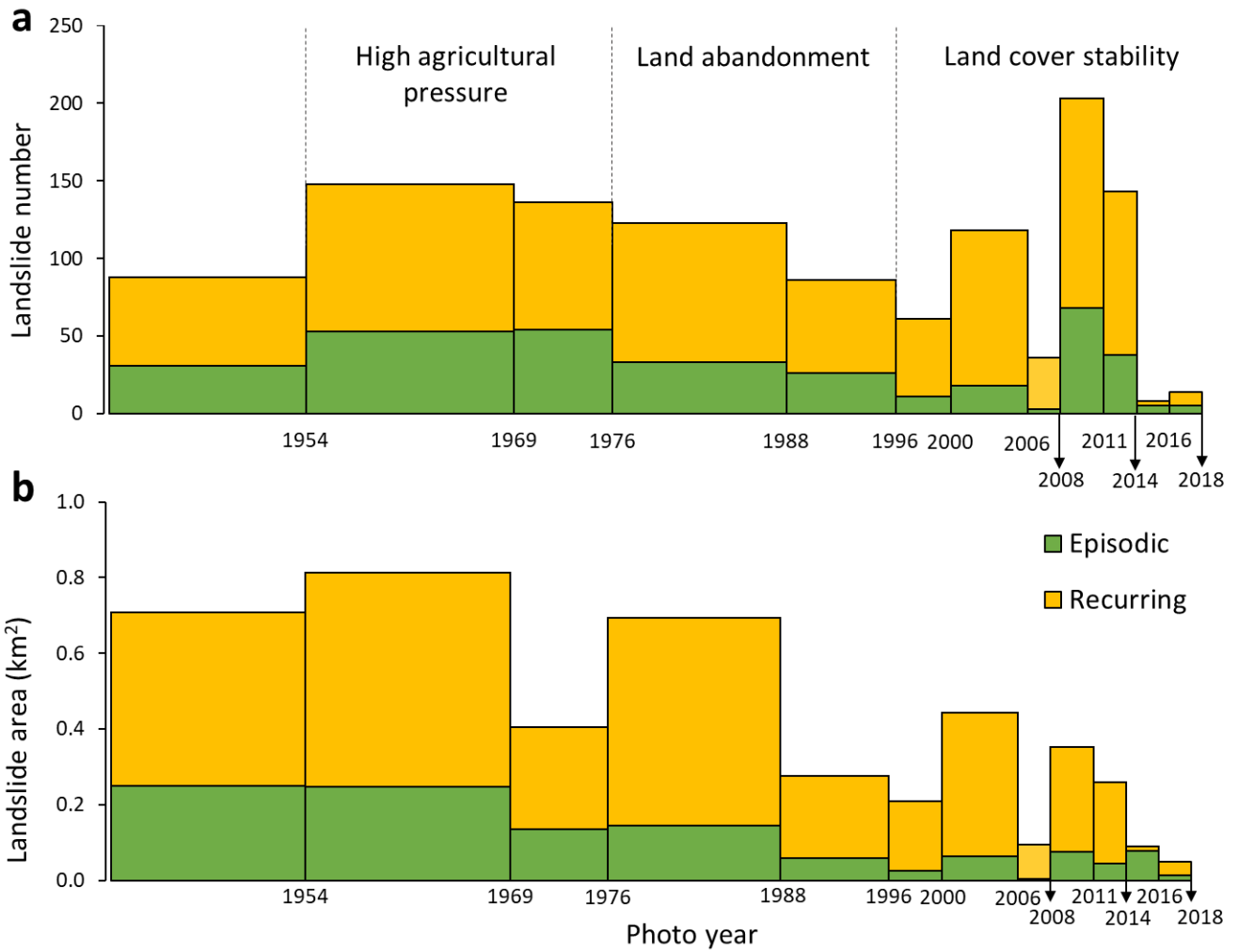


Figure 16. Temporal variability in the (a) number of landslides, and (b) relevant area across time periods bound by historical photo sets used in this study. Green bars indicate episodic landslides; yellow bars indicate recurring landslides.

Results show that landslide densities across land cover types in clayey lithologies differ from those observed in sandstones & marls. Densities are consistently higher through time within badlands, followed by transitional shrubland, managed forest and arable crops (Table 6 and Figure 17a through 17c). In particular, different claystones share a common historical trend in overall activity (i.e., combined height of each stacked bar). Accordingly, after 1954 landslide density decreases in the 1977-1996 period, characterized by highest land abandonment dynamics, and increases sharply between 1997 and 2018, during a period of generalized land cover stability (Table 6). This historical trend is also shared by landslide densities in badlands, managed forest and croplands, whereas transitional shrubs, regardless of lithology, display a progressive increase through time (Table 6). Differently from what described in clayey settings, landslide density in sandstones & marls: (i) scores highest in managed forest, followed by transitional shrubland and arable crops (Figure 17d); and (ii) increases progressively through time (Table 6 and Figure 17d).

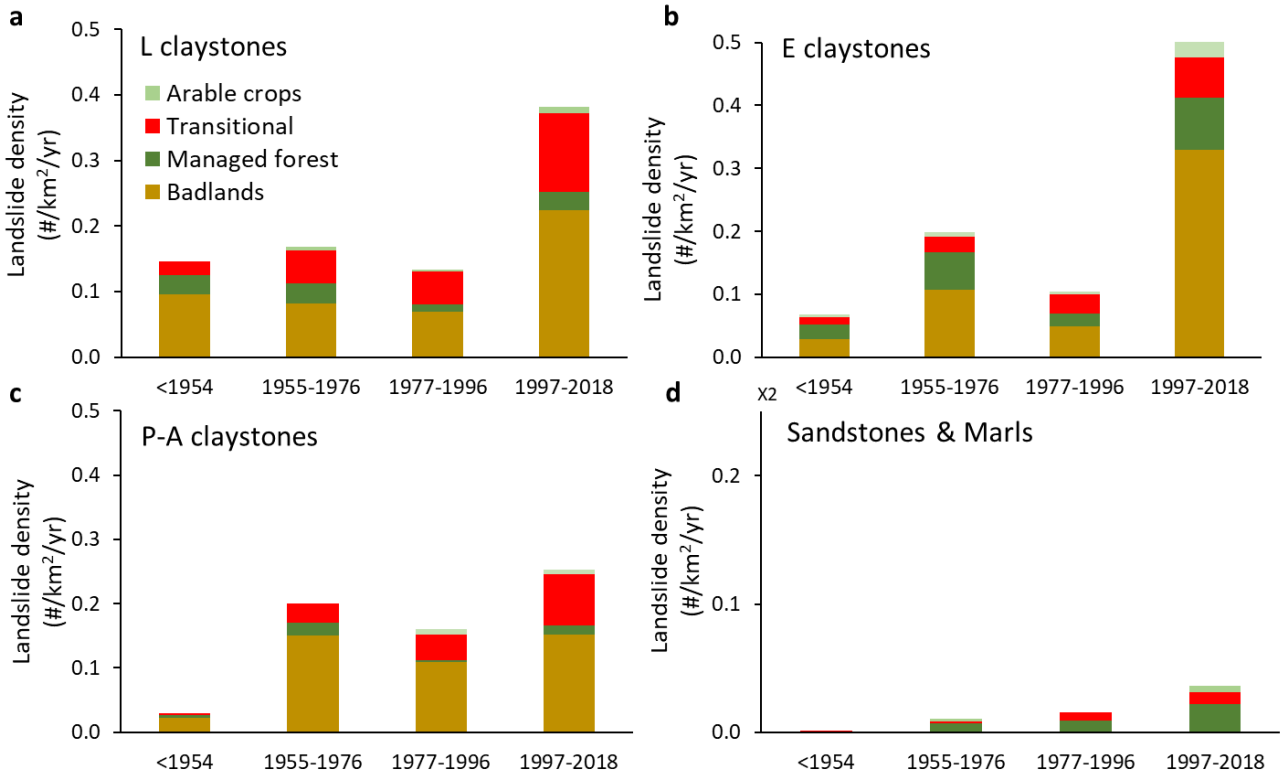


Figure 17. Stacked bar diagrams showing the historical variation in landslide density, stratified by land cover at landslide initiation, in: (a) L claystones, (b) E claystones, (c) P-A claystones, and (d) Sandstones & marls. Numbers are standardized by basin-wide land cover area and years of observation. Note Y-axis exaggeration in panel d.

Table 6. Historical landslide densities stratified by dominant geology and land cover.

Geology	Land use	Landslide density (#/km ² /yr)			
		<1954	1955-1976	1977-1996	1997-2017
L claystones	Badlands	0.10	0.08	0.07	0.22
	Managed forest	0.03	0.03	0.01	0.03
	Transitional	0.02	0.05	0.05	0.12
	Arable crops	0	0.01	0	0.01
E claystones	Badlands	0.03	0.11	0.05	0.33
	Managed forest	0.02	0.06	0.02	0.08
	Transitional	0.01	0.03	0.03	0.06
	Arable crops	0	0.01	0	0.02
P-A claystones	Badlands	0.02	0.15	0.11	0.15
	Managed forest	0	0.02	0	0.01
	Transitional	0	0.03	0.04	0.08
	Arable crops	0	0	0.01	0.01
Sandstones & marls	Badlands	0	0	0	0
	Managed forest	0	0.01	0.01	0.02
	Transitional	0	0	0.01	0.01
	Arable crops	0	0	0	0.01

To explore the possible influence of slope gradient on land use effects across lithologies, we calculate and compare landslide densities across three slope classes. These classes in a given geologic domain are defined

so that each includes approximately one third of the total number of landslides (i.e., comparable numbers of observations). In E claystones, P-A claystones, and sandstones & marls this criterion yielded classes with slope < 0.35 m/m, comprised between 0.35 and 0.45 m/m, and > 0.45 m/m. In agreement with the gentler, basin-wide slope frequency distribution (Figure 2c), classes in L claystones bound comparably gentler terrain, including slopes < 0.29 m/m, comprised between 0.29 and 0.38 m/m, and > 0.38 m/m. In each geologic context, we examine the range of variability of landslide density, controlling for land cover and slope gradient at landslide initiation (Figure 18 and Table 7). Considering the limited number of landslides in arable crops, as well as in sandstones & marls, densities are reported for completeness and should be evaluated with care.

Examination of Figure 18 shows a composite picture. Landslide density ranges across slope classes are widest and tend to reach highest values in badlands (i.e., ~36 #/ha/yr in E claystones), followed by transitional shrubland (i.e., ~37 #/ha/yr in P-A claystones), hence by managed forest (i.e., ~24 #/ha/yr in E claystones) and arable crops (Table 7). This ranking differs in E-claystones, where density ranges in managed forest, although broadly comparable to those in transitional shrubs, exhibit higher maxima across the three slope classes (Figure 18b).

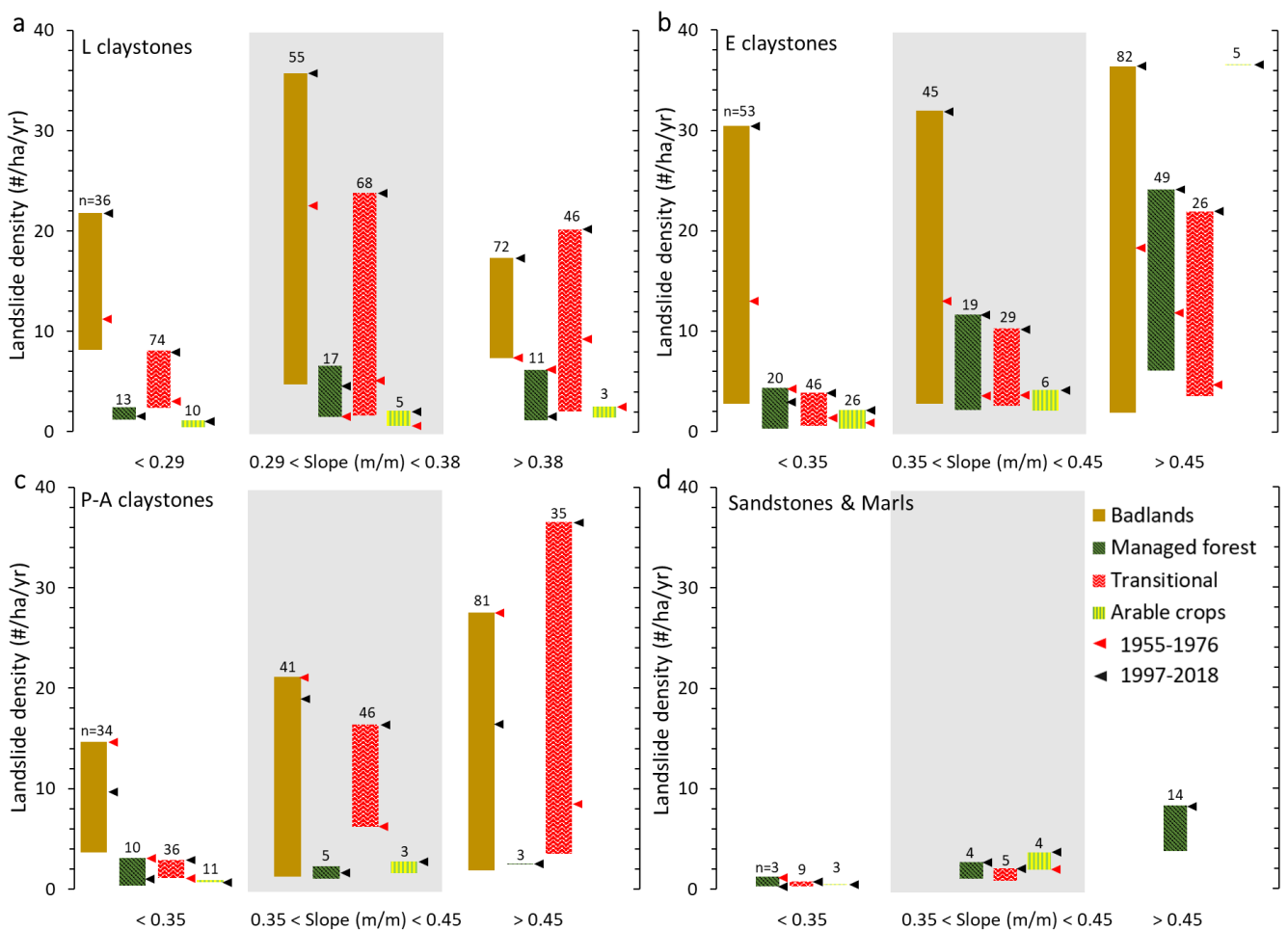


Figure 18. Ranges of historical landslide density across land cover types and slope classes in: (a) L claystones; (b) E claystones; (c) P-A claystones; and (d) Sandstones & marls. Red arrows mark landslide density values observed in the 1955-1976 period. Black arrows mark landslide density values observed in the 1997-2018 period. Numbers refer to the landslide counts used to compute the landslide densities.

When densities are calculated from a comparable number of landslides across slope and land cover categories, density ranges and maxima tend to increase with slope gradient. This is the case of: (i) managed forest in all lithologies except in P-A claystones, where historical forest cover however is very limited (Figure 10c); (ii) transitional shrubland in all lithologies, with the caveat of limited numbers in sandstones & marls; and (iii) arable crops, where present, despite the limited number of observations noted earlier. In L claystones, increase in landslide density range and maxima applies only at the transition between low and intermediate slope classes (see patterns of managed forest and transitional shrubs in Figures 18a), whereas it continues up to steepest slopes in managed forest and shrubland underlain by E claystones (Figure 18b) and in shrubland underlain by P-A claystones (Figure 18c).

Landslide densities in badlands across claystone types display a complex behaviour across slope classes. If on one hand densities appear to be insensitive to slope increase in L claystones (i.e., note density maxima at intermediate slopes in Figure 18a); on the other, in E- claystones, and even more so in P-A claystones, density exhibits high sensitivity to slope gradient, as ranges of variation broaden with increasing slope and attain progressively higher maxima (Figure 18c).

Table 7. Historical landslide densities stratified by dominant geology, land cover and slope.

Geology	Land use	Slope (m/m)	Landslide density (#/ha/yr)				Range
			<1954	1955-1976	1977-1996	1997-2017	
L claystones	Badlands	<0.29	10.96	11.48	8.13	21.80	8.13-21.80
	Managed forest		2.44	1.62	1.21	1.70	1.21-2.44
	Transitional		2.37	3.19	4.09	8.06	2.37-8.06
	Arable crops		0	0.44	0	1.08	0.44-1.08
	Badlands	0.29< S <0.38	8.96	22.34	4.72	35.71	4.72-35.71
	Managed forest		6.54	1.46	1.50	4.50	1.46-6.54
	Transitional		1.56	5.15	7.49	23.80	1.56-23.80
	Arable crops		0	0.56	0.78	2.04	0.56-2.04
	Badlands	> 0.38	9.52	7.33	12.16	17.32	7.33-17.32
	Managed forest		1.48	6.17	1.14	1.81	1.14-6.17
	Transitional		2.00	9.56	2.35	20.13	2.00-20.13
	Arable crops		0	2.47	1.37	0	1.37-2.47
E claystones	Badlands	<0.35	2.73	13.53	5.14	30.42	2.73-30.42
	Managed forest		0.63	4.32	0.31	2.86	0.31-4.32
	Transitional		0.56	1.74	2.09	3.88	0.56-3.88
	Arable crops		0.36	0.89	0.30	2.15	0.30-2.15
	Badlands	0.35< S <0.45	4.94	12.99	2.77	31.94	2.77-31.94
	Managed forest		4.60	3.86	2.12	11.64	2.12-11.64
	Transitional		2.53	3.82	2.54	10.26	2.54-10.26
	Arable crops		2.05	0	3.10	4.16	2.05-4.16
	Badlands	> 0.45	1.86	18.05	6.60	36.39	1.86-36.39
	Managed forest		6.05	11.98	7.66	24.13	6.05-24.13
	Transitional		3.51	4.64	16.13	21.92	3.51-21.92
	Arable crops		0	0	0	36.54	NA
P-A claystones	Badlands	<0.35	3.64	14.65	5.14	9.81	3.64-14.65
	Managed forest		0	3.09	0.31	1.04	0.31-3.09
	Transitional		0	1.07	2.72	2.91	1.07-2.91
	Arable crops		0	0	0.90	0.67	0.67-0.90
	Badlands	0.35< S <0.45	1.24	21.11	8.32	19.16	1.24-21.11
	Managed forest		2.30	1.93	1.06	1.79	1.06-2.30
	Transitional		0	6.20	7.62	16.41	6.20-16.41
	Arable crops		0	0	1.55	2.77	1.55-2.77
	Badlands	> 0.45	1.86	27.55	19.08	16.79	1.86-27.55
	Managed forest		0	0	0	2.50	NA
	Transitional		3.51	8.36	9.22	36.53	3.51-36.53
	Arable crops		0	0	6.23	0	NA
Sandstones & Marls	Badlands	<0.35	0	0	0	0	NA
	Managed forest		0	1.23	0	0.26	0.26-1.23
	Transitional		0	0.27	0.63	0.78	0.27-0.78
	Arable crops		0	0	0	0.40	NA
	Badlands	0.35< S <0.45	0	0	0	0	NA
	Managed forest		0	0	1.06	2.69	1.06-2.69
	Transitional		0.84	0	0.85	2.05	0.84-2.05
	Arable crops		0	1.93	0	2.77	1.93-2.77
	Badlands	> 0.45	0	0	0	0	NA
	Managed forest		0	0	3.83	8.32	3.83-8.32
	Transitional		0	0	0	0	NA
	Arable crops		0	0	0	0	NA

6. Discussion and conclusions

The multi-temporal visibility test conducted on 53 selected landslides allowed constraining a 15-year time window, during which, landslide initiation and transport zones could be consistently identified and mapped (Figure 4a). This figure, which fills a critical empirical gap for the remotely-based detection of landslides in the Northern Apennines, varies with land cover conditions at initiation: from a minimum of 13 years in transitional shrubland, to at least 17 years in forested terrain (Figure 4b). Compared to coastal British Columbia (see Chapter 4), where landslides persist on aerial photos for about 30 years (Rood, 1984; Smith et al., 1986; Brardinoni, 2001), this shorter time frame requires about twice the number of sequential photosets (hence a much onerous operator's effort) in order to obtain a multi-temporal inventory of comparable completeness. With reference to the photosets used in the Sillaro River basin, the two sequential photo sets that are farthest apart (i.e., 1954 and 1969), are still within the minimum requirements for visibility and mapping. Following this logic, when considering climatic and land cover effects, landslide counts and relevant density values in the 1954-1976 period (Figures 16 and 17) should be regarded as minimum estimates.

Results from multi-temporal mapping suggest that landslide activity in the Sillaro River basin is strongly influenced by lithology. For example, when considering landslide density per unit lithologic area as a proxy, landslide activity is 3 to 4 times higher in the Ligurian Allochthonous Complex (i.e., L and E claystones) than in the Flysch Complex (i.e., sandstones & marls) (Table 4, and Figure 12). This 4:1 ratio agrees with prior findings derived from regional inventories conducted on 1954 aerial photos across the same geologic complexes in the Marche and Umbria regions, Central Apennines (Guzzetti et al., 1996). In this context, our multi-temporal mapping approach on the temporal nature of landslide occurrence allows adding that (i) landslide activity at a site in a roughly 80-year time window (Figure 4a) can recur up to 9 times (Figure 13); and (ii) the relative importance of recurring landslide sites, both numerically and in terms of areal extent, varies with lithology. In particular, recurring landslide sites can account respectively for 35% (P-A claystones) to 60% (sandstones & marls) of the total landslide count, and for 65% (P-A claystones) to 90% (sandstones & marls) of the total landslide area, with L and E claystones displaying intermediate percentages (Figure 12).

We find that lithology influences landslide geometry too, with landslides on P-A claystones being distinctively shorter (hence smaller) than the others (Figures 14 and 15). We attribute this difference to terrain morphometry, and specifically to the spatial distribution of P-A claystones, which dominates the lower portion of the Sillaro basin (Figure 1b). Following this logic, we argue that the limited range of variation and the shape of P-A claystones elevation frequency distribution – skewed towards elevations < 400 m a.s.l. (cf., distributions in Figure 2b) – would bound local relief to comparably lower values, hence limiting slope length and maximum landslide runout length.

With reference to the influence of land cover on geometry, we show that landslides have virtually identical shape and size in (coppice) managed forest, in transitional shrubland and within badlands (Figures 14c and 14d; Figures 15b through 15d). This finding suggests that the effect of (herbaceous to arboreal) root reinforcement, which conceptually should limit the size of landslide footprint at initiation, in clayey, earthflow-

dominated terrain, might be less straightforward than previously envisaged. In this context, the shorter length (and smaller area) of landslides in croplands should not surprise. These slope instabilities, which tend to occur on typically gentler terrain (Figure 11f), are typically rotational slumps characterized by limited downslope mobility, and therefore less elongated, as hinted by the area-length scaling exponent that approach unity (i.e., isometric increase) (Figure 15 and Table 5).

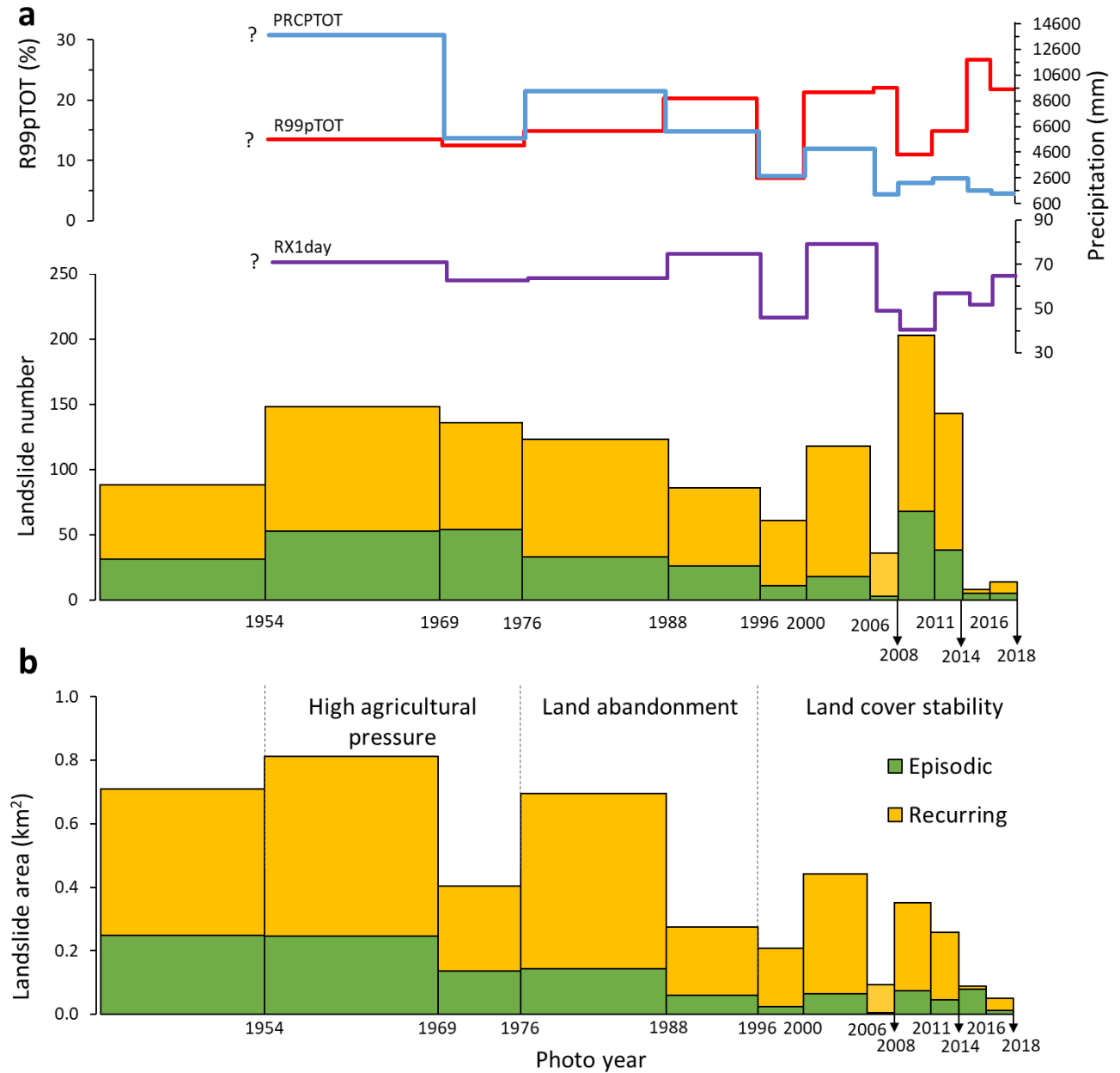


Figure 19. Temporal variability in the (a) number of landslides, and (b) relevant area across time periods bound by the historical photo sets used in this study. Green bars indicate episodic landslides; yellow bars indicate recurring landslides. In panel a, linework indicates concurrent variation in cumulative total precipitation (PRCPTOT; blue), maximum daily precipitation (RX1DAY; purple), and the mean precipitation fraction (%) due to extremely wet days (R99pTOT; red) i.e., when daily precipitation amount exceeds the 99th percentile in the 1950-2020 period.

To evaluate to what extent historical landslide activity in the Sillaro River basin might respond to hydro-meteorological forcing (e.g., Berti et al., 2012; Ciccacese et al., 2020; 2021), we have calculated three climatic

precipitation indices (i.e., cumulative PRCPTOT, maximum RX1DAY and mean R99pTOT) (see sections 3 and 4 in this chapter) across the time intervals that characterize the historical sequential photosets used in this study (Table 1). Qualitatively, the historical trend in cumulative total precipitation (PRCPTOT), which displays an overall – even though discontinuous - declining tendency, appears to mimic closely that of landslide area (Figure 19b), and to a lesser extent, that of landslide frequency (Figure 19a). Simultaneously, despite the higher noise involved, we observe that the relative weight of mean extreme precipitation events (R99pTOT) displays an opposite trend, suggesting that periods with higher total precipitation are dominated by events of low-to-average magnitude, and that vice-versa, as total precipitation decreases, extreme events become progressively more important. Annual maximum daily precipitation (RX1day) does not appear to show a clear historical tendency.

The foregoing qualitative observations are confirmed and corroborated by simple correlation analysis, which excludes the pre-1954 period, due to incomplete gridded precipitation data. Accordingly, landslide count (correlation coefficient = 0.441) and especially landslide area (0.927), are directly related to total precipitation, and consequently, inversely related to R99pTOT (Table 8). In this latter case, correlation is stronger for landslide count (-0.625) than for landslide area. When considering, episodic and recurring landslides separately, correlations change very little (Supplementary Tables 2 and 3).

Table 8. Matrix correlation between the total number of landslides (episodic and recurring), relevant combined landslide area and precipitation indices. Period of investigation: 1955-2018.

Total LS	#LS	LS area	PRCPTOT	RX1day	R99pTOT
#LS	1.000				
LS area	0.674	1.000			
PRCPTOT	0.441	0.927	1.000		
RX1day	0.038	0.428	0.568	1.000	
R99pTOT	-0.625	-0.425	-0.278	0.309	1.000

Evaluation of basin-wide historical landslide activity in relation to land cover changes (Figure 9 and Supplementary Figure 2) in the context of historical precipitation trends (Figures 6, 7 and 19), suggests that badlands dominate the scene and that other land cover changes may not be as important. The lack of badlands in sandstones and marls explains the strong lithologic control noted above on landslide activity, and the 3- to 4-fold decrease in landslide density, compared to claystone-dominated contexts.

Indeed, badlands are associated with highest historical landslide densities across all four time periods examined, followed by transitional shrubland, managed forest, and arable crops (Figure 17 and Table 6). If one excludes arable crops – considering the limited number of landslides and the comparably gentler terrain on which they occur – this land cover stability ranking broadly matches expectations on the stabilizing effect of an increasingly structured and developed vegetation cover.

The land-cover composition of landslide density in the three claystone types remains about constant through time (i.e., relative thickness of the different land-cover categories remains the same within the three stacked bars; Table 6 and Figure 17). When considered alone, this pattern suggests that documented historical variations in land cover extent and agricultural techniques (e.g., the 1977-1996 period, when land abandonment was most intense) and/or precipitation (e.g., the 1997-2018 period, when the weight of extreme events has grown highest in an overall drier climate) have not significantly affected landslide initiation dynamics at the basin scale. However, since land cover distribution in a basin typically reflects logistical access – forested areas occupying more remote and less accessible terrain than cultivated lands – we evaluated land cover effects in relation to landscape ruggedness, and to slope gradient in particular.

This evaluation allowed depicting a more complex picture across different geologic domains (Figure 18). When densities are calculated from comparable numbers of landslides, density ranges and maxima tend to increase with slope gradient in: (i) managed forest, except in P-A claystones; (ii) transitional shrublands; and (iii) arable crops, despite based on very limited numbers of observations. In this context, badlands stand out for their composite behaviour across claystones. If on one hand, landslide density ranges and maxima increase directly with slope gradient in E and especially in P-A claystones, they look rather insensitive to slope in L claystones.

In terms of temporal variability, density stratification by slope and land cover confirms and corroborates a generalized sensitivity of landslide occurrence in the last 20 years. In this drier period, when extreme precipitation events have become increasingly important, landslide density values (i.e., black arrows in Figure 18 refer to 1997-2018) tend to attain their historical high in shrubland and managed forest, but especially in badlands, with the only exception of P-A claystones (Figure 18c). In the latter case, landslide densities in badlands are highest across all slope classes when agricultural pressure peaked, between 1955 and 1976 (i.e., red arrows in Figure 18c). We interpret this finding as consequence of the temporary expansion of cropland onto unstable terrain, such that previously occupied by badlands (cf., Figure 10c), which locally overrode the climatic signal.

Collectively, rates of landsliding indicate that natural reforestation and shrubland development following land abandonment in a clay-dominated setting did not lead to greater slope stability in the last twenty years of generalised land-cover equilibrium (i.e., 1997-2018). This general finding reinforces prior observations made further north in the Northern Apennines by Persichillo et al. (2017). Our analysis indicates that decadal landslide activity responded primarily to changes in precipitation regime, and that this response across land cover types differed markedly among geologic domains. In terms of landsliding, badlands resulted by far the most active and sensitive landscape component, expanding current knowledge on the effect of hydro-meteorological forcing to badlands degradation (Piccarreta et al., 2006), beyond processes of diffused and concentrated surficial erosion, yet providing empirical basis for diversifying landslide susceptibility scenarios (e.g., Pisano et al., 2017).

In order to fully evaluate land cover changes on landslide dynamics in the Sillaro River basin, and make this case study more directly comparable with the Tsitika-Eve one (chapter 4), future work will aim to: (1) analyse confinement and sediment delivery targets to characterize how source-to-sink pathways have changed over time; (2) conduct additional field measurement on landslide thickness to constrain area-volume relations and convert current landslide areas in first-order estimates of mobilized material.

Acknowledgements

Stimulating discussion with Manel Llana helped improving the manuscript. This work was partly funded by Fondazione Cassa di Risparmio in Bologna through 2018/0348 BEDFLOW and 2019/0228 BEDFLOW PLUS projects. SP was funded through a PhD scholarship of the Italian Ministry of University (cycle XXXIV). We greatly acknowledge constructive reviews conducted by Federica Fiorucci and Roy Sidle.

References

- ARPAE (Agenzia prevenzione ambiente energia Emilia-Romagna) (2021a). Annali idrologici. <https://www.arpae.it/it/temi-ambientali/meteo/report-meteo/annali-idrologici> (Last accessed: October 2021).
- ARPAE (Agenzia prevenzione ambiente energia Emilia-Romagna) (2021b). Tabelle climatologiche. <https://www.arpae.it/it/temi-ambientali/clima/dati-e-indicatori/tabelle-climatiche> (Last accessed: November 2021).
- Ávila A., Justino F., Wilson A., Bromwich D., & Amorim M. (2016). Recent precipitation trends, flash floods and landslides in southern Brazil. *Environmental Research Letters*, 11, 114029.
- Ballesteros-Cánovas J.A., Corona C., Stoffel M., Lucia-Vela A., & Bodoque J.M. (2015). Combining terrestrial laser scanning and root exposure to estimate erosion rates. *Plant and Soil*, 394, 127–137.
- Benito G., Gutiérrez M., & Sancho C. (1992). Erosion Rates in Badland Areas of the Central Ebro Basin (NE-Spain). *Catena*, 19, 269-286.
- Berti M., Martina M.L.V., Franceschini S., Pignone S., Simoni A., & Pizziolo M. (2012). Probabilistic rainfall thresholds for landslide occurrence using a Bayesian approach. *Journal of Geophysical Research*, 117, F04006.
- Brardinoni, F. (2001). Identification of natural and logging-related landslides in the Capilano River basin (Coastal British Columbia): a comparison between remotely sensed survey and field survey (Master's thesis). Retrieved from UBC Library. Vancouver, British Columbia: Department of Geography, University of British Columbia.
- Brardinoni F., Hassan M. A., Rollerson T., & Maynard D. (2009). Colluvial sediment dynamics in 1142 mountain drainage basins. *Earth and Planetary Science Letters*, 284(3-4), 310-319.

- Bryan R., & Yair A. (1982). Perspectives on studies of badland geomorphology. In: Bryan R.B., & Yair A. (Eds), *Badland Geomorphology and Piping*. Geobooks: Norwich; 1–12.
- Buendia C., Batalla R.J, Sabater S., Palau A., & Marcé R. (2015). Runoff trends driven by climate and afforestation in a Pyrenean basin. *Land Degradation & Development*, 27, 823–838.
- CDS (Climate Data Store) (2021) - E-OBS daily gridded meteorological data for Europe from 1950 to present derived from in-situ observations. <https://cds.climate.copernicus.eu/cdsapp#!/dataset/insitu-gridded-observations-europe?tab=form> (Last accessed: October 2021).
- Ciccarese G., Mulas M., Alberoni P.P., Truffelli G., & Corsini A. (2020). Debris flows rainfall thresholds in the Apennines of Emilia-Romagna (Italy) derived by the analysis of recent severe rainstorms events and regional meteorological data. *Geomorphology*, 358, 107097.
- Ciccarese G., Mulas M., & Corsini A. (2021). Combining spatial modelling and regionalization of rainfall thresholds for debris flows hazard mapping in the Emilia-Romagna Apennines (Italy). *Landslides* 18, 3513–3529.
- Clotet-Perarnau N., Gallart F., & Balasch J.C. (1988). Medium-term erosion rates in small scarcely vegetated catchment in the Pyrenees. *Catena Supplement* 13, 37–47.
- Coscarelli R., Aguilar E., Petrucci O., Vicente-Serrano S.M., & Zimbo F. (2021). The Potential Role of Climate Indices to Explain Floods, Mass-Movement Events and Wildfires in Southern Italy. *Climate*, 9, 156.
- Gallart F., Llorens P., Latron J., & Rabadà D. (1997). Hydrological functioning of Mediterranean mountain basins in Vallcebre, Catalonia: Some challenges for hydrological modelling. *Hydrological Processes*, 11, 1263–1272.
- Gallart F., Solé A., Puigdefábregas J., & Lázaro R. (2002). Badland systems in the Mediterranean. In: Bull J.L., & Kirkby M.J. (eds.), *Dryland Rivers: Hydrology and Geomorphology of Semi-arid Channels*, 299-326, Wiley, Chichester.
- García-Ruiz J.M., Lasanta T., Ruiz-Flaño P., Ortigosa L., White S., González C., & Martí C. (1996). Land-use changes and sustainable development in mountain areas: a case study in the Spanish Pyrenees. *Landscape Ecology* 11 (5), 267–277.
- Guzzetti F., Cardinali M., & Reichenbach P. (1996). The influence of structural setting and lithology on landslide type and pattern. *Environmental and Engineering Geosciences*, 2-4, 531-555.
- Hoelzle M., Haeberli W., Dischl M., & Peschke W. (2003). Secular glacier mass balances derived from cumulative glacier length changes, *Global Planet. Change*, 36, 295–306.
- Howard A. D. (1994) – Badlands. In: Abrahams A. D. and Parsons A.J. (eds.), *Geomorphology of desert environments*, 213–242, Chapman and Hall, London.
- ISPRA (Istituto Superiore per la Protezione e la Ricerca Ambientale) (2021) – *Annali Idrologici Storici*. <http://www.acq.isprambiente.it/annalipdf/> (Last accessed: October 2021).
- Kasanin-Grubin M. (2013). Clay mineralogy as a crucial factor in Badlands hillslope processes. *Catena* 106, 54–67.

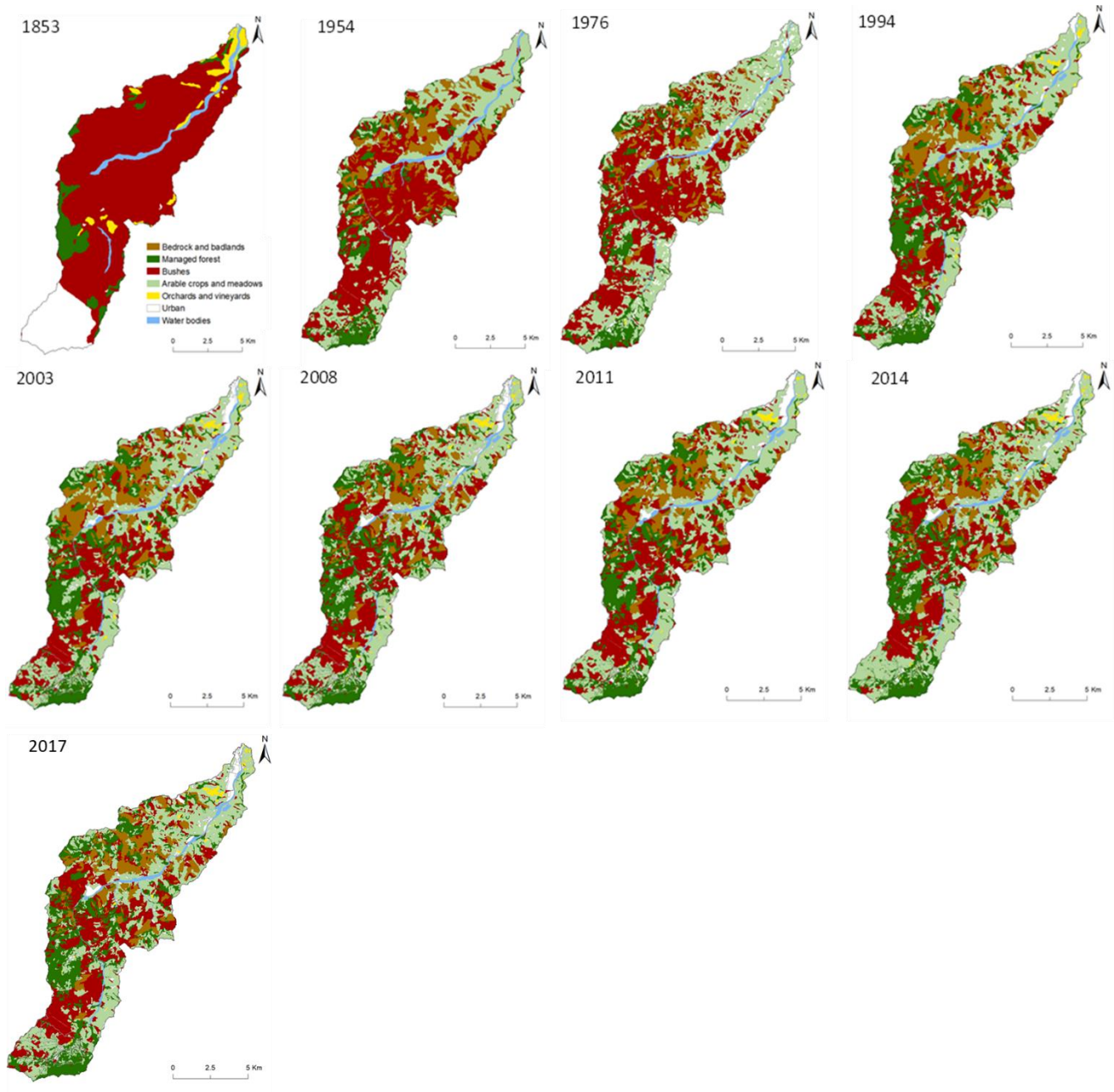
- Llena M., Batalla R.J., Smith M.W., & Vericat D. (2021). Do badlands (always) control sediment yield? Evidence from a small intermittent catchment. *Catena*, 198, 105015.
- Llena M., Vericat D., Smith M.W., & Wheaton J.M., (2020). Geomorphic process signatures reshaping sub-humid Mediterranean Badlands: 1. Methodological development based on high-resolution topography. *Earth Surface Processes and Landforms*, 45 (5), 1335–1346.
- Llorens P., Poch R.M., Latron J., & Gallart F. (1997). Rainfall interception by a *Pinus sylvestris* forest patch overgrown in a Mediterranean mountainous abandoned area. Monitoring design and results down to the event scale. *Journal of Hydrology*, 199, 331–345.
- Mathys N., Brochot S., Meunier M., & Richard D. (2003). Erosion quantification in the small marly experimental catchments of Draix (Alpes de Haute Provence, France). Calibration of the ETC rainfall–runoff–erosion model. *CATENA*, 50 (2-4), 527-548.
- Moreno-de las Heras M., & Gallart F. (2018). The origin of badlands. In: Nadal-Romero E., Martínez-Murillo J.F., & Kuhn N.J. (Eds.), *Badland Dynamics in the Context of Global Change*. Elsevier: Amsterdam.
- Mysiak J., Torresan S., Bosello F., Mistry M., Amadio M., Marzi S., Furlan E., & Sperotto A. (2018). Climate risk index for Italy. *Philosophical Transactions of The Royal Society A Mathematical Physical and Engineering Sciences*, 376, 2017030.
- Nadal-Romero E, Lana-Renault N., Serrano-Muela P., Regüés D., Alvera B., & García-Ruiz J.M. (2012). Sediment balance in four catchments with different land cover in the Central Spanish Pyrenees. *Zeitschrift für Geomorphologie*, 56, Suppl. 3, 147-168.
- Nadal-Romero E., Revuelto J., Errea P., & López-Moreno J.I. (2015). The application of terrestrial laser scanner and SfM photogrammetry in measuring erosion and deposition processes in two opposite slopes in a humid badlands area (central Spanish Pyrenees). *SOIL*, 1, 561–573.
- Nadal-Romero E., Rodríguez-Caballero E., Chamizo S., Juez C., Cantón Y., & García-Ruiz J.M. (2021). Mediterranean badlands: Their driving processes and climate change futures. *Earth Surface Processes and Landforms*, 1-15.
- Patzelt G. (1985). The period of glacier advances in the Alps, 1965 to 1980, *Z. Gletscherkd. Glazialgeol.*, 21, 403–407.
- Pavanelli D., Cavazza C., Lavmic S., & Toscano A. (2019). The Long-Term Effects of Land Use and Climate Changes on the Hydro-Morphology of the Reno River Catchment (Northern Italy). *Water*, 11, 1831.
- Persichillo M.G., Bordoni M., & Meisina C. (2017). The role of land use changes in the distribution of shallow landslides. *Science of the Total Environment*, 574, 924–937.
- Piccarreta M., Capolongo D., Boenzi F., & Bentivenga M. (2006). Implications of decadal changes in precipitation and land use policy to soil erosion in Basilicata, Italy. *Catena*, 65, 138-151.
- Pisano L., Zumpano V., Malek Ž., Rosskopf C.M., & Parise M. (2017). Variations in the susceptibility to landslides, as a consequence of land cover changes: A look to the past, and another towards the future. *Science of The Total Environment*, 601-602, 1147-1159.

- Pittau S., Pizziolo M., Rossi M., & Brardinoni F. (2021). A multi-temporal mapping approach for improving the temporal and spatial characterization of landslide activity in clay-rich terrain. *Rendiconti Online della Società Geologica Italiana*, 54, 17-31.
- Preciso E., Salemi E., & Billi P. (2012). Land use changes, torrent control works and sediment mining: effects on channel morphology and sediment flux, case study of the Reno River (Northern Italy). *Hydrological Processes*, 26 (8), 1134-1148.
- Regüés D., Pardini G., & Gallart F. (1995). Regolith behaviour and physical weathering of clayey mudrock as dependent on seasonal weather conditions in a badland area at Vallcebre, Eastern Pyrenees. *Catena*, 25, 199-212.
- Rood, K. M. (1984). An Aerial Photograph Inventory of the Frequency and Yield of Mass Wasting on the Queen Charlotte Islands, British Columbia. Land Management Report. (Vol. 34). Victoria, Canada: BC Ministry of Forests.
- Scotti R., Brardinoni F., & Crosta G.B. (2014). Post-LIA glacier changes along a latitudinal transect in the Central Italian Alps. *Cryosphere*, 8, 2235–2252.
- Sidle R.C., & Ochiai H. (2006). *Landslides Processes, Prediction, and Land Use*. Water Resources Monograph Series, 18. Washington DC, USA: American Geophysical Union.
- Smith, R.B., Commandeur, P.R., & Ryan, M.W., (1986). Soils, vegetation, and forest growth on landslides and surrounding logged and old-growth areas on the Queen Charlotte Islands. Land Management Report. (Vol. 41) Victoria, Canada: BC Ministry of Forests.
- Torri D., Rossi M., Brogi F., Marignani M., Bacaro G., Santi E., Tordoni E., Amici V., & Maccherini S. (2018). Badlands and the dynamics of human history, land use, and vegetation through centuries. In: Nadal-Romero E., Martínez-Murillo J.F., & Kuhn N.J. (Eds.), *Badland Dynamics in the Context of Global Change*. Elsevier: Amsterdam.
- Torri D., Santi E., Marignani M., Rossi M., Borselli L., & Maccherini S. (2013). The recurring cycles of biancana badlands: Erosion, vegetation and human impact. *Catena*, 106, 22-30.
- Vericat D., Smith M.W., & Brasington J. (2014). Patterns of topographic change in sub-humid badlands determined by high resolution multi-temporal topographic surveys. *Catena*, 120, 164-176.
- Yair A., Lavee H., Bryan R.B., & Adar E. (1980). Runoff and erosion processes and rates in the Zin Valley badlands, Northern Negev, Israel. *Earth Surface Processes* 5: 205–225.

Supplementary materials



Supplementary Figure 1. Map of the E-OBS precipitation data grid.



Supplementary Figure 2. Historical land cover maps of the Sillaro River basin from 1853 to 2017.

Supplementary Table 1. Number and area of episodic and recurring landslides mapped in this inventory.

	Number		Area (ha)	
	Episodic	Recurring	Episodic	Recurring
1954	31	57	25	46
1969	53	95	25	57
1976	54	82	14	27
1985-88	33	90	14	55
1996	26	60	6	22
2000	11	50	2	18
2006	18	100	6	38
2008	3	33	0.4	9
2011	68	135	7	28
2014	38	105	5	21
2016	5	3	8	1
2018	5	9	1	4
Total	345	819	110	330

Supplementary Table 2. Matrix correlation between the number of episodic landslides, landslide area and precipitation indices (PRCPTOT, RX1day and R99pTOT). Period of investigation: 1955-2018.

Episodic LS	#LS	LS area	PRCPTOT	RX1day	R99pTOT
#LS	1.000				
LS area	0.624	1.000			
PRCPTOT	0.467	0.902	1.000		
RX1day	-0.029	0.355	0.568	1.000	
R99pTOT	-0.610	-0.280	-0.278	0.309	1.000

Supplementary Table 3. Matrix correlation between the number of recurring landslides, landslide area and precipitation indices (PRCPTOT, RX1day and R99pTOT). Period of investigation: 1955-2018.

Recurring LS	#LS	LS area	PRCPTOT	RX1day	R99pTOT
#LS	1.000				
LS area	0.710	1.000			
PRCPTOT	0.400	0.880	1.000		
RX1day	0.072	0.431	0.568	1.000	
R99pTOT	-0.597	-0.454	-0.278	0.309	1.000

CHAPTER 4

Glaciated landscape structure, cutblock location, and the response of shallow rapid failures to forest clearing in coastal British Columbia

Francesco Brardinoni ¹, Sharon Pittau ¹, Mauro Rossi ²

1. Department of Biological, Geological and Environmental Sciences, University of Bologna, Bologna, Italy

2. CNR-IRPI, Perugia, Italy

Manuscript in preparation for submission to ESPL

Abstract

Forest harvesting and the construction of logging roads are major sources of slope instability; however their effects on landslide size and frequency remain unclear. By integrating field- and remotely-derived landslide inventories with historical information on logging, we examine the geometry of debris slides and long runout failures (i.e., debris flows and avalanches) relative to the effects of forest harvesting on landslide frequency and size in formerly glaciated watersheds of Vancouver Island, Canada. Results display no relationships among landslide type, landslide scour depth, and forest harvest history. Further, area-volume relations are not significantly different in cleared and pristine forest. Post-logging landslide occurrences are highest after 7-9 years and recover to undisturbed rates after 16-19 years since clearing has ceased. Logging generates landslides at low elevations and low slopes, where they would not normally occur. Owing to the characteristic topographic positions where cutblocks are developed within the landscape, at relatively low elevations and low slopes, logging-related long runout failures are distinctively shorter than natural counterparts. In pristine forest, our analysis suggests that glaciated landscape structure exerts primary control on the elevation and slope gradient of landslide initiation, imposing constraints on local relief (available energy), slope length, and therefore maximum landslide length. When morphologic position at initiation is considered, constraints on landslide size and consequently on the size-frequency relation become apparent. Accordingly, the rollover plots at the transition between distinct initiation morphologies, with large landslides (open slope and gully headwall initiations) on one side, conditioned by first-order valley wall geometry, and small counterparts (gully sidewall and escarpment initiations) on the other side, conditioned by the geometry of second-order features, including incisions on the hillslopes (gully depth) and valley floors (escarpment depth). Our findings suggest that future empirical and modelling efforts concerned with global environmental change should consider explicitly logging effects in relation to the morphologic and topographic diversity at initiation associated with different landslide types across hillslopes and steep headwater streams.

Keywords:

Forest harvesting, landslide type, morphologic position at initiation, glaciated landscape structure, cutblock position, size-frequency relation.

Key Points:

Glaciated landscape structure controls landslide initiation (elevation and slope), imposing local relief, slope length, and landslide maximum length.

Cutblock positioning induces distinctively shorter runout lengths to debris flows and avalanches compared to natural counterparts.

Different morphologic positions at initiation occupy distinct portions of the landslide size-frequency spectrum about the rollover.

1. Introduction

In humid, forested mountain watersheds, rapid shallow landslides are prominent players of sediment transfer (Tsukamoto, 1973; Dietrich and Dunne, 1978; Sidle et al., 1985, Benda & Dunne, 1997). Their magnitude and frequency control sediment flux on the slopes (e.g., debris slides and debris avalanches) and along the colluvial channel network (e.g., channelized debris flows). Their spatial distribution modulates the degree of hillslope-channel coupling, hence the downstream propagation of geomorphic disturbance cascades (Nakamura et al., 2000). In so doing, shallow landslides dictate the morphology, the geometry, and the channel bed texture of steep, headwater streams (e.g., Grant & Swanson, 1995; Benda et al., 2003; Brummer & Montgomery, 2003; Montgomery et al., 2003; Brardinoni & Hassan, 2007; Green et al., 2013), which typically act as temporary storage sites for colluvial material (e.g., Bovis & Jakob, 1999; May & Gresswell, 2003; Jakob et al., 2005; Lancaster & Casebeer, 2007; Brayshaw & Hassan, 2009).

In similar settings, timber harvesting and the construction of logging roads are major sources of hydro-geomorphic disturbance (see Sidle & Ochiai, 2006 for a comprehensive review), bringing about direct and indirect effects on sediment yield (McEachran et al., 2020). Forest clearing in newly developed cutblocks (e.g., 3 to 20 year-old) can compromise slope stability by reducing root strength and by increasing soil water content by factors including reduction of interception loss (e.g., Asdak et al., 1998; Reid & Lewis, 2009; Winkler et al., 2010). Logging roads can impart instability and promote local incision by altering hillslope hydrology, for example inducing water diversion and runoff concentration along the road network (Montgomery, 1994), which typically would require careful maintenance or deactivation. Decreased slope stability and altered hydrologic pathways may increase sediment delivery to streams (e.g., Reid & Dunne, 1984; Rood, 1990; Guthrie, 2002; Jordan et al., 2010), hence cause severe modification of the sediment budget at the watershed scale (e.g., Swanson et al., 1982; Roberts & Church, 1986). More recently, historical forest clearing has also shown to increase contemporary rates of seismically-induced landslides (Koyanagy et al., 2020).

A great deal of field investigations around the Pacific Rim and in particular across the Pacific coastal ranges of North America, has addressed quantitative aspects of post-logging landslide sediment transfer in temperate and sub-tropical forests, where a secondary forest cover is regenerated through natural succession and/or plantation. These studies, mostly clustered in the 1970's and 80's, have indicated that timber harvesting (i.e., not including road construction) during a post-logging period comprised between 3 and 20 years (e.g., Swanson & Dyrness, 1975; Ziemer & Swanson, 1977; Ziemer, 1981), can increase landslide sediment flux from less than 2 times up to 2 orders of magnitude (e.g., O'Loughlin, 1972; Morrison, 1975; Swanson & Dyrness, 1975; Swanson & Swanson, 1976; Swanson & Swanson, 1977; Marion, 1981; Amaranthus et al., 1985; Sidle et al., 1985). In this context, advances in GIS technology and in the acquisition of Digital Elevation Models have led to georeferenced integration between remotely-sensed and field-based landslide inventories (e.g., Reid & Dunne, 1996; Montgomery et al., 2000; Brardinoni et al., 2003a; 2003b; Guthrie & Evans, 2004), hence to rapid characterization of natural (old-growth forest) and disturbed (cutblocks) topographic conditions associated with shallow landslides over large areas.

With reference to formerly glaciated mountain settings, logging-related landslides and debris flows have been found on less steep terrain than counterparts on uncut areas (Swanston & Marion, 1991; Jakob, 2000; Brardinoni et al., 2003a; Wolter et al., 2010), indicating that logging operations can favour slope failures at different sites than how observed in old-growth forest. In turn, different initiation positions within the landscape may reflect different movement types in cut and uncut forests. Following this logic, landslide type and morphologic position at initiation may be regarded as critical attributes for evaluating logging effects with enhanced experimental control. Incidentally, previous work on how forest harvesting may alter the size of shallow landslides has yielded conflicting results, with logging-related slope failures found to be larger (e.g., Schwab, 1983), smaller (e.g., Swanston & Marion, 1991; Johnson et al., 2000; Brardinoni et al., 2003a; Wolter et al., 2010), smaller or larger depending on failure positioning on the slope (e.g., Rood, 1990; Martin et al., 2002), and not significantly different (e.g., Jakob, 2000) than natural counterparts. We hypothesize that these contrasts, to some extent, may reflect the variability of movement types (e.g., slides, avalanches, flows, and falls) included in each inventory, as well as the positioning of logged terrain within variable glaciated settings.

Our ability to predict the effects of forest management on landslide frequency and size is currently hampered by a lack of studies that compare landslides on similar morphologic positions. Without studies of this nature, suitable comparisons of landslides on cutblocks and old-growth remain problematic. This limitation in turn holds implications and useful applications in hazard assessment (e.g., Hungr *et al.*, 1999; Guzzetti *et al.*, 2002), as well as for modelling slope stability (e.g., Cislighi et al., 2017), landslide size and shape (e.g., Milledge et al., 2014), and sediment fluxes across landscape components (e.g., Benda & Dunne, 1997; Benda et al., 1998; Bennett et al., 2014; Schmitt et al., 2016). Addressing these issues gains further importance beyond the local and regional scales, considering that mountain forests worldwide are undergoing increasing anthropogenic pressure (e.g., Forbes & Broadhead, 2013; Zeng et al., 2018). In formerly glaciated settings, a systematic statistical evaluation of the effects of forest harvesting on the magnitude and frequency of shallow landslides, stratified by movement type and morphologic position at initiation, in relation to glaciated landscape structure, is still missing.

To address this gap, we present a multi-temporal (1961-2003) landslide inventory compiled by means of aerial photo interpretation (API) and extensive field surveys in the Tsitika and Eve River basins, Vancouver Island, British Columbia (**Figure 1**). The inventory includes debris slides, debris avalanches, and debris flows (Cruden & Varnes, 1996; Hungr et al., 2001), and records their occurrence in relation to a well-documented history of timber harvesting. This paper aims to: (i) constrain the timing, intensity and duration of post-logging disturbance in terms of landslide density and sediment flux; and (ii) evaluate to what extent this disturbance alters the magnitude-frequency relation of “simple” debris slides and long runout failures of the flow type (i.e., initial debris slides that develop into unconfined debris avalanches or into channelized debris flows) (Hungr, 2005; Hungr et al., 2008).

2. Study area

Study areas are the entire Eve River basin and 82% of the Tsitika River basin, which cover a combined area of 612 km² in northeastern Vancouver Island, British Columbia (**Figure 1**). Most of the watersheds are characterized by rugged topography of the Insular Ranges (Holland, 1964). Elevation rises from sea-level, at the basins' outlets, to over 1800 m. The area was repeatedly overridden by the Cordilleran Ice Sheet in the Pleistocene. Today, river main stems flow across deeply-scoured troughs, flanked by over-steepened valley walls. As a result, median slope increases rapidly as a function of elevation up to about 900-1000 m a.s.l. (**Figure 2a**), where an inflection, associated with the occurrence of relict glacial cirques and hanging valley floors, is observed.

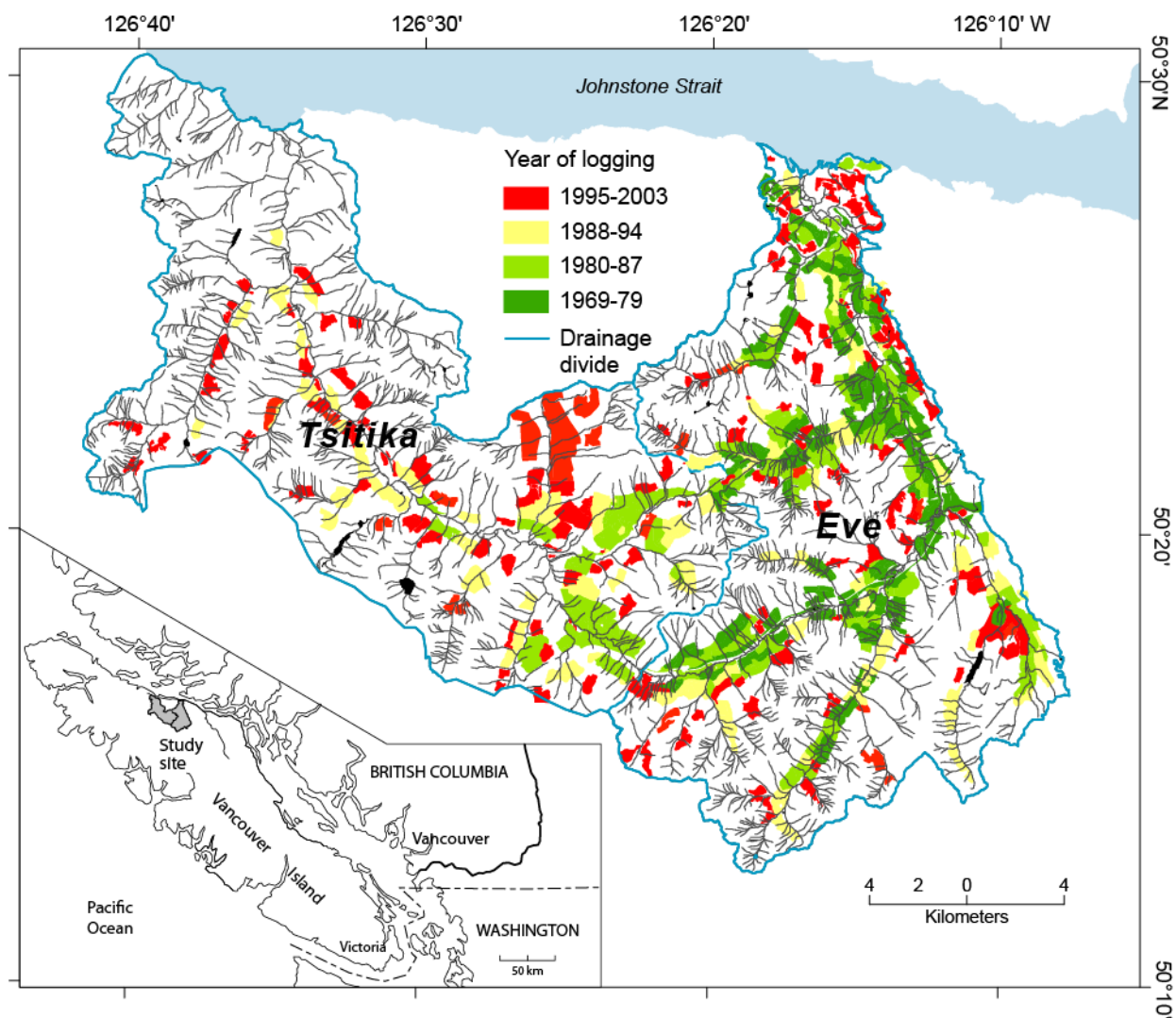


Figure 1. Map of land use history in the Tsitika and Eve River basins between 1961 and 2003 (logging data provided by Weyerhaeuser Ltd.). Black linework indicates the main drainage network, including lakes (filled black polygons).

By first approximation, surficial materials display an altitudinal zonation (**Figure 2a**), and therefore characteristic slope ranges (note offset among interquartile slope ranges **Figure 2b**). Accordingly, topography of upper slopes and summits is bedrock-controlled (R); colluvium (C) covers the valley walls, forming thin, continuous to discontinuous mantles on most of the mid to upper slopes and thicker, more continuous aprons

and blankets on lower slopes below bedrock-dominated sites. Further downslope, glacial till (M) is the dominant surficial material. Deposits are usually thickest along valley floors and lower slopes. In some places, high stream banks and road cuts expose sequences of till in excess of 10-m thickness. Erosional scarps cut into thick till are common along segments of most of the main tributaries. Till mantles usually are thinner (0.5-3 m) and more discontinuous on mid to upper slopes. This is commonly the case where rock and colluvium dominate much of the upper elevations. Most till deposits conform to the underlying bedrock topography and rarely mantle gradients exceeding 70%. Steep till landforms, which do occur, are erosional surfaces (scarp faces, gully walls) formed by postglacial fluvial downcutting through thick valley-fill deposits.

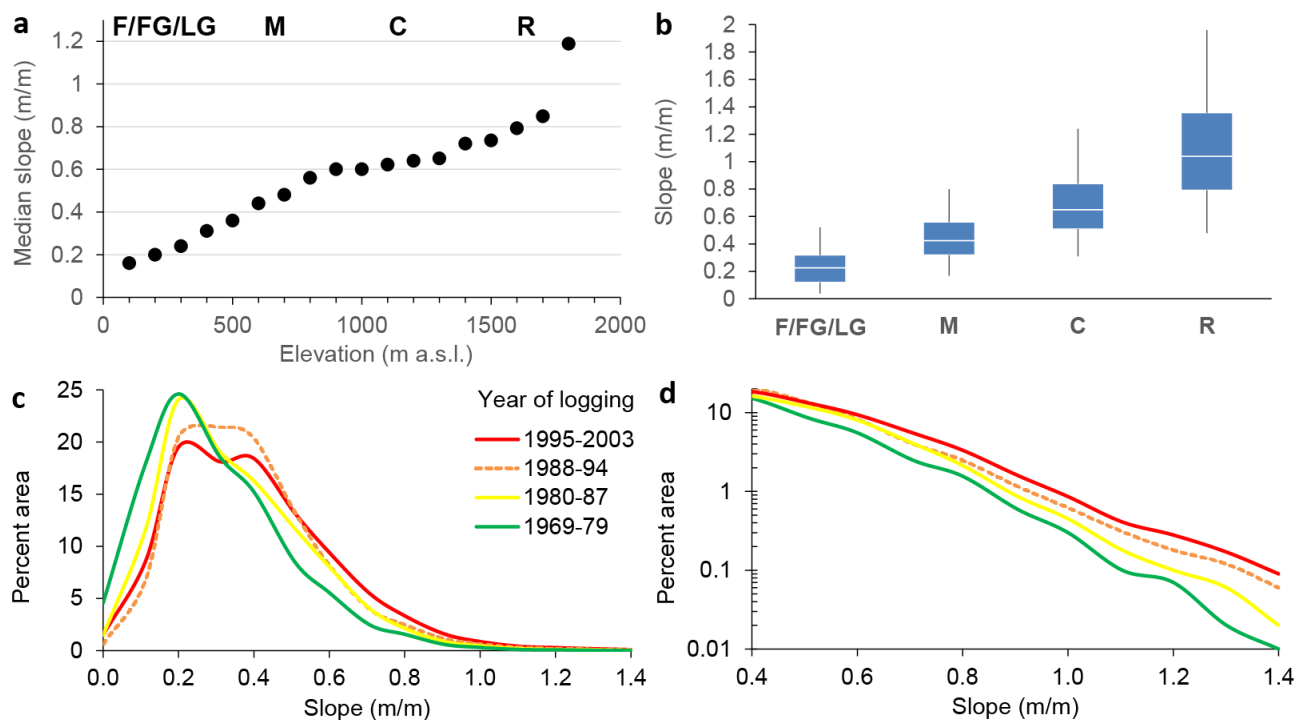


Figure 2. a) Median slope as a function of terrain elevation across (natural and logged) terrain of the Tsitika and Eve watersheds; b) Boxplot representation of slope distribution across surficial materials; c) Historical slope frequency distribution of logged terrain; and d) close-up view of logged terrain steeper than 40%. Logarithmic scale in y-axis is used to help discriminating differences among the four data series. In panel a, boxes enclose interquartile ranges, whiskers span from 5% to 95%. In panels a and b, codes for surficial materials follow the BC Terrain Stability Classification scheme (Howes & Kenk, 1997). C: colluvium; F: fluvial deposits; FG: glaciofluvial deposits; LG: glaciolacustrine deposits; M: glacial till; R: bedrock.

Along the main tributary valleys, deglacial materials occur as mantles of variable thickness overlying till and bedrock, and as constructional forms (terraces, hummocks) of variable areal extent. Deglacial materials were deposited by glacial meltwater, at the edge of or in close proximity to downwasting or retreating glacier ice. They consist mainly of glaciofluvial (FG) sands and gravels, but, in places, may be in association with well-sorted, fine-textured deposits of glaciolacustrine (LG) or glaciomarine origin. Typically, as valleys on this part of Vancouver Island became ice free, substantial volumes of meltwater were generated, so erosional downcutting, reworking of existing materials, and transportation and deposition of meltwater-entrained sediments remained highly active. Mass movements can be common at escarpment faces where thick till and/or

deglacial deposits have been reworked and undercut by fluvial incision along the main stem of Tsitika and Eve Rivers, as well as along tributary valleys.

Landslide types in the study area include falls, slumps, slides, avalanches, flows, and complex movements resulting from assorted combinations of these (Brardinoni et al., 2009). In particular, we distinguish between debris flows and debris avalanches, which are dominant long runout failures in coastal British Columbia. The former are rapid shallow flows of saturated mixtures travelling along steep, ephemeral colluvial channels, also termed gullies in this part of the Pacific Northwest. The latter are rapid shallow flows of partially or fully saturated debris on a steep slope, without confinement in an established channel (Hungr et al., 2001; 2008; Hungr, 2005). Toe-slope and valley-floor areas associated with mass-wasting deposition host cones and colluvial fans. Along the main tributary valleys, blocky talus slopes (particle size >256 mm) are common along the base of rock walls.

Bedrock geology is dominated by extrusive rocks of the upper Triassic Karmutsen Formation (basalt lava, pillow lava, volcanic breccia, tuff, and greenstone), and to a lesser extent by younger intrusive rocks of the Jurassic Island Intrusions of the Pacific Rim Complex (quartz diorite, granodiorite, quartz monzonite, and quartz feldspar porphyry) (Muller et al., 1974).

The study area is covered with old-growth and second-growth conifer forests of the Coastal Western Hemlock (*Tsuga heterophylla*) and Mountain Hemlock (*Tsuga mertensiana*) Biogeoclimatic Zones (Krajina, 1969). The former is prevalent from sea level up to about 900 m elevation. The Mountain Hemlock Biogeoclimatic Zone occupies higher elevations (i.e., 900-1800 m) and has a significantly lower capability for forestry (Meidinger & Pojar, 1991). The former is considered one of the wettest and most productive forest zones in British Columbia, with annual precipitation varying with location between 1650 and 6650 mm (Krajina, 1969). Northeastern Vancouver Island has a generally leeward exposure to storms from the Pacific Ocean and as such experiences lesser amounts of high-intensity precipitation, compared to watersheds on the western side of the Island. Mean annual precipitation (i.e., 1960-2010) about sea level is comprised between 1900 mm and 3400 mm with a wet season that extends from October through May, and a much drier regime that characterises June through September (**Supplementary Figure 1**).

Oldest documented forest harvesting dates back to 1969, with a total of 30 km² harvested by 1977, 72 km² by 1987, and 106 km² by 1994. In 2003, at the end of the study period, a cumulative area of 155 km² had been logged, corresponding to about 25% of the Tsitika and Eve basins extent (**Table 1**). Cutblocks are typically distributed on the floor of relict glacial troughs and on lower-to-mid valley walls (**Figure 1**). Through the years, logging operations have moved from gentler and most accessible locations, to progressively steeper sites on the valley walls (**Figures 2c and 2d**).

3. Methods

3.1 Landslide inventories

This work is concerned with rapid shallow failures occurring in natural forests (nf), in clearcuts (cc), and following the construction of logging roads (rd). We mapped 519 slope failures in pristine forested terrain and 229 in logged terrain (Brardinoni et al., 2009). Of the latter, 50 were related to logging roads. To maximize experimental control, in our comparative assessment of natural and logging related landslides, we will consider only 418 movements in natural forest (out of 519) that have mobilized surficial materials (i.e., debris mobilizing failures). In so doing, we exclude bedrock-mobilizing failures (e.g., rock falls, rock slides, and rock avalanches) occurred in rugged, bedrock dominated terrain, which, for logistical reasons and in compliance with provincial forest practices regulations (BC Forest Practices Code, 1995) are typically not harvested. In this paper, landslide sediment transfer is associated with debris slides, debris avalanches, and debris flows only and does not include other chronic processes such as soil creep, dry raveling, as well as sheetwash and channelized erosion.

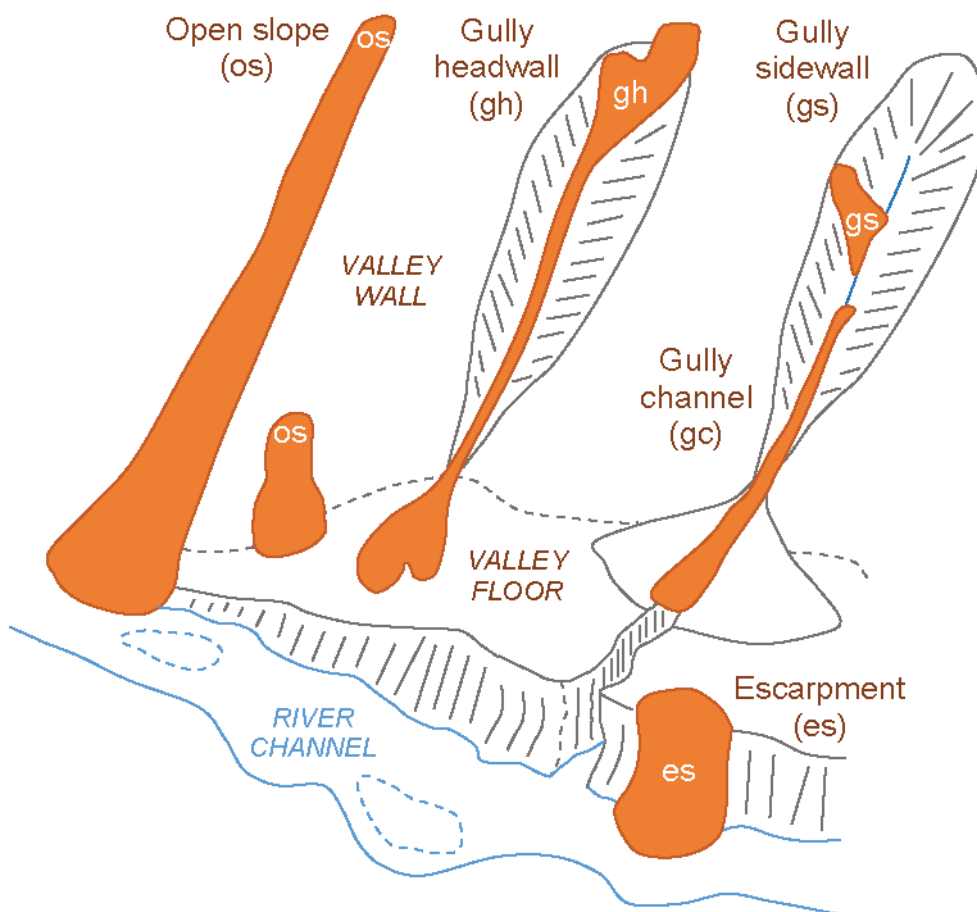


Figure 3. Schematic diagram of the main morphologic positions of landslide initiation in the study watersheds. Gully headwall (gh) and sidewall (gs) positions characterize the steep low-order drainage network and may result in debris flows. Open slope (os) positions characterize steep planar slopes and are typically associated to debris avalanches. Debris slide initiations at (gullied or unchannelled) escarpment (es) positions are associated with postglacial valley incisions carved in glacial, fluvial and glaciofluvial materials along the main tributary floodplains.

We compiled the Tsitika–Eve multi-temporal landslide inventory through stereoscopic inspection of five sequential aerial photosets (1961, 1977-79, 1987, 1994, and 2003) that range in nominal scale from 1:10,000 to 1:20,000. This methodology is a versatile way to compile regional landslide inventories (e.g., Reid & Dunne 1996; Hovius et al., 1997; Martin et al. 2002), especially in rugged terrain with difficult field access. However, in humid and densely forested watersheds, identification and accurate delineation of landslide scars on aerial photos is hampered by the forest canopy so that a population of mass movements remains undetected (Brardinoni et al., 2003b; Turner et al., 2010). Prior work conducted in comparable topographic and forest cover conditions in coastal British Columbia indicates that smallest, assuredly detectable, landslide size in old-growth forests (or in plantations older than 50 years) is 650 m². In recently harvested cutblocks (i.e., logged < 15 years earlier), this figure lies between 150 m² and 270 m² (Brardinoni et al., 2003b). Similar threshold sizes should be regarded as first-order estimates, as landslide visibility depends on several terrain characteristics, including slope steepness, landslide positioning within a hillslope (e.g., upper, mid, or lower portion) and landscape structure (e.g., valley width), other than land use conditions (e.g., tree height) alone.

For each landslide, we recorded attributes including land use, movement type, and morphologic position at initiation point. Information on movement type is important to separate landslides involving bedrock from those mobilizing debris derived from surficial materials (e.g., colluvium, glacial till, fluvial and glaciofluvial deposits). During aerial photo interpretation (API) we have identified three main types of debris-mobilizing landslides: debris slides (ds), and long runout failures; the latter including: (i) debris slides that have reached a gully channel (or a permanent tributary channel) and have transformed into channelized debris flows (dsdf); and (ii) debris slides transforming into debris avalanches in unconfined slope positions (dsda) (Hung, 2005). Surface expression of landslide initiation is critical for addressing logging effects on dominant topographic sites of sediment production on the hilllopes (unchannelled topography) and about the ephemeral (gullies) and permanent (stream channels) drainage network. Initiation sites were stratified into six classes, including concave (zero order) headwater basins (ch), escarpments (es), gully channels (gc), gully headwalls (gh), gully sidewalls (gs), and open slopes (os) (**Figure 3**). Among these, initiations at headwater basins and gully channels occurred in a handful of cases only. In this paper, the term gully refers to steep, ephemeral, first and second order streams that experience recurrent debris-flow activity on a decadal time scale.

Landslide tracks identified and mapped on the sequential photo sets, were subsequently digitized on a 2003 ortho-photo mosaic, and a series of GIS operations was performed so that landslide attributes (e.g., length, width, area, photo year of first identification, and land use) could be extracted for each track. Although for each landslide was outlined the total disturbed area, the delineation of landslide polygons to constrain landslide lengths, areas, and volumes of mobilised debris follows the specifics adopted by Brardinoni et al. (2009), and as such includes the initiation and the transportation zones - down to the point where scouring is manifestly visible - and excludes the deposition zone.

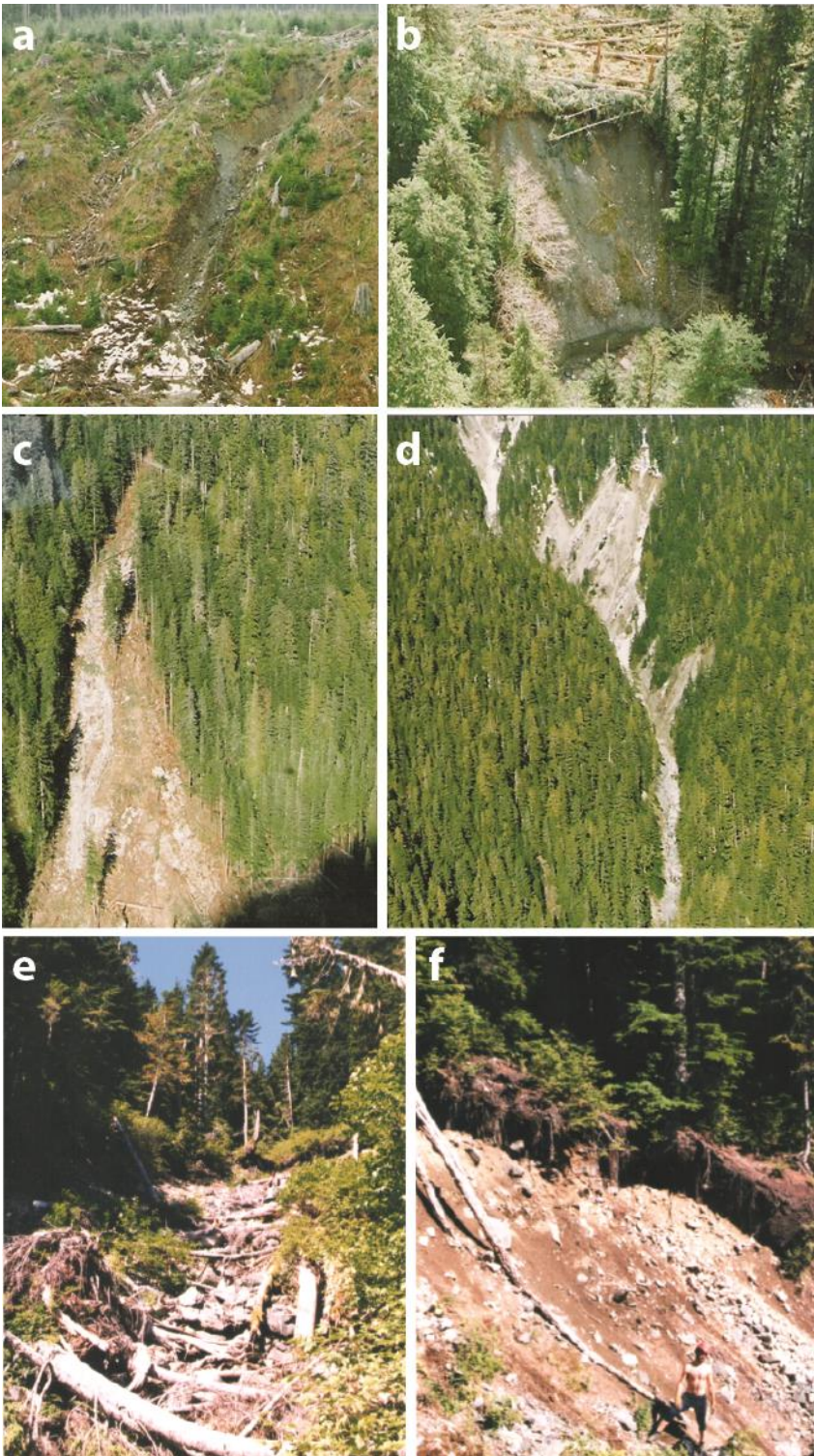


Figure 4. Examples of rapid shallow landslides in the Tsitika River basin. (a) Debris slide in logged terrain, originated at the upper edge of an escarpment (es) developed in thick sandy till, which transformed into a debris flow reaching the escarpment base; (b) Debris slide that initiated at an escarpment face (es), developed in thick sandy till and directly entering a stream channel; (c) Large, open-slope (os) debris avalanche that initiated in a mid-slope colluvial-bedrock complex in old-growth forest and reached the slope base; (d) Debris slides originating from a gully sidewall (gs) entering an active debris-flow channel (gully) in old-growth forest. Open-slope (os) debris slide that developed into a channelized debris flow in old-growth forest: (e) comprehensive view looking upslope, and (f) close-up view of the headscarp.

In the API-derived inventory the photo year represents the minimum age for each landslide, i.e., the temporal constraint is defined by the date of the preceding aerial photo set. In the case of post-logging occurrences, this figure is further constrained by the date of forest harvesting. Prior work conducted in the Queen Charlotte Islands (e.g., Rood, 1984; Smith et al., 1986) and in the Pacific Ranges of the Coast Mountains (Bardinoni, 2001) indicates that API-derived identification and mapping of landslide tracks (i.e., polygon outlines and distinction between initiation, transport and deposition zones) older than 30 years is not consistently reliable, and that younger occurrences can be detected systematically on the basis of vegetation dynamics, even though small tracks may become "not visible" in shorter time scales. Applying this logic, it is reasonable to hypothesize that landslide tracks inventoried in the 1961 photo set could date as far back as the early 1930's. Owing to the uncertainty associated with the decadal resolution of the landslide inventory, and the lack of weather stations at suitable elevations, we believe it is not possible to pursue causal linkages between precipitation trends and landslide occurrence through time. Consequently, in this paper post-logging disturbance will be evaluated without considering the temporal variability in annual and/or seasonal precipitation.

This apparent limitation on meteorological effects, indeed avoids possible experimental confounding associated with the direct comparison of initiation sites on cutblocks, typically implemented on the most easily accessible terrain (**Figure 1**), and natural counterparts that often occur in more rugged topography at higher elevations (e.g., **Figure 3c** and **3d**). In particular, sites located at respectively high and low elevation within a given valley side are different meteorologically and have different soil hydrology in at least four ways: (i) regolith is developed on different surficial materials across elevations (**Figure 2a**); (ii) precipitation is typically greater at higher elevation, (iii) soil saturation is typically greater at lower elevation, given greater contributing area; and (iv) wind pattern, which has been associated with greater landslide activity, is typically greater at higher elevation. In this context, considering morphologic position at initiation ensures that landslides in cut and uncut forest are compared from similar locations in the landscape, with implicitly improved experimental control.

The effect of forest harvesting was assessed on the API-based inventory by comparing the number of landslides and mobilized debris in relation to time since clearcut and/or road construction occurrence and in relation to the amount of area logged. Owing to the limited number of road-related landslides ($n = 50$), in the magnitude-frequency analysis this land-use category was merged with "clearcuts" to form the broader "logged" category, whose behavior is then evaluated against the so-called "natural forest" (control) counterpart. Similarly to what just described for field-measured data, given the small number of debris avalanches in natural forest ($n = 37$) and logged terrain ($n = 38$), in the magnitude-frequency analysis of the API-based inventory, we have merged debris flows (dsdf) and debris avalanches (dsda) into one movement category of the flow type (**section 4.3**). Data stratification across movement types and land use categories adopted in the various analytical stages of this work are summarized in **Table 2**.

3.2 Landslide magnitude-frequency analysis

Post-logging effects on the size distribution of landslides, mapped over the 1960-2003 period, were analyzed using LAND-Stat (Rossi, 2014; Rossi & Malamud, 2014) (implemented in R and available at <https://github.com/maurorossi/dcs-LAND-Stat> where size (i.e., area and volume) is regarded as a proxy for landslide magnitude. The software uses two different statistical distributions to model the probability density of landslide size: (i) the Double Pareto (Stark & Hovius, 2001); and (ii) the Inverse Gamma (Malamud et al., 2004). Both models describe the right (or upper tail, i.e., medium- to high-magnitude spectrum) portion of the landslide size distribution with an inverse power-law scaling, using a Pareto probability density function with a negative exponent, reproducing the increase of landslide occurrences with the decrease of their size until a value corresponding to the maximum probability density, the so-called “rollover” (i.e., the modal or the most frequent landslide size value), is reached.

The main difference between the two models is the description of the left (or lower tail, i.e., low-magnitude spectrum) portion of the distribution. Double Pareto uses an additional power-law function that gradually censors the upper tail, from the rollover to the smaller landslide area values. In this range, the probability density is described through a positive power-law scaling (i.e., a Pareto density function with a positive exponent). Therefore, in the Double Pareto model, the rollover is a probability density peak that separates two scaling regimes, a positive power-law scaling for the lower tail and a negative one for the upper tail, which reflects a crossover.

The Double Pareto model may have three (i.e., Double Pareto Simplified (DPS)) or five parameters (i.e., Double Pareto (DP)), with the latter using two additional parameters for constraining landslide size between a minimum and a maximum value. The Inverse Gamma (IG) model includes 3 parameters and describes the lower tail using an exponential rollover. While the Inverse Gamma must always have a maximum (i.e., it assumes by definition the existence of a rollover), the Double Pareto does not. These two different statistical models of the landslide size distribution can converge to similar probability density function estimates.

LAND-Stat implements different parametric and non-parametric approaches to estimate the parameters of the three distributions (i.e., DP, DPS, and IG) and the associated uncertainty. These include: (i) Histogram Density Estimation (HDE); (ii) Kernel Density Estimation (KDE); and (iii) Maximum Likelihood Estimation (MLE). Each of these approaches exploits different optimization procedures, which sometimes can yield slightly different results. However, they all typically reach convergence when representative and unbiased landslide size samples are analysed (e.g., Rossi et al., 2012). Statistics derived from these distributions have been used: (i) for characterizing inventories obtained from different data sources (e.g., Fiorucci et al., 2011), or from different regions (e.g., Malamud et al., 2004; Fan et al., 2019); (ii) for determining the potential magnitude of a given landslide event size (and corresponding mass transfer); and (iii) for providing probabilistic hazard and risk estimates (e.g., Guzzetti et al., 2005; Corominas & Moya, 2008).

In this work, we use the magnitude-frequency analysis and LAND-Stat outputs to characterize the possible effect of logging on landslide size distribution and infer relevant changes on landslide hazard. To this purpose, we select, compare and discuss the Double Pareto Simplified parameters obtained using the Maximum Likelihood Estimation (MLE) method. This choice is justified by the ability of DPS density function to model landslide size distributions that do not necessarily display a distinct rollover. Indeed, DPS was built to reflect the possible under-sampling of those landslides that are too small to be mapped systematically and accurately. Maximum likelihood estimation (MLE) was preferred as estimation method, due to its reduced subjectivity.

DPS is defined by parameters α , β , and t , which control the shape of the probability distribution. The parameter α controls the slope of the upper (i.e., large size) tail, β controls the slope of the lower (i.e., small size) tail, and t controls indirectly the rollover position. Larger α values correspond to steeper tails, which indicate a reduced proportion of large landslides within the size range above the rollover. Larger β values correspond to steeper small-size tails, which indicate a reduced proportion of small landslides within the size range below the rollover.

To evaluate the significance of the modelled parameters (α , β , t), LAND-Stat performs t-tests. In the tests, the t-statistics is used and the corresponding p-value can be compared across different confidence levels to rank the significance of single parameters (**Table 7**). This information is useful to evaluate the suitability of the selected model in relation to the study dataset and its possible representativeness. In addition, LAND-Stat performs the two-sided Kolmogorov-Smirnov (KS) test, estimating D-statistics and the corresponding p-value, in order to verify whether DPS was appropriate for describing the frequency-size distribution of landslide areas of all data stratifications examined (Kolmogoroff, 1933; Smirnov, 1939). The KS test fails when the p-value is below 0.05, the level of significance we selected for this study. Finally, to evaluate the uncertainties associated with the probability density estimates, their parameters and the rollovers, LAND-Stat implements a bootstrap resampling procedure. Such uncertainties are critical to derive statistically robust comparisons of modelled distributions generated from inventories with different sample size.

4. Results

4.1 Integrating field-based and API-derived landslide data

In this section, field measurements of landslide geometry (i.e., depth, width, and length) are used to constrain a landslide area-volume relation (where area = width • length, and volume = depth • area) to be applied to the API-based inventory and translate relevant planform areas into volumes of mobilized debris. Before proceeding, we conduct exploratory analysis: (i) to examine how landslide depth, width and length vary across movement types (i.e., ds vs dsda & dsdf) and land uses (i.e., natural vs logged); and (ii) evaluate whether specific area-volume relations hold statistical significance or a single relation may apply to the whole field-based dataset.

Field-measured landslides range in planform area between 8 m² and 48,000 m². Relevant landslide depths span from 0.2 m to 5 m, with median and average values respectively equal to 0.50 m and 0.81 ±0.06 m (1 Std Error) (**Table 3**). Headscarp depths exceed soil thickness, and therefore typically mobilize part of the underlying surficial materials (i.e., colluvium, glacial till and deglacial deposits) both in logged and natural occurrences. Landslide scouring down to bedrock is limited to a handful of cases.

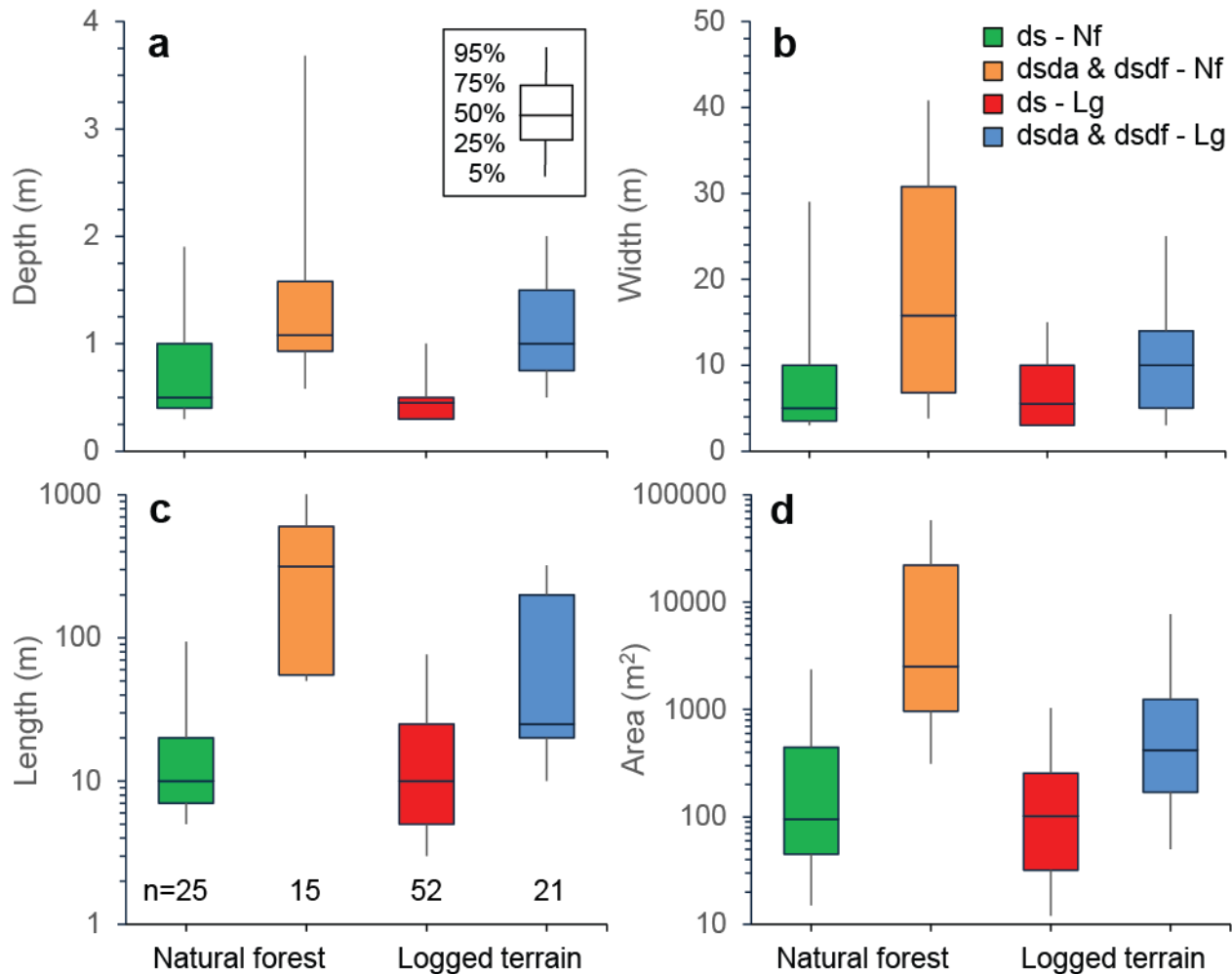


Figure 5. Boxplots showing (a) depth, (b) width, (c) length, and (a) area distributions of field measured landslides classified by land use (Natural forest and Logged terrain) and movement type (ds = debris slides; dsda = debris avalanches; dsdf = debris flows). Length and area are represented in logarithmic scale to improve boxplot readability. Boxes enclose interquartile ranges, whiskers span from 5% to 95%.

Interquartile ranges (i.e., the boxes bounding the 75th-to-25th percentiles) in boxplots of landslide depths stratified by land use and movement type show that logging-related debris slides (ds) tend to be triggered, on average, within shallower surficial material depths than natural counterparts, although median values are the same i.e., 0.5 m (**Table 3** and **Figure 5a**). This finding, when considered alone, is consistent with lower cohesion in logging-related initiations. Landslides do not differ substantially in terms of width, length, and consequently in terms of landslide area (see overlap between interquartile ranges in **Figures 5b**, **5c** and **5d**). In long runout failures (dsdf & dsda) we do not observe a clear land-use effect on landslide depth (median

depth equals 1 m in both categories; **Table 3**). However, typically smaller landslide widths and lengths in logged terrain (**Figure 5b** and **5c**) give rise to markedly smaller landslide areas than observed in natural forest (**Figure 5d**). Overall, the variability of scar width, length, and area, as quantified by the interquartile range, is less pronounced for debris slides (ds) than for dsda & dsdf (**Figure 5**).

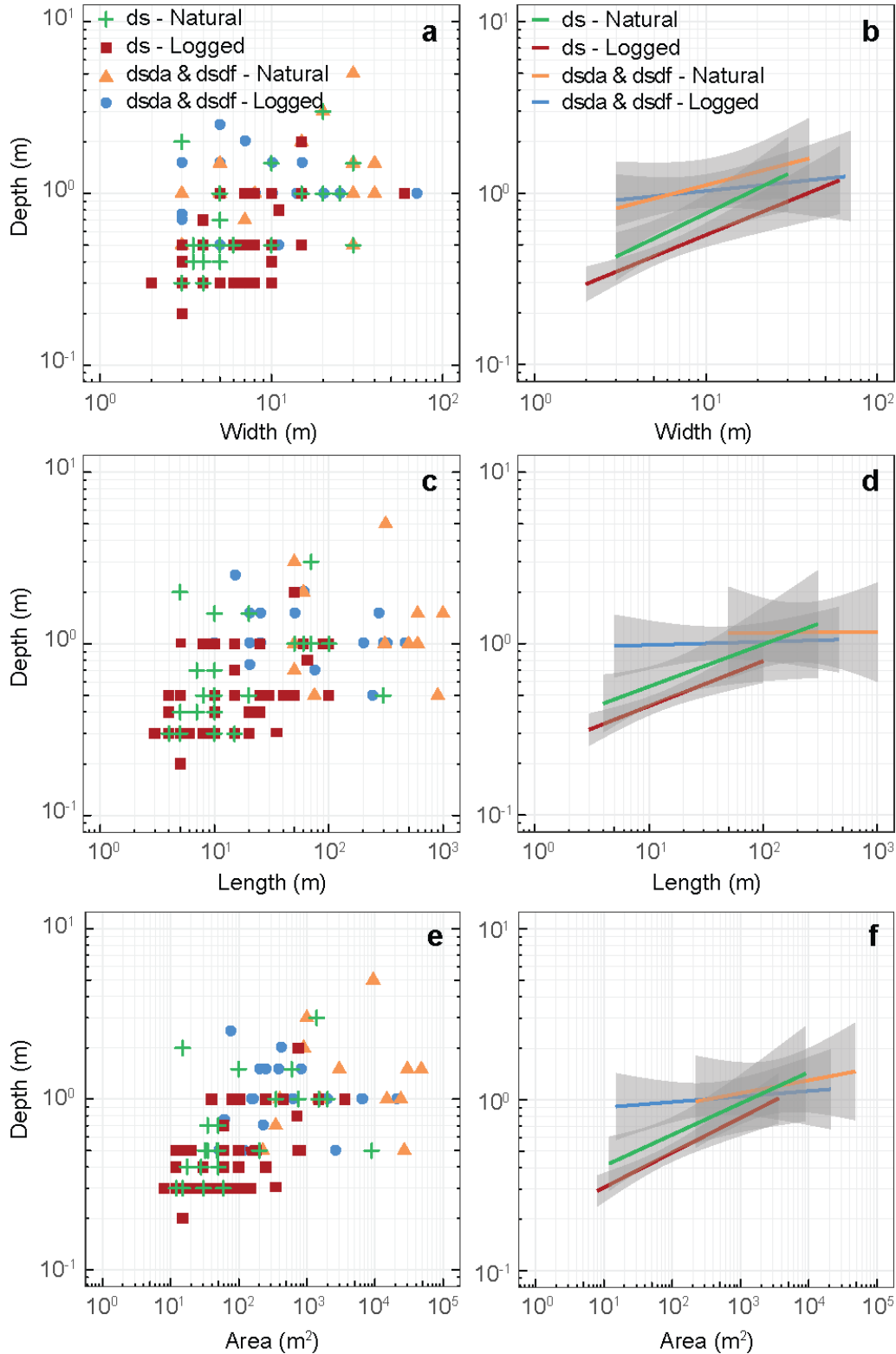


Figure 6. Scatterplots representing landslide depth as a function of (a) landslide width; (b) landslide length; and (c) landslide area. Relevant 95% prediction intervals of the linear fitting in logarithmic scale are reported in panels (b), (d), and (f).

Analysis of Pearson’s linear correlation coefficients (r_s) shows that simple planimetric variables (i.e., width and length) are directly related. Correlation is stronger for landslides in natural forest ($r_s > 0.65$) than in logged terrain ($r_s \sim 0.40$) (**Table 4**). Interestingly, direct correlation of width and length with area seems to be land-use dependent, since natural landslide length exhibits higher correlation, while in logged terrain width correlates higher.

Landslide depth appears to have no significant or consistent linear dependency with the other geometric variables, regardless of land use and movement type (**Table 4**). To investigate this question further, we explored the existence of possible power-law dependencies (i.e., linear for log transformed variables) of landslide depth as a function of width (**Figure 6a**), length (**Figure 6b**), and area (**Figure 6c**) across land use and movement types. In general, depth is positively related with width, length and area. Dependence appears to be stronger for debris slides, compared to long runout failures (i.e., the slope of dsda & dsdf fitting is consistently lower – in some cases close to null – than that of debris slides). In particular, the best fit line of natural debris slides plots consistently above the logged counterpart. Collectively, the high degree of overlapping among the respective 95% prediction intervals (shaded areas in **Figure 6**) suggests that available field data do not allow to constrain distinct relations for different land use or movement types.

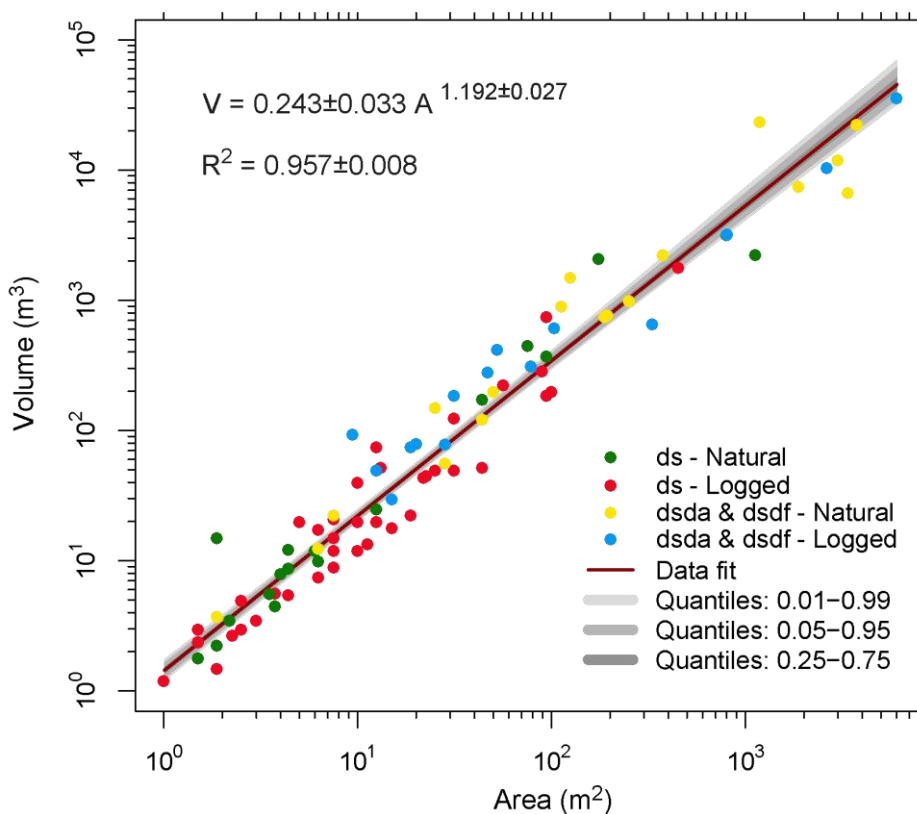


Figure 7. Area-volume scaling relation of slope failures measured during fieldwork conducted in the Tsitika and Eve watershed ($n = 113$). Data are stratified by land use (natural vs logged) and movement type (debris slides vs debris flows/avalanches). Grey-shaded areas indicate prediction intervals of the fitting for different percentile ranges.

In agreement with these findings, the area-volume power-law (least-squares) fitting on data stratified by land use (i.e., logged vs natural) and movement type (i.e., debris slide vs debris flow & avalanche) did not show significant statistical difference in terms of intercept and scaling exponent (t-test p-values < 0.05). Consequently, we fitted a common function to all data points in log-log space (**Figure 7**). This combined area-volume relation shows a well-constrained positive trend (i.e., $V_L = 0.243A_L^{1.192}$; $R^2 = 0.957$), with data scatter that increases for larger landslides. The power-law parameters were obtained by fitting a linear model (dark red line in **Figure 7**) to the logarithm of the landslide area ($\log_{10}(A_L)$) and volume ($\log_{10}(V_L)$) using a similar approach to that described in Guzzetti et al. (2009) and applying a bootstrap resampling to estimate the modelling uncertainties (grey shades in **Figure 7**). The combined area-volume relation is very similar to that compiled by Guthrie & Evans (2004) for shallow landslides in logged terrain of Haida Gwaii (i.e., original data drawn from Wise (1997)), British Columbia (n = 124; $V_L = 0.155A_L^{1.091}$; $R^2 = 0.947$). The scaling exponent (1.19) is somewhat lower than what documented in previous global compilations of "soil" landslide geometry, where this parameter varies between 1.33 and 1.45 (Guzzetti et al., 2009; Larsen et al., 2010).

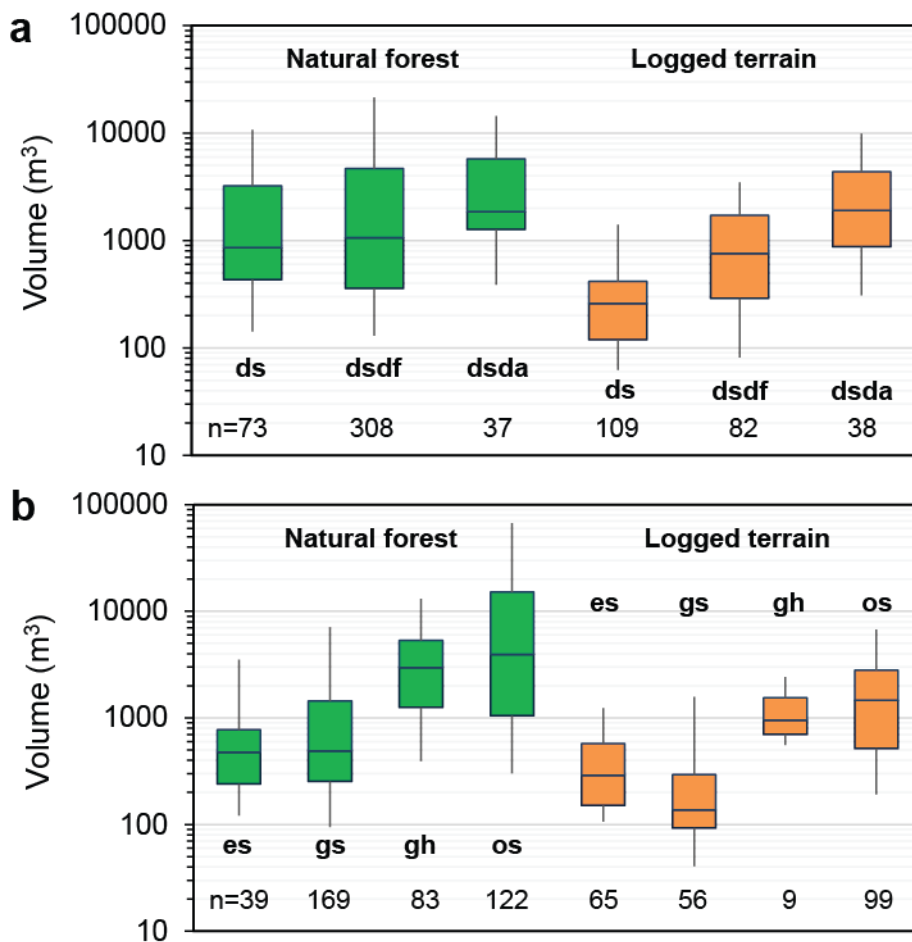


Figure 8. Boxplots representing the volume distribution of API-mapped landslides across land-use categories and stratified by (a) movement type; and (b) morphologic position at initiation point. Boxes enclose interquartile ranges, whiskers span from 5% to 95%. Given the small number of observations, gully headwalls (gh) in logged terrain should be considered with caution.

The area-volume empirical relation was then applied to the API-based inventory, so that landslide activity could be evaluated in terms of volumes (V_L) of mobilized debris (**Table 5**) and volumetric sediment fluxes could be assessed for landslides initiated in natural forest, within clearcuts and about logging roads. Relevant boxplots classified by movement type indicate a consistent behaviour in cut and uncut forest, with debris slides being the smallest, debris avalanches the largest, and debris flows displaying somewhat intermediate volumes (**Figure 8a**). Interestingly, debris slides in natural terrain stand out for mobilizing particularly larger volumes than logging-related counterparts, as shown by the offset of the relevant interquartile ranges.

Data stratification by morphologic position at initiation helps identifying which parts of the slopes and the ephemeral drainage network become more prone to shallow landslides following forest harvesting (**Table 6** and **Figure 8b**). Major changes in the relative proportions of debris slide occurrences relate to open slope positions, whose percent frequency, compared to natural forest, increases by a factor of 2 (from 33.6% to 64.2%) for long runout failures, and greater than 2 (from 8.2% to 20.2%) for debris slides. For the long runout type, this increase is mirrored by 10-fold rise of initiations at escarpments (from 1.7% to 17.5%), suggesting that logging can increase escarpment sensitivity to fluvial undercutting.

In terms of size, gully headwall and open slope landslides are consistently larger (primary movements) than escarpment and gully sidewall counterparts (secondary movements) both in cut and uncut forest, with the former median values plotting around or well above $1,000 \text{ m}^3$, and the latter comprised between 100 and 300 m^3 (**Figure 8b**). Considering specific initiation categories (i.e., es, gs, gh and os) separately, we observe a clear land-use effect in that landslide volumes are consistently larger in natural forest than in logged terrain. For example, median volumes of landslides originating at open slope ($V_{os} \sim 4,000 \text{ m}^3$) and gully sidewall ($V_{gs} \sim 500 \text{ m}^3$) positions in natural forest, are respectively 4 and 5 times larger than logging-related ones (**Figure 8b**).

4.2 Time scales of disturbance and recovery

Analysis of landslide occurrence in relation to cutblock age depicts a post-logging disturbance wave, where occurrences, and the corresponding mobilized volumes, peak respectively 7-9 years and 10-12 years after logging (**Figure 9**). This 3-year offset is associated with the occurrence of a large debris flow (i.e., $> 30,000 \text{ m}^3$) in year 10, and that of fourteen medium- to large-sized long runout failures in year 12 (**Figure 9**).

A similar increase in landslide frequency and volume has been previously associated to a transient period of highest landslide susceptibility, when rooting strength decays after forest harvesting and before substantial regeneration following plantation emerges. In relation to hydro-meteorological forcing, this window of root strength minimum indicates that the probability of a landslide is higher given the likelihood of a triggering storm event (Sidle & Ochiai, 2006). However, to pursue causal linkages between precipitations and landslide time series, thus to further disentangle logging from meteorological effects, we believe one would need an inventory with higher temporal resolution (see section 3.1).

Our post-logging trends in landslide frequency and volume agree, among a number of existing studies on root strength (e.g., O'Loughlin & Ziemer, 1982; Schmidt et al., 2001), with prior findings from comparable

physiographic settings of formerly glaciated southeastern coastal Alaska (Ziemer & Swanston, 1977). Accordingly, Western Hemlock and Sitka Spruce roots were found to lose respectively about 30% and 50% of tensile strength within 2 years after logging, then attaining virtually complete strength loss within 10 years.

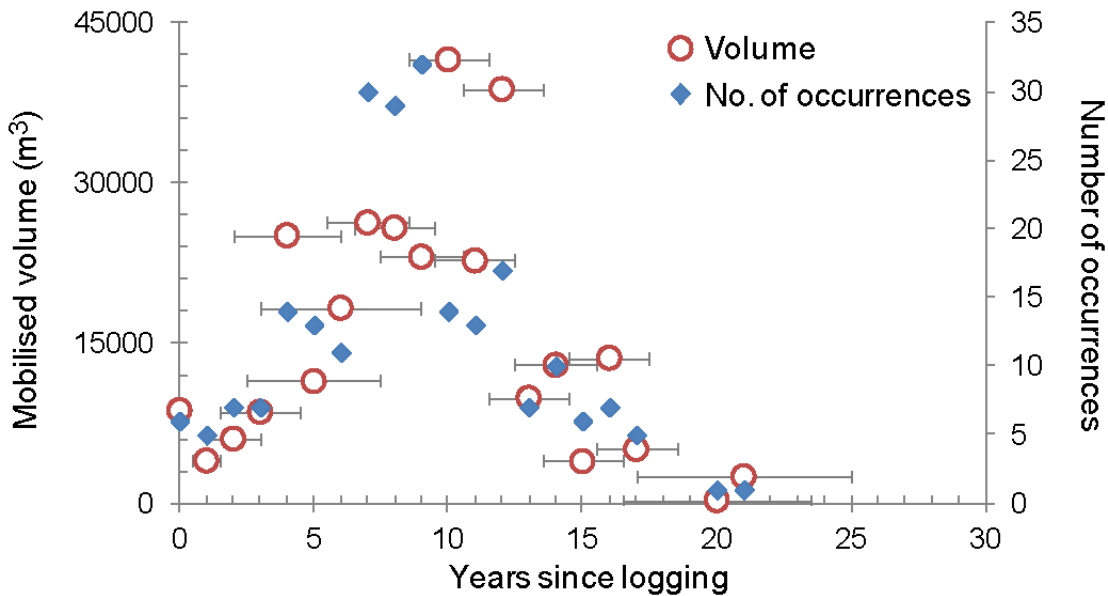


Figure 9. Landslide transient response to forest clearing in Tsitika and Eve watersheds. Post-logging effects are evaluated in terms of: number of occurrences (blue diamonds), and mobilized volume of debris (open red circles). Error bars in the volumetric data series depict the uncertainty associated with the difference between year of cutblock operations and air-photo year in which the landslide was first identified. The same error bars apply to the corresponding number of occurrences for a given post-logging year. After 16-19 years since logging, landslide activity in logged terrain return to pre-logging (undisturbed) levels.

Considering the uncertainty associated with the timing of landslide occurrence in sequential photosets (error bars in **Figure 9**), the disturbance wave displays a relatively symmetric shape, for a combined post-logging recovery cycle comprised between 16 and 19 years. This time frame agrees with the recovery dynamics identified by existing empirical and modelling efforts conducted in the Pacific Northwest (see review by Sidle & Bogaard, 2016 and references therein).

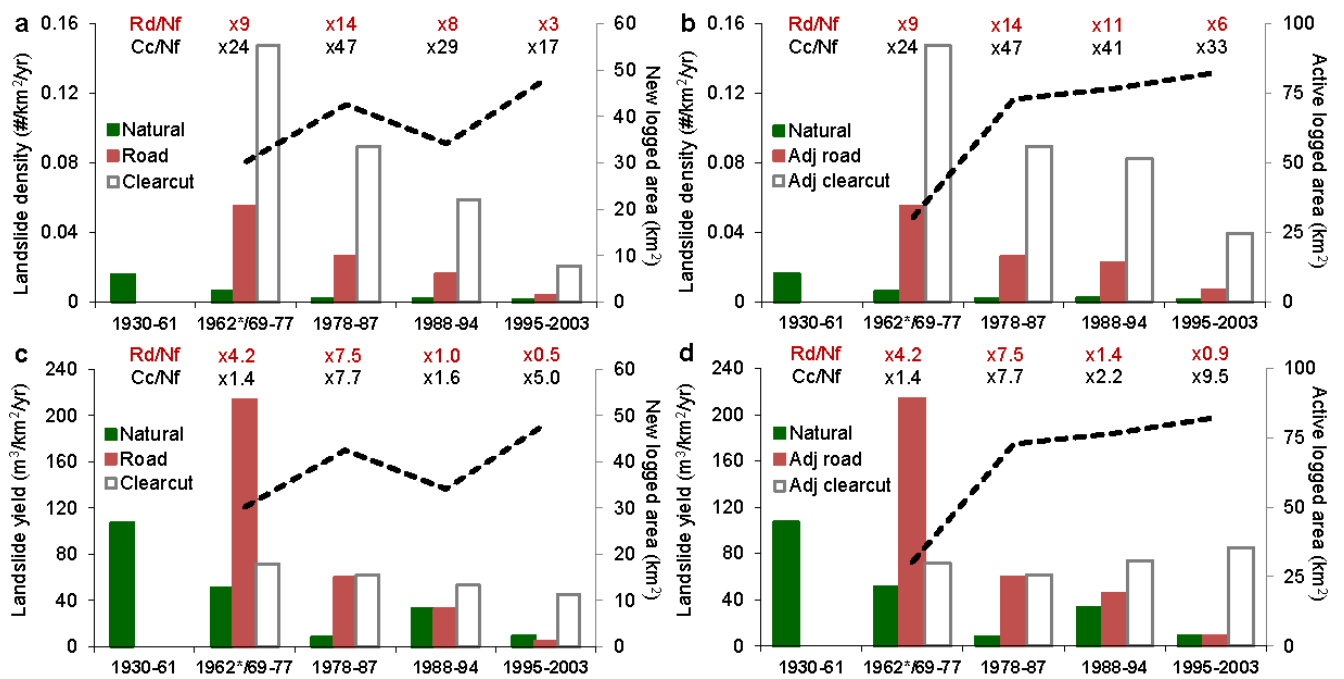


Figure 10. Annual landslide density for the period 1930-2003: (a) calculated by dividing the number of landslides by the area logged between sequential aerial photo sets (dashed line); and (b) adjusted (Adj) for post-logging recovery. Landslide sediment yield for the period 1930-2003: (c) calculated by dividing the number of occurrences by the area logged between sequential aerial photo sets (dashed line); and (d) adjusted (adj) for post-logging recovery. The adjustment each photo year takes into consideration the area logged within the time span (i.e., 19 years) necessary for recovery from logging disturbance (i.e., active logged area). Dashed line indicates the variation of active logged area with time. Logging operations in the watersheds began in 1969. Cc/Nf (Clearcut to Natural forest ratio) and Rd/Nf (Road-related to Natural forest ratio) indicate the acceleration factor induced by logging activities on landslide density and yield. Landslide yield in 1988-94 period is chiefly associated to a single debris slide that transformed into a debris flow and mobilized an estimated volume of 112,000 m³. In that period, the other 6 landslides mobilized 5,500 m³ collectively.

When considering the number of landslides across sequential photosets, clearcut-to-natural landslide density ratio is consistently higher ($17 < Cc/Nf < 47$) than the road-related counterpart ($3 < Rd/Nf < 14$) by roughly a factor of 3 or more (**Figure 10a**). Owing to the larger size of natural landslides (**Figure 8a**), logging effects expressed as clearcut ($1.4 < Cc/Nf < 5.0$) and road-related ($0.5 < Rd/Nf < 7.5$) sediment yield ratios, become milder and comparable (**Figure 10c**).

Landslide density in natural forests shows a general decrease through time (**Figure 10a**). This decrease is also observed for clearcut and road-related occurrences, with the former density outpacing consistently the latter (**Figure 10a**). The trend does not change when landslide density is “adjusted” for the 16-19 yr recovery time window just constrained (i.e., adj clearcuts and adj roads in **Figure 10b**); that is, landslide density (and landslide yield) in each photo year is calculated over the so-called “active logged area”, or the logged area that includes 19-year old (and younger) cutblocks only.

Historical trends are different in terms of specific landslide yield (**Figures 10c and 10d**). In natural terrain we observe a declining trajectory, interrupted temporarily between 1988 and 1995, due to the occurrence of a large (i.e., 112,000 m³) debris flow. In logged terrain, clearcut yield declines slowly but consistently, whereas road-related occurrences display a more rapid drop, after a strong start in the 70's (> 200 m³/km²/yr). In particular,

the road-related specific sediment yield, which was initially outpacing the clearcut counterpart by a factor of 3, by 1995-2003 exhibits values about 5 times lower than in clearcuts (**Figure 10c**).

4.3 Effects on landslide geometry, magnitude and frequency

Landslide planform geometry is typically elongated, with length-to-width ratio varying from less than 1:1 (isometry) to about 100:1 (**Figure 11a**). As landslides grow larger they become increasingly elongated, and this tendency appears to hold across all land-use categories. Larger landslides occurred in pristine forest exhibit the highest length-to-width ratio. Clearcut and road-related landslides are typically shorter (hence smaller) than in natural forest. As will become clear, logging generates landslides at low elevations and gentler slopes where they would not normally occur, and they therefore have limited runout because of the particular topography where logging operations have taken place. In this context, only 11 movements have grown longer than the length of the relevant hosting cutblock (**Figure 11b**).

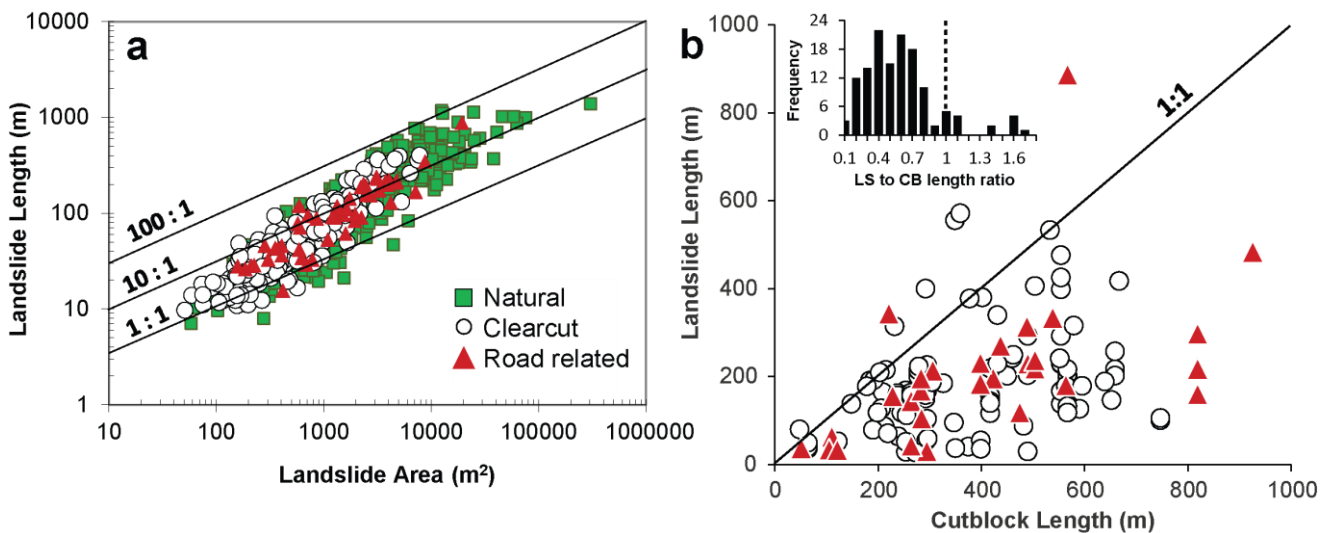


Figure 11. (a) Landslide length as a function of landslide area across land use types. Solid lines indicate reference landslide length-to-width ratios, assuming a rectangular landslide planform. (b) Landslide (LS) to cutblock (CB) length ratio for clearcut and road-related movements. Inset shows the frequency distribution of the relevant LS-to-CB ratios. Ratios plotting above the 1:1 line indicate landslide lengths greater than the hosting cutblocks.

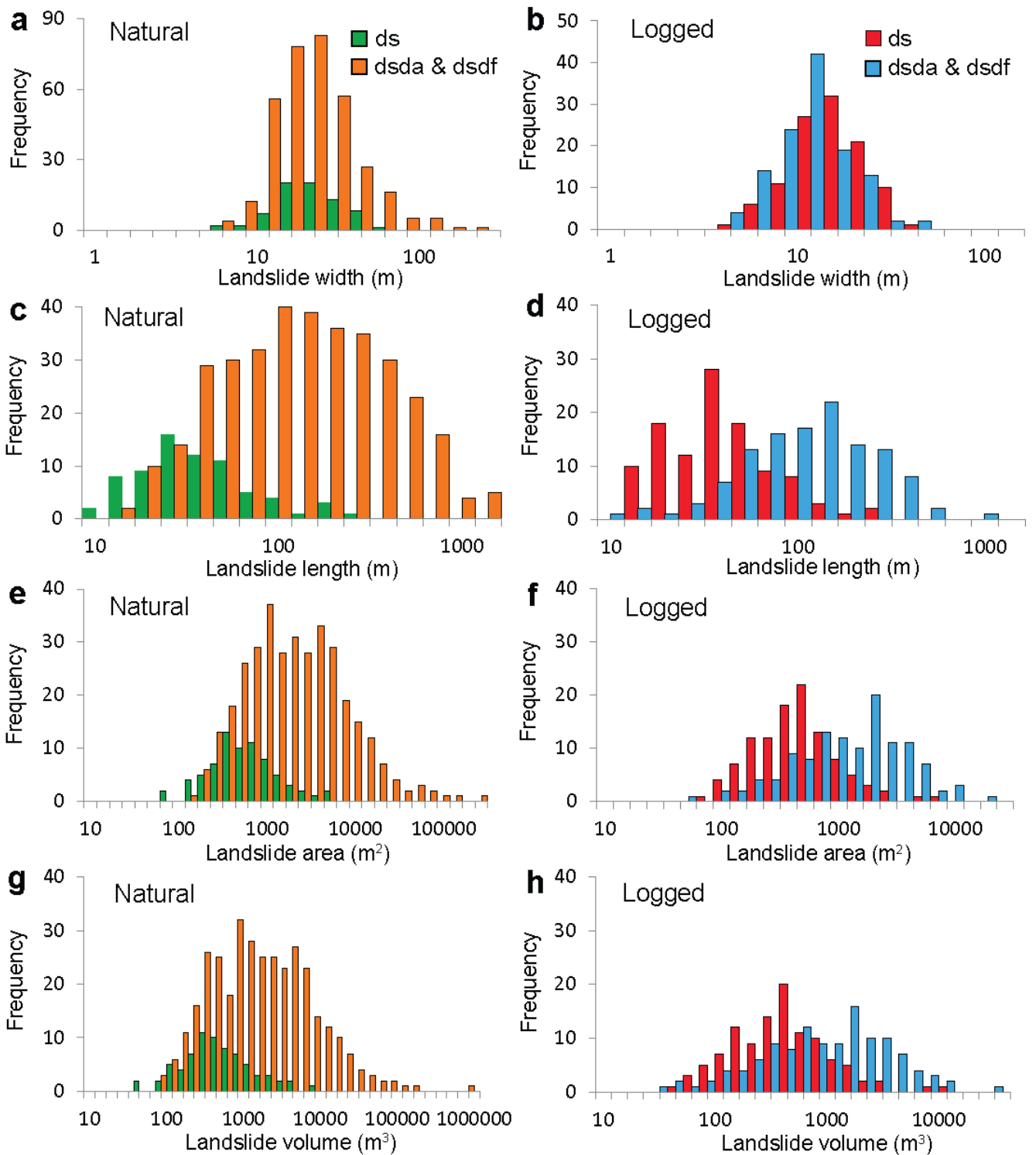


Figure 12. Frequency distributions of debris slides (ds) and long runout shallow failures (dsda & dsdf) geometry measurements. Landslide width in (a) natural forest and (b) logged terrain. Landslide length in (c) natural forest and (d) logged terrain. Landslide area in (e) natural forest and (f) logged terrain. Landslide volume in (g) natural forest and (h) logged terrain. Histograms are built with equally-spaced bins in logarithmic scale. Each order of magnitude includes seven bins.

The effect of logging on landslide frequency distributions is presented to help the reader make a direct connection between row empirical data (**Figure 12**) and modelling outputs (probability density functions), reported in **Figure 13**. Logging-related debris slides (ds) and long runout failures (dsda & dsdf) display

different frequency distributions from natural counterparts in terms of width, length, area, and volume (**Figure 12**). In particular, dsda & dsdf (orange and light blue bars) outpace debris slide occurrences (green and red bars) by a factor of 5 in natural forest; vice versa the two typologies occur with comparable frequencies in logged terrain, with a slight dominance of debris slides (**Table 5** and **Figure 12**). The variability (i.e., the ranges associated to the green and red histograms total widths) and average (i.e., the modal or the most frequent values in the green and red histograms) geometrical characteristics of debris slide (ds) frequency distributions remain similar in natural and logged areas. The same histogram characteristics for long runout failures (dsda & dsdf) display drastic reduction in logged areas (light blue bars) compared to natural ones (orange bars).

Depending on movement type, we also observe diverse land-use effects on the frequency distributions of landslide width (L_W) and length (L_L). In natural forest, widths of long runout failures are positively skewed towards larger values (up to 270 m), display a much broader range of variation (spread of x-axis), and attain a larger modal value (i.e., ~ 27 m) than debris slides (**Figure 12a**). By contrast, in logged terrain the two landslide types describe very similar width distributions (**Figure 12b**). This similarity holds with regard to range of variation, histogram shape (symmetrical in both cases), and modal width (i.e., ~ 14 m).

As expected, landslide lengths of long runout failures display consistently larger modes than debris slides, both in natural ($L_{DS} \sim 38$ m; $L_{DSDF/DA} \sim 140$ m; **Figure 12c**) and logged terrain ($L_{DS} \sim 27$ m; $L_{DSDF/DA} \sim 140$ m; **Figure 12d**). Relevant histogram shapes differ by movement type. Accordingly, debris slides are skewed towards large lengths in both land-use categories, while long runout failures are either negatively skewed in logged terrain (**Figure 12d**), or display an overall symmetrical shape in natural forest (**Figure 12c**).

Histograms of landslide areas (**Figures 12e** and **12f**) retain most of the characteristics observed for landslide lengths, suggesting that length (as opposed to width) exerts a primary control on landslide area. Accordingly, long runout failures display consistently larger modes than debris slides, both in natural ($L_{DS} \sim 380$ m² vs $L_{DSDF/DA} \sim 1000$ m² in **Figure 12e**) and logged conditions ($L_{DS} \sim 520$ m² vs $L_{DSDF/DA} \sim 1930$ m² in **Figure 12f**). Interestingly, logged modal values, centred within substantially bell-shaped distributions (**Figure 12f**), are larger than natural ones. This outcome chiefly derives from the complex, positively skewed shape of the natural histograms (**Figure 12e**), characterized by secondary peaks at larger landslide areas ($L_{DS} \sim 720$ m² vs $L_{DSDF/DA} \sim 3800$ m²). Finally, landslide volumes display histogram shapes that are very similar to those described for areas (cf. **Figure 12e** and **12g**; **Figure 12f** and **12h**).

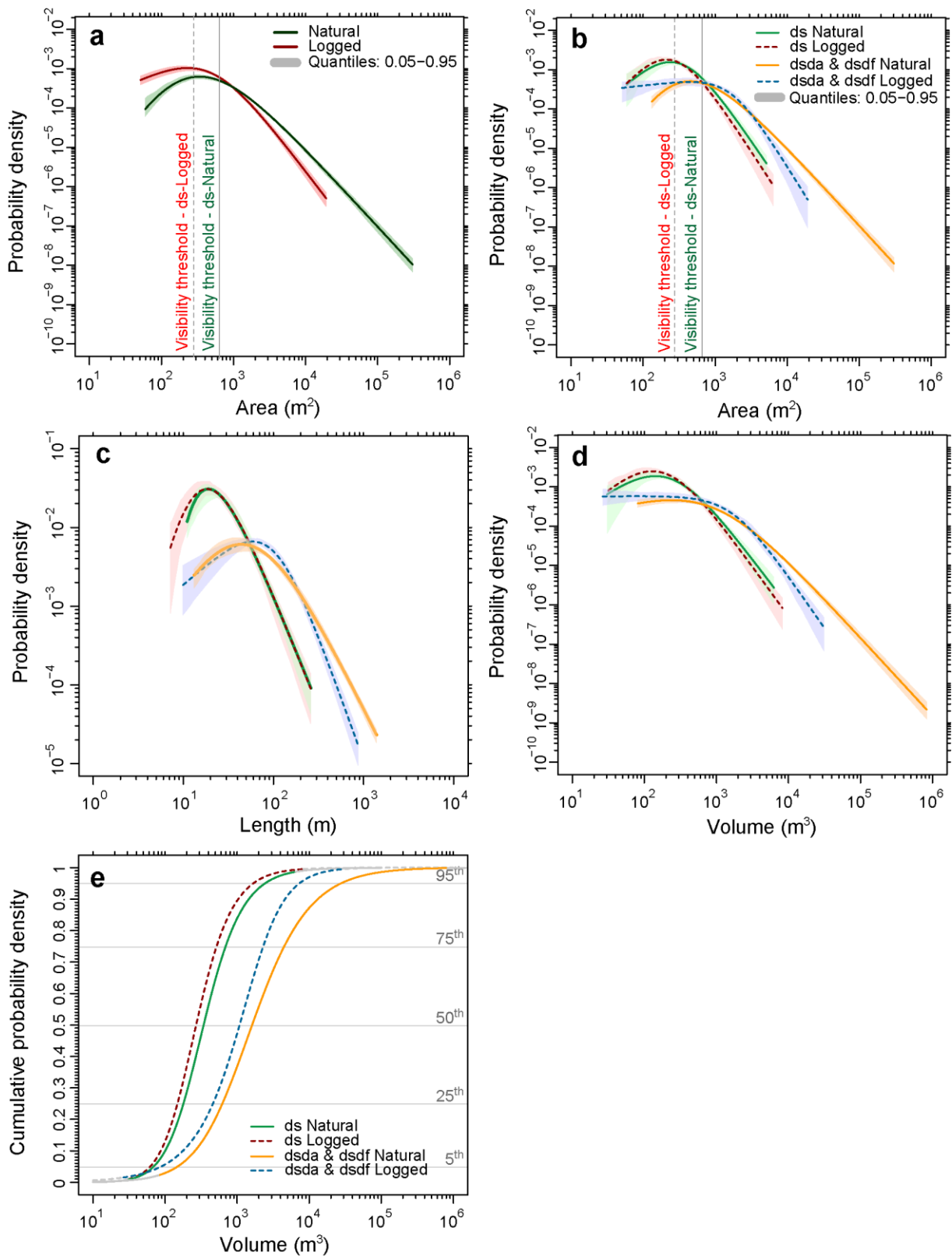


Figure 13. Probability density functions of API-based landslide areas (a, b), lengths (c), volumes (d), and relevant cumulative probability density functions (e). Panel (a) reports functions of occurrences in natural forest, in logged terrain. In the other panels, functions are stratified into four categories combining land use (natural forest and logged terrain) and movement type (debris slides (ds) and long runout failures (dsda & dsdf)). Red and green vertical lines in panels a and b indicate visibility thresholds for shallow rapid failures respectively in cutblocks younger than 15 years, and in old-growth forest (Brardinoni et al., 2003b).

In **Figure 13**, we compare the magnitude-frequency statistics modelled using the Double Pareto Simplified (DPS) distribution for landside area (**Figures 13a and 13b**), length (**Figure 13c**) and volume (**Figures 13d and 13e**), expressed as probability density (PDFs) and cumulative density functions (CDFs). Consistent with the classification scheme used for field-measured occurrences (**Figures 4, 5 and 6**), remotely-based landslides are stratified by land use (**Figure 13a**), and by a combination of land use and movement types (**Figures 13b through 13e**). PDF representation allows direct comparison of data distributions, the straightforward visualization of distribution parameters, the identification of the rollover position, and the possible censoring effect for low-size landslides (i.e., lower distribution tail). Shaded buffers in the plots (**Figure 13**) show the 90% confidence interval on the estimate of the PDF. When confidence intervals do not overlap, the estimated distribution are statistically different. CDF allows for a more direct comparison of quantile/percentile statistics, or the non-exceedance/exceedance probability (i.e., the cumulated probability for a landslide of being smaller (or larger) than a given size), and provides meaningful information for hazard analysis (e.g., Guzzetti et al., 2005; Corominas & Moya, 2008) and the design of possible mitigation measures (e.g., Melzner et al., 2020).

In **Table 7**, we report the parameters (and the relevant tests statistics) describing the landslide area distributions estimated by means of Maximum Likelihood Estimation (MLE) (Rossi & Malamud, 2014). The table summarizes for the DPS model: (i) the parameter controlling the transition between the tails (t), the slope of the upper tail (α), and the slope of the lower tail (β), as well as relevant standard errors and significance, expressed as p-value; (ii) the estimated value of the rollover (R); and (iii) the Kolmogorov-Smirnov (KS) test statistics and the relevant p-value. The KS test fails if the p-value is below 0.05 – the level of significance we selected for this study – meaning that the dataset does not come from a DPS distribution. In **Supplementary Table 1**, we report an estimate of the rollover uncertainty (i.e., 1st, 5th, 25th, 50th, 75th, 95th, and 99th percentiles) derived from the resampling bootstrap procedure for landslide lengths, areas, and volumes.

KS tests show that DPS is appropriate for describing the landslide area distribution of all data stratifications examined, with the estimates of their parameters being consistently significant (DPS parameter p-value < 0.05) (**Table 7**). Probability density functions of landslide areas in natural forest and logged terrain are statistically different (**Figure 13a and Table 7**), they exhibit distinct size ranges and different rollover values ($R_N = 330 \text{ m}^2$; $R_L = 230 \text{ m}^2$) (see lack of overlapping between interquartile ranges of bootstrap resampling in **Supplementary Table 1**). In agreement with the frequency distributions depicted by simple histograms (**Figure 12**) and with the limits to landslide size imposed by cutblock length (**Figure 11b**), PDF representations show that landslides in logged terrain tend to be statistically smaller (i.e., quantile envelopes do not overlap), with large landslides being evidently less frequent (**Figure 13a**).

Further data stratification by movement type (**Figure 13b**) helps gaining insights on the geomorphic causes of such differences modulated by land use. Indeed, we observe that debris slides are consistently smaller than long runout failures, regardless of land-use type (as expected, by definition). Most importantly, we note that debris slides do not display any land-use effect (i.e., ds-natural and ds-logged quantile envelopes overlap) and that long runout failures do. In particular, we observe that (i) logging-related long runout failures are

significantly smaller than in natural forest; and (ii) the rollover in logged terrain stands out for being ill-defined, and bridges small ($< 300 \text{ m}^2$) and large ($> 3,000 \text{ m}^2$) landslides that are significantly more frequent than in natural forest (**Figure 13b**).

The main characteristics described for the PDFs of landslide area apply to length analogues (**Figure 13c**), thus confirming previous observations noted in terms of frequency distribution (**Figure 12**). In this context, the well constrained rollover described by long runout failures (blue linework in **Figure 13c**), which was ill-defined in terms of areas, represents the one main difference. The rollover for debris slide lengths occurs at about 20 m for both land-use types (i.e., $R_N = 18 \text{ m}$; $R_L = 19 \text{ m}$ in **Supplementary Table 1**), and increases progressively for long runout failures in logged terrain ($R_L = 44 \text{ m}$) and natural forest ($R_N = 59 \text{ m}$) (i.e., see lack of overlap between interquartile ranges in **Supplementary Table 1**).

Similar to areas, volume distributions show statistically significant differences (confidence intervals do not overlap) only in terms of long runout failures (dsda & dsdf in **Figure 13d**). For these movements, occurrences larger than roughly $4,000 \text{ m}^3$ (i.e., values larger than the natural-logged intersection of long runout failures) are significantly more frequent, with the 5% (**Figure 13e** i.e., corresponding respectively to a non-exceedance probability of 0.95, or to an exceedance probability of 0.05) of occurrences being respectively larger than about: $7,000 \text{ m}^3$ in logged terrain (blue dashed line) and $30,000 \text{ m}^3$ in natural forest (solid orange line). Regardless the overlap between volume-based PDFs (**Figure 13d**), the corresponding CDFs of simple debris slides and long runout failures, for values larger than 100 m^3 , show a consistent decrease of volume from natural to logged conditions across all the main percentiles (**Figure 13e**).

5. Discussion

5.1 Effects of landslide geometry and sediment transfer

The direct estimation of landslide depth is a fundamental, yet challenging, prerequisite for evaluating landslide volume and associated sediment flux. Without this type of information, land-use effects may be evaluated with regard to number of occurrences, landslide densities and disturbed areas (e.g., Jakob, 2000; Wolter et al., 2010). Challenges in volumetric estimation may vary with movement style, for example due to the recurring or episodic nature of occurrence, the partial or complete evacuation of the mobilized material from the initiation site, and the coalescence with adjacent (or antecedent) landslides.

Despite increasingly available higher-resolution airborne and/or satellite imagery (e.g., Van den Eeckhaut et al., 2007; Tanyas et al., 2019; Bunn et al., 2020), the visibility issue of shallow rapid failures over multi-temporal scales remains unresolved in rugged, humid, densely-forested watersheds; unless costly, high (temporal and spatial) resolution LiDAR surveys are performed. In similar settings, small landslide scars may be: (i) simply not imaged (Turner et al., 2010); (ii) only partly visible, with their perimeter mapped only to a limited extent (Pyles & Froehlich, 1987); (iii) subject to a varying degree of coalescence with adjacent scars; or (iv) too difficult to detect unambiguously under the forest canopy (Brardinoni et al., 2003b). For these reasons, field measurements form a critical complement to remotely-based inventories.

Published, field-based measurements on shallow landslide geometry, stratified by land use are rare (e.g., Rickli & Graf, 2009; Koyanagi et al., 2020). This is particularly the case in formerly glaciated settings of the Pacific Northwest, where valley walls are often mantled by glacial till. Swanston & Marion (1991) in southeast coastal Alaska (Chicagof and Prince of Wales islands), while considering 164 debris flows in cut and uncut forest, report that initial failure sizes, transport distances, erosion in the transport zones, and volumes of deposited material are larger in unlogged than in logged portions of old-growth forest. They further report that initial failure depth in old-growth forest and logged terrain was in both instances equal to $0.7 \text{ m} \pm 0.5$ (1 Std deviation) and that according to t-tests there was insufficient evidence to reject the null hypothesis i.e., failure zone depth is the same in logged and unlogged conditions. These findings match more recent field-measured geometries from Prince of Wales Island (Johnson et al., 2000), where 45 landslides, randomly selected from a larger unpublished inventory, exhibit virtually identical mean landslide depth in old-growth ($L_d = 1.2 \text{ m} \pm 0.5$), second-growth ($1.1 \text{ m} \pm 0.7$) and clearcut ($1.2 \text{ m} \pm 0.4$) terrain. In coastal British Columbia, these mean depth values are typically associated to the characteristic thickness of regolith over bedrock, which on till-mantled slopes correspond to the surface of preferential subsurface water flow and consequent weakness that develops between weathered and unweathered till (e.g., Brardinoni & Church, 2004).

In this context, the Tsitika and Eve field-based data, stratified by movement type, provide additional insights. On one hand, they confirm that logging has an almost negligible effect on the depth of long runout failures, as testified by equal median values and comparable interquartile ranges observed in natural and logging-related scars (**Figure 5a**); on the other hand, they indicate that debris slides are somewhat shallower than natural counterparts, as suggested by the much tighter interquartile spread of the former land use type (**Figure 5a**). Despite these indications, low correlations of landslide depth with length, width, and therefore with landslide area (**Table 4**), impart high scatter to depth-based power-law relations stratified by land use and movement type, yielding high overlap between the relevant prediction intervals (**Figure 6**). In turn, this scatter generates area-volume relations that are not significantly different across land uses and movement types.

Spatially-distributed information on cutblock development through time, in conjunction with year of first landslide detection in the API inventory, reveals that landslide occurrences (and the associated sediment yield) in Tsitika-Eve describe a wave-like disturbance function. This function peaks 7-9 years after logging, hence declines steadily, and resets at undisturbed rates after 16-19 years since harvesting operations ceased. A similar time frame agrees with documented post-logging trend of total reinforcement by live and dead roots, which, in formerly glaciated settings of the Pacific Northwest coast, has been estimated to reach a minimum within 7-11 years after logging (e.g., Ziemer and Swanston, 1977; O'Loughlin and Ziemer, 1981; Sidle and Ochiai, 2006). The 19-year window for hillslope recovery matches results from previous inventory-based studies conducted elsewhere in coastal British Columbia (Brardinoni et al., 2003a), but it appears much shorter than the 31-35 years observed in a small (8.5 km^2) unglaciated mountain watershed of central Japan (Imaizumi et al., 2008). Such a discrepancy, may either have to do with the limited basin area examined, or reflect characteristic dynamics of regolith development and vegetation regrowth in a sub-tropical climatic context.

Across the 34 years of logging activity examined, this wave-like trend translates into increased landslide sediment yield. Increase is comparable on cutblocks and logging roads. Depending on the airphoto-year, logging effects on sediment yield range from no increase up to an 8-fold acceleration, in comparison to natural counterparts. These figures plot in the lower bound of previously documented, airphoto-based accelerations along the formerly glaciated coastal ranges of the Pacific Northwest (O'Loughlin, 1972; Fiksdal, 1974; Rood, 1984; Brardinoni et al., 2003a; Hassan et al., 2005), but agree with field-coupled, airphoto-based rates in selected tributary basins of the Capilano River (Brardinoni et al., 2003b).

Both clearcut and road-related landslide yields decrease systematically with time (**Figure 10c**). However, the trend of the former reverses, when logged area (over which landslide yield is computed) is adjusted for the 19-year time window (cf. white bars in **Figures 10c** and **10d**). While we attribute the sharp decline in road-related yield to a generalized improvement of road building techniques, in compliance with the British Columbia Forest Practices Code (1995) (see also Wolter et al., 2010), we explain the rising of clearcut-related yield (**Figure 10d**) with the increasingly steeper terrain that have been subject to timber harvesting from 1969 through 2003 (**Figure 2**).

5.2 Landscape structure, cutblock positioning and the size-frequency relation of shallow rapid failures

Considering the logistical challenges, the geometric assumptions and the uncertainties involved in the field-based estimation of landslide volumes, as obtained from the integration of landslide planform area and depth measurements (e.g., Guzzetti et al., 2009; Larsen et al., 2010), size-frequency analysis is typically regarded more reliable when performed on landslide areas (e.g., Hovius et al., 1997; Pelletier et al., 1997; Stark & Hovius, 2001; Guzzetti et al., 2002; Tanyas et al., 2019). Following the same logic and wishing to minimize uncertainty, in the next section we will limit our discussion to landslide length and area only.

Previous work concerned with the effects of forest harvesting on the size and frequency of shallow rapid failures has yielded contrasting results (e.g., Schwab, 1983; Swanston & Marion, 1991, Jakob, 2000; Martin et al., 2002). We hypothesize that these contrasts may reflect interactions between the variety of movement types (e.g., slides, avalanches, flows, and falls) embedded in a given landslide inventory, the way in which logging activities have approached different landscape components through time (i.e., historical spatial distribution of cutblocks), and the structure of the landscape under consideration. To some extent, this working hypothesis is corroborated by recent modelling efforts concerned with seismically-induced landslides, indicating that landscape structure, among other factors, can exert constraints on landslide size and frequency (e.g., Jeandet et al., 2019; Medwedeff et al., 2020).

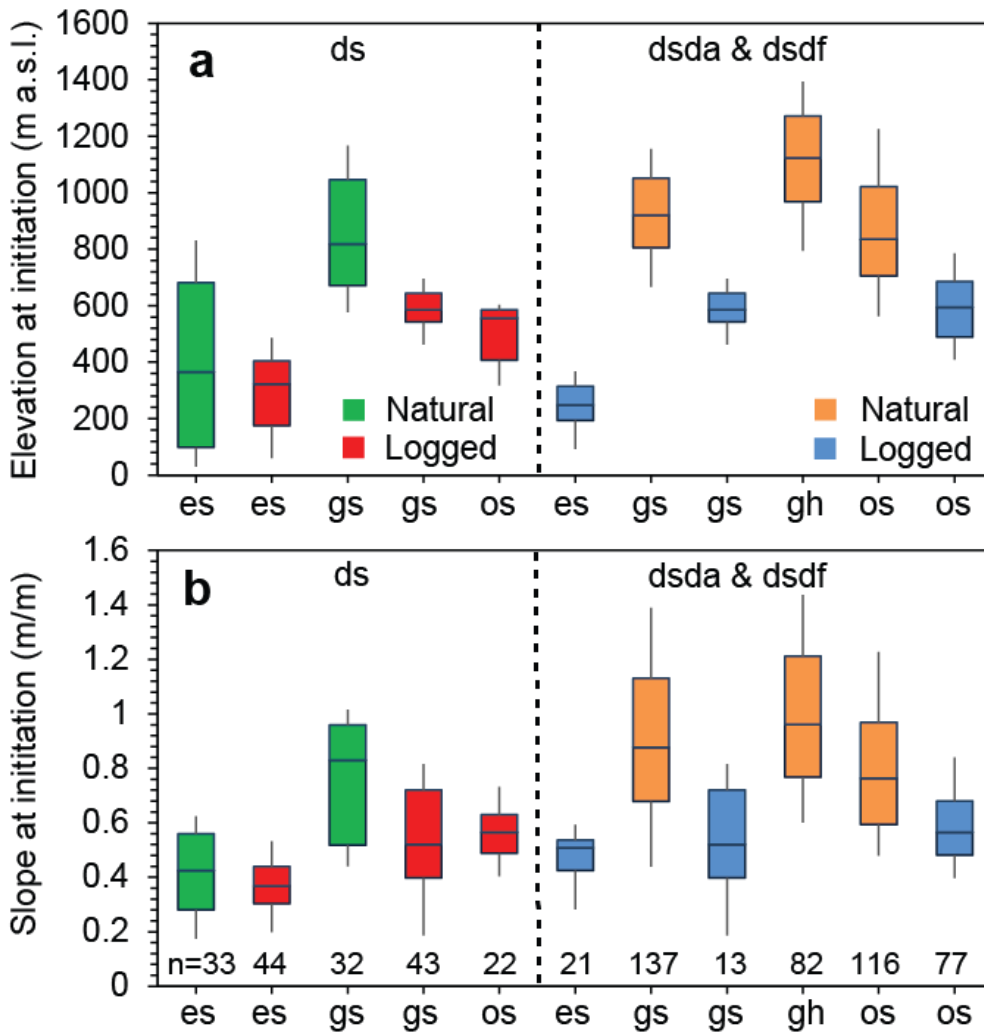


Figure 14. Boxplots of debris slides and long runout failures showing: (a) elevation at initiation; and (b) slope at initiation. All representations are stratified by morphologic position at initiation and land use. Boxes enclose interquartile ranges, whiskers span from 5% to 95%.

To identify possible morphometric controls that could explain differences in size-frequency relations observed across movement types and land uses (Figures 12 and 13), we expand our focus to the pristine, formerly glaciated landscape structure of the study basins and the positioning of cutblocks and logging roads on the valley walls. Preliminary analysis on morphologic position at landslide initiation have shown that this attribute could discriminate between small and large landslide occurrences (Figure 8b). Following this lead, we will explore linkages between landslide geometry (i.e., length and area), the spatial distribution of Quaternary surficial materials, and the topo-morphological characteristics of landslide initiation sites.

Indeed, data integration on landslide initiation, including elevation (Figure 14a) and slope gradient (Figure 14b) across morphologic positions and movement types, reveals contrasting topographic conditions in logged and natural settings. In natural forest, median elevations at initiation sit consistently above 800 m a.s.l. (Figure 14a), that is, in the mid-to-upper portions of valley walls and below the bedrock-dominated belt (e.g., Figures 15a and 15b). Logging-related landslides initiate at comparably lower elevations i.e., upper whiskers (95 percentile) plot below 800 m a.s.l. (Figure 14a), a value that roughly corresponds to the upper altitudinal limit

of cutblock and logging road development in the study basins: on the low-to-mid portions of the valley walls (e.g., **Figures 15c** and **15d**).

In view of the Tsitika and Eve morphometric landscape structure, where median slope increases with elevation (**Figure 2a**), higher elevation in natural forest means higher slope gradient at initiation (**Figure 14b**). It follows that, considering the same morphologic positions in unchannelled (i.e., open slope) and channelized (i.e., gully headwall and sidewall) conditions, we see that forest clearing tends to destabilize sites at lower elevations (hence at lower slope gradient), which naturally would not fail, or would fail less frequently (**Figure 14a**). In this context, debris slides (ds) originating at escarpments (Nf-es) are the exception and their altitudinal (hence slope) distribution largely overlaps that of logged counterparts (Lg-es) (**Figures 14a** and **14b**). This pattern is consistent with the spatial distribution of steep escarpment faces, which, in the postglacial landscape of coastal British Columbia occur along incisions carved into glacial and glaciofluvial valley fills in distal reaches of the main valley floors (e.g., **Figures 15e** and **15f**).

We argue that the location of cutblocks and logging roads on the slopes, in conjunction with a landscape structure composed of glacial troughs, adjoining oversteepened valley walls, hanging valleys and postglacial incisions of sedimentary fills, by exerting primary control on initiation site characteristics (i.e., elevation and slope gradient), impose heavy constraints on local relief (i.e., available energy), slope length, and therefore on potential maximum landslide length (**Figure 15**). Accordingly, open slope (os) and gully headwall (gh) initiations in natural forest, typically located at highest elevations (**Figures 14a, 15b** and **15d**), display much longer landslide lengths than escarpment (es) counterparts (see boxplots in **Figure 16a**), which have comparably less local relief available in both natural and logged conditions (**Figure 15f**). Similarly, gully sidewalls (gs), whose local relief is dictated by sidewall height (**Figure 2**), display shortest landslide lengths across movement types and land uses (see boxplots in **Figures 16a** and **16b**).

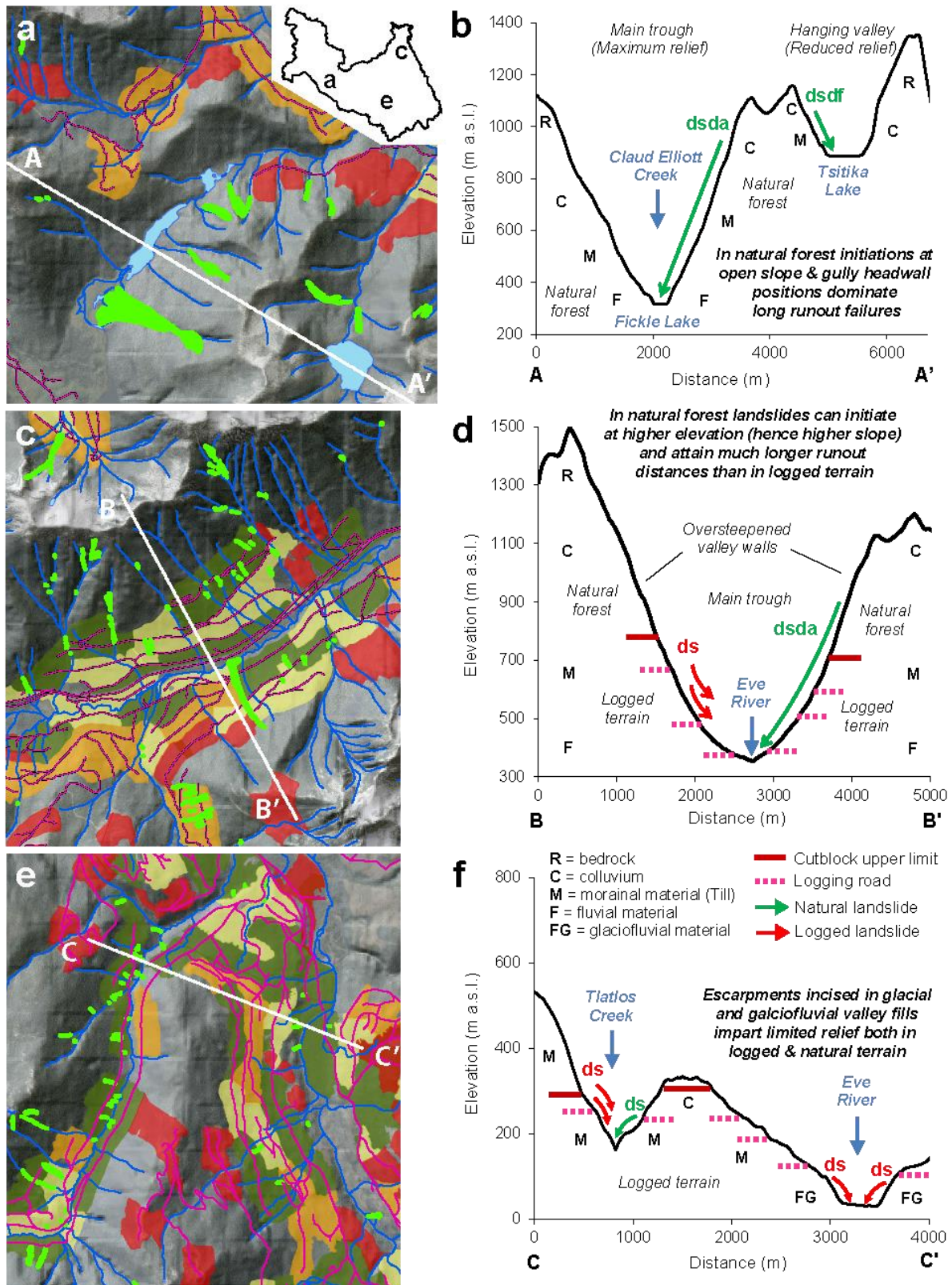


Figure 15. Plan views (panels a, c, e) and cross-sectional transects (panels b, d, f) of the Tsitika and Eve watersheds illustrating the spatial distribution of shallow rapid failures in relation to cutblock position and landscape structure. In the plan views, light green polygons indicate landslide tracks, purple linework indicate logging roads, and blue linework the main drainage network. Cutblock period of development include: 1969-79 (dark green), 1980-87 (yellow), 1988-94 (orange) and 1995-03 (red polygons). In cross-sectional transects, green and red arrows represent respectively natural and logging-related landslides. Panel a highlights how the length of long runout failures in natural forest is constrained by hillslope length (i.e., starting from the base of the bedrock belt, down to the valley floor). Panel c exemplifies how logging-related landslide length may be

limited by cutblock length (e.g., orange-shaded cutblock at panel bottom), as opposed to natural landslides triggered above the cutblock belt (e.g., landslide track running parallel to B-B' trace). Panel e shows that the limited length of landslides occurring at escarpments, in proximity of the main valley floors (e.g., Tlatlos Creek on mid to top left of panel), is constrained by the height of such incisions.

Overall, we observe that landslides originating at distinct morphologic positions characterize different portions of the length (**Figure 16a** and **16b**) and area (**Figures 16c** and **16d**) size-frequency domains. Specifically, open slopes (os) and gully headwalls (gh) occupy the high-magnitude spectrum (i.e., inverse power law), whereas gully sidewalls (gs), and to a lesser extent escarpments (es), populate the mid-to-low magnitude portions (i.e., direct power law), including the rollover zone. This morphologic transition at the rollover may reflect diverse instability thresholds within the landscape. Accordingly, larger thresholds would have to be crossed for triggering large debris avalanches on the valley walls or large debris flows at gully headwalls, compared to gully sidewall and escarpment positions, which may represent local adjustments to slope undercutting operated respectively by debris-flow scouring along gully channels and by fluvial lateral migration along stream channels.

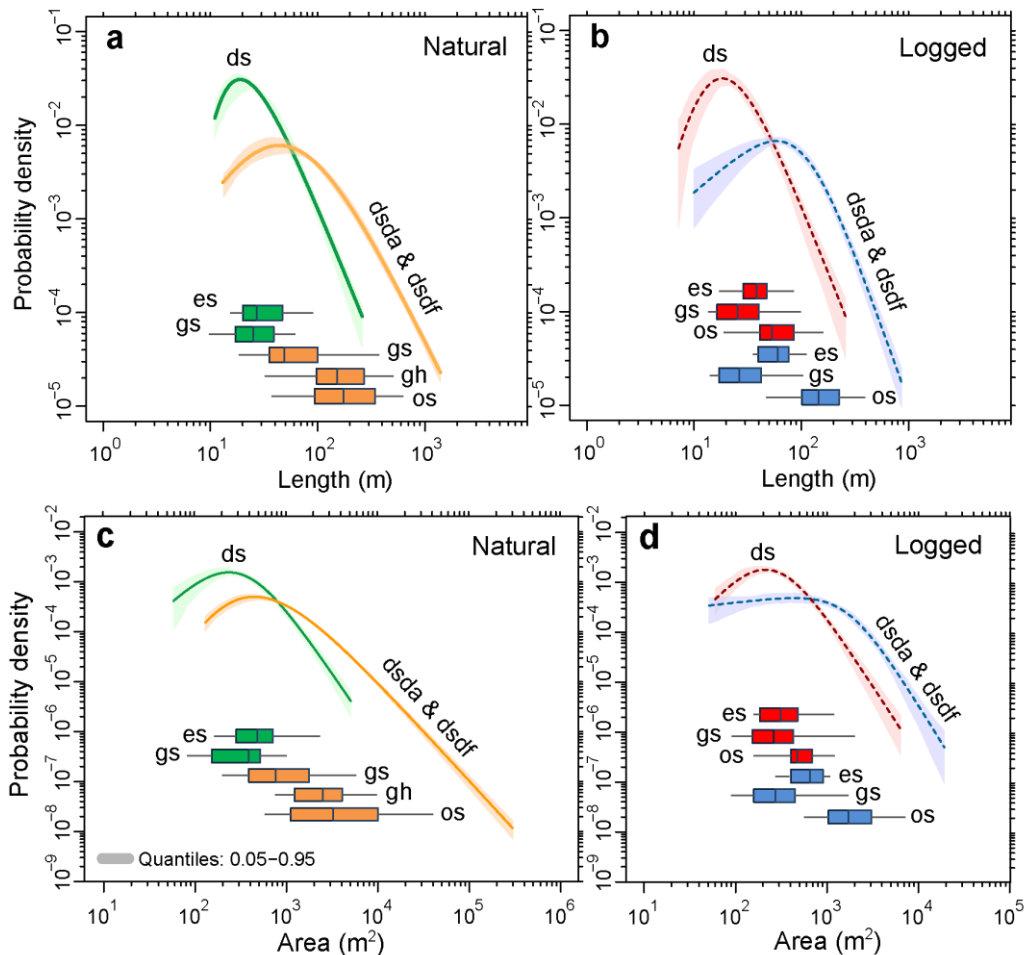


Figure 16. Probability density functions of API-based: (a) landslide lengths in natural forest; (b) landslide lengths in logged terrain; (c) landslide areas in natural forest; and (d) landslide areas in logged terrain. In each panel, probability density functions are stratified according to movement types including debris slides (ds) and long runout failures (dsda & dsdf). Probability density functions are shown in conjunction with the corresponding empirical distributions of landslide lengths (a, b) and areas (c, d), represented as boxplots and stratified by movement type and morphologic position at initiation. Boxes enclose interquartile ranges. Whiskers span from 5% to 95%.

Incidentally, both gully sidewall and escarpment positions are characterized by “low visibility” conditions (Brardinoni et al., 2003b, cf. their Figure 11), as they typically occur on steep slope faces: the former on narrow v-notched incisions, the latter at the slope base of fluvial gorges. For this reason, we argue that the shape and position of the rollover in **Figure 13**, which starts between 300 and 700 m², is influenced by undersampling (Stark & Hovius, 2001; Miller & Burnett, 2007), and as such depicts a minimum frequency scenario. This interpretation agrees with existing landslide visibility thresholds constrained for coastal British Columbia (Brardinoni et al., 2003b), which plot between the rollover and the point in which the PDF functions of our inventory start deviating from the negative power-law relation (**Figures 13a** and **13b**). Our interpretation about undersampling finds further support from documented rollover’s sensitivity to survey-type (the rollover of an API-based inventory shifts to smaller sizes when additional “not visible” landslides are added to the inventory i.e., Brardinoni & Church, 2004), and from recent work conducted in a 5-km² basin of New Zealand (Bernard et al., 2020). Although the question of coalescence between landslide scars may still apply, by differencing repeat LiDAR surveys conducted before and after an M_w 7.8 seismic event, the authors claim they could detect 1431 distinct landslides, and could fit a simple declining power-law relation for all slide sizes down to areas of 20 m².

In the study watersheds, the position of the rollover associated to landslide areas and lengths varies with movement type, but seems insensitive to land use for “simple” debris slides (**Figures 13b** and **13c**), where natural and logged rollovers virtually coincide (i.e., see overlap between interquartile ranges of bootstrap resampling in **Supplementary Table 1**). In the context of previous modelling efforts and interpretations that have explained the rollover as expression of the competition between friction- and cohesion-dominated landslides (e.g., Stark & Guzzetti, 2009; Frattini & Crosta, 2013; Jeandet et al., 2019), our empirically-based finding forms an element of surprise. In fact, the combination of lower visibility threshold and lower (inferred) root cohesion in logging-related debris slides should promote a rollover at smaller sizes compared to natural counterparts. Following this logic, in our inventory we do not observe a rollover dependence on (root) cohesion but we propose an alternative explanation linked to the topo-morphologic constraints of the failure sites, as indicated by classification of landslides by morphologic position at initiation (**Figure 16**).

Logging generates an ill-defined rollover on areas of long runout failures (**Figure 13b** and **16d**), the origin of which is difficult to explain, considering (i) that this landslide category includes unconfined debris avalanches and channelized debris flows; and (ii) the limited number of logging-related debris avalanches (n = 38; **Table 5** and **Figure 8a**).

The population of landslides that logging activities add to natural landsliding holds implications for hazard assessment (e.g., Rollerson et al., 2005). Assuming that larger size means a possible increase in the energy involved, hence in the destructiveness of a landslide, the effect of logging, as shown by the different percentile values in the cumulative probability representation (**Figure 13e**), tends to increase the number of small and less destructive failures. However, since post-logging hazard estimation - assuming it being dependent from landslide energy/destructiveness - should also account for the change in landslide initiation position; although

smaller, logging-related landslides initiate preferentially at lower elevations and slopes (**Figures 15a and 15b**), which in the study area, on average, means being closer to valley floors or within postglacial gorges. Consequently, these landslides have a high probability to enter fish-bearing streams and alter fish habitat conditions, when appropriate buffer zones are not implemented.

6. Conclusions

By combining historical data on cutblock development, field- and remotely-derived information on landslide geometry and occurrence -- controlled for movement type, as well as for morphologic position, elevation and slope gradient at initiation -- we link aspects of landslide response to forest harvesting. Accordingly, we show that logging activity on the formerly glaciated slopes of the Tsitika and Eve River basins does not affect significantly landslide depth, and consequently, the corresponding area-volume relation. Cutblock development and road construction introduce in the landscape an additional population of landslides, whose activity peaks after 7-9 years and resets to undisturbed rates 16-19 years since logging operations have stopped. Compared to natural forest, we find that logging promotes disproportionately higher landslide initiation at certain morphologic locations, including open slopes on valley sides and escarpment faces of incised postglacial valley floors.

The interaction between logging operations and the morphometry of the landscape, where slope gradient increases directly with elevation, holds a number of implications. Specifically, we show that landslide yield has increased through time, as cutblocks were developed at increasingly higher elevations. In this context, cutblock development, which normally occurs at relatively low slopes and elevations, generates distinctively shorter landslides in natural forest. This topographic constraint has virtually no effect on the size-frequency relation of debris slides, but limits drastically the size of long runout failures, such as debris avalanches and channelized debris flows.

Further landslide stratification by morphologic position at initiation is instructive. Our findings indicate that the rollover occurs at transitions among different morphologic positions at initiation (**Figure 16**), which in turn, may reflect different triggering thresholds and different geometric constraints to runout propagation, as set by the spatial organization of this formerly glaciated landscape. Specifically, the rollover may stem from the transition between primary (i.e., open slope and gully headwall) and secondary (i.e., gully sidewall and escarpment) occurrences. Following this logic, the former would be controlled by first-order valley wall geometry (i.e., length of regolith- or till-mantled hillslopes), the latter by the geometry of second-order features, such as incisions on the hillslopes (i.e., gully depth) and valley floors (i.e., escarpment depth) developed in glacial and deglacial sedimentary covers (**Figures 3 and 4**). Our results and interpretations suggest that future empirical and modelling efforts in glaciated and unglaciated settings should address the morphologic and topographic diversity at initiation associated with different shallow failure types across hillslopes and steep headwater streams.

Acknowledgements

S.P. was supported by a PhD scholarship funded by the Italian Ministry of University and Research. Data on landslide scar geometry were collected both in Eve (by Terry Rollerson in 1981) and Tsitika (by Denny Maynard in 1991). Additional field measurements were conducted in Tsitika in the summer of 2004 by F.B. Historical aerial photos, digital orthophotos, and land-use data were made available by Weyerhaeuser Ltd. Terrain stability mapping associated with surficial materials was conducted by Denny Maynard. The initial airphoto-based landslide identification and classification was conducted by Terry Rollerson. Sid Tsang and Heather Blyth helped with the compilation of the landslide inventory. Terry Rollerson and Danny Maynard were partly funded through the British Columbia Forest Investment Account. We thank Michael Church, Marwan Hassan, Olav Slaymaker and Colin Stark for thoughtful discussions on an earlier draft.

References

- Amaranthus, M. P., Rice, R. M., Barr, N. R., & Ziemer, R. R. (1985). Logging and Forest Roads to Increased Debris Slides in Southwestern Oregon. *Journal of Forestry*, 83(4), 229-233.
- Asdak, C., Jarvis, P. G., van Gardingen, P., & Fraser, A. (1998). Rainfall interception loss in unlogged and logged forest areas of Central Kalimantan, Indonesia. *Journal of Hydrology*, 206(3-4), 237-244. [https://doi.org/10.1016/S0022-1694\(98\)00108-5](https://doi.org/10.1016/S0022-1694(98)00108-5)
- Benda, L., & Dunne, T. (1997). Stochastic forcing of sediment supply to the channel network from landsliding and debris flow. *Water Resources Research*, 33(12), 2849-2863. <https://doi.org/10.1029/97WR02388>
- Benda, L. E., Miller, D. J., Dunne, T., Reeves, G. H., & Agee, J. K. (1998). Dynamic landscape systems. In R. J. Naiman, & R. E. Bilby (Eds.), *River Ecology and Management: Lessons from the Pacific Coastal Ecoregion* (pp. 261-288). New York: Springer-Verlag.
- Benda, L., Veldhuisen, C., & Black, J. (2003). Debris flows as agents of morphological heterogeneity at low-order confluences, Olympic Mountains, Washington. *Geological Society of America Bulletin*, 115(9), 1110–1121. <https://doi.org/10.1130/B25265.1>
- Bennett, G. L., Molnar, P., McArdeell, B. W., & Burlando, P. (2014). A probabilistic sediment cascade model of sediment transfer in the Illgraben. *Water Resources Research*, 50(2), 1225-1244. <https://doi.org/10.1002/2013WR013806>
- Bernard, T. G., Lague, D., & Steer, P. (2020). Beyond 2D inventories: synoptic 3D landslide volume calculation from repeat LiDAR data, *Earth Surface Dynamics Discussions* [preprint], <https://esurf.copernicus.org/preprints/esurf-2020-73/esurf-2020-73.pdf>
- Bovis, M. J., & Jakob, M. (1999). The role of debris supply conditions in predicting debris flow activity. *Earth Surface Processes and Landforms*, 24(11), 1039-1054. [https://doi.org/10.1002/\(SICI\)1096-9837\(199910\)24:11%3C1039::AID-ESP29%3E3.0.CO;2-U](https://doi.org/10.1002/(SICI)1096-9837(199910)24:11%3C1039::AID-ESP29%3E3.0.CO;2-U)
- Brardinoni, F. (2001). Identification of natural and logging-related landslides in the Capilano River basin (Coastal British Columbia): a comparison between remotely sensed survey and field survey (Master's

- thesis). Retrieved from UBC Library. (<https://dx.doi.org/10.14288/1.0090429>). Vancouver, British Columbia: Department of Geography, University of British Columbia.
- Brardinoni, F. (2006). Glacially-induced scaling relations in mountain drainage basins (Doctoral dissertation). Retrieved from UBC Library. (<https://dx.doi.org/10.14288/1.0092947>). Vancouver, British Columbia: Department of Geography, University of British Columbia.
- Brardinoni, F., & Church, M. (2004). Representing the landslide magnitude–frequency relation: Capilano River basin, British Columbia. *Earth Surface Processes and Landforms*, 29(1), 115-124. <https://doi.org/10.1002/esp.1029>
- Brardinoni, F., & Hassan, M. A. (2007). Glacially-induced organization of channel-reach morphology in mountain streams. *Journal of Geophysical Research*, 112, F03013. <https://doi.org/10.1029/2006JF000741>
- Brardinoni, F., Hassan, M. A., Rollerson, T., & Maynard, D. (2009). Colluvial sediment dynamics in mountain drainage basins. *Earth and Planetary Science Letters*, 284(3-4), 310-319. <https://doi.org/10.1016/j.epsl.2009.05.002>
- Brardinoni, F., Hassan, M. A., & Slaymaker, H. O. (2003a). Complex mass wasting response of drainage basins to forest management in coastal British Columbia. *Geomorphology*, 49(1-2), 109-124. [https://doi.org/10.1016/S0169-555X\(02\)00166-6](https://doi.org/10.1016/S0169-555X(02)00166-6)
- Brardinoni, F., Slaymaker, O., & Hassan, A. M. (2003b). Landslide inventory in a rugged forested watershed: a comparison between air-photo and field survey data. *Geomorphology*, 54(3-4), 179-196. [https://doi.org/10.1016/S0169-555X\(02\)00355-0](https://doi.org/10.1016/S0169-555X(02)00355-0)
- Brayshaw, D., & Hassan, M. A. (2009). Debris flow initiation and sediment recharge in gullies. *Geomorphology*, 109(3-4), 122-131. <https://doi.org/10.1016/j.geomorph.2009.02.021>
- British Columbia Government. (1995). *Forest Practices Code of British Columbia*. Victoria, British Columbia.
- Brummer, C. J., & Montgomery, D. R. (2003). Downstream coarsening in headwater channels. *Water Resources Research*, 39(10), 1294. <https://doi.org/10.1029/2003WR001981>
- Brunetti, M. T., Guzzetti, F., & Rossi, M. (2009). Probability distributions of landslide volumes. *Nonlinear Processes in Geophysics*, 16(2), 179–188. <https://doi.org/10.5194/npg-16-179-2009>
- Bunn, M., Leshchinsky, B., & Olsenc, M. J. (2020). Estimates of three-dimensional rupture surface geometry of deep-seated landslides using landslide inventories and high-resolution topographic data. *Geomorphology*, 367, 107332. <https://doi.org/10.1016/j.geomorph.2020.107332>
- Cislaghi, A., Chiaradia, E. A., & Bischetti, G. B. (2017). Including root reinforcement variability in a probabilistic 3D stability model. *Earth Surface Processes and Landforms*, 42(12), 1789-1806. <https://doi.org/10.1002/esp.4127>
- Corominas, J., & Moya, J. (2008). A review of assessing landslide frequency for hazard zoning purposes. *Engineering Geology*, 102(3-4), 193-213. <https://doi.org/10.1016/j.enggeo.2008.03.018>
- Cruden, D. M., & Vames, D. J. (1996). Landslide types and processes. In A. K Turner, & R. L. Schuster (Eds.),

- Landslides: Investigation and Mitigation. Transportation Research Board, Special Report 247 (pp. 36-75). Washington DC: National Research Council.
- Dietrich, W. E., & Dunne, T. (1978). Sediment budget for a small catchment in mountainous terrain. *Zeitschrift für Geomorphologie, Supplement*, 29, 191-206.
- Fan, X., Scaringi, G., Korup, O., West, A. J., van Westen, C. J., Tanyas, H., Hovius, N., Hales, T. C., Jibson, R. W., Allstadt, K. E., Zhang, L., Evans, S.G., Xu, C., Li, G., Pei, X., Xu, Q., & Huang, R. (2019). Earthquake-induced chains of geologic hazards: Patterns, mechanisms, and impacts. *Reviews of Geophysics*, 57(2), 421-503. <https://doi.org/10.1029/2018RG000626>
- Fiksdal, A. J. (1974). A landslide survey of the Stequaleho Creek watershed. Supplement to Final Report FRI-UW-7404. Seattle, WA: Fisheries Resources Institute, University of Washington.
- Fiorucci, F., Cardinali, M., Carlà, R., Rossi, M., Mondini, A. C., Santurri, L., Ardizzone, F., & Guzzetti, F. (2011). Seasonal landslide mapping and estimation of landslide mobilization rates using aerial and satellite images. *Geomorphology*, 129(1-2), 59-70. <https://doi.org/10.1016/j.geomorph.2011.01.013>
- Forbes, K., & Broadhead, J. (2013). Forests and landslides: The role of trees and forests in the prevention of landslides and rehabilitation of landslide-affected areas in Asia (RAP Publication No. 2013/02). Bangkok, Thailand: Food and Agriculture Organization of the United Nations, Regional Office for Asia and the Pacific. Retrieved from <http://www.fao.org/3/i3245e/i3245e.pdf>
- Fratini, P., & Crosta, G. B. (2013). The role of material properties and landscape morphology on landslide size distributions. *Earth and Planetary Science Letters*, 361, 310-319. <https://doi.org/10.1016/j.epsl.2012.10.029>
- Grant, G. E., & Swanson, F. J. (1995). Morphology and Processes of Valley Floors in Mountain Streams, Western Cascades, Oregon. In J. E. Costa, A. J. Miller, K.W. Potter, P.R. Wilcock (Eds.), *Natural and Anthropogenic Influences in Fluvial Geomorphology*, Geophysical Monograph Series (Vol. 89, pp. 83-101). Washington, DC: American Geophysical Union. <https://doi.org/10.1029/GM089p0083>
- Green, K. G., Brardinoni, F., & Alila, Y. (2013). Channel morphology and bed-load yield in fluvial, formerly-glaciated headwater streams of the Columbia Mountains, Canada. *Geomorphology*, 188, 96-109. <https://doi.org/10.1016/j.geomorph.2012.05.004>
- Guthrie, R. H. (2002). The effects of logging on frequency and distribution of landslides in three watersheds on Vancouver Island, British Columbia. *Geomorphology*, 43(3-4), 273-292. [https://doi.org/10.1016/S0169-555X\(01\)00138-6](https://doi.org/10.1016/S0169-555X(01)00138-6)
- Guthrie, R. H., & Evans, S. G. (2004). Analysis of landslide frequencies and characteristics in a natural system, coastal British Columbia. *Earth Surface Processes and Landforms*, 29(11), 1321-1339. <https://doi.org/10.1002/esp.1095>
- Guzzetti, F., Ardizzone, F., Cardinali, M., Rossi, M., & Valigi, D. (2009). Landslide volumes and landslide mobilization rates in Umbria, central Italy. *Earth and Planetary Science Letters*, 279(3-4), 222-229. <https://doi.org/10.1016/j.epsl.2009.01.005>

- Guzzetti, F., Malamud, B. D., Turcotte, D. L., & Reichenbach, P. (2002). Power-law correlations of landslide areas in central Italy. *Earth and Planetary Science Letters*, 195(3-4), 169–183. [https://doi.org/10.1016/S0012-821X\(01\)00589-1](https://doi.org/10.1016/S0012-821X(01)00589-1)
- Guzzetti, F., Reichenbach, P., Cardinali, M., Galli, M., & Ardizzone, F. (2005). Probabilistic landslide hazard assessment at the basin scale. *Geomorphology*, 72(1-4), 272-299. <https://doi.org/10.1016/j.geomorph.2005.06.002>
- Hassan, M. A., Church, M., Lisle, T. E., Brardinoni, F., Benda, L., & Grant, G. E. (2005). Sediment transport and channel morphology of small, forested streams. *Journal of the American Water Resources Association*, 41(4), 853-876. <https://doi.org/10.1111/j.1752-1688.2005.tb03774.x>
- Holland, S. S. (1964). Landforms of British Columbia, a Physiographic Outline. Bulletin, 48. Victoria, BC: British Columbia Geological Survey.
- Howes, D. E., & Kenk, E. (1997). Terrain classification system for British Columbia (Version 2). Victoria, BC: Recreational Fisheries Branch Ministry of Environment and Surveys and Resource Mapping Branch Ministry of Crown Lands.
- Hovius, N., Stark, C. P., & Allen, P. A. (1997). Sediment flux from a mountain belt derived by landslide mapping. *Geology*, 25(3), 231–234. [https://doi.org/10.1130/0091-7613\(1997\)025%3C0231:SFFAMB%3E2.3.CO;2](https://doi.org/10.1130/0091-7613(1997)025%3C0231:SFFAMB%3E2.3.CO;2)
- Hungr, O., (2005). Classification and terminology. In M. Jakob, & O. Hungr. (Eds.), *Debris–flow Hazard and Related Phenomena* (pp. 9-24). Berlin, Heidelberg: Springer Praxis
- Hungr, O., Evans, S. G., Bovis, M. J., & Hutchinson, J. N. (2001). A review of the classification of landslides of the flow type. *Environmental and Engineering Geoscience*, 7(3), 221–238. <https://doi.org/10.2113/gseegeosci.7.3.221>
- Hungr, O., Evans, S. G., & Hazzard, J. (1999). Magnitude and frequency of rock falls and rock slides along the main transportation corridors of southwestern British Columbia. *Canadian Geotechnical Journal*, 36(2), 224–238. <https://doi.org/10.1139/t98-106>
- Hungr, O., McDougall, S., Wise, M., & Cullen, M. (2008). Magnitude–frequency relationships of debris flows and debris avalanches in relation to relief. *Geomorphology*, 96(3-4), 355–365. <https://doi.org/10.1016/j.geomorph.2007.03.020>
- Imaizumi, F., Sidle, R. C., & Kamei, R. (2008). Effects of forest harvesting on the occurrence of landslides and debris flows in steep terrain of central Japan. *Earth Surface Processes and Landforms*, 33(6), 827-840. <https://doi.org/10.1002/esp.1574>
- Jakob, M. (2000). The impacts of logging on landslide activity at Clayoquot Sound, British Columbia. *Catena*, 38(4), 279-300. [https://doi.org/10.1016/S0341-8162\(99\)00078-8](https://doi.org/10.1016/S0341-8162(99)00078-8)
- Jakob, M., Bovis, M., & Oden, M. (2005). The significance of channel recharge rates for estimating debris-flow magnitude and frequency. *Earth Surface Processes and Landforms*, 30(6), 755-766. <https://doi.org/10.1002/esp.1188>

- Jeandet, L., Steer, P., Lague, D., Davy, P., 2019. Coulomb mechanics and relief constraints explain landslide size distribution. *Geophysical Research Letters*, 46, 4258–4266.
- Johnson, A. C., Swanston, D. N., & McGee, K. E. (2000). Landslide initiation, runout, and deposition within clearcuts and old-growth forests of Alaska. *Journal of the American Water Resources Association*, 36(1), 17-30. <https://doi.org/10.1111/j.1752-1688.2000.tb04245.x>
- Jordan, P., Millard, T. H., Campbell, D., Schwab, J. W. Wilford, D. J., Nicol, D., & Collins, D. (2010). Forest Management Effects on Hillslope Processes. In R. G. Pike, T. E. Redding, R. D. Moore, R. D. Winker, K. D. Bladon (Eds), *Compendium of forest hydrology and geomorphology in British Columbia, Land Management Handbook* (Vol. 66, pp. 275-329). British Columbia Ministry of Forests and Range, Forest Science Program, Victoria, B.C. and FORREX Forum for Research and Extension in Natural Resources, Kamloops, BC.
- Kolmogoroff, A. (1933). *Grundbegriffe der wahrscheinlichkeitsrechnung* (Vol. 2). Springer-Verlag. 62 p. doi <https://doi.org/10.1007/978-3-642-49888-6>
- Koyanagi, K., Gomi, T., & Sidle, R. C. (2020). Characteristics of landslides in forests and grasslands triggered by the 2016 Kumamoto earthquake. *Earth Surface Processes and Landforms*, 45(4), 893-904. <https://doi.org/10.1002/esp.4781>
- Krajina, V. J. (1969). Ecology of forest trees in British Columbia. *Ecology of Western North America*. (Vol. 2 No. 1). Vancouver, Canada: Department of Botany, University of British Columbia.
- Lancaster, S.T., & Casebeer, N.E. (2007). Sediment storage and evacuation in headwater valleys at the transition between debris-flow and fluvial processes. *Geology*, 35(11): 1027–1030. <https://doi.org/10.1130/G239365A.1>
- Larsen, I. J, Montgomery, D. R., & Korup, O., (2010). Landslide erosion controlled by hillslope material. *Nature Geoscience*, 3, 247-251. <http://www.nature.com/doi/10.1038/ngeo776>
- Malamud, B. D., Turcotte, D. L., Guzzetti, F., & Reichenbach, P. (2004). Landslide inventories and their statistical properties. *Earth Surface Processes and Landforms*, 29(6), 687-711. <https://doi.org/10.1002/esp.1064>
- Marion, D. A. (1981). Landslide occurrence in the Blue River drainage, Oregon (Master's thesis). Retrieved from Scholars Archive, Oregon State University. (https://ir.library.oregonstate.edu/concern/graduate_thesis_or_dissertations/rf55zd19w). Corvallis, OR: Department of Geography, Oregon State University.
- Martin, Y., Rood, K., Schwab, J. W., & Church, M. (2002). Sediment transfer by shallow landsliding in the Queen Charlotte Islands, British Columbia. *Canadian Journal of Earth Sciences*, 39(2), 189-205. <https://doi.org/10.1139/e01-068>
- May, C. L., & Gresswell, R. E. (2003). Processes and rates of sediment and wood accumulation in headwater streams of the Oregon Coast Range, USA. *Earth Surface Processes and Landforms*, 28(4), 409-424. <https://doi.org/10.1002/esp.450>

- McEachran, Z. P., Karwan, D.L., & Slesak, R. A. (2020). Direct and Indirect Effects of Forest Harvesting on Sediment Yield in Forested Watersheds of the United States. *Journal of the American Water Resources Association*, 57(1), 1-31. <https://doi.org/10.1111/1752-1688.12895>
- Medwedeff, W.G., Clark, M.K., Zekkos, D., & West, J. (2020). Characteristic landslide distributions: An investigation of landscape controls on landslide size. *Earth and Planetary Science Letters*, 539, 116203. <https://doi.org/10.1016/j.epsl.2020.116203>
- Meidinger, D., & Pojar, J. (1991). *Ecosystems of British Columbia*. Special Report Series, 06. British Columbia: BC Ministry of Forests.
- Melzner, S., Rossi, M., & Guzzetti, F. (2020). Impact of mapping strategies on rockfall frequency-size distributions. *Engineering Geology*, 272, 105639. <https://doi.org/10.1016/j.enggeo.2020.105639>
- Milledge, D. G., Bellugi, D., McKean, J. A., Densmore, A. L., & Dietrich, W. E. (2014). A multidimensional stability model for predicting shallow landslide size and shape across landscapes. *Journal of Geophysical Research: Earth Surface*, 119(11), 2481–2504. <https://doi.org/10.1002/2014JF003135>
- Miller, D. J., & Burnett, K. M. (2007). Effects of forest cover, topography, and sampling extent on the measured density of shallow, translational landslides. *Water Resources Research*, 43(3), W03433. <https://doi.org/10.1029/2005WR004807>
- Montgomery, D.R. (1994). Road surface drainage, channel initiation, and slope instability. *Water Resources Research*, 30(6), 1925-1932. <https://doi.org/10.1029/94WR00538>
- Montgomery, D. R., Massong, T. M., & Hawley, S. C. S. (2003). Influence of debris flows and log jams on the location of pools and alluvial channel reaches, Oregon Coast Range. *Geological Society of America Bulletin*, 115(1): 78–88. [https://doi.org/10.1130/0016-7606\(2003\)115<0078:IODFAL>2.0.CO;2](https://doi.org/10.1130/0016-7606(2003)115<0078:IODFAL>2.0.CO;2)
- Montgomery, D. R., Schmidt, K. M., Greenberg, H. M., & Dietrich, W. E. (2000). Forest clearing and regional landsliding. *Geology*, 28(4), 311-314. [https://doi.org/10.1130/0091-7613\(2000\)28%3C311:FCARL%3E2.0.CO;2](https://doi.org/10.1130/0091-7613(2000)28%3C311:FCARL%3E2.0.CO;2)
- Morrison, P. H. (1975). *Ecological and geomorphological consequences of mass movements in the Alder Creek watershed and implications for forest land management* (Bachelor's thesis). Eugene, OR: University of Oregon.
- Muller, J. E., Northcote, K. E., & Carlisle, D. (1974). *Geology and mineral deposits of Alert Bay-Cape Scott map Area, Vancouver Island, British Columbia*. Geological Survey of Canada. (Paper 74-8). <https://doi.org/10.4095/102543>
- Nakamura, F., Swanson, F. J., & Wondzell, S. M. (2000). Disturbance regimes and riparian systems – a disturbance-cascade perspective. *Hydrological Processes*, 14(16-17), 2849-2860. [https://doi.org/10.1002/1099-1085\(200011/12\)14:16/17%3C2849::AID-HYP123%3E3.0.CO;2-X](https://doi.org/10.1002/1099-1085(200011/12)14:16/17%3C2849::AID-HYP123%3E3.0.CO;2-X)
- O'Loughlin, C. L. (1972). *An investigation of the slope stability of the steep-land forest soils in the coast mountains, southwest British Columbia* (Doctoral dissertation). Retrieved from UBC Library.

- (<https://dx.doi.org/10.14288/1.0101126>). Vancouver, British Columbia: Department of Forestry, University of British Columbia.
- O'Loughlin, C.L., & Ziemer, R.R. (1982). The importance of root strength and deterioration rates upon edaphic stability in steepland forests. In *Carbon Uptake and Allocation in Subalpine Ecosystems as a Key to Management*, pp.70-78. Proceedings of a IUFRO Workshop, Aug. 2-3, 1982, Oregon State University, Corvallis.
- Pelletier, J. D., Malamud, B. D., Blodgett, T., & Turcotte, D. L. (1997). Scale-invariance of soil moisture variability and its implications for the frequency-size distribution of landslides. *Engineering Geology*, 48(3-4), 255–268. [https://doi.org/10.1016/S0013-7952\(97\)00041-0](https://doi.org/10.1016/S0013-7952(97)00041-0)
- Pyles, M. R., & Froehlich, H. A. (1987). Discussion and Replay: Rates of Landsliding as Impacted by Timber Management Activities in Northwestern California. *Environmental and Engineering Geoscience*, 24 (3), 425-431. <https://doi.org/10.2113/gseegeosci.xxiv.3.425>
- R Core Team (2016). R: A language and environment for statistical computing. Vienna, Austria: R Foundation for Statistical Computing. URL <https://www.r-project.org/>
- Reid, L. M., & Dunne, T. (1984). Sediment production from forest road surfaces. *Water Resources Research*, 20(11), 1753-1761. <https://doi.org/10.1029/WR020i011p01753>
- Reid, L. M., & Dunne, T. (1996). *Rapid Evaluation of Sediment Budgets*. Reiskirchen, Germany: Catena Verlag.
- Reid, L. M., & Lewis, J. (2009). Rates, timing, and mechanisms of rainfall interception loss in a coastal redwood forest. *Journal of Hydrology*, 375(3-4), 459-470. <https://doi.org/10.1016/j.jhydrol.2009.06.048>
- Rickli, C., & Graf, F. (2009). Effects of forests on shallow landslides– case studies in Switzerland. *Forest Snow and Landscape Research*, 82(1), 33-44.
- Roberts, R. G., & Church, M. (1986). The sediment budget in severely disturbed watersheds, Queen Charlotte Ranges, British Columbia. *Canadian Journal of Forest Research*, 16(5), 1092-1106. <https://cdnsiencepub.com/doi/10.1139/x86-189>
- Rollerson, T., Maynard, D., Higman, S., & Ortmayr, E. (2005). Phillips River Landslide Hazard Mapping Project. In: *Landslide Risk Management – Hungr, O., R. Fell, R. Couture, and E. Eberhardt (eds)*. 2005. Taylor & Francis Group, London.
- Rood, K. M. (1984). An Aerial Photograph Inventory of the Frequency and Yield of Mass Wasting on the Queen Charlotte Islands, British Columbia. Land Management Report. (Vol. 34). Victoria, Canada: BC Ministry of Forests.
- Rood, K. M. (1990). Site characteristics and landsliding in forested and clearcut terrain, Queen Charlotte Islands, British Columbia. Land Management Report. (Vol. 64). Victoria, Canada: BC Ministry of Forests.
- Rossi, M. (2014). D. 5.3. R Code for Prototype Software for Landslide Statistics (LSTATS). Deliverable of Lampre Project accessible at <http://www.lampre->

project.eu/index.php?option=com_phocadownload%20&view=category&id=6:wp5-triggered-event-landslides&Itemid=203

- Rossi, M., Cardinali, M., Fiorucci, F., Marchesini, I., Mondini, A. C., Santangelo, M., Ghosh, S., Riguer, D. E. L., Lahousse, T., Chang, K. T., & Guzzetti, F. (2012). A tool for the estimation of the distribution of landslide area in R. EGU General Assembly Conference Abstracts, 14, 9438.
- Rossi, M., & Malamud, B. D. (2014). D. 5.3. Report on Prototype SW for determination of landslide statistics from inventory maps (LSTATS). Deliverable of Lampre Project accessible at http://www.lampre-project.eu/index.php?option=com_phocadownload&view=category&id=6:wp5-triggered-event-landslides&Itemid=203
- Schmidt, K. M., Roering, J. J., Stock, J. D., Dietrich, W. E., Montgomery, D.R., & Schaub T. (2001). The variability of root cohesion as an influence on shallow landslide susceptibility in the Oregon Coast Range. *Canadian Geotechnical Journal*, 38(5), 995–1024. <https://doi.org/10.1139/t01-031>
- Schmitt, R. J. P., Bizzi, S., & Castelletti, A. (2016). Tracking multiple sediment cascades at the river network scale identifies controls and emerging patterns of sediment connectivity. *Water Resources Research*, 52(5), 3941–3965. <https://doi.org/10.1002/2015WR018097>
- Schwab, J. W. (1983). Mass wasting: October-November 1978 storm, Rennell Sound, Queen Charlotte Islands, British Columbia. Research Note. (Vol. 91). Victoria, Canada: BC Ministry of Forests.
- Sidle, R. C., & Bogaard, T. A. (2016). Dynamic earth system and ecological controls of rainfall-initiated landslides. *Earth-Science Reviews*, 159, 275–291. <https://doi.org/10.1016/j.earscirev.2016.05.013>
- Sidle, R. C., & Ochiai, H. (2006). *Landslides Processes, Prediction, and Land Use*. Water Resources Monograph Series. (Vol. 18). Washington DC, USA: American Geophysical Union.
- Sidle, R. C., Pearce, A. J., & O’Loughlin, C.L. (1985). *Hillslope stability and land use*. Water Resources Monograph Series. (Vol. 11). Washington DC, USA: American Geophysical Union.
- Smith, R.B., Commandeur, P. R., & Ryan, M. W., (1986). Soils, vegetation, and forest growth on landslides and surrounding logged and old-growth areas on the Queen Charlotte Islands. Land Management Report. (Vol. 41) Victoria, Canada: BC Ministry of Forests.
- Smirnov, N. V. (1939). Estimate of deviation between empirical distribution functions in two independent samples. *Bulletin Moscow University*, 2(2), 3-16.
- Stark, C. P., & Guzzetti, F. (2009). Landslide rupture and the probability distribution of mobilized debris volumes. *Journal of Geophysical Research*, 114, F00A02. <https://doi.org/10.1029/2008JF001008>
- Stark, C. P. & Hovius, N. (2001). The characterization of landslide size distributions. *Geophysical Research Letters*, 28(6), 1091–1094. <https://doi.org/10.1029/2000GL008527>
- Swanson, F. J., & Dyrness, C. T. (1975). Impact of clear-cutting and road construction on soil erosion by landslides in the western Cascade Range, Oregon. *Geology*, 3(7), 393-396. [https://doi.org/10.1130/0091-7613\(1975\)3%3C393:IOCARC%3E2.0.CO;2](https://doi.org/10.1130/0091-7613(1975)3%3C393:IOCARC%3E2.0.CO;2)

- Swanson, F. J., & Swanson, M. M. (1977). Inventory of Mass Erosion in the Mapleton Ranger District, Siuslaw National Forest (Final Report). Corvallis, Oregon: Siuslaw National Forest and Pacific Northwest Forest and Range Experiment Station.
- Swanson, F.J., Janda, R.J., Dunne, T., & Swanston, D. N. (1982). Sediment budgets and routing in forested drainage basins, U.S.D.A. Forest Service, Pacific Northwest Forest and Range Experiment Station. General Technical Report, PNW-141, 165 pp.
- Swanston, D. N., & Marion, D. A. (1991). Landslide response to timber harvest in southeast Alaska. Proceedings of the Fifth Federal Interagency Sedimentation Conference, 2, 10.49-10.56.
- Swanston, D. N., & Swanson, F. J. (1976). Timber harvesting, mass erosion, and steepland forest geomorphology in the Pacific Northwest. In D.R. Coates (Eds), *Geomorphology and Engineering* (pp. 199-221). Stroudsburg, Pennsylvania: Dowden, Hutchinson & Ross, Inc.
- Tanyas, H., van Westen, C. J., Allstadt, K. E., & Jibson, R. W. (2019). Factors controlling landslide frequency–area distributions. *Earth Surface Processes and Landforms*, 44(4), 900-917. <https://doi.org/10.1002/esp.4543>
- Tsukamoto, Y. (1973). Study on the growth of stream channel (I). Relationship between stream channel growth and landslides occurring during heavy storm. *Shin sabo*, 25, 4-13 (in Japanese). https://doi.org/10.11475/sabo1948.25.4_4
- Turner, T. R., Duke, S. D., Fransen, B. R., Reiter, M. L., Kroll, A. J., Ward, J. W., Bach, J. L., Justice, T. E., & Bilby, R. E. (2010). Landslide densities associated with rainfall, stand age, and topography on forested landscapes, southwestern Washington, USA. *Forest Ecology and Management*, 259(12), 2233-2247. <https://doi.org/10.1016/j.foreco.2010.01.051>
- Van Den Eeckhaut, M., Poesen, J., Verstraeten, G., Vanacker, V., Nyssen, J., Moeyersons, J., van Beek, L. P. H., & Vandekerckhove, L. (2007). Use of LIDAR-derived images for mapping old landslides under forest. *Earth Surface Processes and Landforms*, 32(5), 754-769. <https://doi.org/10.1002/esp.1417>
- Winkler, R. D., Moore, R. D., Redding, T. E., Spittlehouse, D. L., Smerdon, B. D., & Carlyle-Moses, D. E. (2010). The Effects of Forest Disturbance on Hydrologic Processes and Watershed Response. In R. G. Pike, T. E. Redding, R. D. Moore, R. D. Winker, K. D. Bladon (Eds), *Compendium of forest hydrology and geomorphology in British Columbia, Land Management Handbook* (Vol. 66, pp. 179-212). British Columbia Ministry of Forests and Range, Forest Science Program, Victoria, B.C. and FORREX Forum for Research and Extension in Natural Resources, Kamloops, B.C.
- Wise, M. P. (1997). Probabilistic Modelling of Debris Flow Travel Distance Using Empirical Volumetric Relationships (Master's thesis). Retrieved from UBC Library. (<https://dx.doi.org/10.14288/1.0050298>). Vancouver, British Columbia: Department of Civil Engineering, University of British Columbia.
- Wolter, A., Ward, B., & Millard, T. (2010). Instability in eight sub-basins of the Chilliwack River Valley, British Columbia, Canada: A comparison of natural and logging-related landslides. *Geomorphology*, 120(3-4), 123-132. <https://doi.org/10.1016/j.geomorph.2010.03.008>

- Zeng, Z., Estes, L., Ziegler, A. D., Chen, A., Searchinger, T., Hua, F., Guan, K., Jintrawet, A., & Wood, E. F. (2018). Highland cropland expansion and forest loss in Southeast Asia in the twenty-first century. *Nature Geoscience*, 11, 556–562. <https://doi.org/10.1038/s41561-018-0166-9>
- Ziemer, R. R. (1981). The role of vegetation in the stability of forested slopes. *Proceedings of the International Union of Forestry Research Organizations, XVII World Congress*, 1, 297-308.
- Ziemer, R. R., & Swanston, D. N. (1977). Root strength changes after logging in southeast Alaska. *Research Note PNW-306*. Portland, Oregon: USDA Forest Service, Pacific Northwest Forest and Range Experiment Station.

Tables

Table 1. Land-use history in Tsitika and Eve watersheds.

Land use (km ²)	Time period				
	1961-68	1969-77	1978-87	1988-94	1995-03
Newly logged area	0.0	30.2	42.5	34.1	48.2
Cumulative logged area	0.0	30.2	72.7	106.8	155.0
Active logged area*	0.0	30.2	72.7	76.6	82.3
Natural area	612.1	575.3	539.4	505.3	457.1

* Area logged within the time period necessary for post-logging recovery (i.e., 18-25 years).

Table 2. Summary of land use and movement type classes adopted for analyses conducted on field and API landslide data. Different data grouping across analyses aimed at achieving a minimum representative number of observations per class.

Data	Landslide variable	Analysis	Land-use classes	Movement type classes
Field	Depth	Descriptive statistics	Natural forest (nf)	Debris slides (ds)
	Width	Simple pairwise correlation	Logged (cc & rd)	Long runout (dsda & dsdf)
	Length	Univariate boxplots		
	Area	Depth-based power-law fitting		
	Area	Power-law fitting	Natural forest (nf)	Debris slides (ds)
	Volume		Logged (cc & rd)	Long runout (dsda & dsdf)
	Volume	Univariate boxplots	Natural forest (nf)	Debris slides (ds)
Air-photo Interpretation	No. of occurrences	Post-logging recovery	Clearcut (cc)	No stratification
	Volume			
	Landslide density	Temporal response	Natural (nf)	No stratification
	Landslide yield		Clearcut (cc)	
			Logged (rd)	
	Volume	Univariate boxplots	Natural (nf)	Debris slides (ds)
			Logged (cc & rd)	Long runout (dsda & dsdf)
Area	Magnitude-frequency analysis	Natural (nf)	Debris slides (ds)	
Volume		Logged (cc & rd)	Long runout (dsda & dsdf)	

Table 3. Descriptive statistics on landslide depth across land use (natural and logged) and movement type (debris slides, debris avalanches and debris flows) classes.

	All	ds		dsdf		dsda & dsdf	
		Natural	Logged	Natural	Logged	Natural	Logged
Median	0.50	0.50	0.45	1	1	1	1
Mean	0.81	0.78	0.52	1.53	1.17	1.46	1.12
Std Err	0.06	0.13	0.04	0.34	0.13	0.30	0.11
Mode	0.50	0.50	0.30	1	1.50	1	1
Std Dev	0.68	0.64	0.32	1.23	0.55	1.17	0.52
Min	0.20	0.30	0.20	0.50	0.50	0.50	0.50
Max	5	3	2	5	2.5	5	2.5
Number of obs.	113	25	52	13	17	15	21

Table 4. Spearman's pairwise correlation coefficients of landslide depth, width, length, and area, as measured in the field. Area is given by the width by length product. Coefficients > 0.6 are indicated in bold.

ds-Natural (n=25)	Depth	Width	Length	Area
Depth	1.000	0.443	0.119	0.0677
Width	-	1.000	0.684	0.682
Length	-	-	1.000	0.979
Area	-	-	-	1.000
ds-Logged (n=52)	Depth	Width	Length	Area
Depth	1.000	0.409	0.465	0.426
Width	-	1.000	0.407	0.928
Length	-	-	1.000	0.638
Area	-	-	-	1.000
dsda & dsdf-Natural (n=15)	Depth	Width	Length	Area
Depth	1.000	0.291	-0.0914	-0.0307
Width	-	1.000	0.654	0.846
Length	-	-	1.000	0.903
Area	-	-	-	1.000
dsda & dsdf-Logged (n=21)	Depth	Width	Length	Area
Depth	1.000	-0.0425	-0.109	-0.101
Width	-	1.000	0.398	0.914
Length	-	-	1.000	0.643
Area	-	-	-	1.000

Table 5. Number of debris mobilizing mass movements mapped via aerial photo interpretation, stratified by movement type and land-use at initiation point. The corresponding estimated volumes of mobilized debris in cubic meters are reported in brackets.

Movement type	Debris slides	Debris flows	Debris avalanches
	(ds)	(dsdf)	(dsda)
Natural (1930-2003)	73	308	37
(Volume – m ³)	(50,240)	(1,144,910)	(1,765,580)
Clearcut (1969-2003)	92	66	21
(Volume – m ³)	(37,980)	(71,950)	(54,200)
Road (1969-2003)	17	16	17
(Volume – m ³)	(15,830)	(52,090)	(64,250)
Logged (1969-2003)	109	82	38
(Volume – m ³)	(53,810)	(124,040)	(118,450)
Total	182	390	75
(Volume - m ³)	(104,050)	(1,268,950)	(1,884,030)

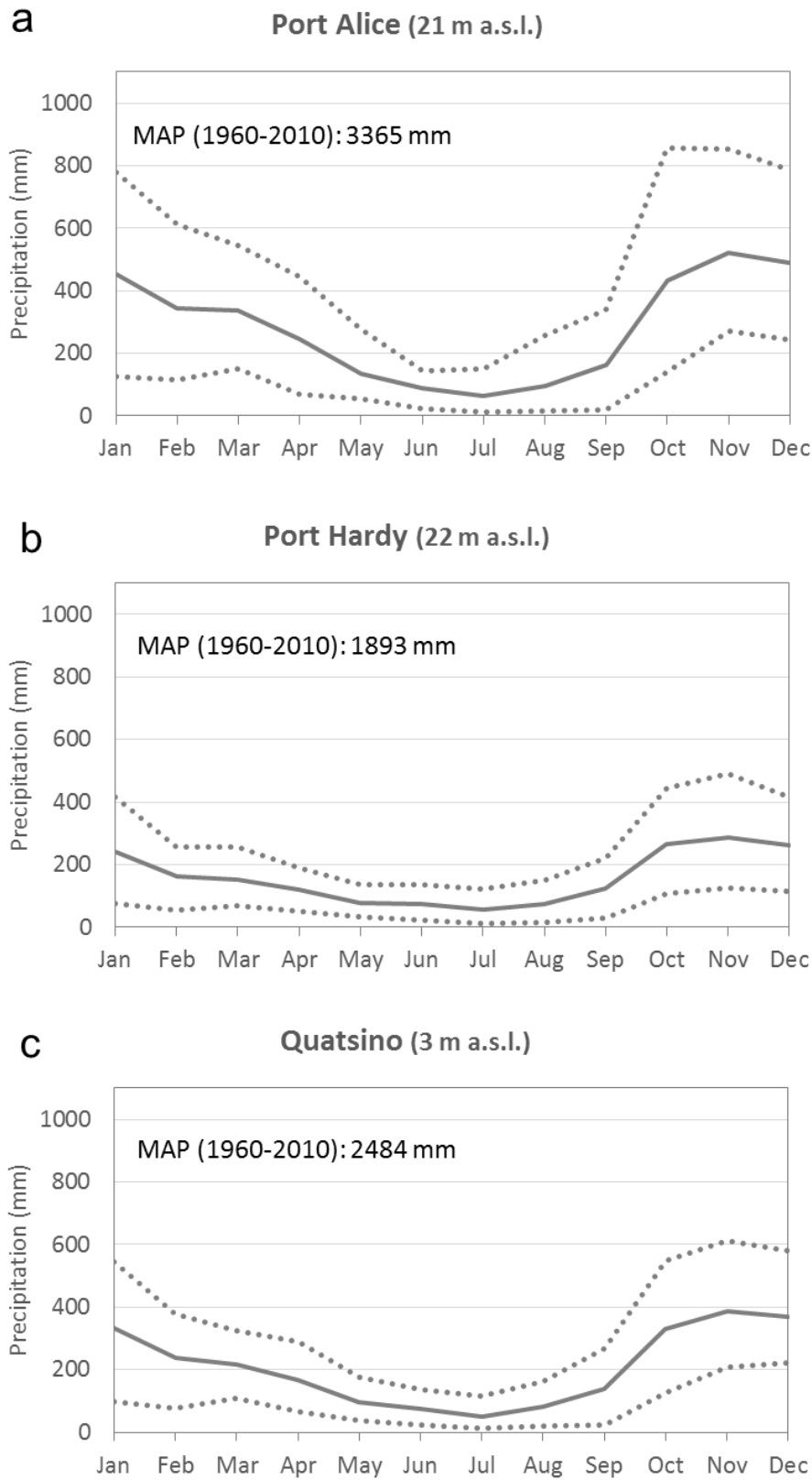
Table 6. Number of occurrences (n) and corresponding mobilized volumes of shallow landslides (expressed in cubic meters) mapped via aerial photo interpretation, stratified by morphologic position at initiation, movement types and land use. Corresponding percent values are reported in brackets.

Movement type & land use		Morphologic position at initiation					Combined
		es	gs	gh	os	others	
ds -Natural	n (%)	33 (45.2)	32 (43.8)	1 (1.4)	6 (8.2)	1 (1.4)	73
	m ³	25,390	12,750	740	11,200	160	50,240
ds -Logged	n (%)	44 (40.4)	43 (39.4)	-	22 (20.2)	-	109
	m ³	16,420	21,870	-	15,520	-	53,810
dsda & dsdf -Natural	n (%)	6 (1.7)	137 (39.7)	82 (23.8)	116 (33.6)	4 (1.2)	345
	m ³	20,010	256,990	362,660	2,252,070	18,760	2,910,490
dsda & dsdf -Logged	n (%)	21 (17.5)	13 (10.8)	9 (7.5)	77 (64.2)	-	120
	m ³	10,680	2,200	11,160	218,450	-	242,490

Table 7. Parameters of Double Pareto Simplified distribution and related test statistics obtained for landslide areas in Tsitika and Eve watersheds. The following significance codes rank the significance of the parameters, from highly to not significant; [*****] = p-value < 0.001, [****] = p-value < 0.01, [***] = p-value < 0.05, [**] = p-value < 0.1, [*] = p-value ≥ 0.1.

Figure	Stratification	DPS Distribution parameters					KS test	
		Parameter	Estimate	Standard Error	p-value	Significance		
13a	Natural	Alpha	0.98	0.06	< 0.0001	*****	D	0.056
		Beta	4.33	1.89	0.02	***		
		t	196	129	0.13	*	p-value	0.55
		Rollover	330	na	na	na		
	Logged	Alpha	1.41	0.13	< 0.0001	*****	D	0.09
		Beta	1.89	0.38	< 0.0001	*****		
		t	465	137	0.0007	*****	p-value	0.31
		Rollover	230	na	na	na		
13b	ds Natural	Alpha	1.71	0.29	< 0.0001	*****	D	0.110
		Beta	2.78	1.16	0.01	***		
		t	303	146	0.03	***	p-value	0.78
		Rollover	240	na	na	na		
	ds Logged	Alpha	1.82	0.28	< 0.0001	*****	D	0.081
		Beta	3.13	1.27	0.01	***		
		t	245	107	0.02	***	p-value	0.80
		Rollover	210	na	na	na		
	dsda & dsdf	Alpha	1.18	0.08	< 0.0001	*****	D	0.055
		Natural	Beta	1.82	0.31	< 0.0001		
		t	997	285	0.0004	*****	p-value	0.64
		Rollover	440	na	na	na		
	dsda & dsdf	Alpha	1.98	0.37	< 0.0001	*****	D	0.089
		Logged	Beta	1.21	0.24	< 0.0001		
		t	1686	498	0.0007	*****	p-value	0.63
		Rollover	440	na	na	na		

Supplementary material



Supplementary Figure 1. Mean monthly precipitation (1960-2010) at: (a) Port Alice (lat: 50.39; long: -127.46); (b) Port Hardy (lat: 50.68; long: -127.37); and (c) Quatsino (lat: 50.53; long: -127.65). Dashed lines enclose 5th-95th percentile envelopes. Data source: https://climate.weather.gc.ca/historical_data/search_historic_data_e.html

Supplementary Table 1. Uncertainty of the Double Pareto Simplified distributions (i.e., parameters and rollover), as obtained for bootstrap resampling.

LANDSLIDE AREA					LANDSLIDE LENGTH				
Percentile	Alpha	Beta	t	Rollov	Percentile	Alpha	Beta	t	Rollov
All					ds - Natural				
1%	1.01	2.45	226.14	230	1%	1.53	2.87	1.26	14
5%	1.02	2.59	243.86	250	5%	1.59	3.32	1.78	15
25%	1.05	3.05	260.25	260	25%	1.73	5.41	5.72	16
50%	1.07	3.05	274.92	270	50%	1.93	7.67	11.65	18
75%	1.09	3.05	295.95	280	75%	2.09	18.55	16.3	19
95%	1.13	3.05	355.86	300	95%	2.57	100	23.25	22
99%	1.14	3.05	392.03	320	99%	2.77	100	28.85	24
Natural					ds - Logged				
1%	0.9	2.37	134.89	280	1%	1.62	3.04	1.93	17
5%	0.92	2.69	141.79	290	5%	1.69	4.11	2.25	17
25%	0.96	3.5	173.15	310	25%	1.8	7.89	2.55	18
50%	0.99	4.34	205.72	340	50%	1.88	100	3.25	19
75%	1.03	4.85	282.37	350	75%	2.08	100	14.22	21
95%	1.08	4.85	381.19	380	95%	2.51	100	25.11	24
99%	1.09	4.85	538.93	390	99%	2.83	100	33.88	27
Logged					AREA: dsda & dsdf - Natural				
1%	1.27	1.66	368.07	180	1%	1.06	1.83	836.97	360
5%	1.29	1.89	399.21	200	5%	1.11	1.83	876.24	380
25%	1.37	1.89	441.81	220	25%	1.15	1.83	954.98	418
50%	1.41	1.89	473.55	230	50%	1.18	1.83	1010.7	450
75%	1.48	1.89	515.52	253	75%	1.22	1.83	1080.9	480
95%	1.58	1.89	563.88	280	95%	1.28	1.83	1142.28	510
99%	1.73	1.89	660.46	290	99%	1.31	1.83	1190.33	540
ds - Natural					dsda & dsdf - Logged				
1%	1.35	2.03	97.88	170	1%	1.28	0.91	646.09	121
5%	1.38	2.11	107.53	180	5%	1.49	0.97	910.46	230
25%	1.55	2.41	201.45	210	25%	1.75	1.07	1293.25	360
50%	1.69	2.88	306.26	230	50%	2.01	1.2	1768.18	440
75%	1.85	3.8	358.41	260	75%	2.36	1.44	2136.84	510
95%	2.07	7.5	386.65	291	95%	2.94	1.87	2543.72	596
99%	2.2	7.5	386.65	310	99%	3.34	2.19	2723.8	712
ds - Logged					dsda & dsdf - Natural				
1%	1.36	2.03	130.14	160	1%	1.1	1.82	1.02	34
5%	1.51	2.12	138.97	170	5%	1.17	1.9	12.76	36
25%	1.66	2.74	173.62	190	25%	1.23	2.27	28.61	41
50%	1.8	3.52	222.3	210	50%	1.33	3.13	46.91	44
75%	1.94	4.43	284.98	230	75%	1.46	4.36	73.13	47
95%	2.37	4.52	407.61	251	95%	1.55	8.8	100	51
99%	2.63	4.52	412.54	270	99%	1.62	82.02	100	54
ds - Natural					dsda & dsdf - Logged				
1%	1.53	2.87	1.26	14	1%	1.84	1.67	74.2	43
5%	1.59	3.32	1.78	15	5%	1.97	1.72	82.95	47
25%	1.73	5.41	5.72	16	25%	2.12	1.92	100	55
50%	1.93	7.67	11.65	18	50%	2.24	2.03	100	59
75%	2.09	18.55	16.3	19	75%	2.33	2.22	100	64
95%	2.57	100	23.25	22	95%	2.53	2.53	100	70
99%	2.77	100	28.85	24	99%	2.71	2.77	100	73

Supplementary Table 1 (continued)

LANDSLIDE VOLUME				
Percentile	Alpha	Beta	t	Rollov
All				
1%	0.83	1.71	154.36	130
5%	0.84	2.07	165.45	140
25%	0.87	2.59	178.82	150
50%	0.89	2.59	190.94	155
75%	0.91	2.59	207.43	160
95%	0.95	2.59	286.57	170
99%	0.97	2.59	428.22	180
Natural				
1%	0.76	1.84	85.43	160
5%	0.77	2.1	90.81	170
25%	0.81	2.86	107.26	190
50%	0.83	3.83	129.04	200
75%	0.86	4.09	208.37	220
95%	0.91	4.09	357.83	240
99%	0.93	4.09	456.8	260
Logged				
1%	1.06	1.36	287.44	88
5%	1.08	1.48	297.78	92
25%	1.14	1.59	342.56	110
50%	1.19	1.59	382.94	130
75%	1.24	1.59	402.89	140
95%	1.34	1.59	455.84	150
99%	1.4	1.59	568.36	160
ds - Natural				
1%	1.07	1.75	40.8	94
5%	1.17	1.84	68.26	120
25%	1.36	2.15	145.09	140
50%	1.49	2.45	229.87	150
75%	1.59	3.42	273.2	170
95%	1.82	7.5	273.2	190
99%	1.85	7.5	273.2	200
ds - Logged				
1%	1.23	1.63	76.5	91
5%	1.28	1.75	94.53	110
25%	1.45	2.33	127.67	120
50%	1.56	2.77	170.27	130
75%	1.72	3.38	213.33	143
95%	2.03	3.79	294.77	161
99%	2.2	3.79	294.77	170
dsda & dsdf - Natural				
1%	0.9	1.53	682.28	170
5%	0.92	1.53	764.34	190
25%	0.95	1.53	867.51	220
50%	1	1.53	925.6	250
75%	1.03	1.53	1005.9	270
95%	1.08	1.53	1115.18	310
99%	1.12	1.53	1235.84	350
dsda & dsdf - Logged				
1%	1.29	0.73	891.23	44
5%	1.35	0.79	974.31	91
25%	1.51	0.88	1280.61	168
50%	1.72	1.01	1734.88	215
75%	1.98	1.23	2244.43	280
95%	2.45	1.29	2906.2	367
99%	2.64	1.29	3561.34	460

CHAPTER 5

Concluding Remarks and Summary

Multi-temporal inventories are practical tools for characterizing landslide occurrence as well as for evaluating relevant decadal responses to external forcing over large spatial scales, from single watersheds up to regions. In this doctoral thesis, we have compiled multi-temporal inventories in two physiographic settings with contrasting land-cover history, where different styles and intensities of human disturbance have occurred. Variable anthropogenic forcing in time and space inherently controls the spatial distribution and turnover of land-cover patches, and therefore affects the quality and resolution of historical land-cover mapping through which we evaluate relevant landslide responses.

Landslide identification and delineation via aerial photo interpretation is not a simple task and is conditioned by the quality and availability of historical optical imagery, landscape morphometry, land cover, density of forest canopy, landslide type, and landslide temporal nature. In turn, these components influence the completeness of an inventory, hence the uncertainty associated with relevant quantitative evaluations. For example, in the Tsitika and Eve River basins (Chapter 4), we have seen how forest canopy can hamper landslide identification, imparting landslide visibility thresholds related to forest age (i.e., cutblocks vs old-growth forest), and that landslides may remain consistently visible for about 30 years since occurrence. These thresholds influence the manual delineation of landslide areas, as well as our ability to distinguish between initiation, transportation and deposition zones, and consequently affect relevant estimations of disturbed areas and volumes of mobilized debris. In the Sillaro River basin (Chapters 2 and 3), we found forest cover to be not particularly limiting, due to the lower density of the forest canopy and to less rugged topography. In this setting, we found that landslide identification and area delineation was more difficult within badlands, due to the poor contrast between the substrate and freshly displaced sediment, and by the virtually “chronic” nature of recurring earthflows within gully systems. Our ability to detect these frequent sediment pulses influences the completeness of an inventory. For example, the availability of photo year 2006 has been instrumental for capturing the earthflow surge associated to a rotational slump, which otherwise would have gone undetected (Figure 1). In this respect, the effort spent in the compilation of the inventory over 12 sequential photosets: (i) ensures higher temporal resolution, compared to existing inventories across the Mediterranean, which typically rely on two to four sets; (ii) has allowed to constrain a temporal window of 15 years for consistent landslide identification and mapping. This window was found to highest in managed forest, where the footprint of landslide scars on aerial photos tend to persist for about 17 years, and lowest in transitional shrubland, where highly dynamic vegetation patches induce landslide obliteration after about 13 years.

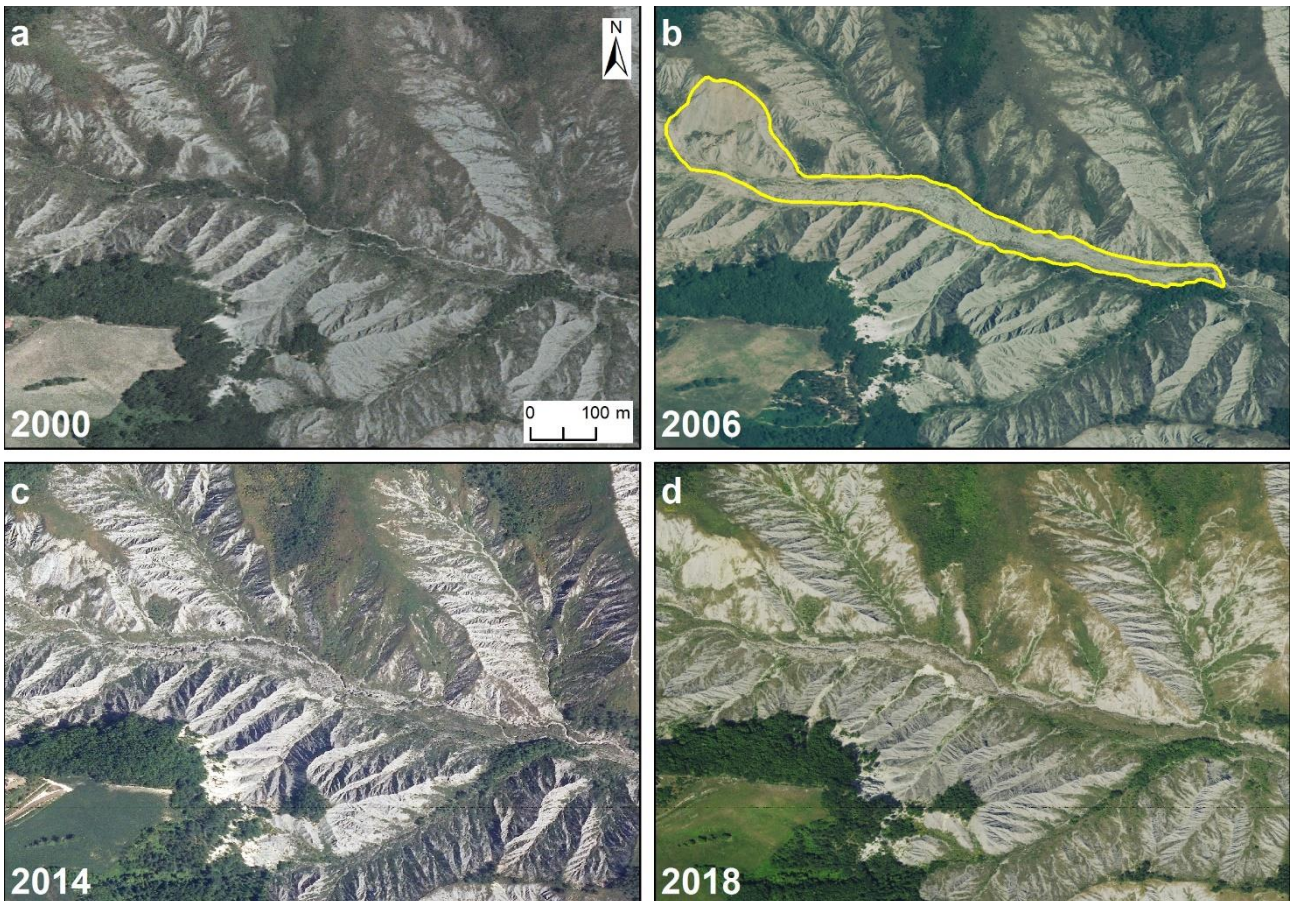


Figure 1. Dynamic plan-view of a badland complex in photo year: (a) 2000 (b) 2006, (c) 2014, and (d) 2018. Compare vegetation cover along the main tributary valley floor, before (i.e., 2000), and after (i.e., 2014 and 2018) appearance of a channelized earthflow (yellow polygon outline) in photo year 2006.

The nature of the surficial materials involved directly affects the landslide types that dominate the two different study areas. In coastal British Columbia, debris slides, avalanches, and flows are all characterized by a high degree of mobility (i.e., high efficiency of sediment transfer) from the initiation-transportation zone down to the relevant deposition zone, making it feasible in the field to measure depths (of erosion or deposition) to constrain area-volume relations and estimate volumes of mobilized debris. On the contrary, in the clay-rich lithologies of the Sillaro River basin, where earthflows and earth slides are dominant, “fine and sticky” sediment pulses can produce elusive memory effects associated with more complex runout dynamics over time and space, thus making the estimation of landslide depths and volumes trickier. In this context, ad hoc field-based surveys are in progress, but are beyond the scope of this thesis, considering the logistical and temporal efforts required. For this reason, the thesis component of the Sillaro River basin does not include estimates and analysis of mobilised volumes.

In this thesis, the advantages of multi-temporal landslide inventorying have been explored in Chapter 2. Here, a novel dynamic mapping approach was applied to four landslide sites of the Sillaro River basin, and compared with the existing (static) mapping of the Emilia-Romagna inventory. Results show that multi-temporal

mapping allows not only to identify occurrences and recurrences, but may also improve landslide detection, and reduce the uncertainties on existing landslide polygons. In addition, the proposed approach provides insights on process understanding and on scenarios of evolution at the site-scale, through detection of (i) source-to-sink pathways, (ii) revegetation patterns, (iii) headscarp migration, and (iv) changes at landslide terminus and/or induced changes in the geometry and sediment texture of the channel bed.

In Chapter 3, we applied the multi-temporal mapping approach at the basin scale (1954-2018), in relation to dominant lithologies, and to historical changes in land-cover and precipitation regime. Results display that landslide in the Sillaro River basin are predominantly recurring in nature and that they occur mainly in badlands and transitional shrubs of Epiligurian and Ligurian claystones, and subordinately in the Padano-Adriatic claystones. Landslide geometry is typically elongated and is controlled by lithology and terrain morphometry. By contrast, land-cover affects landslide geometry in a limited way. Accordingly, landslides are distinctively shorter and smaller on arable crops and meadows. Considering the temporal variability, number and areas of recurring movements are always dominant over episodic counterparts. In the roughly 80-year time window considered, landslides at a site can recur up to 9 times. Analyses on landslide temporal variability in relation to land-cover changes across geologic domains show that badlands are associated with highest historical landslide densities across all four time periods examined, followed by transitional shrubland, managed forest, and arable crops. Excluding arable crops - due to the limited number of landslides and the comparably gentler terrain on which they occur - this land cover stability ranking broadly agrees with expectations on the stabilizing effect of an increasingly structured vegetation cover. When land use effects are assessed as a function of slope gradient, different behaviours are observed in the four geologic domains. Our findings indicate that landslide activity is highest in the last twenty years, during a period of generalized land-cover stability, but where changes in precipitation regime are apparent (i.e., decrease in precipitation totals increasingly dominated by extreme events). Accordingly, we find high correlation between landslide activity and specific precipitation indices. In this context, badlands turned out being the most sensitive sites to changes in precipitation, with highest landslide densities between 1997 and 2018 in all but the Padano-Adriatic claystones. These stand out for their highest density scores between 1955 and 1976, a pattern that we explain with the agricultural encroachment of unstable badlands terrain.

In Chapter 4 landslide geometry of the Tsitika and Eve basins have been analysed to evaluate the effects of forest harvesting on landslide size and frequency. Main results display no significant dependency of landslide depth with length, width and therefore area, regardless of land use and movement type. For this reason, the same area-volume relation was applied to the whole inventory. Post-logging landslide occurrences are highest after 7-9 years and recover to undisturbed rates after 16-19 years since harvesting operations ceased. Data stratification by movement type, display that debris slides are smallest than long runout failures, while considering the morphologic position at initiation, primary movements (i.e., gully headwall and open slope) are bigger than secondary movements (i.e., gully sidewall and escarpment). Due to the low elevation of cutblock development, logging generates landslides at low elevations and low slopes, where they would not

normally occur. This topographic position has no effect on the size-frequency relation of debris slides but limits the size of logging-related long runout failures (i.e., debris avalanches and debris flows). The landscape structure combined with the location of cutblocks and logging roads on the slopes, exert primary control on initiation site characteristics (i.e., elevation and slope gradient), impose heavy constraints on local relief (i.e., available energy), slope length, and therefore on landslide length. The rollover occurs at transition among different morphologic position at initiation, controlled by first-order valley wall geometry for primary movements and by the geometry of second-order features, such as incisions on the hillslopes (i.e., gully depth) and valley floors (i.e., escarpment depth), for secondary movements.